A FUNDAMENTAL STUDY OF HIGH TEMPERATURE PROTON EXCHANGE MEMBRANES FOR FUEL CELLS

ZENG JIE

School of Mechanical & Aerospace Engineering

Nanyang Technological University

2012

A FUNDAMENTAL STUDY OF HIGH TEMPERATURE PROTON EXCHANGE MEMBRANES FOR FUEL CELLS

ZENG JIE

School of Mechanical & Aerospace Engineering

A thesis submitted to the Nanyang Technological University in fulfillment

of the requirements for the Degree of Doctor of Philosophy

2012

ABSTRACT

Proton exchange membrane fuel cells (PEMFC) have been considered as an attractive energy source for both portable and automobile applications because of their high energy conversion efficiency, high power density, quiet operation and low greenhouse gas emission. The efficiency and performance of PEMFCs can be further enhanced by increasing the operating temperature to 120-250 ^{o}C due to the improved reaction kinetics and significantly reduced catalyst poisoning by CO. Water and heat management of fuel cells systems becomes easier at high temperatures. However the grand challenge is to develop proton exchange membranes with high proton conductivity and stability at elevated temperatures and low humidity. For instance, the state-of-the-art PEM is the perfluorosulfonic acid (PFSA) polymers membrane due to their good mechanical properties, excellent chemical stability and relatively high proton conductivity under highly hydrated conditions. But the conductivity of PFSA-based membranes decreases significantly at elevated temperatures due to the dehydration and degradation of the membranes under elevated temperature (over 100 ^{o}C) and low relative humidity (RH) environment.

It has been well known that heteropolyacid (HPA) is a superionic conductor in its fully hydrated states. Among various HPAs, the highest stability and strongest acidity are observed for phosphotungstic acid ($H_3PW_{12}O_{40}$, abbreviated as HPW or PWA). Despite their high acidity, stability and high proton conductivity, the application of HPAs in proton exchange membranes of fuel cells is limited due to the sensitivity of their conductivity to the relative humidity of the surrounding environment in addition to their solubility in water. The risk of the leakage of HPAs during cell operation is thus high. In this thesis, a novel inorganic progon exchange membrane using HPAs as a proton carrier and mesoporous silica as framework materials is successfully developed as proton exchange membranes for fuel cells. Mesoporous silica is used as the host material to stablize HPAs which are introduced by a vacuum impregnation method. The threshold for a good proton conductivity of the HPW-meso-silica nanocomposite is ~10 wt%. The best proton conductivity is 0.07 Scm^{-1} at 25^{o}C under 100 %RH with activation energy of ~13.5 kJ mol^{-1}, obtained on the 67-83% HPW-meso-silica nanocomposites. The high stability of the Keggin anions of HPW within the meso-silica host most likely due to the formation of $(\equiv SiOH_2^+)$ $(H_2P_4W_{12}O_{40}^-)$ species. The proton conductivity and performance of HPW-meso-silica nanocomposites also increase with RH, but are far less sensitive to RH changes as compared to conventional PFSA polymers such as Nafion. These properties make the the HPW-meso-silica nanocomposite a promising proton conductor under high temperature and low RH environment.

Several effects were clearly observed during the synthesis of the mesoporous silica: Firstly, the structural symmetry of mesoporous silica can be altered by changing the surfactants used during the hydrothermal synthesis process; secondly, the pore size of mesoporous silica can be effectively controlled by carefully selecting the heat treatment temperature and/or heat treatment time. Those results provide insight into the materials engineering based on which we can synthesize mesoporous silica matrix material with tailored structural properties, i.e. surface area, pore volume, pore symmetry and pore size. The intrinsic relationship among the proton conductivity, thermal stability and structural symmetry of HPW-functionalized mesoporous silica membrane was investigated for different mesostructures of HPW-meso-silica. The HPW-meso-silica nanocomposites with 3D mesostructures show significantly high proton conductivity and high stability as a function of RH in comparison to 2D mesostructure, due to the higher interconnectivity of the $Fm\bar{3}m$, $Im\bar{3}m$ and $Ia\bar{3}d$ structures. The best result was obtained with the body-centered cubic ($Im\bar{3}m$) HPW-meso-silica, showing proton conductivities of 0.061 and 0.150 S cm^{-1} at 25 and 150 ℃, respectively, and an activation energy of 10.0 kJ mol^{-1}. The effects of pore size on the HPW leakage under water or fuel flowing were also investigated. The speed durability tests indicated that the smaller pore size leads to reduce leakage of HPW, and results in more stable membrane in terms of proton conductivity and mechanical property. The HPW-meso-silica membrane with pore size of ~5.0 nm showed both the highest proton conductivity and the best stability upon water washing. Various types of heteropoly acids including phosphotungstic acid, silicotungstic acid, phosphomolybdic acid and silicomolybdic acid were used as functional reagents to prepare different HPA-meso-silica nanocomposites. The good performance for the HPA-meso-silica nanocomposite materials is observed for phosphotungstic acid due to its highest stability and strongest acidity among various heteropoly acids.

Keywords: Silicon dioxide; direct methanol fuel cell (DMFC); Mesoporous structure; Proton exchange membrane fuel cell (PEMFC); Heteropoly acid (HPA); Proton exchange membrane (PEM)

ACKNOWLEDGEMENTS

Here I would like to express my sincere appreciation to my supervisors, Professor Jiang San Ping (Department of Chemical Engineering, Curtin University, Australia) and Professor Li Lin (School of Mechanical and Aerospace Engineering, Nanyang Technological University, Singapore) for their invaluable advice, supervision, encouragement and supports. Their profound background on fuel cell science helps me a lot and I really feel fortunate to pursue my Ph.D study under them.

My sincere thanks also extend to Dr. Tang Haolin, Dr. Lu Shanfu, Dr. Wang Deli, Mr. Lu Jinlin, Mr. Ge Xiaoming, Mr. He Hongquan and Dr. Zhang Lan, for their valuable help and discussions in carrying out this project. Special thanks go to all technicians in Fuel Cell Laboratory and Materials Laboratory: Mr. Chan Ming Jiu, Mr.Lee Koh Yiak, and Ms. Ho Agnes for their kind technical assistance.

Last but not least, I am grateful to my wife Li Huijun for her patience, support and encouragement.

TABLE OF CONTENTS

ABSTRACT..I
ACKNOWLEDGEMENTS...V
TABLE OF CONTENTS...VI
LIST OF ABBREVIATIONS...XI
LIST OF TABLES VII
LIST OF FIGURES XI
CHAPTER 1. INTRODUCTION...1

1.1 Background...1

1.1.1 Fuel Cell..2
1.1.2 Types of Fuel Cells 3

1.2 Types of PEM fuel cells..6

1.3 Objectives and Scope..8

1.5 Thesis Layout..10

CHAPTER 2. LITERATURE REVIEW...12

2.1 General introduction to PEM fuel cells 12

2.1.1 Fuel Cell Thermodynamics, Efficiency, Actual Performance.............14
2.1.2 Electrode Kinetics and Electrocatalysis..19
2.1.3 PEM fuel cells system...22

2.1.3.1 Single cell 22

2.1.3.2 Fuel cell stack 23

2.1.3.3 Proton exchange membranes for PEM fuel cells..........................24

2.2 Why high temperature PEM fuel cells...25

2.2.1 Enhanced tolerance to impurities in reformed fuels 26
2.2.2 Better Water and Thermal Management 29
2.2.3 Faster Electrode Kinetics 30
2.2.4 Improved O_2 mass transport...32

2.3 Major Challenges for PEMs under high temperature/low relative humidity operation 32

2.3.1 Low Relative Humidity Operation...33
2.3.2 Degradation in membrane conductivity...34

2.3.3 Degradation in membrane mechanical stability....................................35
2.3.4 Degradation in membrane chemical stability 36

2.4 Requirements for ideal high temperature PEMs..37

2.4.1 Electrolytic Function...38

2.4.1.1 Proton conductivity requirement for PEMs 38

2.4.1.2 Proton conductance mechanism in the PEMs...38

2.4.1.3 Microstructure of the PEMs...40

2.4.2 Fuel Separating Function 41

2.5 Development of High Temperature Proton Conductive Materials 42

2.5.1 Fluorinated polymers 42

2.5.1.1 The state of the art: perfluorosulfonic acid (PFSA) polymer membranes42

2.5.1.2 Modified PFSA polymer membranes...45

2.5.2 Polybenzimidazoles (PBI) 47

2.5.2.2 Modified PBI membrane..50

2.5.3 Inorganic proton conductors based on heteropoly acids (HPAs).........52

2.5.3.1 Basic types of heteropoly acids (HPAs)...52

2.5.3.2 Heterpoly acid functionalized materials 54

2.5.4 Glass membrane based on a acid phosphates and phosphosilicate......56
2.5.5 Inorganic proton conductors based on ordered nanoporous or mesoporous materials...58
2.5.6 The organic-inorganic hybrid membranes 62

2.6 Summary...64

CHAPTER 3. EXPERIMENTAL..67

3.1 Chemicals...67

3.2 Fabrication of HPA-meso-silica inorganic proton conductive materials...............68

3.2.1 Synthesis of mesoporous silica framework materials..........................68
3.2.2 Heterpoly acid functionalization of mesoporous silica with the assistance of vacuum impregnation devices 69

3.3 Fuel cell assembly and cell performance measurement 70

3.3.1 Gas diffusion electrode and catalyst layer 70

3.3.2 Membrane electrode assembly (MEA) and Catalyst coating membrane (CCM) 72
3.3.3 Full cell testing system 73

3.4 Electrochemical characterization 74

3.4.1 Membrane conductivity test using electrochemical impedance spectroscopy (EIS) 74
3.4.2 Methanol crossover current measurements 79
3.4.3 The electrode overvoltage measurement 80

3.5 Physical characterization 81

3.5.1 Small Angle X-ray Spectra (SAXS) 81
3.5.2 X-ray Diffraction (XRD) 82
3.5.3 N2 sorption isotherms 83
3.5.4 Transmission Electronic Microscopy (TEM) 84
3.5.5 Fourier Transform Infrared Spectroscopy (FTIR) 84
3.5.6 Raman scattering spectroscope 84
3.5.7 Thermal Gravimetric Analysis (TGA) 85
3.5.8 Weight increase, water uptake and swelling ratio of the membranes 85
3.5.9 Membrane wettability measurements 86
CHAPTER 4. Phosphotungstic Acid Functionalized Mesoporous Silica Nanocomposites 87

4.1 Introduction 87

4.2 Experimental 90

4.2.1 Preparation of HPW-meso-silica membranes 90
4.2.2 Cell preparation and characterization 90

4.3 Results and discussion 92

4.3.1 Structural properties and thermal stability of HPW-meso-silica nanocomposite measured through SAXS, N_2 absorption isotherms, TGA and TEM 92
4.3.2 Water uptake and conductivity of the HPW-meso-silica nanocomposites 103
4.3.3 Single cell performance 108
4.3.4. Proton transfer in HPW-meso-silica nanocomposites 113

4.4 Summary 115

CHAPTER 5. HPW-meso-silica Membrane With Tunable Bicontinuous Mesoporous Structure 116

5.1 Introduction 116

5.2 Experimental 119

5.2.1 Powder and cell preparation 119

5.2.2 Characterization 119

5.3 Results and discussion 121

5.3.1 Structural properties and thermal stability of HPW-meso-silica nanocomposite measured through SAXS, N_2 absorption isotherms, TGA and TEM 121
5.3.2 Conductivity, stability and water uptake 129
5.3.3 Influence of relative humidity on cell performance 135

5.4 Summary 138

CHAPTER 6. The HPW-meso-silica Nanocomposite Membranes and Performance in DMFC 140

6.1 Introduction 140

6.2 Experimental 142

6.2.1 Synthesis of meso-silica and HPW-meso-silica nanocomposites 142
6.2.2 Measurements of conductivity, cell performance, methanol crossover 142

6.3 Results and discussion 144

6.3.1. SAXS, TGA, TEM of HPW-meso-silica nanocomposites 144
6.3.2. Proton conductivity and cell performance 153
6.3.3 The on/off durability test on DMFC 159

6.4 Summary 161

CHAPTER 7. Heteropoly Acids Functionalized Silica Nanocomposites as Proton Conductors 163

7.1 Introduction 163

7.2 Experimental 165

7.3.2 Membrane wettability and conductivity 168
7.3.3 Influence of temperature on direct methanol fuel cell peroformance 172
7.3.4 Influence of methanol concentration on cell performance 174

7.4 Summary 177

CHAPTER 8. CONCLUSIONS 178

8.1 Conclusions 178

8.2 Major achievements 180

LIST OF PUBLICATIONS 181
REFERENCE 183

LIST OF ABBREVIATIONS

AAEM	Alkali Anion Exchange Membrane
AEM	Anion Exchange Membrane
AFC	Alkaline Fuel Cell
AFM	Atomic Force Microscopy
AMT	Ammonium Metatungstate
BET	Brunauer–Emmett–Teller
BJH	Barrett–Joyner–Halenda
CA	Chronoamperometry
CCM	Catalyst-Coated Membrane
CE	Counter Electrode
CMC	Critical Micellization Concentration
CMT	Critical Micellization Temperature
DAFC	Direct Alcohol Fuel Cell
DMFC	Direct Methanol Fuel Cell
ECSA	Electrochemical Surface Area
EDS	Energy Dispersive Spectroscopy
EIS	Electrochemical Impedance Spectroscopy
FE-SEM	Field Emission Scanning Electron Microscope
FRA	Frequency Response Analysis
FT-IR	Fourier Transform Infrared
FTIR	Fourier Transform Infrared Spectroscopy
GDE	Gas Diffusion Electrode
GDL	Gas Diffusion Layer
HPA	Heteropolyacid
HPW	Phosphotungstic Acid
HSiW	Silicotungstic acid
HPMo	Phosphomolybdic acid
HSiMo	Silicomolybdic acid

HRTEM	High Resolution Transmission Electronic Microscopy
IEC	Ion Exchange Capacity
ITO	Indium Tin Oxide
KU	Keggin unit
LSV	Linear Sweep Voltammetry
MCFC	Molten Carbonate Fuel Cell
MEA	Membrane Electrode Assembly
MOR	Methanol Oxidation Reaction
MWCNT	Multi-walled Carbon Nanotube
NLDFT	Non-Linear Density Function Theory
OCV	Open Circuit Voltage
PAFC	Phosphoric Acid Fuel Cell
PBI	Polybenzimidazole
PEEK	Polyether-etherketones
PEM	Proton Exchange Membrane
PFSA	Perfluorosulfonic Acid
SDBS	Sodium Dodecyl Benzene Sulfonate

LIST OF TABLES

Table 1. 1 Electrochemical characteristics of different types of fuel cells 4
Table 1.2 Leading types of fuel cells classified by operational temperature 5
Table 1. 3 Types of PEM fuel cells classified by operational temperature................................ 7
Table 2. 1 Standard enthalpy, Gibbs function of reaction for candidate fuels and oxidants, corresponding standard reversible cell potential, and efficiency (at 25 ℃ and 1 atm) 16
Table 2.2 Summary of modification of PFSA based membranes 45
Table 2.3 Advantages and disadvantages of some polymer membranes for PEM fuel cells ... 64
Table 4.1 Experimental conditions for HPW/meso-silica electrolyte fabrication 90
Table 4.2 Parameters of meso-silica and HPW-meso-silica nanocomposites with different HPW contents. .... **Error! Bookmark not defined.**
Table 5. 1 Experimental conditions for HPW-meso-silica electrolyte fabrication 119
Table 6.1 Synthesis conditions for Ia3d, Im3m, and Fm3m structure 142
Table 6.2 Textural parameters of *meso*-silica and HPW-*meso*-silica nanocomposites with different structure symmetries. 145
Table 7. 1 Water contact angle, the water uptake and the coresponding swelling ratio of several membrane materials of Nafion 117 membrane, meso-silica/PA membrane and aged meso-silica/PA membrane 168
Table 6.1 Synthesis conditions for Ia3d, Im3m, and Fm3m structure 142
Table 6.2 Textural parameters of *meso*-silica and HPW-*meso*-silica nanocomposites with different structural symmetries 145

LIST OF FIGURES

Figure 1. 1 A fuel cell system 2

Figure 2.1 Comparison of the thermodynamic efficiency between a heat engine and a H_2/O_2 fuel cell.(Larminie et al., 2003) 18
Figure 2.2 Fuel cell polarization curves showing various potential losses.............................. 19
Figure 2.3 Fuel cell descriptions 22
Figure 2.4 Schematic of a Fuel Cell stack.. 23
Figure 2.5 Absorption of CO on Pt... 27
Figure 2.6 CO coverage on a platinum as a function of temperature and CO concentration. The partial pressure of H_2 is 0.5 bar.(Yang et al., 2001) 28
Figure 2.7 Changes in vapor pressure of water with temperature 33
Figure 2.8 Radicals formation mechanism.. 36
Figure 2.9 Proton conductance mechanisms assisted by the dynamics of structural molecules. Above: the Grotthűss mechanism (proton transfer and subsequent molecular reorientation). Below: the vehicle mechanism (co-operative motion of neutral molecules and charged molecule/ proton complexes) (Kreuer, 1988) 39
Figure 2.10 Illustration depicting a phase-segregated system, where the minority phase (1) is interspersed within the majority phase (2) (shaded region). (a) All of the minority phase is isolated (I); (b) the minority phase contains both parts that are isolated (I) and accessible (A); (c) all of the minority phase is accessible (A). Transport occurs through the interconnected accessible pathways.(Elabd et al., 2003) 41
Figure 2.11 General structures of commercial available perfluorosulfonic acid (PFSA) polymers 42
Figure 2.12 Structure evolution of Nafion depending on the water content(Gebel, 2000) 44
Figure 2.13 Proton transport in a nanocomposite membrane(Hogarth et al., 2005c)............. 46
Figure 2.14 Chemical structure of various polybenzimidazoles (PBIs) (a) meta-PBI[poly(2,2’-(1,3-phenylene)5,5’-bibenzimidazole))], (b) AB-PBI [poly(2,5- benzimidazole)], (c) para-PBI[poly(2,2’-(1,4-phenylene)5,5’-bibenzimidazole))], (d)PPBI [pyridine-based PBIs], and (e) 2OH-PBI [poly(2,2’-(2,5-dihydroxy-1,4-phenylene) 5,5’-bibenzimidazole))](Xiao et al., 2005) 48
Figure 2.15 The PBI polymer membrane with mesoporous structure and increased phosphoric acid loading (Weber et al., 2008)... 50
Figure 2.16 Keggin structure of a phosphotungstic acid molecular. three types of exterior oxygen atoms were given: O_b, O_c, and O_d in the Keggin unit. O_a is the central oxygen atom (Yang et al., 2005b)... 53
Figure 2.17 A SEM micrograph of the cross-section of the MEA based on the P_2O_5-SiO_2 glass membrane after testing in the fuel cell (Uma and Nogami, 2007b)................................ 56
Figure 2.18 Two inorganic proton conductors based on mesoporous materials (left) Honeycomb layer structure of Metal-organic frameworks and Hydrogen-bond arrangements of -COOH, H_2O, and NH_4 in the interlayer. The colors of red, green, gray, and blue correspond to oxygen, nitrogen, carbon, and zinc atoms, respectively.(Sadakiyo

et al., 2009) (right)Aluminium porous frameworks serving as host frameworks for the preparation of proton-conductive materials(Bureekaew et al., 2009) 58

Figure 2. 19 Photographs of membrane of (a) 10 wt% organics and 90% $Sn_{0.9}In_{0.1}P_2O_7$ composite and (b) a pure $Sn_{0.9}In_{0.1}P_2O_7$ pellet from reference (Heo et al., 2007a) 63

Figure 3.1 Procedure of the synthesis processes of mesoporous silica 68

Figure 3.2 Procedure of the HPA impregnation step and HPA-meso-silica 69

Figure 3.3 Optical micrograph of a hot-pressed (a)80 wt% HPW-meso-silica nanocomposite disc (b)5%PVDF80%HPW15%meso-silica composite membrane before the electrochemical performance test. 70

Figure 3.4 Schematic diagrams of (a) Membrane Electrode Assembly (MEA) and (b)Catalyst Coating Membrane (CCM) with the home-made electrolyte membrane......................... 72

Figure 3.5 The picture and (b) the scheme of the DMFC test arrangement 73

Figure 3.6 Schematic of experimental setup for proton conductivity measurement in a temperature range of 25-300 ℃. The effective electrodes area was 4 cm^2...................... 74

Figure 3.7 Photos of a single cell used for proton conductivity test....................................... 76

Figure 3.8 (a) typical Nyquist plots measured for the cell with an inorganic membrane, the frequency range of 1M-1Hz and (b) the schematic of the EIS equivalent circuits 78

Figure 3. 9 Schematic illustration of the methanol permeation measurement in the actual DMFC 79

Figure 4.1 Small-Angle X-ray Scattering (SAXS) patterns of $Ia\bar{3}d$ mesoporous silica and HPW-meso-silica composite with different HPW contents. 92

Figure 4.2 (a) FTIR spectra and (b) Raman scattering spectra of HPW, meso-silica and HPW-meso-silica nanocomposites measured at room temperature. 94

Figure 4.3 TGA spectra of HPW, meso-silica and HPW-meso-silica nnaocomposites with different HPW contents.. 97

Figure 4.4 (a) N_2 absorption isotherms and (b) pore size distribution of (■) meso-silica, (●) 20%HPW-meso-silica, (▲) 40%HPW-meso-silica, (♦) 60%HPW-meso-silica and (▼) 80%HPW-meso-silica nanocomposites. 98

Figure 4.5 TEM images of (a) pure meso-silica; (b) 20%HPW-meso-silica, (c) 80%HPW-meso-silica; the left images were viewed from the [110] direction while the right images were viewed from the [111] direction. 100

Figure 4.6 (a)concentration of HPW within the mesoporous silica matrix and (b)distance between two nearest HPW molecules calculating from experimental results 102

Figure 4.7 Water uptake of pure meso-silica, pure HPW and HPW-meso-silica with various HPW contents. 104

Figure 4.8 (a) Proton conductivity versus temperature for the HPW-meso-silica composite membranes as a function of HPW content, (b) Proton conductivity versus HPW content measured at 25°C, and (c) Activation energy versus HPW content of the HPW-meso-silica membrane. Conductivity and activation energy of pure HPW are obtained from reference. (Osamu Nakamura et al., 1979) 105

Figure 4.9 Polarization and power density of single cell employing a 80%HPW-meso-silica nanocomposite membrane in (a) H_2/O_2 and at 80°C under different RH and (b) H_2/air at

80^{o}C under different RH. 108

Figure 4.10 (a) Methanol crossover limiting current curves of a 80%HPW-meso-silica nanocomposite membrane measured at different temperatures and (b) polarization and power density of single cells employing a 80%HPW-meso-silica membrane in methanol/air at different temperatures without external humidification, and (c) cell stability measured at a constant cell potential of 0.50 V at 150 ℃ in methanol/air without external humidification. 110

Figure 4.11 The proton transportation was proposed to occur effectively in two ways. One is that protons-hop on isolated phosphotungsitc acid molecules, briefly as an intramolecular proton transfer pathway. The other is called the intermolecular proton transfer pathway, in which the proton transfer process is achieved through a series of “hops” among HPW molecules and water molecules along the hydrogen bond between HPW and water. 113

Figure 5.1 Small-Angle X-ray Scattering spectra of mesoporous silica (solid line) and 80wt%HPW-meso-silica nanocomposites (dotted lines) synthesized at hydrothermal treatment temperatures: (a) 60 ^{o}C; (b) 100 ^{o}C and (c) 160 ^{o}C. 121

Figure 5.2 N_2 absorption isotherms and pore size distribution of (a, b) mesoporous silica synthesized with hydrothermal treatment temperatures of 60 ^{o}C, meso-silica-60 (□); 100 ^{o}C, meso-silica-100 (○); and 160 ^{o}C, meso-silica-160 (△); and of (c, d) HPW-meso-silica-60 (■); HPW-meso-silica-100 (●); and HPW-meso-silica-160 (▲). 122

Figure 5.3 TGA spectra of (a) HPW, (b) meso-silica, (c) HPW-meso-silica-60, (d) HPW-meso-silica-100, and (e) HPW-meso-silica-160 nanocomposites....................... 125

Figure 5.4 TEM images of pristine meso-silica and 80wt% HPW-meso-silica nanocomposites synthesized at different hydrothermal treatment temperatures; (a) meso-silica-60; (b) meso-silica-100; (c) meso-silica-160, (d) meso-silica-60 viewed along the pore axis (e) HPW-meso-silica-60; (f) HPW-meso-silica-100; (g) HPW-meso-silica-160; and (h) HPW-meso-silica-60 viewed along the pore axis. 127

Figure 5.5 (a) Arrhenius plots of (◊) pristine meso-silica-60, (▲) HPW-meso-silica-60, (●) HPW-meso-silica-100 and (■) HPW-meso-silica-160, measured under 100%RH. (b) Proton conductivity stability of the (▲) HPW-meso-silica-60, (●) HPW-meso-silica-100, and (■) HPW-meso-silica-160, measured at 80^{o}C under a constant water flow at 50 ml min^{-1}. 129

Figure 5.6 The conductivity of HPW-meso-silica-60 nanocomposite (■) as a function of humidity, measured at 80^{o}C. The conductivity data of Nafion 115 membrane (●) measured at 30 ℃ as a function of RH were taken from references.(Zhang et al., 2008) 131

Figure 5. 7 (a) Performance of single cells with HPW-meso-silica-60 nanocomposite membrane, measured in H_2/O_2 at 80^{o}C and different RH, and (b) performance of single cells with Nafion 115 membranes measured in H_2/O_2 and at 80^{o}C and different RH; (c) maximum power density of cells with HPW-meso-silica nanocomposite and Nafion 115 membranes as a function of RH; and 136

Figure 6.1 a) SAXS patterns of mesoporous silica with $P6mm$, $Fm\bar{3}m$, $Im\bar{3}m$ and $Ia\bar{3}d$ symmetries arranging from left to right (solid line); and the corresponding HPW-meso-silica nanocomposite: HPW-$P6mm$, HPW-$Fm\bar{3}m$, HPW-$Im\bar{3}m$ and HPW-

$Ia\bar{3}d$ arranging from left to right (dotted line) and b) The schematic structures of $P6mm$, $Fm\bar{3}m$, $Im\bar{3}m$ and $Ia\bar{3}d$ mesoporous silica from reference.(Wan and Zhao, 2007)... 144

Figure 6.2 N_2 sorption isotherms and pore size distribution of *meso*-silica (empty symbols) and HPW-*meso*-silica nanocomposites (filled symbols) with $P6mm$, $Fm\bar{3}m$, $Im\bar{3}m$, $Ia\bar{3}d$ symmetries; a, c) N_2 sorption isotherms; b, d) pore size distribution; Symbols in a-d: triangles, $P6mm$ and HPW-$P6mm$; circles, $Fm\bar{3}m$ and HPW-$Fm\bar{3}m$; squares, $Im\bar{3}m$ and HPW-$Im\bar{3}m$; and inverted triangles, $Ia\bar{3}d$ and HPW-$Ia\bar{3}d$ 146

Figure 6.3 TEM images of *meso*-silica (left micrograph) and HPW-*meso*-silica nanocomposites (middle and right micrographs); a) $P6mm$ and HPW-$P6mm$; b) $Fm\bar{3}m$ and HPW-$Fm\bar{3}m$; c) $Im\bar{3}m$ and HPW-$Im\bar{3}m$; d) $Ia\bar{3}d$ and HPW-$Ia\bar{3}d$. The left and middle images of each sets are viewed from [111] direction while the right images are viewed from [110] direction. 149

Figure 6.4 TGA curves of HPW, meso-silica and HPW-meso-silica nanocomposites; a) pure HPW; b) $Im3m$ silica; c) HPW-$P6mm$; d) HPW-$Fm3m$; e) HPW-$Im3m$; f) HPW-$Ia3d$. The numbers shown in the figures are the weight loss percentage at 200 ℃. 151

Figure 6.5 a) Conductivity as a function of (inverse) test temperature; b) conductivity as a function of RH measured at 80 ^{o}C. Triangles, HPW-$Ia\bar{3}d$; Inverted triangles, HPW-$Im\bar{3}m$; circles, HPW-$Fm\bar{3}m$ and squares, HPW-$P6mm$. The content of HPW in the HPW-meso-silica nanocomposites was 67 %HPW... 153

Figure 6.6 a)Polarization and power density of single cell employing a meso-silica/PA membrane in methanol/O_2 at 100-150 ℃; b) Evolution of the cell voltage during the durability test (the single cell polarized at 200 mA cm^{-2}, T=150 ℃, methanol/O_2=1 atm/1 atm) 158

Figure 6.7 Evolution of the cell voltage during the intermittent durability test (10 days for 16h at 200 mA cm^{-2}; T=80 ℃; methanol/O_2=1 atm/1 atm), only running hours are shown. Dashed lines indicate the overnight break. 159

Figure 7.1 FTIR spectra of mesoporous silica, 4 types of HPAs (HPW, HSiW, HPMo and HSiMo) and the coresponding 80% HPA-meso-silica nanocomposites measured at room temperature. 165

Figure 7.2 TGA spectra of 4 types of HPAs [(a)HPW, (b) HSiW, (c) HPMo, and (d) HSiMo], meso-silica and the coresponding 80%HPA-meso-silica nnaocomposites.................... 167

Figure 7.3 Water contact angle on the surface of Nafion 117, HPW-meso-silica, HSiW-meso-silica, HPMo-meso-silica and HSiMo-meso-silica membrane 168

Figure 7.4 Arrhenius plots of (▼) pristine meso-silica, (●) 80%HSiMo-meso-silica, (▲) 80%HPMo-meso-silica (■) 80%HSiW-meso-silica and (◀)80%HPW-meso-silica, measured under 90 %RH. 171

Figure 7.5 Influence of temperatures on (a) cell performance (b) methanol limit current density (c) electrode overvoltage and (d) open circuit voltage and methanol crossover current of a vapor-fed meso-silica/HPW membrane based DMFC.. 172

Figure 7.6 Influence of methanol concentration on (a) cell performance (b) methanol limit current density (c) electrode overvoltage and (d) open circuit voltage and methanol crossover current of a vapor-fed HPW-meso-silica membrane based DMFC............... 175

CHAPTER 1. INTRODUCTION

1.1 Background

The history of fuel cells dates back to 1839 when Sir W.R. Grove (1811 -1896) first demonstrated that electricity can be generated using hydrogen and oxygen gases. His invention was made soon after British scientists William Nicholson and Anthony Carlisle(Perry and Fuller, 2002) had described the process of using electricity to decompose water into hydrogen and oxygen on platinum electrodes. The term “fuel cell” was not used until researchers Mond and Langer(Mond and Langer, 1889) attempted the first practical design of the fuel cell, utilizing coal gas and air. A great deal of work on fuel cells was carried out in Germany in the early 20th century. Interest in fuel cells faded due to widespread exploitation of cheap fossil fuels and the advent of internal combustion engines. During the 1960s, the U.S. National Aeronautics and Space Administration (NASA) needed an auxiliary source of electricity for their space shuttles which led to the discovery of a Proton Exchange Membrane Fuel Cell (PEMFC) by General Electric Co.(GE), which utilized a sulfonated polystyrene ion-exchange membrane as the electrolyte (Shair et al., 1967). Major automobile manufacturers and various government agencies have invested billions of dollars in the development of fuel cell technology for automobile and other applications. The fuel cell as a power supply is expected to replace the traditional power sources, from secondary batteries used in cell phones and laptops to internal combustion engines in cars (Zhao et al., 2007).

1.1.1 Fuel Cell

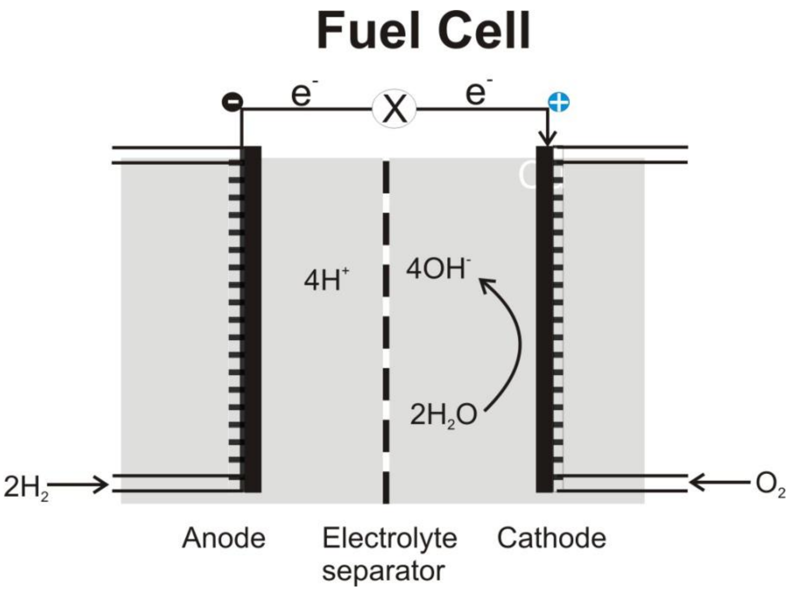

Figure 1. 1 A fuel cell system

A general representation of fuel cells is depicted in Figure 1.1. Fuel cells and batteries both generate electrical energy via chemical reduction-oxidation (redox) reactions. These reactions occur at electrodes comprised of an anode and a cathode. The anode reactions generally take place at a lower potential than the cathode. The anode and cathode in fuel cells are present for charge transfer, while the active mass, or fuel, is delivered externally making it an open system, while batteries are closed systems where the anode and cathode act not only as the charge transfer medium but also as part of the active mass. While batteries have a finite lifespan, fuel cells will continue to function as long as active mass, or fuel, is fed into the system, making fuel cells attractive alternatives in applications requiring continuous power sources. Fuel cells were mainly intended to displace internal combustion engines. However, more extensive uses are now targeted to displace batteries in portable electronic devices (i.e. cellular phones and laptops) and as sources of stationary power.

1.1.2 Types of Fuel Cells

Fuel Cells can be classified based on their temperature of operation into high, medium and low temperature fuel cells or based on the type of electrolyte used. Primarily, the latter method of classification is used for easier understanding and practical reasons. Table 1.1 and table 1.2 provide six common types of fuel cells: Proton Exchange Membrane Fuel Cells (PEMFC & DMFC), Alkaline Fuel Cells (AFC), Phosphoric Acid Fuel Cells (PAFC), Molten Carbonate Fuel Cells (MCFC) and Solid Oxide Fuel Cells (SOFC). The classification determines the chemical reactions that take place, type of catalysts and electrolyte required, operating temperature and fuel used. These factors in turn determine the most suitable applications for each type of fuel cell. The essential characteristics of the major types of fuel cells are listed in Table 1.2. PEMFCs have become the focus for automotive propulsion efforts because of their relatively low operational temperature and their potential for low cost mass production. PEMFCs present several advantages comparing to other types of fuel cells. They are compact, lightweight and can generate electricity with both high power density and high current density. PEMFCs are constituted with an electrolyte working at low temperature allowing rapid start-up at low temperatures. Other advantages result from the electrolyte being a solid material, compared to a liquid. The sealing of the anode and cathode gases is simpler with a solid electrolyte, and therefore, less expensive to manufacture. The solid electrolyte does not have the difficulty in orientation and has fewer problems with corrosion, compared to many of the other electrolytes, thus leading to a longer cell and stack life. Currently, the hydrogen and direct methanol PEM fuel cells are studied extensively in the automotive field. For the foreseeable future, DMFCs seem to be more promising for portable power application than high-power application such as motor vehicles.

Table 1. 1 Electrochemical characteristics of different types of fuel cells

Fuel cell systems	Electrodes reactions	Conductive ions
Proton Exchange Membrane Fuel Cell (PEMFC)	Anode: $H_2 \rightarrow 2H^+ + 2e^-$ $Cathode$: $1/2O_2 + 2H^+ + 2e^- \rightarrow H_2O$	H^+
Direct Methanol Fuel Cell (DMFC)	Anode: $CH_3OH + H_2O \rightarrow CO_2 + 6H^+ + 6e^-$ $Cathode$: $3/2O_2 + 6H^+ + 6e^- \rightarrow 3H_2O$	H^+
Alkaline Fuel Cell (AFC)	Anode: $H_2 + 2OH^- \rightarrow 2H_2O + 2e^-$ Cathode: $2H_2O + 2e^- + 1/2O_2 \rightarrow 2OH^-$	OH^-
Phosphoric Acid Fuel Cell (PAFC)	Anode: $H_2 \rightarrow 2H^+ + 2e^-$ $Cathode$: $1/2O_2 + 2H^+ + 2e^- \rightarrow H_2O$	H^+
Molten Carbonate Fuel Cell (MCFC)	$Anode$: $H_2 + CO_3^{2-} \rightarrow H_2O + 2e^-$ Cathode: $CO_2 + 2e^- + 1/2O_2 \rightarrow CO_3^{2-}$	CO_3^{2-}
Solid Oxide Fuel Cell (SOFC)	Anode: $H_2 \rightarrow 2H^+ + 2e^-$ $Cathode$: $1/2O_2 + 2H^+ + 2e^- \rightarrow H_2O$	O^{2-}

Table 1.2 Leading types of fuel cells classified by operational temperature

Fuel cell systems	PEM fuel cells (PEMFC/DMFC)	AFC	PAFC	MCFC	SOFC
Temperature Range (℃)	20-150	60-120	160-220	620-660	800-1000
Electrolyte	Proton exchange membrane	KOH	H_3PO_4	Molten $LiCO_3$+K_2CO_3	ZrO_2+Y_2O_3
CO	Poison	Poison	Poison	Fuel	Fuel
CO_2	Diluent	Poison	Diluent	Diluent	Diluent
Internal Reforming	No	No	No	Yes	Yes

1.2 Types of PEM fuel cells

Park(Park et al.) classified PEM fuel cells into three categories depending on their operating temperature as given in table 1.3: high-temperature PEM fuel cells over 120 ℃, medium-temperature PEM fuel cell from 80 to 120 ℃, and low- temperature PEM fuel cells below 80 ℃. High temperature PEM fuel cells are generally operated under non-humidified conditions because water boils at 100 ℃. Low-mid temperature PEM fuel cells are operated either under fully humidified conditions below 100 ℃ or under reduced humidity conditions over 100 ℃. The literatures investigation indicates that most of the research on PEM based fuel cells (e.a. PEMFC and DMFC) is orientated toward high temperature PEM fuel cells (Laberty-Robert et al., 2011, Zhang et al., 2006a). The term "high temperature" refers to the temperature range, 120-250 ℃. PEM fuel cells operating at high temperatures are considered as one of the potential solutions for the technical challenge faced during low temperature operation. Beside many advantages in terms of faster reaction kinetics, simpler heat and humidity control system and higher capacity of hydrogen storage system; high temperature operation also opens a gate for the use of more complex alcohols such as ethanol, propane as fuels which leads to new types of PEM fuel cell system, as listed in Table 1.4. In the current state of the art, development of high temperature PEM fuel cell is also very important in the field of materials science and engineering. The main technical obstacle during high temperature operation comes from the proton-exchange-membranes, to their poor mechanical properties above about 100 ℃ and to the high methanol crossover.

Table 1. 3 Types of PEM fuel cells classified by operational temperature

Types	Operational temperature (℃)	More fuels for use	Membranes available
Low temperature PEM fuel cells	< 80	Pure H_2, methanol	PFSA, SPEEK
Medium temperature PEM fuel cells	80-120		Modified PFSA, inorganic-organic hybrid membrane, solid salt membrane
High temperature PEM fuel cells	120-150	Reformatted H_2	PBI/PA, inorganic-organic hybrid
	150-250	Ethanol	PBI/PA
	≥250	Propane	N.A.

1.3 Challenge and motivation

Despite the substantial efforts in the development of PEMFC technologies in last decades, there are still significant challenges to the large-scale production and commercialization of the technology. One of the key challenges is related to the limited functionality of current proton exchange membranes (PEMs). The state-of-the-art PEM is the perfluorosulfonic acid (PFSA) polymers (e.g., Nafion developed by DuPont) due to their good mechanical properties, excellent chemical stability and relatively high proton conductivity at highly hydrated conditions.(Feindel et al., 2007, Mauritz and Moore, 2004) However, the conductivity of PFSA-based membranes decreases significantly at elevated temperatures (≥100 ^{o}C) due to the dehydration and degradation of the membranes over 100 ^{o}C and at low relative humidity (RH) environment.(Yang et al., 2004, Sone et al., 1996, Anantaraman and Gardner, 1996, Hogarth et al., 2005b) And a fully hydrated membrane requires using an external humidifier, which results in a more complex and expansive fuel cell system. Thus, a limitation of the water-thermal management is imposed on PEM fuel cells. To address these problems, we need new membrane materials with sufficient proton conductivity operating at low humidity and temperatures above 100 ℃. We also need to solve another problem: the thermo-mechanical properties of membranes must be improved. Many polymer membranes swell up upon hydration, which causes mechanical stress and deteriorates membranes' mechanical properties. Furthermore, methanol easily permeates these polymer membranes, which limits the performance of direct methanol fuel cells (DMFC). The polymer membranes also exhibit poor thermal and chemical stability and limited durability in operational environments. A suitable membrane is the main obstacle in the PEM fuel cell technology and requires further development.

1.4 Objectives

The objectives of the project include fundamental research and development on novel high temperature membranes in the field of materials science and engineering for high temperature PEM fuel cells (e.g. PEMFCs and DMFCs). The fuel cell system optimization will also be addressed to improve power density by reducing membrane resistance to proton conductance and fuel crossover through the proton exchange membrane. The creation of a new high-temperature membrane with desired performance characteristics requires significant fundamental research and development. The membrane has to be thermally and dimensionally stable, be resistant to fuel permeation, and be highly proton conductive under high temperature and low RH conditions.

1.5 Scope

The main objective of this project is to synthesize and develope a novel composite membrane and fundamentally study proton conduction mechanism in such a composite membrane. Thus, the scope of the project includes:

1. Synthesize and characterize mesoporous silica materials with well ordered mesoporous structure with inter-connective pores and tunable pore sizes.
2. Study effects of various structure symmetries and pore sizes of the mesoporous silica materials, which can be used as framework materials in a proton exchange membrane, on the membrane conductivity, stability and cell performance for both hydrogen and methanol;
3. Examine effects of different types of heteropoly acids on the membrane conductivity, thermal stability;
4. Explore mechanism of proton conductance within mesoporous structure of the inorganic proton exchange membrane.

1.6 Thesis Layout

This thesis consists of eight chapters. Chapter 1 provides the reader with an introduction to the background and objectives of this study. Chapter 2 gives a literature review on the topic, which covers the challenges faced by fuel cell technology and provides detail about the high temperature operation as an effective solution to these challenges. The main focuses of this literature are the development of high temperature proton exchange membrane materials used in PEMFC and DMFC systems. Chapter 3 describes synthesis of mesoporous silica and the measurement techniques including experimental system for measuring the conductivity of inorganic proton conductors under wide ranges of temperature and relative humidity. Chapter 4 presents the preparation and characterization of HPW-functionalized mesoporous silica (HPW-meso-silica) membrane. The dependence of the conductivity of HPW-meso-silica nanocomposites on the HPW loading is measured and discussed. Chapter 5 provides experimental results on the influence of structural properties of silica host such as pore size, pore volume and surface area on the proton conductivity. The stability property of HPW-meso-silica nanocomposite has been investigated in detail. Chapter 6 reports the results on the relationship among the proton conductivity, thermal stability and structure symmetries of mesoporous silica host materials. Chapter 7 gives the synthesis and characteristics of high temperature proton exchange membranes based on various heterpoly acids. The system factors that influenced the cell performance were also investigated in detail for DMFC. Chapter 8 gives an overall summary of the completed research, draws the most important conclusions.

CHAPTER 2. LITERATURE REVIEW

This chapter starts with fundamental part describing proton-exchange-membrane (PEM) based fuel cells and the roles of a PEM playing in fuel cells, followed by a timely review on the major advances and challenges that concern the high temperature operation for fuel cells. Thereafter, the state of the art of functional polymers such as Nafion and polybenzimidazoles (PBI) will be briefly summarized. In the end the different families of inorganic membranes will be presented together with a discussion of their performance and limits.

2.1 General introduction to PEM fuel cells

The Proton Exchange Membrane Fuel Cell (PEMFC), formerly known as the Solid Polymer Electrolyte Fuel Cell or Polymer Electrolyte Fuel Cell was invented by General Electric Company and was used in the Gemini space flights. A 1 kW system was used as an auxiliary power source and the product water served as drinking water for the astronauts. This fuel cell utilized a polystyrene sulfonic acid membrane electrolyte with platinum electrocatalysts. Though the fuel cells performed well in space missions for up to two weeks, problems were encountered with the stability of the membrane electrolyte. Additionally low attainable power densities and high loadings of the platinum electrocatalyst limited the stack practicality. A major breakthrough in PEM fuel cells technology was attained by the use of Nafion, a perfluorinated sulfonic acid (produced by DuPont) as the electrolyte. Application of the PEM fuel cells as a primary power source has received increasing attention during the past decades with its proposed use in passenger buses and cars. Compared to other types of fuel cells, PEMFCs provide the advantages including simple fabrication, absence of corrosive liquid, minimal corrosion problems and long lifetimes. They are also compact, lightweight and they generate a specific power (W kg^{-1}) and power density (W cm^{-2}) higher than any other type of fuel cells and hence are favored for a variety of applications-namely, transportation, stationary and portable applications. The most dramatic advances in research and development of stack have been made during the past 25 years. Through the mid-1980s, the energy and power densities of stack were so low and the necessary loading of platinum catalysts was so high that most commercial applications, let alone automotive use, seems out of question. Platinum requitements for the GE stack in 1960s were on the order of 100g kW^{-1}, costing US$1400 kW^{-1}.(Appleby and Yeager, 1986) Costs appeared prohibitive due to both expensive membranes and especially the high platinum catalyst loading. In 1983, Ballard started its research and development work on PEM stack. Ballard's work was the first serious engineering effort with PEM technology since GE's effort two decades ago. The company was able to address membrane, electrode, flow field, and other issues adequately, to the point of where major performance improvements were achieved by 1986. Announcement of these results at a fuel cell conference that year sparked broader attention to the potential of PEM technology. Even as of 1990s, the quantity of platinum catalysts required for a stack cost was on the order of $75/kW.

(Srinivasan et al.) Then, largely through the continuing efforts at Ballard, platinum cost was decreased by one order of magnitude within a few years, to \$6/kW by 1993 in static application. Based on laboratory demonstrations of improved catalyst deposition techniques, platinum catalysts cost levels of \$2-3/kW now appear possible. The US Department of Energy (DOE) has targeted a large scale fuel cell for transportation application manufacturing at \$30 kW^{-1} by 2015.

2.1.1 Fuel Cell Thermodynamics, Efficiency, Actual Performance

Fuel cells are galvanic cells, in which the free energy of a chemical reaction is converted into electrical energy (or electrical current). The Gibbs free energy of a chemical reaction is related to the cell voltage via:

$$\Delta G = -nFE \tag{2.1}$$

Where n is the number of electrons involved in the reaction, F is the Faraday constant, and E is the cell voltage under thermodynamic equilibrium in the absence of a current flow. The anode reaction in a fuel cell is either the direct oxidation of hydrogen or the oxidation of hydrocarbons. An indirect oxidation via a reforming step can also occur. The cathode reaction in a fuel cell is oxygen reduction. In most cases oxygen comes from air. In the case of hydrogen/oxygen fuel cells, the overall reaction is:

$$H_2 + \frac{1}{2}O_2 = H_2O(liquid) \qquad \Delta G = -237.3\ kJ\ mol^{-1} \tag{2.2}$$

Meanwhile, the electric work obtained from the external load is 2FE. If we assume that there are no losses in the cell voltage or if the process is reversible, all the energy from this reaction, Gibbs free energy, is converted to electric energy. The reversible/ideal/ theoretical voltage under standard conditions will be $E° = -\Delta G°/2F$ = 237,300 / (2 × 96,485) = 1.23 V. For a generic fuel cell reaction involving n-electron charge transfer, the reversible voltage will be:

$$E_r = \frac{-\Delta G}{nF} \tag{2.3}$$

The relationship between the reversible voltage Er and standard reversible voltage E °is express by Nernst equation:

$$E_r = E^0 \bullet \frac{RT}{nF} ln \frac{a_{product}}{a_{reactant}} \tag{2.4}$$

Here a_{produc}t and $a_{reactant}$ are the chemical activities of the reaction product and reactant respectively. The activities of pure solid or liquid phases are taken as unity. R is the universal gas constant (8.314 J $K^{-1}mol^{-1}$); T is the temperature in Kelvin. It should be noted that the actual voltage is always lower than the reversible voltage due to the irreversibility of the reaction and ohmic and mass transport losses in the electrolyte and electrode. Although the free energy represents all the energy that can be converted into electric energy, the fuel cell efficiency is defined against the enthalpy instead of the free energy of the cell reaction. The efficiency of the fuel cell is usually defined as:

$$\xi = \frac{electric\ energy\ produced}{-\Delta H} = nFE/-\Delta H$$

Here E is the operational voltage of the fuel cell. So the theoretical efficiency limit is:

$$\xi = \Delta G\ /\Delta H \tag{2.5}$$

If water is produced in the fuel cell reaction, there is some ambiguity in the reaction enthalpy depending on whether the water is produced as liquid or gas. The difference is the water vaporization enthalpy. The lower heating value (ΔH_{LHV} = -242 kJ mol^{-1}), which corresponds to the reaction enthalpy when water is produced as gas, is usually used in the calculation of the fuel cell efficiency unless otherwise stated (Larminie et al., 2003). As discussed above, one of the benefits from a fuel cell over a traditional internal combustion engine is the high efficiency. Table 2.1 gives some thermodynamic parameters for candidate fuels and oxidants under the standard conditions (Zhao et al., 2007).

Table 2. 1 Standard enthalpy, Gibbs function of reaction for candidate fuels and oxidants, corresponding standard reversible cell potential, and efficiency (at 25 ℃ and 1 atm)

Reaction	$-\Delta H$ $(J\, mol^{-1})$	$-\Delta G$ $(J\, mol^{-1})$	E_r^o (V)	Theoretical Efficiency (%)
$H_2 + 0.5O_2 \rightarrow H_2O(l)$	286.0	237.3	1.229	82.97
$CH_4 + 2O_2 \rightarrow CO_2 + 2H_2O(l)$	890.8	818.4	1.060	85.01
$CH_3OH(l) + 1.5O_2 \rightarrow CO_2 + 2H_2O(l)$	726.6	702.5	1.214	96.68
$CO + 0.5O_2 \rightarrow CO_2$	283.1	257.2	1.333	90.86

In conventional power sources like the steam power plant and internal combustion engines, the heat evolved during a chemical reaction is converted to mechanical energy and subsequently into electrical energy. The efficiency of a heat engine can be defined by the Carnot cycle, which involves stepwise isothermal and adiabatic expansion and compression of the reactant gas. Fuel cells are not limited by the Carnot cycle of thermodynamics. (Kordesch and Simander, 1996) Fuel cells, with their inherent quiet operation and lower or minimal emissions of pollutants have a wide range of site flexibility and thereby are used for commercial and residential purposes-both outdoors and indoors. The lack of moving parts also provides a simpler design and a highly reliable system. The waste heat from the fuel cell, depending on the temperature of operation can be utilized for water and space heating, owing to their cogeneration applications, the overall efficiency of the fuel cell system is increased.(Matsumoto et al., 1994, Echigo et al., 2003)

For the fuel cell reactions that involve gaseous fuel and liquid water product, ΔS is negative. In other words, a $T\Delta S$ amount which is not convertible to work of the total heat ΔH from the reaction is released to the environment under a reversible process. This leads to a less negative free energy change compared to the enthalpy change in the fuel cell reaction. In addition, the absolute value of free energy available diminishes, i.e., the theoretical potential of the fuel cell decreases with temperature due to the negative entropy change. However, it is not the case for the actual performance of a fuel cell, which depends on thermodynamics, kinetics and many other factors as will be discussed later. For instance, a H_2/O_2 fuel cell has a standard reaction enthalpy change of -286.0 kJ mol^{-1} when liquid water is produced. The enthalpy is more negative than the Gibbs free energy due to the negative entropy of this reaction (conversion of gaseous reactants into liquid product in addition to the reduction in the number of molecules). Both enthalpy and entropy vary a little with temperature, while the free energy is strongly temperature-dependent. The absolute value of free energy decreases with temperature. Thus the theoretical efficiency limit decreases with temperature. The external potential difference between the two electrodes, the actual working voltage, is the outcome of the thermodynamic reversible potential (E_r) and potential losses due to electrochemical reaction kinetics or electrical resistance. The actual efficiency of a fuel cell depends on its operational voltage, which decreases with the current drawn from the cell. The highest practical efficiency is achieved at the minimum current when the cell operates at an open circuit potential (OCP). Fuel cells are often set to operate at a lower voltage (around 0.6V for H_2/O_2 fuel cell) to achieve high power densities. Nevertheless, the realistic efficiencies (~50%) of fuel cells are much higher than those of present heat engines. This can be understood when the theoretical efficiency of a fuel cell is compared to that of a heat engine as illustrated in Figure 2.1.

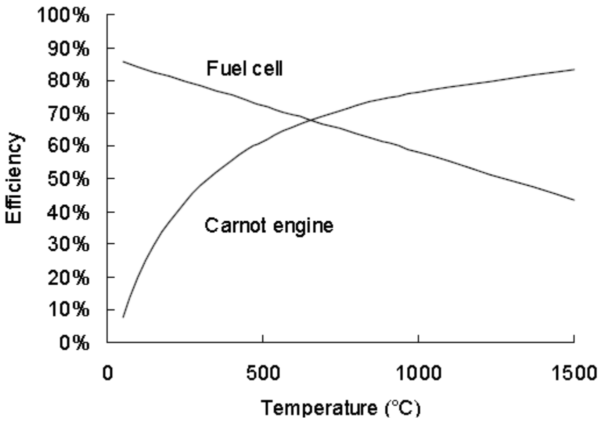

Figure 2.1 Comparison of the thermodynamic efficiency between a heat engine and a H_2/O_2 fuel cell.(Larminie et al., 2003)

2.1.2 Electrode Kinetics and Electrocatalysis

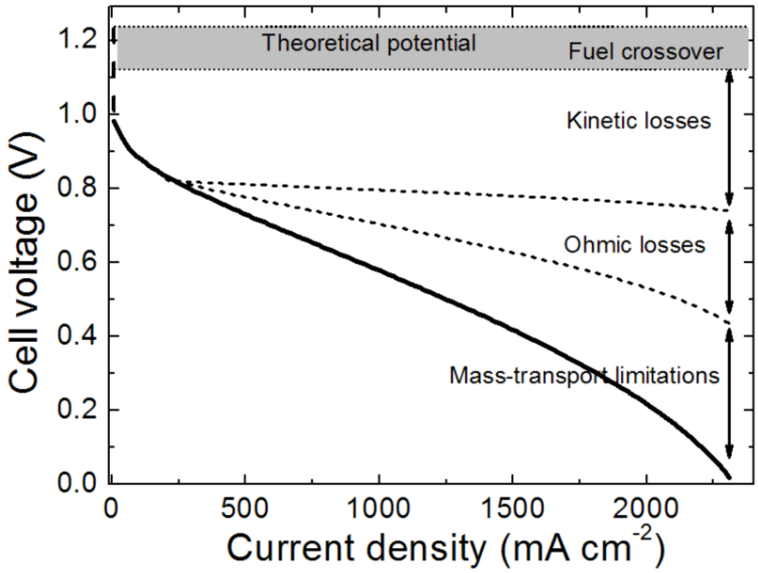

Figure 2.2 Fuel cell polarization curves showing various potential losses

The performance of PEM fuel cells are often reported in the form of a polarization curve, as shown in Figure 2.2. Based on the thermodynamics discussed above, a H_2/O_2 fuel cell is expected to give a cell potential around 1.2 V when operated under ambient conditions. However, from the potential vs. current density polarization curve, the operating potential of the fuel cell is found to start around 1.0 V and is less than the theoretical value even when the circuit is open. Above zero current density, a rapid initial potential drop is often observed, of which the magnitude varies with temperature and pressure of the fuel cell. Then the cell potential decreases slowly and linearly with current density. Sometimes there is a final rapid drop of potential starting at a very high current density. The different regions of the polarization curve are described as follows:

a) Mixed potential. Oxygen reduction reaction competes against the oxidation of platinum and some impurities on the cathode electrocatalyst. The exhibited open circuit potential for a fuel cell with intimate electrode-electrolyte interfaces, lower than the theoretical potential, is a result of the kinetic losses from the above reactions (Bockris and Srinivasan, 1969, Costamagna and Srinivasan, 2001). Fuel crossover also causes additional potential drop. Smaller thickness of electrolyte of the same kind ofgenerally results in a higher fuel crossover.

b) Activation losses. The rate of an electrochemical reaction is proportional to the current density passed through. A portion of cell potential generated is consumed to drive the electrochemical reaction when a current is drawn from the fuel cell. This kinetic activation loss of potential is strongly dependent on the electrocatalyst and cell operation temperature and pressure. Higher active area, which is determined by the size, loading, interface and activity of the catalyst usually lead to smaller activation losses. Activation losses are more important to low and intermediate temperature fuel cells due to the sluggish kinetics under these conditions. The relationship between the potential and current density is non-linear and observes Tafel equation (Costamagna and Srinivasan, 2001).

c) Ohmic losses. The ohmic resistances in the electrolyte and electrode-electrolyte interface cause a voltage drop when a current is passed through. The voltage drop is linear with the current density if the resistance is constant in the current range of interest. A shorter current path, as a result from a smaller electrolyte thickness and better connected interface, helps reduce the ohmic losses.

d) Mass transport losses. At very high current densities, the reaction goes so fast that the reactant at the electrode surface is partially depleted even though the bulk concentration of the reactant is unchanged. The decreased reactant concentration at the electrode results in another drop of the cell potential that is called mass transport or concentration losses. Mass transport losses are more distinct when air instead of pure oxygen is used as the oxidant. The smaller pressure gradient generated by the consumption of oxygen in air compared to pure oxygen gas and the build-up of unreacted nitrogen gas restrain the oxygen from accessing to the electrode surface.

All of the above losses exist at any given current density, while different losses dominate in different current density regions. It is noteworthy that these voltage losses have been reduced to a minimal amount by employing high performance electrodes and electrolyte membranes. The employment of high performance cell components and optimized systemic design, together with the direct energy conversion, provide fuel cells with a higher efficiency than that of heat engines.

2.1.3 PEM fuel cells system

2.1.3.1 Single cell

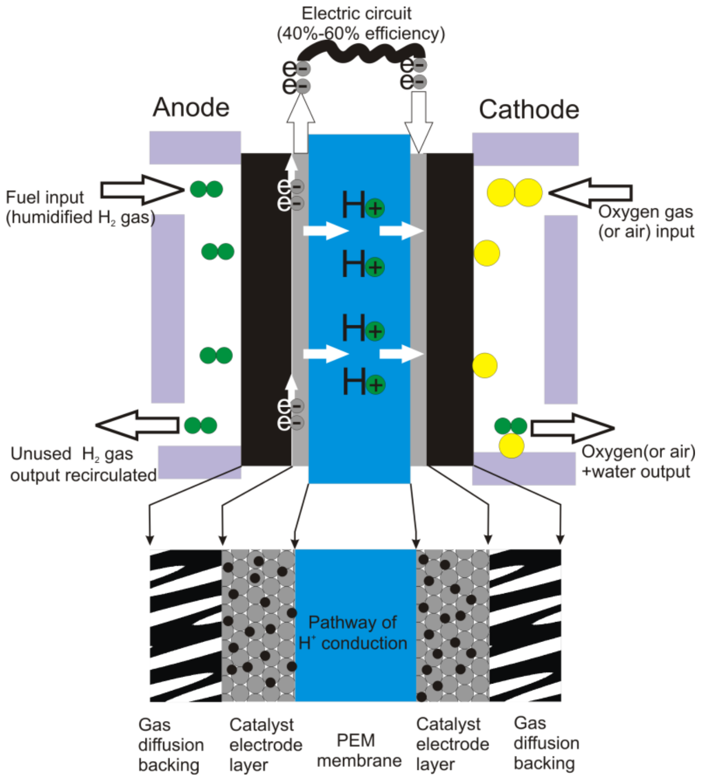

Figure 2.3 Fuel cell descriptions

The fundamental building block of a fuel cell is an electrochemical cell (see Figure 2.3) consisting of two electrodes separated by an ion cond`ucting medium (or membrane). This conducting medium can be an acid, a base, or a salt or a solid ceramic that conducts ions; the choice of electrolyte is depending on the nature of the fuel, the temperature of operation, and the specific application of the technology. The electrodes serve several functions: (i) they must be electronically conducting and (ii) they contain the electrocatalyst materials that facilitate the reaction. At the anode, a highly dispersed Pt-based catalyst oxidizes hydrogen, turning it into a positively charged proton and an electron (see Figure 2.3). The generated electrons travel through a conducting element yielding an electrical current. The protons travel through the electrolyte, which is specifically designed to strictly allow the diffusion of protons to the cathode where they react with oxygen in the presence of electrons to generate water.

2.1.3.2 Fuel cell stack

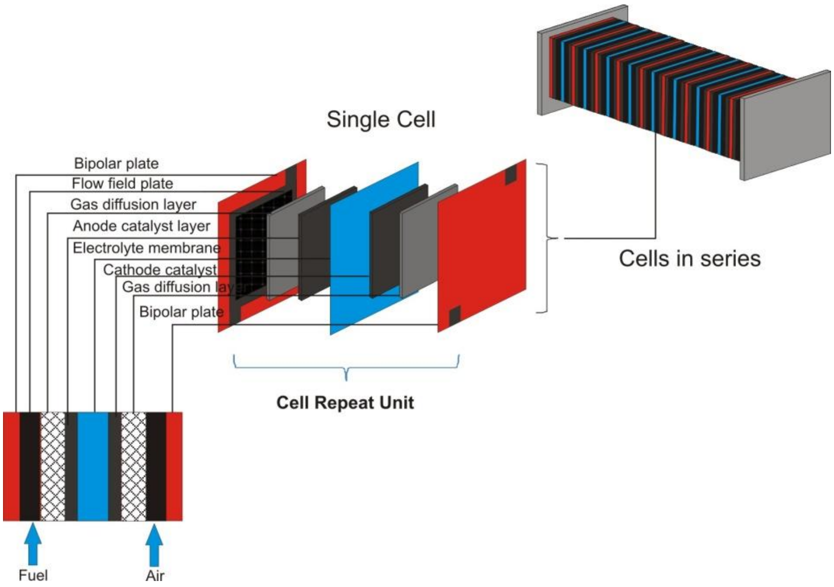

Figure 2.4 Schematic of a Fuel Cell stack

A single cell produces about $0.4\ W\ cm^2$ and numerous cells are connected in series or parallel depending on the voltage and current requirements for specific applications. The main components of a PEMFC power plant are illustrated in Figure 2.4: (i) Single cell consistes of anodic and cathodic electrocatalysts, the membrane electrolyte and current collectors with flow field pattems; (ii) Series of cell stacks with current collectors serving as the bipolar plates; (iii) other components not shown in Figure 2.4, including auxiliaries for compression of gases and uxiliaries for water and thermal management.

PEM based fuel cell can be broadly divided into two categories: hydrogen-fueled PEM based fuel cells (PEMFC) and DMFC using small alcohols like methanol as fuels. PEMFCs can be considered ecofriendly, zero emission power sources, as the only generated byproduct is water. Among the most developed fuel cell technologies, for portable applications, safety concerns and practical issues associated with the onboard storage of hydrogen at high energy density have spurred the development of DMFCs, which benefit from the high energy density and easier storage of organic fuels. Unlike PEMFCs, DMFCs produce the greenhouse gas carbon dioxide (CO_2), via organic fuel cell electrooxidation, but the emission rate per energy unit is significantly lower than the CO_2 production rate of conventional energy conversion systems because of much higher efficiency of fuel-cell-based systems. DMFCs have experienced moderate success in niche applications, namely, military and telecommunications.

PEM fuel cells will, in the future, be used not only in the automotive industry and also in the distributed power supply. Due to its excellent dynamic characteristics, PEM fuel cells can be used as emergency generating set for users who have special requirements for their critical equipment in case of power failure.

2.1.3.3 Proton exchange membranes for PEM fuel cells

Modern PEM fuel cells utilize sub-millimeter acidic PEMs to selectively conduct ions and block the passage of un-reacted fuels and reaction byproducts as shown in Figure 2.4, which give PEMFCs additional advantages. The electrolyte membrane being a solid material, compared to a liquid. The sealing of the anode and cathode gases is simpler with a solid electrolyte membrane, and therefore, less expensive to manufacture. The electrolyte membranes should exhibit (i) high protonic conductivity, (ii) low electronic conductivity, (iii) low permeability to fuel and oxidant, (iv) low water transport through diffusion and electro-osmosis, (v) oxidative and hydrolytic stability, (vi) good mechanical properties in both dry and hydrated states; (vii) low cost and (viii) easy processing.

2.2 Why high temperature PEM fuel cells

Despite some success, widespread market penetration of fuel cell technologies has yet to be realized mainly because of high system cost and system performance limitations. First, the limited availability of expensive platinum (Pt) is a significant concern, as it is typically the main component of fuel cell catalysts on both anode and cathode. As Pt is produced ainly in only South Africa and Russia, its natural abundance is low. Furthermore, with future large-scale productions of fuel cells, Pt prices would likely increase causing significant perturbations in the market. Thus, minimizing or eliminating the Pt content of fuel cell catalysts while maintaining acceptable power output and electrode durability remains a major challenge. In addition, despite continued advance in the synthesis theory of proton conductor, PEM materials remain prohibitively expensive.

Second, the performance of PEM-based fuel cells is often limited by membrane-related water management, such as anode dryout occurring during operation at higher current densities because of the osmotic drag of water molecules along with the proton transport to electrocatalytic sites. Also, operating fuel cells based on current PEM at elevated temperatures (≥80 ºC) further complicate water management, as the PEM must stay fully hydrated to maintain sufficient conductivity and thus optimal performance. Several active (i.e., electroosmotic pumps) and passive (i.e., component modification) water management strategies have been proposed to overcome this limitation.(Ge et al., 2005) Unfortunately, such strategies often require ancillary components that complicate fuel cell design and reduce overall system energy density. Fuel crossover occurs when unreacted fuel migrates (via electroosmotics and/or diffusion) through the membrane and reacts on the cathode causing mixed potentials, thereby reducing performance.(Kuver and Vielstich, 1998)

The above mentioned challenges are to some extent related to the low operational temperature for a traditional PEM fuel cell: firstly the operating temperature is near or below 80 ℃ a temperature which is not high enough to perform efficient cogeneration and to avoid CO contamination of the Pt based catalyst. Also, since the electrolyte is required to be saturated with water to operate optimally, careful control of the moisture of the anode and cathode stream is important. Increasing the operating temperature is a possible solution to overcome these issues and the benefits of high temperature operation are explained from 2.2.1 to 2.2.4:

2.2.1 Enhanced tolerance to impurities in reformed fuels

Hydrogen is an ideal fuel for fuel cell systems. Currently the practical way for hydrogen production is a steam reforming process/partial oxidation of gasoline and other hydrocarbons. Hydrogen produced by this process, contains traces of carbon monoxide (CO) in its product stream as a result of thermodynamic limitations, which strongly adsorbs on the surface of Pt, occupying hydrogen oxidation reaction sites, as illustrated in Figure 2.5. Trace CO dramatically reduces the activity of Pt or Pt-alloys in the anode.

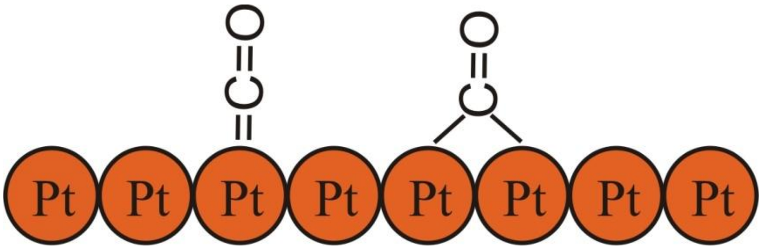

Figure 2.5 Absorption of CO on Pt

The adsorption of CO on Pt is associated with high negative entropy, indicating that adsorption is strongly favored at low temperatures, and disfavored at higher temperatures. As reported by Yang et al. (Yang et al., 2001), the adsorption is Langmuirian in nature. CO adsorbs associatively on Pt below 500 K, whereas H_2 adsorbs dissociatively:

$$\mathrm{CO\ (g) + \ Pt\ \rightarrow Pt–CO} \tag{2.6}$$

$$\mathrm{H_2\ +\ 2Pt\ \rightarrow 2Pt–H} \tag{2.7}$$

Equations 2.8 and 2.9 give the fractional coverages (θ) of CO and H_2 on the surface of the Pt-based catalyst:

$$\theta_{\mathrm{CO}} = \frac{K_{\mathrm{CO}}P_{\mathrm{CO}}}{1+K_{\mathrm{CO}}P_{\mathrm{CO}}+K_{\mathrm{H}}^{1/2}P_{\mathrm{H_2}}^{1/2}} \tag{2.8}$$

$$\theta_{\mathrm{H_2}} = \frac{K_{\mathrm{H}}^{1/2}P_{\mathrm{H_2}}^{1/2}}{1+K_{\mathrm{CO}}P_{\mathrm{CO}}+K_{\mathrm{H}}^{1/2}P_{\mathrm{H_2}}^{1/2}} \tag{2.9}$$

Where K_{CO} and K_{H_2} are the equilibrium constants for adsorption, and P_{CO} and P_{H2} are the partial pressures of CO and H_2 in the gas phase, respectively. Because hydrogen adsorption is less exothermic than CO and H_2 adsorption requires two adsorption sites, increasing the temperature leads to a beneficial shift towards higher H_2 coverage at the expense of CO coverage.

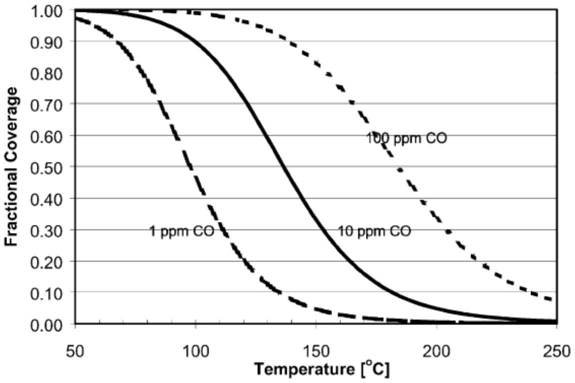

Figure 2.6 CO coverage on a platinum as a function of temperature and CO concentration. The partial pressure of H_2 is 0.5 bar.(Yang et al., 2001)

CO produced during the steam reforming process causes poison for the Pt-electrocatalyst and a few ppm of the CO results in a significant degradation in the performance of the fuel cell. An effective approach to enhance CO tolerance is to increase the operating temperature of the fuel cell since the free energy of adsorption of CO on Pt increases with increasing temperature.(Dhar et al., 1987, Dhar et al., 1986, Li et al., 2003a) this behavior can be explained by a Langmuir adsorption isotherm shown in Figure 2.6. The CO tolerance increases from 10-20 ppm at 800 ℃ to 1000 ppm at 130 ℃.(Yang et al., 2001)

2.2.2 Better Water and Thermal Management

Water management is a challenge for PEM fuel cell because water is both needed and not needed at the same time during fuel cell operation. Water is needed by the membrane and the ionomers within the catalyst layers in order to achieve good proton conductivity. Water is also needed in the catalyst layers for not slowing down the reaction because the reaction involves the protons and the movement of protons depends on the water content. At the same time, water is not needed because liquid water will block the gas transportation passes to result in higher mass transportation loss in cell voltage, and water vapor may slow down the reactant gases to reach the catalyst sites. Qi et.al (Qi and Kaufman, 2002) reported that introducing a microporous PTFE/carbon layer between the carbon support and the catalyst layer showed an enhanced ability to manage water and thus helped PEMFC performance. This method however needs high Pt loadings. A simpler approach for better water management is high temperature operation along with low relative humidity conditions. Fluid or water handling is simplified since free-flowing gases (hydrogen, oxygen, air, methanol vapor and water vapor) are involved above 120 ℃.

Thermal management is an issue strongly related to water management. It includes removal of heat produced during fuel cell operation, mainly due to irreversibility of electrochemical reactions and the joule heating effects. Temperature distribution in the cell strongly influences the cell performance as it impacts the water distribution in the cell by condensation and also affects the gas diffusion transport characteristics. Since the temperature difference between the cell and the surroundings is only about 50 ℃ for the current PEMFCs, convection or air-cooling are ineffective heat removal methods. Higher temperature operation helps in effective heat removal, as the temperature difference between the cell and surroundings is higher. If the operational temperature is elevated to 200 ℃, a steam of up to 15 atm can be produced from a fuel cell stack. This heat can be directly used for increasing the overall efficiency of a fuel cell system. The system efficiency will also be significantly improved as higher temperatures aid in preheating water and fuels for the steam reforming process.

2.2.3 Faster Electrode Kinetics

Electrochemical reactions occurring in a fuel cell follow Arrhenius rate kinetics and hence become faster with higher temperature. The voltage losses with current density, specifically at low current densities, are determined by the activation energy of the oxidation and reduction reactions. The rate of hydrogen oxidation on a Pt-catalyst surface is very high and exhibits small overpotentials in the order of 20 mV in the fuel cell operating at 1 A cm^{-2}. However oxygen reduction reaction exhibits overpotential of 400 mV under the same conditions. The exchange current density for the electrochemical oxygen reduction reaction (ORR, ~10^{-8} to 10^{-9} A cm^{-2}) is much smaller than that of the hydrogen oxidation reaction (HOR, ~10^{-3} to 10^{-4} A cm^{-2}). Since HOR at the Pt nanoparticle/PEM interface is reversible,(Jiang and Kucernak, 2004) the overpotential for HOR is negligibly small compared with that of ORR when the anode is adequately hydrated. The overall electrochemical kinetics of PEMFCs is therefore determined by the relatively slow oxygen reduction reaction (ORR). The performance of a PEMFC in the kinetically controlled regime can be represented by the Tafel equation:

$$E = E_{rev} + b\ log i_0 - b\ log i \tag{2.10}$$

$$b = -2.3\ \frac{RT}{\alpha n F} \tag{2.11}$$

Where E, E_{rev}, b, I, i_0, n and α are the electrode potential, reversible potential, Tafel slop, current density, exchange current density, the number of electrons transferred in the rate determining step and the transfer coefficient, respectively. Theoretically increasing the cell temperature will increase the exchange current density of the oxygen reduction reaction and hence reduce the activation overpotential losses, which can be confirmed by the investigation using EIS (electrochemical impedance spectroscopy) and LSV (linear sweep voltammetry) in a solid-state electrochemical cell using microelectrodes.(Xie and Holdcroft, 2004) Beattie et al. (Beattie et al., 1999) report i_0 values for Nafion 117 and BAM 407, an experimental sulfonated polytrifluorostyrene-based membrane, ranging from 2.08×10^{-10} to 3.71×10^{-9} A cm^{-2} and 8.80×10^{-11} to 4.38×10^{-10} A cm^{-2}, respectively, over the temperature range 303-343 K. Parthasarathy et al.(Parthasarathy et al., 1992) report that i_0 at Pt/Nafion® 117 interfaces in the low current density region increases from 1.69×10^{-10} to 5.54×10^{-9} A cm^{-2} as the temperature is increased from 303 to 343 K. It is likely that the increase in i_0 will deviate from this relationship above 100 ℃ but data at temperatures >100 ℃

are notably absent from the literature, presumably due to the experimental difficulties in operating solid state cells at elevated temperatures and lower humidity.

2.2.4 Improved O_2 mass transport

The diffusion coefficient of oxygen through water vapor is several orders of magnitude larger than through liquid water. With increasing operating temperature (for a given current density), the ratio of liquid water to water vapor inside cathode catalyst layers and gas diffusion layers decreases. This will serve to increase the effective diffusion coefficient of oxygen. Therefore, high temperature operation facilitates oxygen transport through the gas diffusion layers and the cathode catalyst layers and should lead to an increase in fuel cell performance in the mass transport controlled regime.

2.3 Major Challenges for PEMs under high temperature/low relative humidity operation

Although operating PEM fuel cells at temperatures above 100 ℃ has many attractive features, there are several major challenges. For example, lower temperature PEMFCs employ aqueous based polyelectrolyte membranes, for which the proton conductivity depends strongly upon the relative humidity. At a higher operating temperature, membrane dehydration and the subsequent decrease in proton conductivity is a significant issue. In addition, various components of PEMFCs experience structural and chemical degradation at elevated temperatures. This section outlines the challenges faced by operating PEMFCs at high temperatures.

2.3.1 Low Relative Humidity Operation

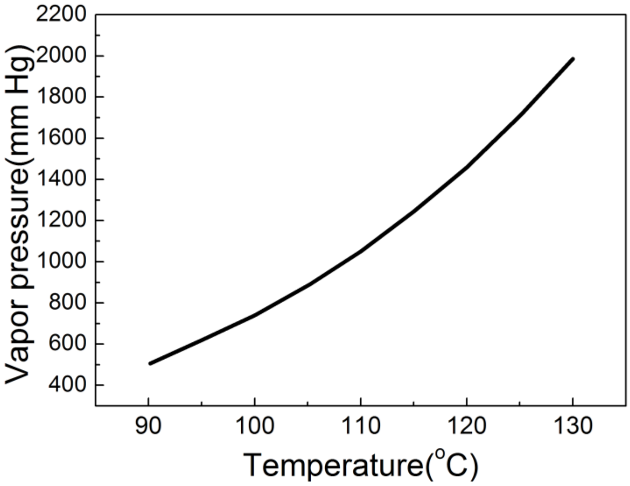

Figure 2.7 Changes in vapor pressure of water with temperature

The equilibrium water content of Nafion and thereby its proton conductivity depends directly on the temperature and relative humidity in the fuel cell. It has been shown that the conductivity of perfluorinated sulfonic acid membranes varies over several orders of magnitude depending on temperature and water activity.(Thampan et al., 2000) A detailed analysis on the effect of water activity on conductivity of Nafion has been reported by Yang et al.(Yang et al., 2001) The relative humidity (RH) is a measure of the chemical potentials of water in liquid and vapor phases. The chemical potential of liquid water is constant while that of vapor varies according to the following equation:

$$\mu_g = \mu_l + RTln\frac{P_{vap}}{P_{sat}} \tag{2.12}$$

Where P_{vap} is the vapor pressure and P_{sat} is the saturated vapor pressure at a given temperature, μ_l is -237.14 kJ mol^{-1}. The change in vapor pressure with temperature above 90 ℃ is shown in Figure 2.7. At RH less than 100%, the chemical potential of vapor phase is lower than the liquid phase as P_{vap} is smaller than P_{sat}. Liquid water evaporates to equal the chemical potentials in both phases. The difference in chemical potentials between the two phases is even higher at much lower RH resulting in a faster evaporation rate. Similar phenomenon occurs in a fuel cell when the operating temperature is above 100 ℃ under atmospheric pressure. The membrane resistance increases under such conditions, as there is not enough water in the membrane to help proton conduction. Pressurizing the system hence becomes inevitable for high temperature operation to maintain 100% RH. However, parasitic losses caused by the compressor lowers the overall efficiency of the fuel cell system and high pressures complicate system design.

2.3.2 Degradation in membrane conductivity

Typical proton-exchange membranes based on hydrated sulfonic acids dehydrate at elevated temperatures or lower RH. For instance, when operating at elevated temperatures (80-140 ℃), the conductivity of Nafion 115 drops significantly along with remarkable loss in water activity.(Yang et al., 2004) It is therefore important to determine the influence of high temperature/low RH conditions on the conductivity of existing and emerging membranes so that limitations of operation may be identified. Perfluorosulfonic acid (PFSA) membranes (e.g., Nafion) are the most widely used membrane for PEM fuel cells. Even these relatively robust materials lose their mechanical attributes when dehydrated, resulting in shrinking, and cracking. The water swelling in membrane leads to speed fuel crossover which results in loss in both cell voltage and energy density. Crossover also compromises safety since H_2 and O_2 may combine exothermically on Pt catalyst generating local hot spots that lead to pinholes, which in turn accelerates gas crossover-initiating a destructive cycle of increased crossover and membrane degradation.

2.3.3 Degradation in membrane mechanical stability

A loss of mechanical stability with increasing temperature is to be expected in the fuel cell. Unfortunately, the failure mechanism of membranes in the fuel cell is not well understood. However, morphological changes occurs above the glass transition temperature (T_g) of a polymer, which may have an adverse effect on mechanical properties of the membrane.(Kim et al., 2003) The glass transition temperature of the membrane must be well above the operating temperature of the fuel cell. T_g of hydrated polymer is dependent on not only chemical structure of the polymer but also water content due to its plasticizing effect. Nafion has a T_g between 130 and 160 ℃ when it is dry, and between 80 and 100 ℃ at hydrated state. Several studies have addressed the issue of thermal stability of PFSA membranes. The PTFE-like backbone of Nafion is relatively stable due to the strong C-F bond and the shielding effect of the electronegative fluorine atoms. Nafion begins to decompose via its side chains. Surowiec and Bogoczek(Surowiec and Bogoczek, 1988) conducted a study using thermal gravimetric analysis (TGA), differential thermal analysis, and infrared spectroscopy, and concluded that Nafion loses only water below 280 ℃, while above 280 ℃ sulfonic acid groups are lost. Chu et al.(Chu et al., 1990) used infrared spectroscopy to study the effect of heating Nafion® coated onto platinum in air and concluded that Nafion loses sulfonic acid groups after being heated at 300 ℃ for 15 min. Wilkie et al.(Firestone and Siegel, 1991) using TGA and FTIR spectroscopy, reports that, while being heated between 35 and 280 ℃ in an inert atmosphere, Nafion loses ~5 wt.%, producing water and small amounts of sulfur dioxide and carbon dioxide. Between 280 and 355 ℃, the evolution of sulfur dioxide and carbon dioxide increased. The detailed mechanisms for the decomposition of Nafion are reported (Firestone and Siegel, 1991).

2.3.4 Degradation in membrane chemical stability

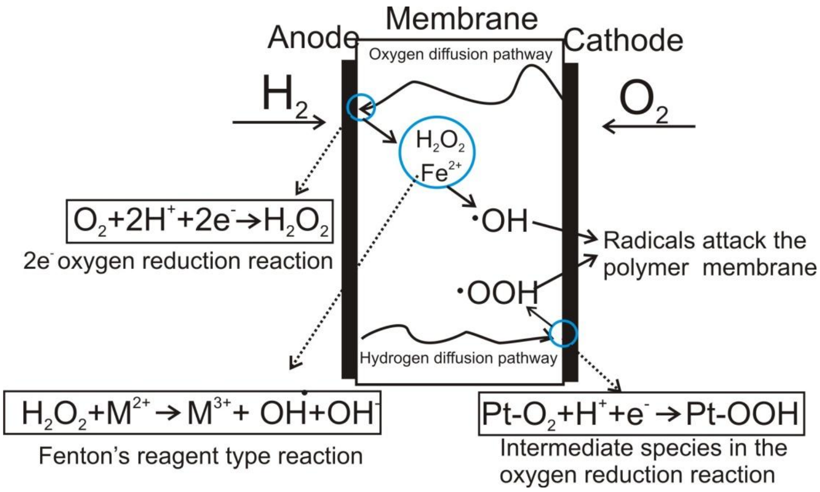

Figure 2.8 Radicals formation mechanism

During fuel cell operation, it is believed that radicals HOO• and HO• are responsible for chemical attack on the membrane, and initiate the degradation process (Buchi et al., 1995, Wang and Capuano, 1998) as shown in Figure 2.8. Water in the membrane provides a pathway for hydrogen and oxygen crossover from opposite sides of the membrane. Diffusion rates are slow and generally represent only a 1-3% loss in fuel cell efficiency; however, oxygen crossover provides a means for the formation of peroxide and hydroperoxide radicals, which may slowly deteriorate the membrane. Consequently, the loss of ionic groups has been observed to begin at the anode side of the membrane and progresses towards the cathode.(Yu et al., 2003, Anderson and Albu, 2000) All these degradation processes are expected to be exacerbated at temperatures above 100 ℃, so that any consideration of new membranes for high temperature operation must be based on highly thermal stable components, or engineered in a way to reduce free radical formation.

2.4 Requirements for ideal high temperature PEMs

The most important functions of the proton exchange membranes are: (1) electrolyte, (2) fuel separator and (3) electronic separator, which reflect the very specific conditions in the fuel cells.

2.4.1 Electrolytic Function

2.4.1.1 Proton conductivity requirement for PEMs

The most important characteristic of the PEMs is its proton conductivity. In use of these membranes in a PEMFC system, the ionic conductivity should be as high as and the membrane should remain stable over time under the fuel cell conditions (e.g. various humidity conditions and various oxygen partial pressure, $P(O_2)$). For a membrane to be suitable for use in PEM fuel cells, a minimum conductivity of 0.1 Scm^{-1} under steady-state conditions and 0.025 Scm^{-1} at 20 ℃ is required for automotive applications. (Birgersson et al., 2003)

2.4.1.2 Proton conductance mechanism in the PEMs

The protonic charge carriers are solvated by very few types of species including water (e.g., in hydrated acidic polymers), oxo-acid anions (e.g., in adducts of basic polymers with phosphoric acid), heterocycles (e.g., intercalated into acidic polymers or immobilized via flexible spacers), or oxide ions (forming a hydroxide on the oxygen site of an oxide lattice). These species participate in the formation of protonic charge carriers and the conduction mechanism. In some cases, they are also the protogenic groups: i.e., they generate protonic charge carriers by self-dissociation (e.g., in the case of phosphoric acid and to some extent in heterocycles such as imidazole).

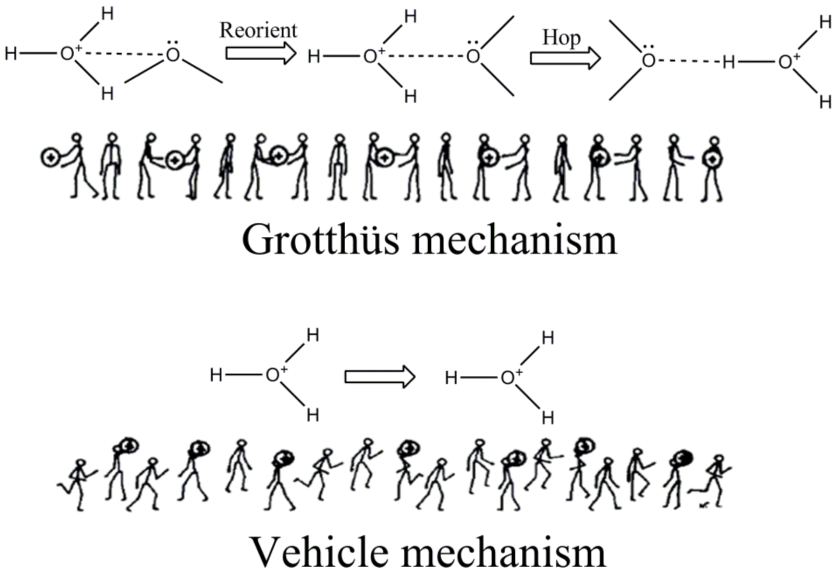

Figure 2.9 Proton conductance mechanisms assisted by the dynamics of structural molecules. Above: the Grotthűss mechanism (proton transfer and subsequent molecular reorientation). Below: the vehicle mechanism (co-operative motion of neutral molecules and charged molecule/ proton complexes) (Kreuer, 1988)

One common and important characteristic of all these species mentioned above is their involvement in hydrogen bonding. The structural and dynamic nature of this interaction governs the long-range proton transport in these environments. Long-range proton transport does generally require rapid bond breaking and forming processes, which is mainly expected to occur in weakly hydrogen bonded systems. Because of the existence of different levels of hydrogen bonding, different mechanisms exist and have been proposed: (i) the vehicle mechanism and (ii) the structure diffusion mechanism. In the vehicle mechanism, the proton diffuses together with a vehicle (e.g., H_3O^+, $H_2O_5^+$) where the counter-diffusion of non-protonated vehicles (e.g, H_2O) allow the net transport of protons. The rate for the observed conductivities is that of vehicle (molecular) diffusion. In the structure diffusion mechanism (or Grotthűss),(Kreuer, 1997) the motion of protonic defects (excess or deficient transport) occurs via inter-molecular proton transfer coupled with hydrogen bond breaking and forming processes. In this case, the protons are transferred within hydrogen bonds from one “vehicle” to the other. Reorganization of the proton environment, including reorientation of individual species or even more extended ensembles, then results in the formation of an uninterrupted trajectory for proton migration. The reorganization is frequently established by the reorientation of solvent dipoles (e.g., H_2O, H_3PO_4, and $H_3P_4W_{12}O_{40}$, etc) which is thus part of the proton diffusion trajectory.

The relative contributions of “structure diffusion” and “vehicle diffusion” are dependent on temperature, pressure, frequency of proton hopping along a hydrogen bond, the rotational speed of the carriers and their diffusion coefficient.(Kreuer, 1996) The activation energy associated with the structure mechanism is about 9.6 kJ mol^{-1} ($E_{a(vc)}$) while vehicle diffusion has the much larger value of ~38.4 kJ mol^{-1} ($E_{a(sd)}$). (Kreuer et al., 2004)

2.4.1.3 Microstructure of the PEMs

Proton conductivity and methanol permeability of a PEM are strongly dependent on the morphology of the proton exchange membranes. For instance, phase separation of ion-rich hydrophilic domains from the hydrophobic domains in Nafion result in the formation of ion clusters and at high level of hydration eventually channels that allow protons to pass or percolate through the membrane. This is depicted in Figure 2.10.

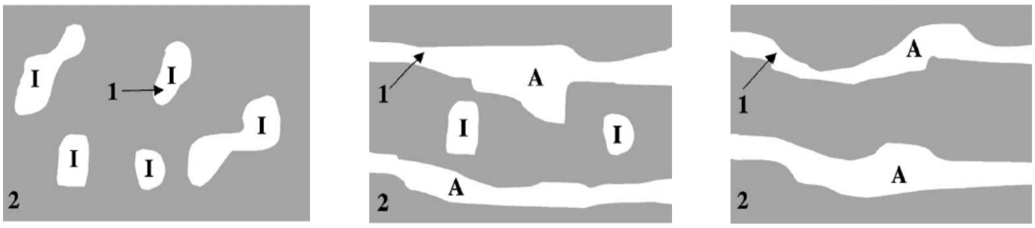

Figure 2.10 Illustration depicting a phase-segregated system, where the minority phase (1) is interspersed within the majority phase (2) (shaded region). (a) All of the minority phase is isolated (I); (b) the minority phase contains both parts that are isolated (I) and accessible (A); (c) all of the minority phase is accessible (A). Transport occurs through the interconnected accessible pathways.(Elabd et al., 2003)

Hydrated acidic materials are the most commonly used membranes for low-temperature fuel cells. Their typical nano-separation leads to the formation of interpenetrating hydrophobic and hydrophilic domains; what the hydrophobic domain contributes to the membrane is fuel barrier and the morphological stability, whereas the hydrated hydrophilic domain facilitates the conduction of protons. The majority of the excess of protons are then located in the central parts of the hydrated hydrophilic nano-channels.

2.4.2 Fuel Separating Function

The membrane should be impermeable to gases fuel (e.g. hydrogen, propane) as well liquid fuels (e.a. methanol, ethanol). If these fuels diffuse through the membrane, this may depolarize the electrodes of the cell by creating a short circuit or create free radicals in the membrane which cause premature aging of the electrolyte. When the separation is not ideal in a H_2/O_2 fuel cell, hydrogen diffuses to the cathode compartment and oxygen to the anode compartment. On both sides, the mixture can react on the platinum electrode to produce water, which is accompanied by the production of heat. This can lead to small pinholes. The side effect of the presence of a mixture of hydrogen and oxygen on both sides is the lowering of the cell voltage, which as reported can reach up to 100 mV. The maximum allowable permeability of amembrane for hydrogen, at a full load (2 A cm^{-2}) is 8×10^{4} ml $cm^{-1}m^{-2}s^{-1}kPa^{-1}$ when accepting a 1% fuel efficiency loss due to crossover and 3×10^{4} ml $cm^{-1}m^{-2}s^{-1}kPa^{-1}$ corresponding to 10% fuel efficiency loss at a low current loading (50 mA cm^{-2}). For oxygen, the maximum allowable permeability is 3×10^{4} ml $cm^{-1}m^{-2}s^{-1}kPa^{-1}$ at full load and 3×10^{4} ml $cm^{-1}m^{-2}s^{-1}kPa^{-1}$ at low current load. (Birgersson et al., 2003)

2.5 Development of High Temperature Proton Conductive Materials

2.5.1 Fluorinated polymers

2.5.1.1 The state of the art: perfluorosulfonic acid (PFSA) polymer membranes

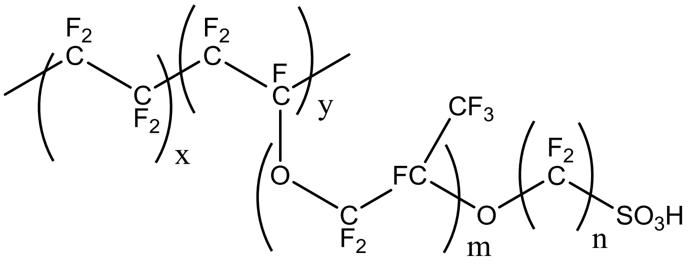

Nafion 117	m>1, n=2, x=5-13.5, y=1000
Flemion	m=0 or 1, n=1-5, y=1000
Aciplex	m=0 or 3, n=2-5, x=1.5-14, y=1000
Dow Mem	m=0, n=2, x=3.6-10, y=1000

Figure 2.11 General structures of commercial available perfluorosulfonic acid (PFSA) polymers

The best-performing PEM fuel cells for operating temperature below 100 ℃ have been composed of Nafion, a perfluoro-sulfonated copolymer developed by DuPont in the 1960s. The introduction of Nafions membranes in 1968 marked the revival of fuel cell proton exchange membrane technologies. Fluorinated or perfluorinated membranes remain good reference for PEM development in terms of electrochemical performance and chemical stability. Their appearance in the PEMFC has validated the viability of these electrochemical generators. These membranes are often composed of a linear backbone of polytetrafluoroethylene (PTFE or Teflons) having statistically pendant chains of perfluorinated vinyl ether type terminated with a sulfonic acid type function. Other perfluorosulfonate cation exchange membranes with similar structures have also been developed by the Asahi Chemical Company (Aciplexs), the Asahi Glass Company (Flemions), and Dow Chemical (Dows membranes) (as shown in Figure 2.8). These modified Nafion membranes exhibit the interesting mechanical, chemical and electrochemical properties for PEMFC operating at different temperatures and humidity. Inspection of the proton conductive mechanism in Nafion membrane (Figure 2.11) reveals that water is needed for proton conduction in this membrane. Water ionizes the sulfonic acid, and water provides a path for proton conduction between sulfonic acid groups. The need for water in the membrane for proton conduction gives rise to many negative consequences. With too little water, there is no proton conduction, because the pendant sulfonic acid groups are neither all ionized nor bridged by water molecules, as shown in Figure 2.9. With three (or more) waters per acid group, the membrane conducts proton, because water bridges completely ionized acid groups. Three waters per acid mean that bulk-like water is in the membrane, so the fuel cell operation temperature must be 80 ℃ or lower at atmospheric pressure, and humidification of feed gases is required to retain liquid water inside the membrane.

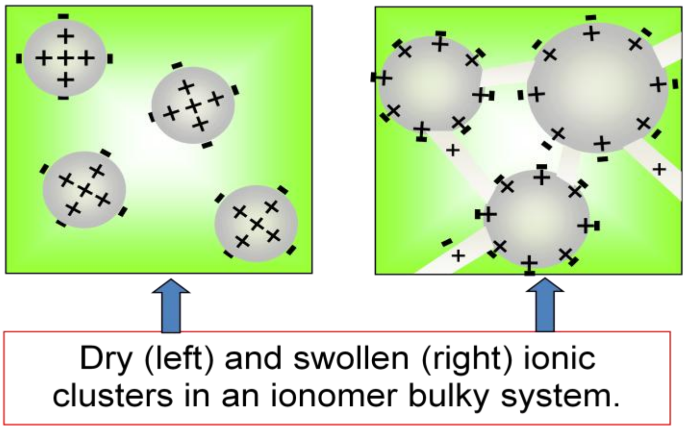

Figure 2.12 Structure evolution of Nafion depending on the water content(Gebel, 2000)

To date, there are no proton-conducting sulfonated polymer membranes available which satisfy all requirements under high temperature (i.e. T>120 ℃) and low humidity (25% RH). The most obvious limitation is the low proton conductivity, as a result of low hydration levels under these conditions. Because of their super acidity, which results in high hydrophilicity, the highest equilibrium water contents are observed in PFSA polymers. However, even for these, a water content of $2.5H_2O/SO_3H$ (at T>144 ℃, 25% RH) is too low to effectively bridge the separation between neighboring sulfonate groups, which is ~0.8 nm in Nafion series membrane including Nafion 112, Nafion 115 and Nafion 117. Because of the poor connectivity (percolation) of the water structures and the strong local retardation of the water diffusion, fast proton conduction according to a vehicle mechanism is not possible at such low degrees of hydration.

2.5.1.2 Modified PFSA polymer membranes

Theoretical and experimental studies indicate that high proton conductivity may be possible at low hydration levels for the PFSA polymer membranes. This will be achieved for less separated acid functional groups or at least more mobile. Table 2.1 summarizes these effects as well as other modifications of PFSA-based membranes.

Table 2.2 Summary of modification of PFSA based membranes

Perfluorosulfonic (PFSA)	Modifiers	Remarks	Reference
Nafion	PTA-acetic acid	H_2/O_2 fuel cell, 110 ℃, 660 mA cm^{-2} at 0.6V, 1/1 atm, humidifier 50/50 ℃	(Hyun and Kim, 2004)
Nafion	PTA-TBAC	H_2/O_2 fuel cell, 120 ℃, 700 mA cm^{-2} at 0.6V, 1/1 atm, humidifier 50/50 ℃	(Raman et al., 2004)
Nafion	SiO_2	>0.2 S cm^{-1}, 100 ℃/100 %RH	(Adjemian et al., 2002)
Nafion	SiO_2	H_2/O_2 fuel cell, 130°C, 1000 mA•cm^{-2} at 0.4V, 3/3 atm, humidifier 130/130 ℃	(Kim and Honma, 2004)
Nafion	di-isopropyl phosphate	0.4 S cm^{-1} at 25 ℃	(Jung et al., 2007)
Nafion	SiP-PMA/PWA	0.005 S cm^{-1} at 23 ℃, fully hydrated	(Shao et al., 2006)
Nafion	SiWA (+thiophene)	Fuel cell test at 80 ℃,	(Tazi and Savadogo, 2000)
Nafion	SiO_2, PWA-SiO_2, SiWA-SiO_2	DMFC, 140 ℃, 400 mW cm^{-2} for methanol/O_2, 250 mW cm^{-2} for methanol/air, 3/4 atm,	(Wang and Capuano, 1998)

Nafion	PMoA+SiO_2	>0.3 S cm^{-1} at 90 ℃	(Kukino et al., 2005)

The above listed modification techniques of the PFSA membranes using various inorganic fillers with the goal of achieving improved proton conduction above 100 ℃ can be categorized into three approaches as follows:

(1) Hygroscopic composites: The incorporation of hydroscopic inorganic filler (e.g. silica) may result in an increase in membrane swelling at lower relative humidity, and offer resistance to fuel crossover. Hence, the transport of protons through the membrane become easier and the methanol permeability is reduced. Figure 2.13 shows proton transport through a composite membrane.

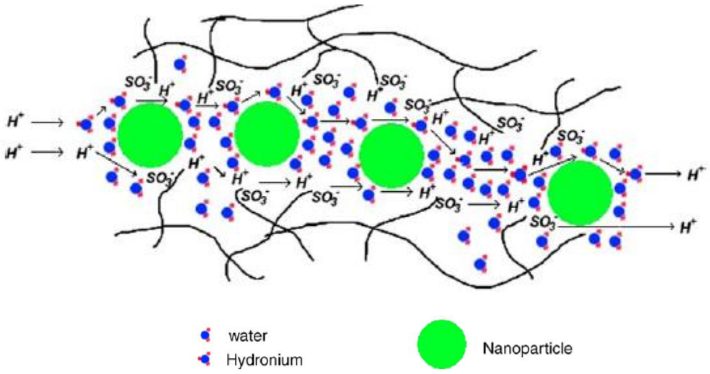

Figure 2.13 Proton transport in a nanocomposite membrane(Hogarth et al., 2005c)

(2) Conducting composites: A conducting species can be introduced into the polymer, which reduces water and methanol permeability significantly. The conducting species tighten the pores of the polymer, which inhibits the molecular migration of fuels, including hydrogen, mechanol and oxygen through the membrane. Furthermore, the incorporation of a conducting material also results in the recovery of conduction loss due to a reduced fraction of water

from the membrane.

(3) Water substituted composite: These composites are based on the polymer matrix and an alternative proton carrier, i.e. use of heteropolyacids. The aim is to immobilize a highly conducting acid in the polymer so that proton conducting is independent of hydration and the electro osmotic drag is reduced.

2.5.2 Polybenzimidazoles (PBI)

2.5.2.1Types of PBI polymers

Poly(benzimidazole)s are another family of polymer for electrolyte membranes. Polybenzimidazoles is an amorphous thermoplastic polymer with a glass transtition temperature ranging from 236 to 425 ℃. The chemical structures given in Figure 2.14 correspond to the polymer reported in reference. This family contains benzoxazole and polybenzothiazole. It has a good chemical resistance and excellent textile fiber properties. In the form of a membrane PBI has received much attention mainly for the use in blood dialysis and reverse osmosis at high temperature and in harsh environments. In addition to the commercially available PBI, AB-PBI in a short form has been prepared.

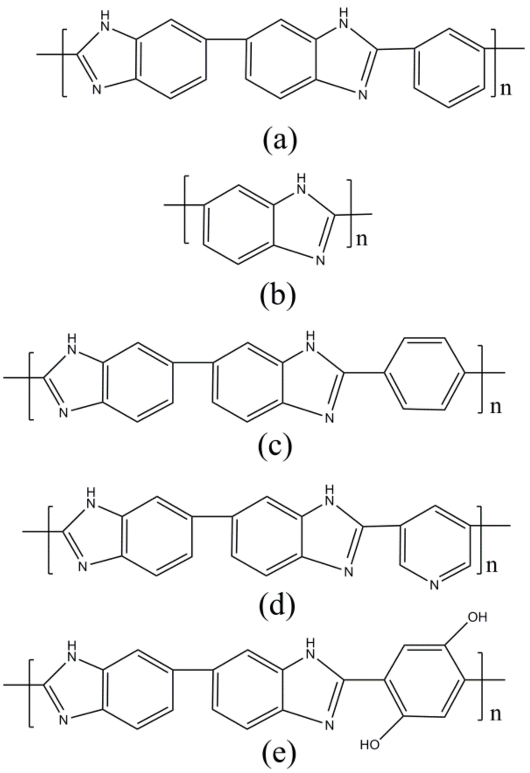

Figure 2.14 Chemical structure of various polybenzimidazoles (PBIs) (a) meta-PBI[poly(2,2’- (1,3-phenylene)5,5’-bibenzimidazole))], (b) AB-PBI [poly(2,5-benzimidazole)], (c) para-PBI[poly(2,2’-(1,4-phenylene)5,5’-bibenzimidazole))], (d)PPBI [pyridine-based PBIs], and (e) 2OH-PBI [poly(2,2’-(2,5-dihydroxy-1,4-phenylene) 5,5’-bibenzimidazole))](Xiao et al., 2005)

Direct sulfonation of PBI with sulfuric or sulfonic acids is difficult and gives a membrane with a poor sulfonation degree and mechanical properties (i.e. they are brittle). Another obvious consideration is to replace sulfuric acid by other materials which have the ability to solvate protons, such as phosphoric acid, which is also subject to electro-osmotic drag as water has a lower boiling point (boiling point of H_3PO_4 85 wt% is ca. 154 ℃) than that of H_3PO_4. Because of its unique proton conduction mechanism by self-ionization and self-dehydration,(Gillespie and Robinson, 1965) H_3PO_4 exhibits an effective proton conductivity even in an anhydrous (100%) form-wherethe conductivity of H_3PO_4 at 150 ℃ is 0.568 S cm^{-1}.

The conductivity of PBI/H_3PO_4 is found to be strongly dependent on the acid-doping level, temperature and atmospheric humidity. The conductivity follows the Arrhenius law, suggesting a hopping-like conduction mechanism. In an acid doping range of 2.0 to 5.6 mol H_3PO_4 per repeat unit, the activation energies were found to be in a range of 18-25 kJ mol^{-1}. (He et al., 2003) The proton hopping from on a N-H site to another contributes little to the conductivity, as pure PBI is not conducting. Many works have been carried out to clarify the interaction between H_3PO_4 and PBI (Stevens et al., 1997, Wieczorek and Stevens, 1997): the characteristic adsorption of H_3PO_4 molecules in the PBI/H_3PO_4 polymer complex was investigated by FTIR. Three characteristic adsorptions of HPO_4^{2-}, HPO^{2-} and $H_2PO_4^-$ groups for PBI/H_3PO_4 polymer complexes appear at 1090, 1008 and 970 cm^{-1}, respectively. The intensity of adsorption band of HPO_4^{2-} increases with increase in the concentration of H_3PO_4. The presence of HPO_4^{2-} and $H_2PO_4^-$ anions implies that proton conduction may occur according to the Grotthűss mechanism as described in Section 2.3.1, which involves an exchange of protons between H_3PO_4 and HPO_4^{2-} or $H_2PO_4^-$. At a doping level of 2 mol H_3PO_4 per unit, the conductivity of membrane is about at 2.5×10^{-2} S cm^{-1} 200 ℃. The presence of the free or unbounded acid is necessary to improve the conductivity. A highest conductivity of 7.9×10^{-2} S cm^{-1} at 200 ℃ with 5.7 mol H_3PO_4 per repeat unit has been reported for the H_3PO_4-doped PBI.(He et al., 2003) This indicates that the successive proton transfer along the mixed anionic chain contributes to the major part of the conductivity. Further improvement of conductivity was observed by increasing the relative humidity, indicating the bridging effect of water molecules in the proton conduction.

On the other hand, high acid contents result in high conductivity but sacrifice mechanical properties, especially at temperature above 100 ℃. Recently Dai et al. reported that the swelling ratio in thickness direction for a H_3PO_4-doped PBI membrane increased from 50 to 175% as the acid loading rised from 2 to 6 mol per repeat unit.(Dai et al., 2010)Another measurement carried out by Kumbharkar et al. indicated that the swelling ratio in volume reached up to 200-700% as acid loading increased to 20 mol per repeat unit.(Kumbharkar et al., 2009) The above mentioned structural instability makes the PBI/ H_3PO_4 membrane potentially vulnerable of acid leaching which may lead to loss in membrane conductivity and the fuel cell performance.

2.5.2.2 Modified PBI membrane

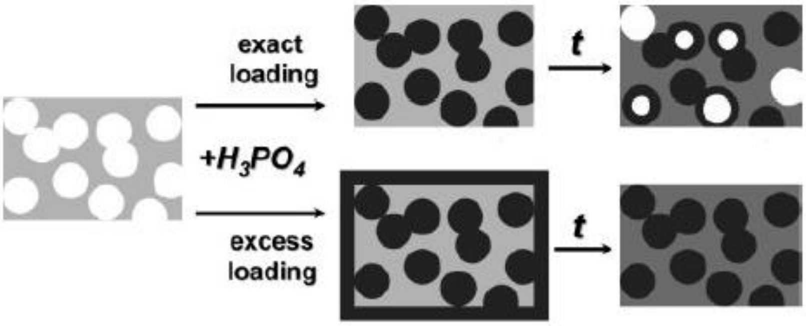

Figure 2.15 The PBI polymer membrane with mesoporous structure and increased phosphoric acid loading (Weber et al., 2008)

As it was demonstrated that proton conductivity in polymer membranes benefits from a biphasic structure (Kreuer, 1996), Kreuer et al. (Kreuer et al., 2004) have developed electrolyte membranes based on mesoporous PBIs filled with nominally dry phosphoric acid. Such materials with the structures as given in Figure 2.15 lead to a two-phase structure, and the development of a well-connected phosphoric acid rich domain allows a higher conductivity to be reached than those observed for a homogeneous sample. The introduction of a defined nanostructure into cross-linked PBI/phosphoric acid composites seems to be a promising approach towards high temperature membranes for fuel cell applications. Such approaches generally lead to some compromise between conductivity and mechanical properties. Cross-linking may suppress phase separation, which is essential for obtaining a high conductivity. Nevertheless, such materials generally lead to poor mechanical properties of the membranes containing high phosphoric acid content.

Great efforts have been attributed to improve the poor mechanical properties of H_3PO_4-doped PBI membranes for fuel cell applications in recent years. One of them is to synthesize membranes with high molecular weight. These modifications are accomplished (i) either by synthetically modifying the monomers prior to polymerization or (ii) by postpolymerization substitution of the reactive benzimidazole N-H sites on the polymer. Related fuel cell technologies have been developed and high temperature PEMFC has been successfully demonstrated at temperatures of up to 200 ℃ under ambient pressure. In general, the fuel cell tests are carried out with a membrane containing a high acid content which therefore exhibits a high proton conductivity. Unfortunately, little information about the influence of phosphoric acid on the catalyst is available. Additionally, the long-term durability measurements on these memrbane under fuel cell conditions are still insufficient. The reasons for failure of a PEMFC based on PBI are numerous and not fully understood. The most possible mechanisms include (i) degradation of the polymer membranes caused by H_2O_2 and its associated radicals species (-OH or -OOH), (ii) leaching of the doping acid from the membrane electrolyte; (iii) loss of catalytic activity due to the catalyst sintering, catalyst dissolution and carbon support corrosion.

As discussed above, although the polybenzimidazole/phosphoric acid (PBI/PPA) membranes have shown some advantages in high temperature PEMFC, some limitations need to be overcome: (i) the low proton conductivity, especially in the low temperature range, which is of importance for the cold start, (ii) slow oxygen reduction kinetics due to the strong surface adsorption of acid anions and low solubility (and diffusivity) of oxygen, (iii) the material development and techniques of stack construction, including selection and evaluation of bipolar plates, seals, and coolant/cooling.

2.5.3 Inorganic proton conductors based on heteropoly acids (HPAs)

2.5.3.1 Basic types of heteropoly acids (HPAs)

Heteropoly acids (HPAs) have been known as superionic conductors in their fully hydrated states.(Kozhevnikov, 1998, Misono, 1987) HPAs are solid crystalline materials with polyoxometalate inorganic cage structures, which resprents the Keggin form with a general formula $H_3AB_{12}O_{40}$, where typically A = P or Si, and B = W or Mo. The highest stability and strongest acidity are observed for phosphotungstic acid ($H_3PW_{12}O_{40}$, abbreviated as PWA or HPW), the molecular structure of which is given in Figure 2.16.

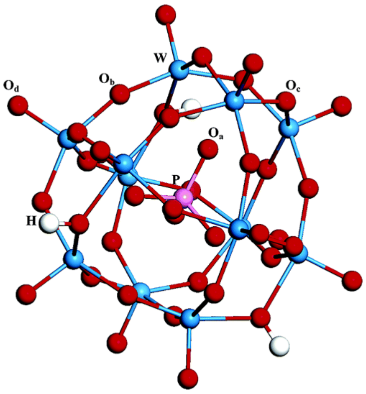

Figure 2.16 Keggin structure of a phosphotungstic acid molecular. three types of exterior oxygen atoms were given: O_b, O_c, and O_d in the Keggin unit. O_a is the central oxygen atom (Yang et al., 2005b).

Superacidic HPAs have structural groups of polyoxometalates, which bring forth the stable proton conductivity of 0.02~0.18 Scm^{-1} at room temperature (Alberti and Casciola, 2001). Because of their high acidity, stability and high proton conductivity, HPA and HPA mixed or embedded with silica supports have been extensively studied as good redox catalysts in homogeneous and heterogeneous reactions.(Garcia et al., 2007, Kim et al., 2006, Blasco et al., 1998, Micek-Ilnicka, 2009, Wee et al., 2010, Zhu and Yang, 2009, Kumar et al., 2006) HPA is also used as additive to promote the electrocatalytic activities of electrocatalysts for methanol oxidation reaction (Cui et al., 2010, Kulesza et al., 2004, Barczuk et al., 2006) and oxygen reduction. (Wlodarczyk et al., 2006, Wlodarczyk et al., 2007, Wang et al., 2010, Stanis et al., 2008)

2.5.3.2 Heterpoly acid functionalized materials

The application of HPAs as proton exchange membranes in fuel cells is limited due to the sensitivity of their conductivity to the relative humidity of the surrounding environment in addition to their solubility in water. The risk of the leakage of HPAs during cell operation is thus high. Various attempts have been made to immobilize the HPAs in silica gel, (Tatsumisago et al., 1994, Rao et al., 2005, Rao et al., 2004) ammonium salt (Mikhailenko et al., 1997), P_2O_5-SiO_2 glasses (Uma and Nogami, 2007d, Uma and Nogami, 2008c), to form HPW composite with room temperature ionic liquids, (Li et al., 2006) and to form hybrid organic/inorganic membranes.(Yamada and Honma, 2006, Staiti et al., 2001, Celso et al., 2009, Cui et al., 2009, Oh et al., 2010) Lakshminarayana and Nogami mixed phosphotungstic acid (HPW) and phosphomolybdic acid (HPMo) with 3-glycidoxypropyltrimethoxysilane (GPTMS), 3-aminopropyltriethoxysilane (APTES), phosphoric acid, and tetraethoxysilane (TEOS) by a sol-gel process and reported a proton conductivity of 3×10^{-2} Scm^{-1} with the composition of 50TEOS-25GPTMS-20H_3PO_4-5APTES-3HPMo-6HPW at 120°C under 90% RH.(Lakshminarayana and Nogami, 2009) Sweikart et al mechanically mixed HPW and a commercially available high temperature epoxy (Duralco 4538N) and reported a conductivity of 6×10^{-5} S cm^{-1} at 165 °C without humidification for a HPW-doped sulfonated epoxy.(Sweikart et al., 2005) The conductivity of mixed HPW/epoxy hybrid membranes is too low for practical fuel cell applications. Tan et al synthesized composite membranes containing sulfonated poly(arylene ether sulfone (SPSU), benzimidazole derivatives (BIzD) and HPW.(Tan et al., 2005) Adding BIzD helps to retain HPW particles and good conductivity, which was reported for the SPSU-BIzD-HPW hybrid membranes (0.084-0.159 Scm^{-1} at 110^{o}C under fully hydrated conditions). The high proton conductivity and excellent cell performance of 510 mWcm^{-2} at 120^{o}C was also reported on the Nafion-HPW/meso-silica hybrid membranes.(Yan et al., 2009) However high swelling ratios associated with polymeric materials are detrimental to structural stability of the membranes. Matsuda et al(Matsushita et al., 1999) used HPW and SiO_2 as basic materials and milled them mechanically to form HPW-SiO_2 composites and achieved a proton conductivity of 3×10^{-3} Scm^{-1} at 30 ^{o}C and 60% RH. Nogami et al(Uma and Nogami, 2009, Uma and Nogami, 2008a, Uma and Nogami, 2008b, Inoue et al., 2008, Uma and Nogami, 2007b, Uma and Nogami, 2007c, Uma and Nogami, 2007a) incorporated various heterpolyacids into silicaphosphate porous glass and yielded an electrolyte membrane with a proton conductivity of 0.1 S cm^{-1} at 85 ℃ and 85% RH. The cell based on HPM and HPW incorporated silicaphosphate glass produced a maximum power of 35~42 mWcm^{-2} under 30 ^{o}C and 30% RH.

2.5.4 Glass membrane based on a acid phosphates and phosphosilicate

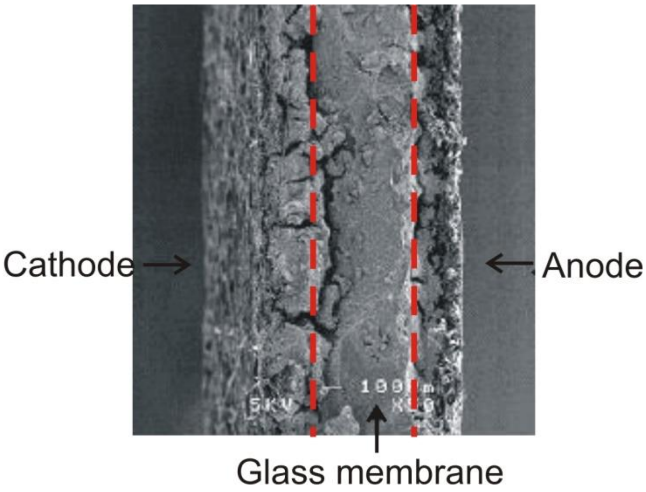

Figure 2.17 A SEM micrograph of the cross-section of the MEA based on the P_2O_5-SiO_2 glass membrane after testing in the fuel cell (Uma and Nogami, 2007b)

Phosphosilicate (P_2O_5-SiO_2) gels synthesized from alkoxysilane and H_3PO_4 by the sol-gel method have been studied for a long time and are promising solid state proton conductors in the low and medium temperature ranges. The phosphosilicate gels consist of thermally stable silica and phosphates and exhibit strong affinity with adsorbed water molecules. This behavior ensures high proton conductivities at medium temperatures even at low humidity. However, the chemical durability of the phosphosilicate gels is poor, due to the leaching of H_3PO_4 under humid conditions. To improve the chemical stability of the gels, the addition of inorganic additives such as Al_2O_3 and B_2O_3 to the phosphosilicate gel has been explored. In this direction, Matsuda et al. (Matsuda et al., 2001, Matsuda et al., 2002b, Matsuda et al., 2002a, Matsuda et al., 2003, Matsuda et al., 2005, Matsuda et al., 2006) investigated a phosphosilicate glasses containing Al_2O_3 or B_2O_3 as a third component. The addition of inorganic moieties in the gels has been found to enhance the conductivity at medium temperatures even at low relative humidity. Phosphosilicate gels with a P_2O_5-SiO_2 network consist of thermally stable silica and phosphate as shown in Figure 2.16. Phosphate has a strong affinity for water molecule adsorption, and is reported to reach a high proton conductivity of 0.015 S cm^{-1} at 130 ℃ and 0.7 % RH [24]. Zirconium hydrogen phosphate $Zr(HPO_4)_2$ is also a promising candidate within this solid acid proton conductor family, for elevated temperature operation due to its good proton conductivity (8.4×10^{-3} S cm^{-1} at room temperature and 100% RH and 10^{-4} S cm^{-1} at 100 ℃ and 95% RH) and insolubility.(Malhotra and Datta, 1997, Samms et al., 1996) Zirconium hydrogen phosphate has much higher intrinsic conductivity than SiO_2, TiO_2 and zeolites. Since $Zr(HPO_4)_2$ is not soluble in water, alcohol, and liquid acids such as phosphoric acid and sulfuric acid, the problem of leaching should not occur.(Malhotra and Datta, 1997, Samms et al., 1996) $CsHSO_4$ and other oxoacid salts have a super-protonic phase transition. When the temperature is above 150 ℃, their proton conductivities increase by several orders of magnitude up to 1×10^{-2} S cm^{-1}.(Otomo et al., 2005, Zisekas et al., 2005) As reported replacing the pure silica with composite silicate of strong acidity, e.g., the $Cs_3(H_2PO_4)(HSO_4)_2/SiO_2$ (Ponomareva and Shutova, 2005), CsH_2SO_4-SiO_2(Ponomareva and Shutova, 2007), P_2O_5-SiO_2(Tung and Hwang, 2005), P_2O_5-TiO_2-SiO_2(Nogami et al., 1999) or P_2O_5-ZrO_2-SiO_2(Nogami et al., 2001) also improves the proton conductivity.

2.5.5 Inorganic proton conductors based on ordered nanoporous or mesoporous materials

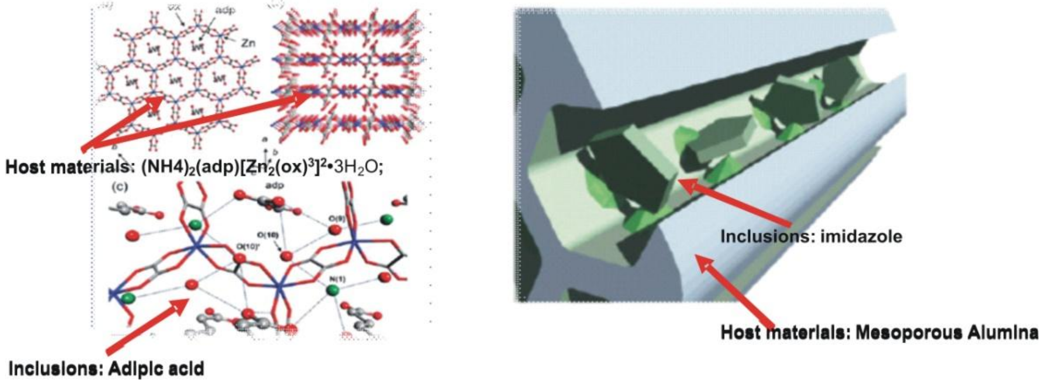

Figure 2.18 Two inorganic proton conductors based on mesoporous materials (left) Honeycomb layer structure of Metal-organic frameworks and Hydrogen-bond arrangements of -COOH, H_2O, and NH_4 in the interlayer. The colors of red, green, gray, and blue correspond to oxygen, nitrogen, carbon, and zinc atoms, respectively.(Sadakiyo et al., 2009) (right)Aluminium porous frameworks serving as host frameworks for the preparation of proton-conductive materials(Bureekaew et al., 2009)

One approach to new inorganic membranes having good thermo-stability and efficient proton conductivity at high temperature and low humidity, other than the materials used presently, is to synthesize functionalized ordered mesoporous solids. Such mesoporous inorganic materials are composed of micro- or nano- particles within which pores of diameter 2-50 nm exist. The pores are of identical size, and in some cases are ordered such that the thickness of the walls between the pores is the same throughout the particles (typically 2-12 nm). They exhibit high structural stability.(Kim et al., 1998, Sakamoto et al., 2002, Yu et al., 2006, Gobin et al., 2007a) The internal pores can be functionalized with protogenic functional groups such as $-SO_3H$, $-PO_3H_2$, -COOH and constitute potential conductive pathways for protons.

The uniformity of pore size and regularity in the arrangement of the pores may ensure even better proton pathways throughout the nanoarchitecture. Ordered mesoporous solids based on silica, and other main groups of solids are well-known and the proton conductivity has been evaluated. Li et al. reported the sol-gel derived mesostructured zirconium phosphates with proton conductivities of about 10^{-6}-10^{-8} S cm^{-1}. (Li and Nogami, 2002a) Colomer et al. synthesized nanoporous anatase films with conductivity values from 10^{-5} to 10^{-3} S cm^{-1} in the range of 33-81% relative humidity at room temperature. (Colomer, 2006a) Although the conductivity values of these mesoporous acid-free silica xerogels, meso-SiO_2 functionalized with perfluoroacid groups or anatase thin films are adequate for fuel cell applications, their performance as an electrolyte in a PEMFC has not been evaluated yet. (Yamada et al., 2005a, Colomer, 2006a, Li and Nogami, 2003a) These studies show that this class of materials is interesting for proton conduction. They possess desirable traits including large internal surface areas, mechanically stable frameworks, chemical inertness, and negligible electronic conductivity. Furthermore, materials functionalized with organic sulfonic acids through grafting or co-condensation have shown better proton conductivities compared to the non-functionalized one.(Hogarth et al., 2005a, Holmberg et al., 2005b, Lin et al., 2007) Davis et al. synthesized acid functionalized zeolite nanocrystals with proton conductivities in the range of 1.2×10^{-3}-1.2×10^{-2} S cm^{-1}.(Holmberg et al., 2005a, Alabi and Davis, 2006) While a few reports address the use of sulfuric acid functionalized mesoporous materials and zeolites, and a nonporous organic carboxylic acid containing silicate for fuel cell applications, there is little information on the effect of the acid strength and the pore structure (i.e. pore size and dimensionality) may influence proton transport under conditions of similar acid loading.(Alabi and Davis, 2006, Halla et al., 2003b)

The functionalized silicabased nano- and mesoporous materials are drawing more and more interest recent years, which are mainly acid-functionalized proton conductors based on mesostructured silica have been prepared by postgrafting [36] or co-condensing functional silica precursors [27, 37]. These materials exhibit promising proton conductivity at elevated temperatures and low RH due to superior water adsorption properties of the porous structure. The conductivity of pristine mesoporous silica is low, 10^{-6} S cm^{-1} to 10^{-4} S cm^{-1} under 40% to 90% RH.(Li and Nogami, 2002b) The conductivity of mesporous silica can be increased significantly by functionalization such as grafting sulfonic side groups on the external Si-O sites.(Marschall et al., 2009a) For instance, Marschall [38] synthesized SO_3H-functionalzied nanoparticles of Si-MCM-41 by co-condensation of mercaptopropyl trimethoxysilane (MPMS, $(CH_3O)_3SiHS$)) and tetraethoxysilane (TEOS, $Si(C_2H_5O)_4$) with a pre-hydrolysis step. At 140 ℃ and 100 % RH, this sample reached a high proton conductivity of 5×10^{-2} S cm^{-1}. Marschall et al.(Marschall et al., 2009b) synthesized imidazole functionalized mesoporous MCM-41 silica by immersing treatment and the highest conductivity was ~10^{-4} S cm^{-1} at 140 ^{o}C and 100% RH. However, the proton conductivity of sulfonic acid and imidazole functionalized mesoporous silica composites is also very sensitive to RH.(Marschall et al., 2009a, Marschall et al., 2009b) Because in these mesoporous proton conductors, sulfonic acid acted as the proton carrier, the conductive mechanism is similar to the PFSA polymer membrane such as Nafion. Alternatively, phosphoric acid and other proton conductive materials can also serve as the functionalization agent. It was reported that amphoteric phosphoric/ phosphonic acids are advantageous over sulfonic acid, which can facilitate proton conduction in the dry state by forming dynamic hydrogen bond networks(Zhou et al., 2006).

McKeen et al. have studied the proton conductivity of a series of pure-silica zeolite beta, mesoporous silica (MCM-41 and MCM-48) containing sulfonic acids, phosphonic acid or carboxylic acid.(McKeen et al., 2008b, McKeen et al., 2008a) They have shown that the aryl sulfonic acid containing samples exhibited the highest proton conductivity values, followed by propyl sulfonic acid containing materials, phosphoric acid containing materials and carboxylic acid materials. Jin(Jin et al., 2006) developed microporous MCM-41 by the co-condensation of diethylphosphatoethyl-triethoxysilane (DPTS, $(C_2H_5O)_3SiCH_2CH_2PO(OC_2H_5)_2$) and TEOS using surfactant cetyltrimethylammonium bromide (CTAB, $(C_{16}H_{33})N(CH_3)_3Br$) as a template. Then, the sample was phosphonated with the phosphoric-acid acidification. The MCM-41silica showed a proton conductivity of 3×10^{-4} to 0.015 S cm^{-1} at 130 ℃ with RH increased from 20 to 100 %. Additionally, the pore size impacts the proton conductivity, MCM-41 and MCM-48 exhibit higher proton conductivities than the corresponding pure-silica zeolite beta samples, and MCM-48 samples are more conductive than the corresponding MCM-41 samples. This may be related to the connectivity of pores in the inorganic network. While these approaches have generally increased bulk hydrophilicity of the respective materials, they have led to moderate improvements in bulk proton conductivity at temperatures above 100 ℃, largely because these hybrid materials still present RH-dependent conductivity.

2.5.6 The organic-inorganic hybrid membranes

To improve the proton conduction of the membranes, the hybrid organic-inorganic approach has been explored and various pathways have been considered. In the following section, we have focused our discussion on some of the most significant examples of recent key developments in this field. In order to achieve hybrid membranes, different strategies are proposed: (a) development of new membranes in which suitable hydrophilic oxygenated acids (e.g., phosphoric or sulfuric acids) are solubilized in a fluorinated polymeric matrix bearing acid groups (e.g. Nafion), (b) development of new membranes in which suitable hydrophilic oxygenated acids (e.g., phosphoric or sulfuric acids) are solubilized in a non-fluorinated polymeric matrix bearing acid groups (e.g., s-PEEK), (c) development of new membranes in which suitable hydrophilic oxygenated acids (e.g., phosphoric or sulfuric acids) are solubilized in a polymeric matrix bearing basic groups (e.g., polybenzimidazole); (d) development of membranes obtained by filling a non-proton conductive polymeric matrix with ionomers or inorganic particles of high proton conductivity. Finally, new types of hybrid organic-inorganic membranes have been suggested on the basis of their diverse and unique properties.

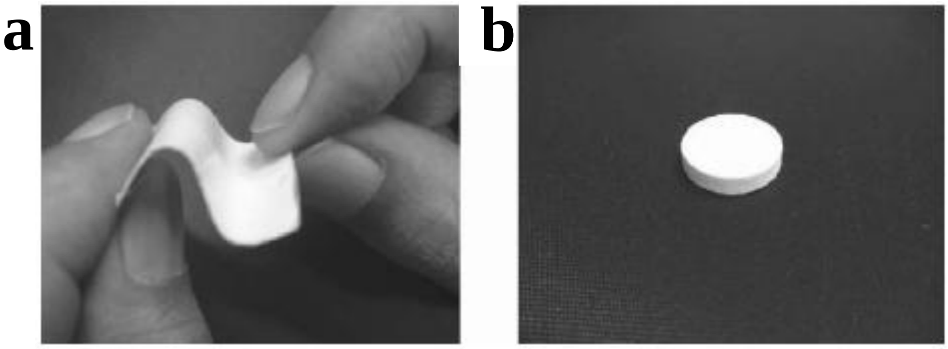

Figure 2. 19 Photographs of membrane of (a) 10 wt% organics and 90% $Sn_{0.9}In_{0.1}P_2O_7$ composite and (b) a pure $Sn_{0.9}In_{0.1}P_2O_7$ pellet from reference (Heo et al., 2007a)

A solid salt electrolyte cannot conduct proton or ionic charge by a vehicular mechanism. Some kind of “hopping” mechanism must be operative. Examples of such membranes were virtually nonexistent at modest temperatures until recently. There are a few examples of solid protic salt membranes but it remains a challenge to learn from these examples in order to make a proton conducting membrane that has all the qualities needed for use in fuel cell, especially a membrane that has suitable mechanical properties, such as flexibility and toughness, while operating over a broad range temperatures without the need for humidification. Nagao et al. have reported that ceramic membrane based on tin phosphate doped with various trivalent ions, such as In^{3+}, exhibit exceptionally high proton conductivity (> 0.05 S cm^{-1}) from room temperature to 200 ℃. (Nagao et al., 2006) Most interesting publication is the report of a composite of 90% $Sn_{0.9}In_{0.1}P_2O_7$ blended with 10% of an equimolar mixture of two organic compounds. This composite is formed into a flexible membrane with high proton conductivity independent of RH. (Tomita et al., 2007) The two organic compounds are 1.8-bis(triethoxysilyl)octane (TES-Oct) and 3-(trihydroxysilyl)-1-propane sulfonic acid [(THS)Pro-SO_3H], of which the conductivity is humidity-dependent. The inorganic/organic composite membrane shown in Figure 2.18a has a conductivity of about 0.04 S cm^{-1} at 150-200 ℃ without humidification. More organic component gives more flexibility to the composite while more ITP gives higher conductivity of the membrane. The membrane with 90 wt% ITP and 10 wt% organic component represents the optimal ratio of inorganic ITP and organic component for making a membrane with both good flexibility and the highest conductivity.

2.6 Summary

Table 2.3 Advantages and disadvantages of some polymer membranes for PEM fuel cells

Polymer membranes	Advantages	Disadvantages
Perfluososulfonic acid (PFSA)	Performance	Working temperature limited to 80 ℃
Modified PFSA composite	Medium operating temperatuere (80-120 ℃) Compromise between performance and thermal stability	Reliance on water content, dehydration at T >80 ℃
PBI	High operating temperature (> 150 ℃)	Low conductivity at low temperature; Limited durability
Modified PBI	Higher acid load, improved proton conductivity	Sensitive to acid leashing, decrease in mechanical properties
Heteropoly acids	Surper proton conductor	Water soluable, sensitive to

		relative humidity
Glass membrane	Mechanical and chemical stability	Low proton conductivity
Nano- or mesoporous membrane	Proton conductivity with less-relience on the relative humidity	Low proton conductivity
Organic-inorganic hybrid membrane	Compromise between flexibility and conductivity.	Heterogeneous, phase separation in membrane structure

Table 2.3 summarizes the main adventages and disadvantages of the various membranes discussed in this chapter. As can be seen, it is difficult to combine performance at high temperature, durability and cost. The PFSA membranes exhibit good performance and durability but they are expensive and its operating temperature is limited to 80 ℃. The PBI-based membranes operate at high temperature, but they exhibit low durability due to the high swollen ratio and the leakage of phosphoric acid. Many inorganic proton conductors including HPAs, glass membrane and porous membrane have been developed for their intrinsic mechanical and chemical stability at high temperature and for their low cost. Nevertheless, there are still unresolved practical issues in the membranes made of inorganic proton conductors due to relatively low proton conductivity compared to PFSA polymer membranes.

As reviewed in this chapter, significant efforts have been made to improve the performance of PEMFCs and DMFCs. Despite some success, widespread market penetration of fuel cell technologies has yet to be realized mainly because of high system cost and system performance limitations (to be specific, the expensive Pt-based catalyst and PFSA polymer membranes in fuel cells); besides, the performance of PEM-based fuel cells is often limited by membrane-related issues, such as water management and fuel crossover. One effective way to tackle these problems is to increase the operational temperature of PEM-based fuel cells; however, the existing proton-exchange-membranes are still unable to meet the needs for high temperature operation, in terms of high proton conductivity and thermal stability under high temperature and low humidity environment. The last section (section 2.5) of this chapter focused on the design, synthesis and properties of alternative proton conductive materials: the development of the sol-gel chemistry allows a fine tuning of the inorganic network, which exhibits acid-based functionalized pores (-SO_3H, -PO_3H_2, -COOH), tunable pore size and connectivity, high surface area and accessibility; the chapter also highlights the important advantage of using functionalized nano-structured or meso-structured materials, as opposed to previous reported simple nanoparticulate materials. For example, the superior properties of composite membranes containing functionalized-SiO_2 nanoparticles or a functionalized mesostructured silica network are discussed in sections 2.5. As such, these composite membranes containing various inorganic materials are a promising family for controlling conductivity, mechanical and chemical properties. It is clear that the field of fuel cells is still under development, and, as stated, the replacement of the Nafion membrane is the main hurdle that inorganic proton-exchange-membranes can help to overcome.

CHAPTER 3. EXPERIMENTAL

In this chapter, the experimental procedures such as fabrication of inorganic proton exchange membranes, preparation of the single cell, setup of the fuel cell operational system, and characterization techniques used in this study are detailed.

3.1 Chemicals

Reagents and materials used in this project include: sulfuric acid (98%, Sigma-Aldrich), hydrochloric acid (37%, Sigma-Aldrich), 1-butanol (99.8, Sigma-Aldrich), Pluronic P123 (poly(ethylene glycol)-block-poly(propylene glycol)-block-poly(ethylene glycol), MW=5800, Sigma-Aldrich), PluronicT F108 (Poly(ethylene glycol)-block-poly(propylene glycol)-block-poly(ethylene glycol), Mw=14600, Sigma-Aldrich), Pluronic F127 (Poly(ethylene glycol)-block-poly(propylene glycol)-block-poly(ethylene glycol), MW=10800, Sigma-Aldrich), Tetraethyl Orthosilicate (TEOS, 99.8%, Sigma-Aldrich), Phosphotungstic Acid (HPW, Sigma-Aldrich), Silicotungstic Acid (HSiW, Sigma-Aldrich), Phosphomolybdic Acid (HPMo, Sigma-Aldrich), Silicomolybdic Acid (HSiMo, Sigma-Aldrich), polyimide (PI, $[C_{40}H_{58}O_6N_2]_n$, $M_w \approx 100{,}000$), 1-methyl-2-pyrrolidone (NMP, Sigma-Aldrich), Teflon emulsion (PTFE, Sigma-Aldrich), carbon black (Vulcan XC-72, Cabot Corp.), methanol (99.99%, Sigma-Aldrich) and Nafion solution (5wt% Nafion polymer in isopropanol and water, DuPont).

3.2 Fabrication of HPA-meso-silica inorganic proton conductive materials

3.2.1 Synthesis of mesoporous silica framework materials

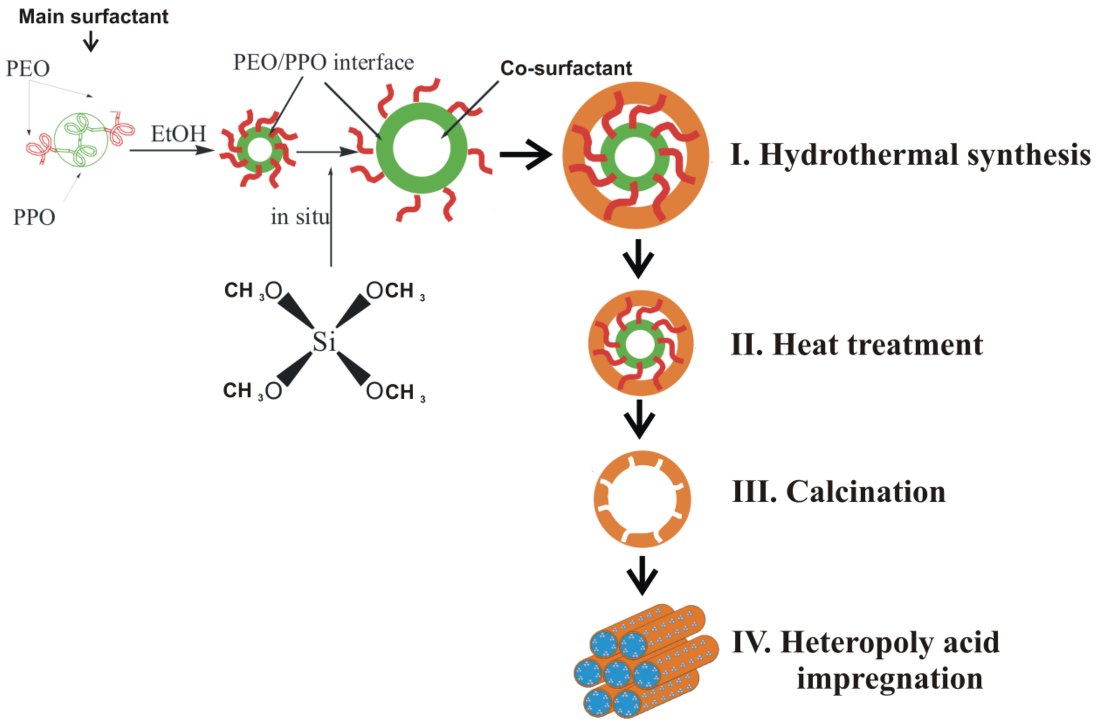

Figure 3.1 Procedure of the synthesis processes of mesoporous silica

The ordered mesoporous silica materials with various symmetries (e. a. $p6mm$, $Fm\bar{3}m$, $Im\bar{3}m$ and $Ia\bar{3}d$) were prepared according the synthesis method reported by Chen and Zheng et al (Li et al., 2007, Chen et al., 2005) and the tailored pore size is achieved according to the structural controlled method reported by Kleitz et al (Kleitz et al., 2003). In the first step, the mesoporous silica framework materials were synthesized by using a triblock copolymer P123 or F127 as a template under an acidic condition. Different types of co-surfactant (e.g. sodium dodecyl benzene sulfonate for Ia3d structure) was selected and used as an additive to induce the self-assembly. In a typical synthesis process, 2.3g of SDBS (6mM) was first dissolved in a solution containing 20g of triblock copolymer P123, 32g of HCl (67%), and 720g deionized water (18.2 MΩ), and stirred until a homogenous solution was formed. Then 43g of TEOS was added to the solution, the mixture was further stirred at 45 ^{o}C for 24h, then transferred and sealed into a hydrothermal reactor for hydrothermal treatment at 60-160 °C for another 24h. The product was filtered out and thoroughly washed with water and then air-dried overnight. In order to remove the block copolymer template, calcinations was carried out in an furnace at 650 ^{o}C in air for 6h. The process started from room temperature with a ramping rate of 1 ^{o}C min^{-1}. N_2 was used as protective atmosphere at temperature below 200 ^{o}C. Figure 3.1 shows the procedure of the synthesis process.

3.2.2 Heterpoly acid functionalization of mesoporous silica through vacuum impregnation method

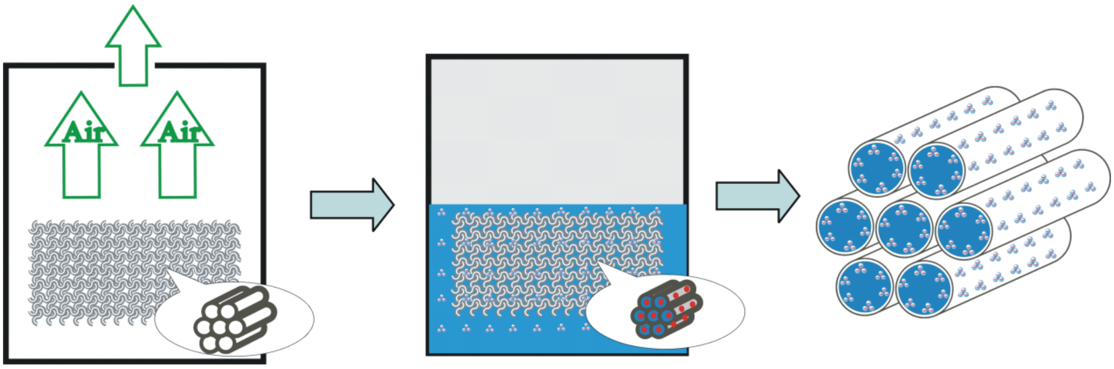

Figure 3.2 Procedure of the HPA impregnation step and HPA-meso-silica

Figure 3.2 shows the procedure of the vacuum impregnation process. In the vacuum impregnation step, the meso-silica powder was firstly placed under vacuum environment with pressure not higher than 0.1 atm, the vacuum state was maintained for 4 hours in order to remove impurities (mainly trapped air) inside the mesopores, and then the pure meso-silica was soaked in an aqueous solution of HPA for 24h. The vacuum impregnation technique was used to ensure a homogeneous distribution of the inclusion within the mesoporous silica framework.

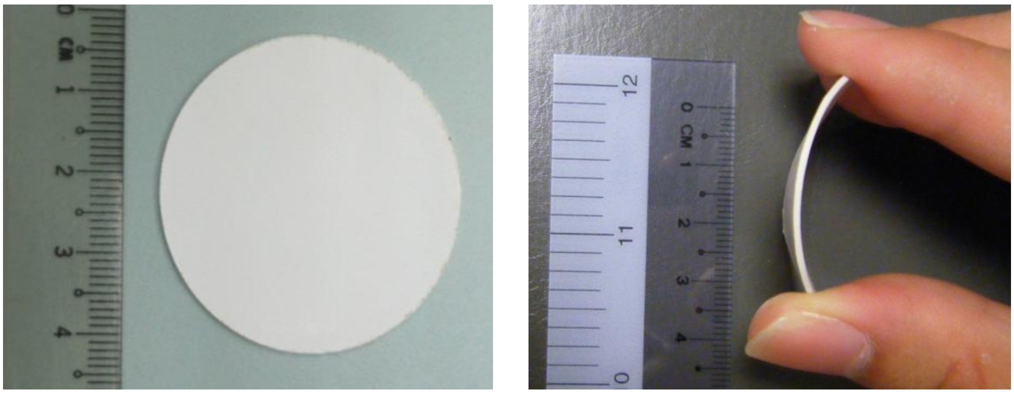

Figure 3.3 Optical micrograph of a hot-pressed (a)80 wt% HPW-meso-silica nanocomposite disc (b)5%PVDF80%HPW15%meso-silica composite membrane before the electrochemical performance test.

The HPA-meso-silica powder was pressed into disc for proton conductivity and single cell performance characterization, the hot press step was carried out under 180 ℃ and a pressure of 0.1 GPa for 20 minutes. The disc-like samples are 4 cm in diameter and 500-800 μm in thickness.

3.3 Fuel cell assembly and cell performance measurement

3.3.1 Gas diffusion electrode and catalyst layer

The wet-proofed carbon paper was prepared by immersing the untreated carbon paper in PTFE dispersion (5%) for 5 min and then dried in air for 30 min. Next, it was sintered in an oven (Carbolite, Eng.) at 350 ℃ for 30 min. The PTFE loading was determined by the difference in the weight of the carbon paper before and after the PTFE treatment. The weight percentage of PTFE on the carbon paper was calculated by PTFE/(Carbon paper+PTFE) and the PTFE loading was about 5 wt%. For the preparation of the diffusion layer, carbon powder with the 5 wt% PTFE dispersion was mixed and stirred in an ultrasonic bath at room temperature for 30 min. Then the suspension was applied to the wet-proof carbon paper. The diffusion layer was dried in air for 30 min and sintered in oven at 350 ℃ for 30 min. The carbon loading in the diffusion layer was about 2 mg cm^{-2}. The weight percentage of PTFE in the diffusion layer was determined by PTFE/(Carbon powder +PTFE) and was about 30 wt% for the diffusion layer.

The catalyst layer for the anode in DMFCs was prepared by making a homogeneous suspension from Pt/Ru black (40% Pt and 20% Ru on Vulcan XC-72R Carbon, Johnson Matthey), Nafion solution (5 wt % in a mixture of aliphatic alcohols, Sigma Aldrich), and isopropyl alcohol (Sigma-Aldrich) was sprayed onto a carbon gas diffusion layer (Toray Graphite Paper, TGPH-120, 40% wet-proofed, E-TEK, Inc.) by airbrushing until a platinum loading of 3 mg cm^{-2} was achieved for the anode. The same procedure was used for the cathode with Pt loading of 2 mg cm^{-2} (60% Pt on Vulcan XC-72R Carbon, Johnson Matthey). The electrode area was 4.0 cm^{2} for both anode and cathode. The suspension was then applied onto diffusion layer. The catalyst layer was dried in air for 20 min and sintered in oven at 80 ℃ for another 20 min.

3.3.2 Membrane electrode assembly (MEA) and Catalyst coating membrane (CCM)

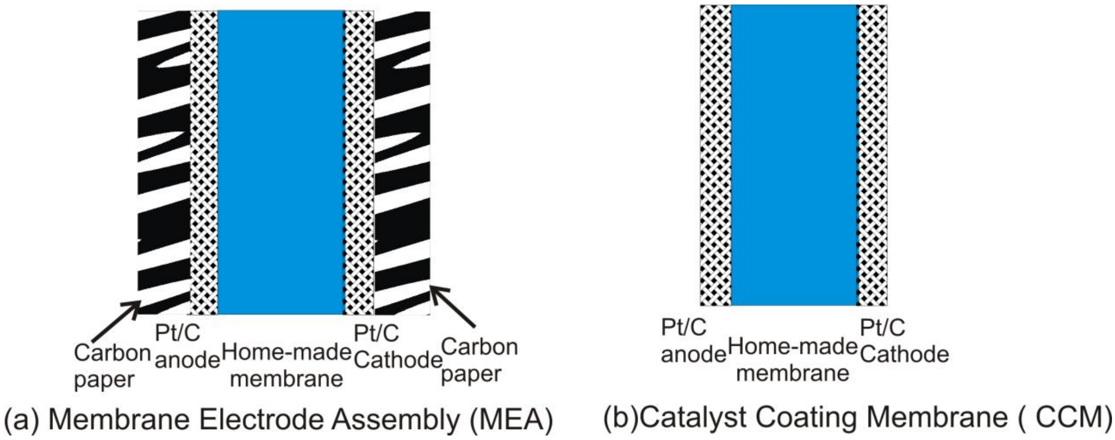

Figure 3.4 Schematic diagrams of (a) Membrane Electrode Assembly (MEA) and (b)Catalyst Coating Membrane (CCM) with the home-made electrolyte membrane

To evaluate the fuel crossover (hydrogen in PEMFC and methanol in DMFC) and the cell performance for PEM fuel cells, the membrane-electrode-assembly (MEA) was made by sandwiching the home-made membrane between an anode catalyst layer and a cathode catalyst layer, both catalyst layers are supported by the carbon papers (Toray TGPH-060) which also act as gas diffusion layer (GDL) for both anode and cathode (Figure 3.3a). The Pt-based catalyst was mixed with homogeneously with 10 wt% Nafion and used for catalyst layer; the loading of Pt was carefully controlled at a certain value. The MEA was then hotpressed at 140 °C and 4 MPa for 90 s. The electrode area was 4 cm^2.

The meso-silica/HPW membrane based single cell is also assembled through a CCM method as shown in Figure 3.4b. A mixture of PtRu/C catalyst (40% Pt and 20% Ru on Vulcan XC-72R Carbon, Johnson Matthey), Nafion emulsion (5 wt % in a mixture of aliphatic alcohols, Sigma Aldrich), and isopropyl alcohol (Sigma-Aldrich) was sprayed directly onto the electrolyte membrane surface by airbrushing until a platinum loading of 3 mg cm^{-2} was achieved for the anode. The same procedure was used for the cathode with Platinum loading of 2 mg cm^{-2}, but a Pt/C catalyst (60% Pt on Vulcan XC-72R Carbon, Johnson Matthey) was used.

3.3.3 Full cell testing system

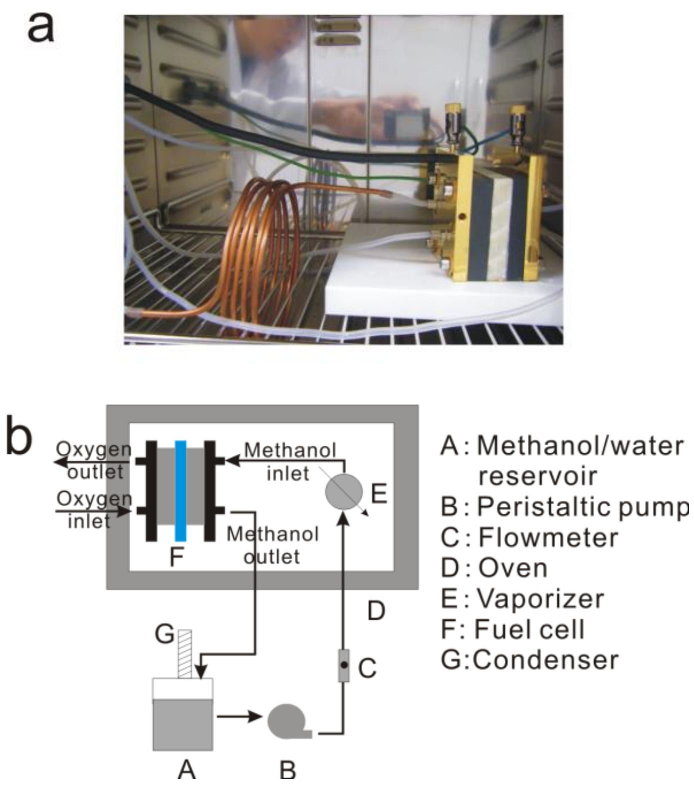

Figure 3.5 The picture and (b) the scheme of the DMFC test arrangement

In a typical single cell test, a MEA or a CCM was inserted between the two graphite plates with a single serpentine flow channel for fuel cell performance characterization. For the PEMFC test, hydrogen and air (or oxygen) flow rates were 20 and 50 ml min^{-1} (10 ml min^{-1} for O_2), respectively. The relative humidity of feeding gas was controlled by the Greenlight PEMFC station. Figure 3.5 shows the scheme of the DMFC test arrangement. Methanol fuel was pumped with a peristaltic pump and the methanol flow rate of 2 mL min^{-1} was regulated with a recirculation loop and measured by a flowmeter (Alicat Scientific) before being fed into a vaporizer. This unit consisted of a 1 m long copper tube coil placed in a heating oven. The steam generated in this way entered the anodic compartment of the DMFC. A fuel recovery system was employed. The exhaust vapor exited from the cell through a PTFE pipeline and was recycled with a water cooled condensing coil.

3.4 Electrochemical characterization

3.4.1 Membrane conductivity test using electrochemical impedance spectroscopy (EIS)

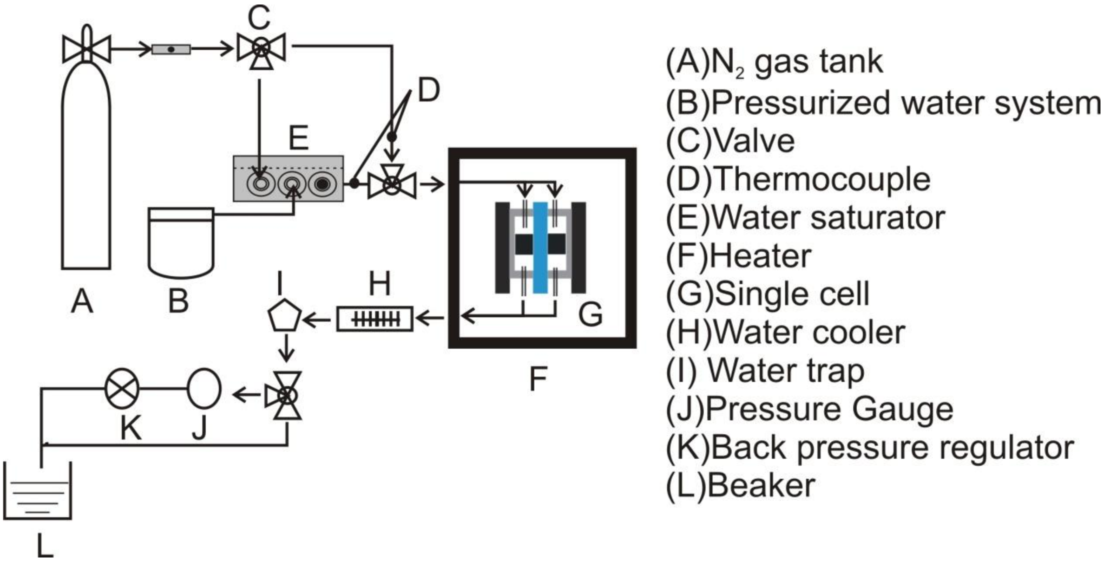

Figure 3.6 Schematic of experimental setup for proton conductivity measurement in a temperature range of 25-300 ℃. The effective electrodes area was 4 cm^2.

Proton conductivity measurement system has been constructed. Figure 3.6 shows the schematic of the system. It consisted of three main parts: the humidification unit, the conductivity cell, and the back-pressure control unit. A humidification system G050 (FCATS-G050, Greenlight, Canada) having a BT-301 pressurized deionized water system and a BT-104 saturator was installed to automatically control RH from 1 to 100 %. Nitrogen was used to carry humidified moisture into the conductivity cell. We controlled the flow rate of N_2 at around 100 ml min^{-1}. A back-pressure control system consisted of an Omega pressure meter and a Swagelok needle valve. We adjusted the back pressure to be higher than the saturated water vapor pressure at each RH to pressurize the conductivity cell. In order to avoid blocking the needle valve, the moisturized exhaust gas out of the conductivity cell was cooled and passed through a water trap. The captured water was emptied out of the water trap periodically, while the dry gas was passed through the pressure meter and then released into air. Three temperatures-the conductivity cell temperature, the cell inlet temperature, and the saturator temperature-needed to be adjusted according to different operating conditions. The cell inlet temperature was adjusted to be higher than that of the conductivity cell to avoid water condensation in the connecting tube. The system allowed the conductivity measurements in the temperature range from 25 to 125 ℃.

Electrochemical impedance spectroscopy (EIS) is a powerful experimental technique to study the different processes that take place in fuel cells. The EIS technique in general involves the measurements of current through a cell when a sinusoidal voltage of low amplitude is applied. The sine wave is used in impedance measurements because a sinusoidal signal (regardless of its amplitude or frequency) has the same wave and angular frequency for its incident and resultant waves signal. AC impedance spectroscopy measurements on dense pellets have been widely used to study the proton conductivity of inorganic materials(Nagao et al., 2006, Heo et al., 2007a, Heo et al., 2007b, Tomita et al., 2007). Different materials have served as blocking electrodes: carbon papers, platinum disks, brass discs, graphite slices, or gold foils. Ionic conductive materials were pressed into pellets at room temperature. A sealed-off cell was used to avoid evaporation of water. An example of the sample arrangement is shown in Figure 3.7.

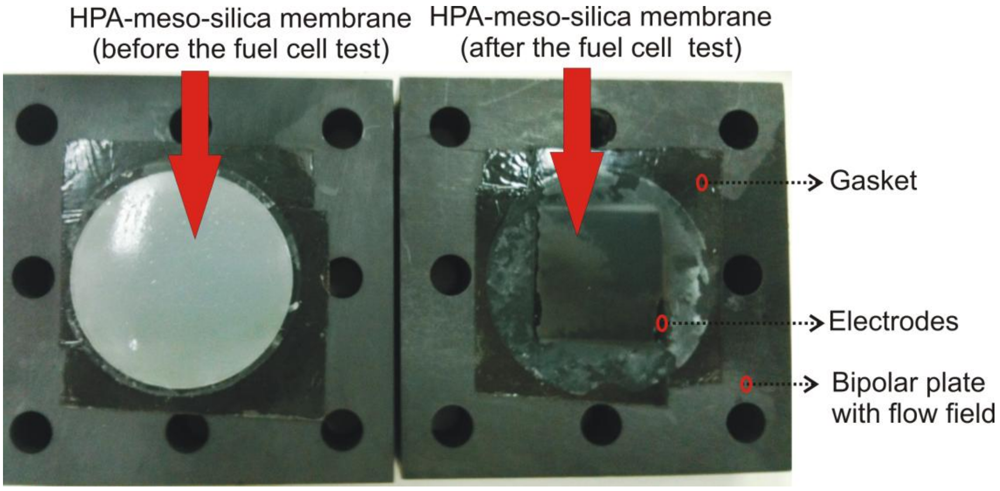

Figure 3.7 Photos of a single cell used for proton conductivity test

During the conductivity measurement, the single cell was put into an oven to provide high operational temperatures, and the single cell was connected to the humidification system G050 as described in the reference(Qi and Kaufman, 2002): by adjusting the temperature in the water tank this system permits a wide range of RH in the cell. Instead to heat up the whole water tank, the G050 system used a saturator (BT-104 BekkTech saturator) to improve the accuracy of the RH adjustment. Note that the single cell was previously developed and successfully used in our laboratory for in-plane conductivity measurements of a verity of polymeric and composite proton conductive membranes such as Nafion membranes. One of the features of the single cell is a relatively small cell chamber, and this allowed for better control of the sample's RH. In our measurements, the RH was calculated from the ratio of the pressures of saturated water vapor at the temperature between the humidification saturator $P(T_h)$ and the conductivity cell $P(T_c)$ as follows:

$$\mathrm{RH}\ (\%) = P(T_h) / P(T_c) \times 100 \tag{3.1}$$

A two-electrode through-plane conductivity measurement method was developed in this study. Inorganic pellet samples were sandwich-held between two carbon paper electrodes (4 cm^2). AC impedance test was carried out using a potentiostat-galvanostat Autolab FRA interfaced to a personal computer. The EIS measurements were conducted at various potentials. The impedance spectra were collected in the frequency between 1MHz and 1Hz.

The EIS equivalent circuit modeling approaches were commonly used to treat the impedance spectroscopy data and to retrieve proton conductivity values for inorganic materials(Uma and Nogami, 2008b, Uma and Nogami, 2008a). In this study, based on the physical characteristics of the inorganic sample assembly, we newly introduced the geometrical cell capacitance. Figure 3.8 shows an equivalent circuit models consisting of resistors and capacitors. An EIS Nyquist plot consists of a y-axis being the negative imaginary impedance and an x-axis representing the real impedance (resistance). Each point is the impedance value for one frequency value. The simple model as shown in Figure 3.8b was used when the complex impedance Nyquist plots simply consisted of a semi-arc and a low frequency tail.

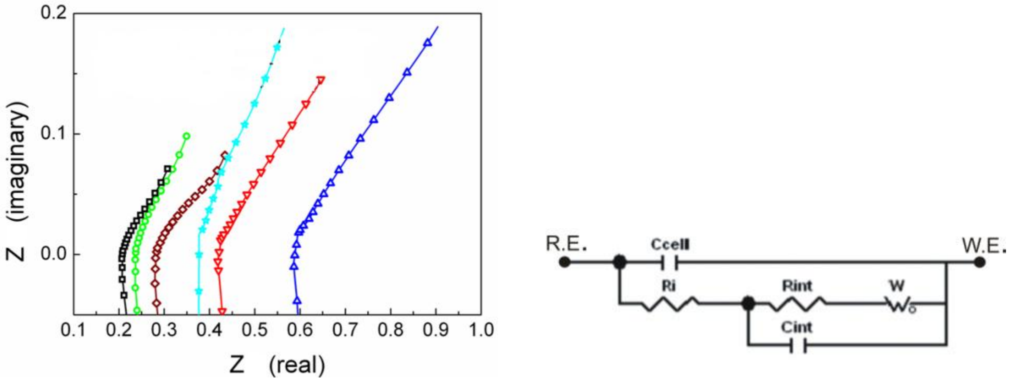

(a) (b)

Figure 3.8 (a) typical Nyquist plots measured for the cell with an inorganic membrane, the frequency range of 1M-1Hz and (b) the schematic of the EIS equivalent circuits

In the models, R_{int} is the resistance of the interface (Ω), R_i is the ionic resistance across the pellet (Ω), R_e is the electronic resistance through the pellet (Ω), W is the Warburg impedance (S), C_{int} is the interface capacitance (F), and C_{cell} is the geometrical cell capacitance (F). The Warburg impedance W and the interface capacitance C_{int} can be defined as:

$$\mathrm{W} = \sigma\omega^{-1/2} - \mathrm{j}(\sigma\omega^{-1/2}) \quad (3.2)$$

$$\mathrm{C_{int}} = \frac{1}{\sigma\omega^{1/2}} \quad (3.3)$$

Thus, the membrane resistance wis given by equation (3.4):

$$R_{mem} = R_p - R_a \quad (3.4)$$

Where R_p and R_a are the cell resistance in the presence and in the absence of membrane, R_{mem} is the membrane resistance. The conductivity σ is determined by equation (3.5):

$$\sigma = \frac{L}{R_{mem}A_{electrode}} \tag{3.5}$$

Where L is the thickness of the membrane, and $A_{electrode}$ is the area. Figure 3.5 shows an example of impedance curve for membrane conductivity test on a carbon paper electrode.

3.4.2 Methanol crossover current measurements

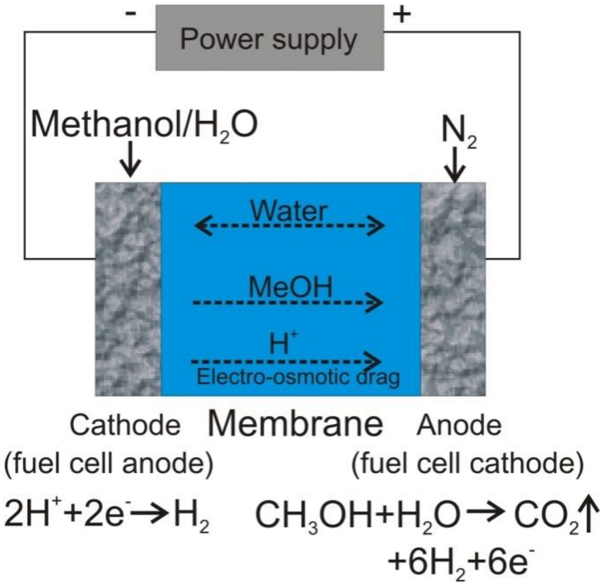

Figure 3. 9 Schematic illustration of the methanol permeation measurement in the actual DMFC

Limiting methanol permeation currents through the membrane in the real fuel cell were measured voltammetrically.(Jiang et al., 2006a) This method includes inverting the cell polarity with respect to that used in the fuel cell normal mode, so that a limiting current density is measured because of the transport-controlled methanol oxidation at the former cathode of the fuel cell (now the anode) fed with inert N_2. In the former anode (now the cathode), hydrogen evolution takes place, serving as a counter and reference electrode. The system is represented in Figure 3.9. The actual crossover current is somewhat larger than the measured limiting current density. This is due to the counter methanol flux associated with the electrode-osmotic drag of solution by the protonic current corresponding to the limiting current. The methanol crossover current ($J_{crossover}$) was calculated according to the following expression (eq.3.6) proposed by Ren et al.(Ren et al., 2000).

$$\frac{J_{crossover}}{J_{lim}} = \frac{6\varepsilon x_0}{\ln(1+6\varepsilon x_0)} \quad (3.6)$$

Where J_{lim} is the limiting methanol permeation current, ε is is the electro-osmotic drag coefficient, and x_0 is the methanol molar fraction.

3.4.3 The electrode overvoltage measurement

The electrode overvoltage is measured using the method as reported by Lobato et al. ((Lobato et al., 2008): in order to measure the open circuit potential of the anode, a nitrogen flow is passed through the cathode, which allows the cathode to be used as a dynamic hydrogen reference electrode (DHE), assuming that changes in its potential are negligible over the range of current densities used. (Barton et al., 2001) The anode potential was thus calculated according to eq.3.7, following the empirical model proposed by Argyropoulos et al (Argyropoulos et al., 2003).

$$E_a=E_{0a}+b_a\log i+iR-C_1\ln(1-C_2i) \quad (3.7)$$

where the parameter Ea is the anode potential, E_{0a} is the open circuit potential of the anode, b_a is the Tafel slope of the methanol oxidation, i is the current density, R is the ohmic resistance of the system, C_1 is related to reaction kinetics and C_2 is related to mass transfer limitations. The anode potential was corrected with the tested R value. The cathode potential was calculated by the addition of experimental anode potential to the cell value (Lobato et al., 2008).

3.5 Physical characterization

3.5.1 Small Angle X-ray Spectra (SAXS)

Small angle X-ray scattering (SAXS) spectra were measured on a SAXSess high-flux small-angle X-ray scattering instrument (AntoPaar GmbH) equipped with two-dimensional wire detector and a Cu (λ=0.1542nm) rotating anode operated at 80 kV and 40 mA at 25 ℃. The angles at which the scattered X-rays are detected can be selected between the small-angle X-ray scattering (SAXS) range of 0.05° to 5° and the small-and-wide-angle X-ray scattering (SWAXS) range of 0.05° to 45°. The scattering profiles was shifted to the origin and normalized to the unit incident-beam intensity. The results can be described by the following equation:

$$q = \frac{4\pi}{\lambda} \sin\left(\frac{\theta}{2}\right) \tag{3.8}$$

Where q is the momentum transfer, λ is the wavelength of the X-rays and θ is the scattering angle (the angle between the incident and the scattered X-rays. The scattering angle is calculated from three factors: the distance of the respective picture pixel, the zero-angle position and the sample-to-detector distance.

$$\theta = \frac{180}{\pi} \cdot \frac{d}{d_0} \tag{3.9}$$

Here, λ = 0.1542nm for Cu-K α radiation, d_0 = 263.3nm for the standard sample holder for solid film samples, d is the d-spacing of the main scattering peaks. Thus the unit cell parameter can be obtained by the following equation

$$\alpha = d_{hkl}\sqrt{h^2 + k^2 + l^2} \tag{3.10}$$

Where d_{hkl} is the d-spacing of the scattering peak hkl; h, k and l are the miller index of the crystal. For example, the unit cell parameter of cubic $Ia\bar{3}d$ pore symmetry is obtained by $\alpha = d_{211}\sqrt{6}$

3.5.2 X-ray Diffraction (XRD)

X-ray diffraction (XRD) patterns for silica nanoparticles were obtained on a diffractometer (Philips PW1710) using Cu Kα source operated at 40 kV and 30 mA. The scan rate was 0.02 °. The sample was obtained by depositing silica nanoparticles on a glass substrate and dried in a vacuum oven at 40 ℃. From the full width at half height of the (111) peak, the volume-average particle size was calculated using the Scherrer equation:

$$d(\text{nm}) = \frac{k\lambda}{\beta\cos\theta} \tag{3.11}$$

Where k is a coefficient (0.9), λ the wavelength of X-ray used (0.154056 nm), β the fullwidth half-maximum of respective diffraction peak (rad) and θ the angle at the position of peak maximum (rad). Meanwhile, lattice constant (α) can be obtained based on the following equation:

$$\alpha = d_{\alpha}\sqrt{h^2 + k^2 + l^2} \tag{3.12}$$

Where d_α is the wavelength of X-ray; h, k and l are the miller index of the crystal.

3.5.3 N$_2$ sorption isotherms

Nitrogen adsorption/desorption isotherms were measured using a Micromeritics ASAP Tristar II 3020 system. The samples were degassed at 300 ^{o}C overnight under nitrogen flow. Specific surface area was calculated using the Brumauer-Emmett-Teller (BET) method in the relative pressure (P/P$_0$) range of 0-0.99. The total pore volumes were estimated from the adsorbed amount at the P/P$_0$=0.99 and the mesopore sizes distribution were obtained from the adsorption branch of the isotherms by using the non-linear density function theory (NLDFT). The calculation of mesopore distribution from nitrogen adsorption data developed by Barret, Joyner and Halenda(Barrett et al., 1951) in1955 (BJH method), is summarized in the formula:

$$V_{ads}(X_K) = \sum_{i=1}^{k} \Delta Vi\big(r_i \leq r_c(X_K)\big) + \sum_{i=1}^{k} \Delta S_i t_i\big(r_i \geq r_c(X_K)\big) \quad (3.13)$$

In this formula, $V_{ads}(X_K)$ is the volume of liquid adsorbed ($\mathrm{cm^3 g^{-1}}$) at relative pressure X_K (calculated from the value of adsorption expressed in ($\mathrm{cm^3 g^{-1}}$ STP) by $V_{ads}(X) = 0.0015468(X)$, V is the pore volume, S is the surface area and t is the thickness of adsorbed layer. According to equation (3.12), the adsorbed amount at k-th point of adsorption isotherms may be divided into two distinct parts: one is a volume in condensate in pores with their pore sizesmaller than a certain characteristic size depending on current relative pressure, $r_c(X_K)$; the other is a volume of adsorbed film on all larger pores, calculated a sum of pore surface area.

3.5.4 Transmission Electronic Microscopy (TEM)

Mesoporous materials were examined using a transmission electronic microscope (TEM, JEOL 2010) under an accelerating voltage of 200kV. A TEM sample was obtained by immersing a copper grid coated with carbon film in the Silica nanoparticle colloid solution and was allowed to dry at room temperature. Pore size and pore wall thickness distribution were obtained by measuring more than 100 particles from the enlarged TEM images. In order to observe the distribution of Heterpoly acid particles inside the ordered channels (or pores) of mesoporous silica, TEM samples were prepared as follows: the copper grid with carbon thinfilm was soaked with a HPA-meso-silica/ethanol mixture for 5 min, and then dried at room temperature. The compositions were determined using TEM equipped with EDS.

3.5.5 Fourier Transform Infrared Spectroscopy (FTIR)

FTIR absorption spectra of the pure HPAs and HPA-meso-silica composite membranes were recorded with a JASCO FTIR-Q250 spectrometer (spectral range of 4000-200cm^{-1}, 50 scans, and a resolution of 2 cm^{-1}). The samples were diluted in KBr (10% sample and 90% KBr) and were pressed into thin wafers for study.

3.5.6 Raman scattering spectroscope

The Raman scattering experiments were performed at room temperature on a computerized Renishaw RM1000 double monochromator, using a Lexel Ar^{+} laser. The 514.5 nm laser line was about $2\,\mathrm{cm}^{-1}$. The scattered light detected in a backscattering geometry was collected on the photocathode of a cooled photomultiplier interfaced to a standard photon counting system.

3.5.7 Thermal Gravimetric Analysis (TGA)

Thermal gravimetric analyses were performed on a Shimadzu DT-30 analyzer. Fresh samples were placed in a cell and heated in nitrogen atmosphere with a flow rate of 60 ml min^{-1}, and at a the temperature ramping rate is $10\,°\mathrm{C}\ \mathrm{min}^{-1}$.

3.5.8 Weight increase, water uptake and swelling ratio of the membranes

The doping level, water uptake of HPA-meso-silica membranes was determined by measuring the weight variation between un-doped and vacuum dried HPA-meso-silica membranes. First, the meso-silica membranes were dried under vacuum at 120 ℃ overnight and the weight (W_{dry}) was recorded. Second, the membrane was immersed in a saturated HPA solution. After 72h, the membrane was taken out, blotted with tissue paper and weighed (W_{wet}). Finally, the acid-doped membrane was dried at 120 ℃ under vacuum for 24 h and weighed again (W_{acid}).

$$\text{Total increased weight (wt.\%)}=\frac{W_{wet}-W_{dry}}{W_{dry}}\times 100\% \tag{3.14}$$

$$\text{Wateruptake (wt.\%)}=\frac{W_{wet}-W_{acid}}{W_{dry}}\times 100\% \tag{3.15}$$

$$\text{Swelling ratio(\%)}=\frac{l_{wet}-l_{dry}}{l_{dry}}\times 100\% \tag{3.16}$$

Where l_{dry} and l_{wet} are the thickness of dried and wet membranes, respectively.

3.5.9 Membrane wettability measurements

The wettability of a solid surface depends on both the surface energy and surface roughness, and with a certain kind of liquid on the solid surface, the wettability is usually represented by the static contact angle. The static contact angle is the angle at the solid, liquid and gas interface. The static contact angle (θ_c) represents the angle measured at the liquid/gas interface on the solid surface from the liquid side. For a liquid water droplet on a solid surface with a static contact angle lower than 90 ℃ is defined as hydrophilic, otherwise it is hydrophobic. On a perfectly flat surface, the static contact angle solely depends on the surface free energies at the interfaces, which are intrinsic material properties. The static contact angle on a perfectly flat surface is commonly represented by the Yound's equation(Jiao and Li, 2010):

$$\cos(\theta_c) = \frac{\gamma_{sg} - \gamma_{sl}}{\gamma_{lg}} \tag{3.17}$$

Where θ_c is the static contact angle, and γ_{sg}, γ_{sl} and γ_{lg} (J cm^{-2}) are the free energies per unit area of solid-gas, solid-liquid and liquid-gas interface.

CHAPTER 4. Phosphotungstic Acid Functionalized Mesoporous Silica Nanocomposites

In this chapter, our study focuses on the interaction between the HPW inclusion and the mesoporous silica host materials in a HPW-meso-silica nanocomposite by SAXS, FTIR, TGA and TEM. The proton conductive mechanism of HPW-meo-silica membrane is discussed and the effects of phosphotungstic acid (HPW) loading on the membranes thermal stability, water uptake and proton conductivity have also been systematically studied. The optimized HPW loading and testing conditions are determined for further investigation.

4.1 Introduction

Proton exchange membrane fuel cells (PEMFCs) have been considered as an attractive energy source for both portable and automobile applications because of their high energy conversion efficiency, high power density, quiet operation and low greenhouse gas emission.(Bauen and Hart, 2000, Steele and Heinzel, 2001) The efficiency and performance of PEMFCs can be further enhanced by increasing the operating temperature of fuel cells to 120-200 ^{o}C due to the improved reaction kinetics and significantly reduced catalyst poisoning by CO.(Yang et al., 2001, Li et al., 2003b, Zhang et al., 2006b) Water and heat management of fuel cells systems becomes easier at high temperatures. Direct methanol fuel cells benefit significantly from the increased operation temperatures.(Ahmad et al., 2010, Neburchilov et al., 2007) However, the proton conductivity of proton exchange membranes of the state-of-the-art perfluorosulfonic acid (PFSA) membranes such as Nafion, depends strongly on the water content of the membrane and decreases significantly with increase in temperature or decrease in relative humidity due to the loss of water from the membrane under conditions of high temperature or low humidities.(Zawodzinski et al., 1993, Yang et al., 2004, Sone et al., 1996, Hickner et al., 2004, Yan et al., 2009, Ciureanu, 2004) Thus the grand challenge is to develop proton exchange membranes with high conductivity and stability at elevated high temperatures (> 100^{o}C) and low humidity.

Surfactant template mesoporous materials such as mesoporous silica have attracted a great deal of attention because of the tunable mesoporous structure. High specific surface area, nano-sized channels or frameworks with an ordered and interconnected internal structure, and high structural stability allow their potential applications as proton exchange membranes operating at elevated temperatures.(Li and Nogami, 2002b, Athens et al., 2007b, Colomer, 2006b, Yamada et al., 2005b, Daiko et al., 2002, Li and Nogami, 2003b, Uma and Nogami, 2007d, Xiong and Nogami, 2006, Vichi et al., 2000, Halla et al., 2003a) Capillary condensation would occur favorably in meso- or nano-sized hydrophilic channels or pores, and the saturation vapor pressure decreases with the decreasing diameters of the capillaries, resulting in the water condensation at reduced humidity. (Bocquet et al., 1998) Rao et al studied the HPW in alumina-grafted silica-gel and mesoporous SBA-15 silica by impregnation and the results show that high surface area and high surface concentration of silanols in SBA-15 are beneficial for the immobilization of HPW catalysts. (Rao et al., 2005) The HPAs such as HPW molecules/clusters can be impregnated into the silica matrix by impregnation or by one-step synthesis process, forming immobilized HPW nanoparticles/clusters in the silica matrix.(Lu et al., 2010, Tang et al., 2010) The proton conductivity of HPW-functionalized MCM-41 reached 0.018 and 0.045 S cm^{-1} at 25 and 150 ^{o}C, respectively. Thus, the combination of the mesoporous silica matrix and proton conducting HPW would offer a promising candidate of high temperature PEMs for fuel cells. Here, we study in detail the relationships between the HPW content, the proton conductivity and stability and cell performance of HPW functionalized mesoporous silica with a cubic bicontinuous structure ($Ia\bar{3}d$). The results demonstrate that the proton conductivity of HPW/meso-silica nanocomposites depends strongly on the HPW content and the threshold for proton conductivity is ~10 wt% of HPW. The HPW-meso-silica membranes exhibited proton conductivity as high as 0.07 S cm^{-1} at 25^{o}C under 100% RH. The cells employing a HPW-meso-SiO_2 electrolyte membrane produced an impressive power output with both hydrogen and methanol fuels. The results indicate that the mesoporous HPW-functionalized silica nanocomposite is a promising PEM material for PEMFCs operated under high temperature and low RH conditions.

4.2 Experimental

4.2.1 Preparation of HPW-meso-silica membranes

The detailed procedures of the synthesis of mesoporous silica and HPW-functionalized meso-silica by the impregnation method are described in section 3.2. HPW-functionalized meso-silica or HPW-meso-silica electrolyte disc samples for the conductivity and cell performance measurements were prepared by hot-pressing at 180 ^oC for 2h. The disc samples have a diameter of 4.0 cm and thickness of ~500 μm. The calcinated powders samples were denoted as Ia3d-x (x is the hydrothermal treatment temperature, ranging from 60^{o}C to 160^{o}C). Table 4.1 shows some experimental conditions of the samples.

Table 4.1 Experimental conditions for HPW/meso-silica electrolyte fabrication

Samples	Heat treatment temperature of host materials	Composition (in weight ratio)
Pure meso-silica	100^{o}C	100% silica
80% HPW-meso-silica	100^{o}C	80% silica + 20%HPW
60% HPW-meso-silica	100^{o}C	60% silica + 40%HPW
40% HPW-meso-silica	100^{o}C	40% silica + 60%HPW
20% HPW-meso-silica	100^{o}C	20% silica + 80%HPW

4.2.2 Cell preparation and characterization

For the cell performance measurement, the 80wt% HPW-meso-silica nanocomposite was used as electrolyte and carbon paper (Toray TGPH-060) was used as the gas diffusion layer (GDL) for both anode and cathode. The single-cell hardware with 4 cm^2 active area and graphite flow field plates were used for PEMFC and DMFC performance characterization. For the PEMFC test, hydrogen and air (or oxygen) flow rates were 20 and 50 ml min^{-1} (10 ml min^{-1} for O_2), respectively. Pt/C (20 wt% Pt/C, E-TEC) was used as catalysts for anode and cathode and Pt loading was 0.4 mg cm^{-2}. The relative humidity of feeding gas was controlled by the Greenlight PEMFC station. A cell with Nafion 115 (DuPont) membrane was also conducted and tested in H_2/O_2 at 80^{o}C under the same conditions.

The methanol crossover through the HPW-meso-silica nanocomposite membranes was measured using a limit current method. A HPW-meso-silica membrane was sandwiched between an anode and a cathode layers with an active electrode area of 4 cm^{2}; 20wt% Pt/Ru/C catalyst was used for the anode and 20wt% Pt/C catalyst was used for the cathode. The loading of Pt was about 0.4 mg cm^{-1}.The anode was fed with 2 M methanol at a flow rate of 0.5 ml min^{-1} and dry nitrogen gas was fed to the cathode side at 50 ml min^{-1} under ambient pressure. The potential was scanned from 0.1 to 1.0 V at a scan rate of 5 mV s^{-1} and the methanol penetrated through the membrane was oxidized on the cathode side. The cell temperature was stabilized for 1h before the test. For the DMFC test, air was fed at 50 ml min^{-1} without humidification and back pressure control at the cathode side. The flow rate of the methanol solution (2.0 M) was 0.5 ml min^{-1}. Cathode Pt loading was 2 mg cm^{-2} 50 wt% Pt/C and anode Pt loading was 4 mg cm^{-2} 50wt% PtRu/C; the effective membrane area is 4 cm^{2}. The cell performance measurements were carried out in the temperature range of 80-160^{o}C. The stability of the methanol/air fuel cell was tested at 150°C under a constant cell potential of 0.5 V for 51.5 hrs. The thickness of the HPW-meso-silica nanocomposite membrane was 0.5 mm.

4.3 Results and discussion

4.3.1 Structural properties and thermal stability of HPW-meso-silica nanocomposite measured through SAXS, N_2 absorption isotherms, TGA and TEM

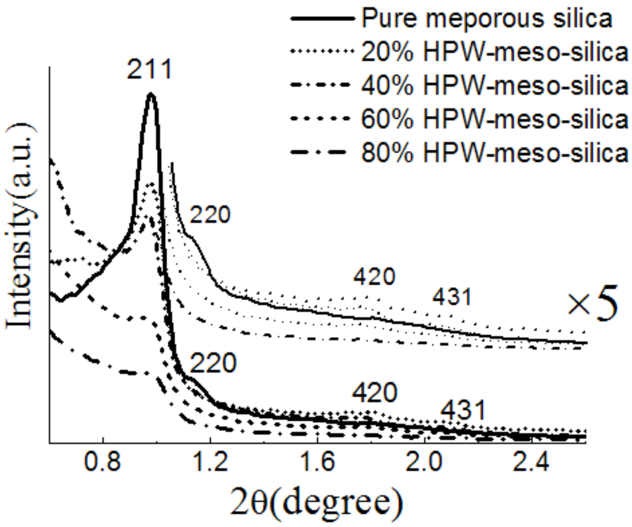

Figure 4.1 Small-Angle X-ray Scattering (SAXS) patterns of $Ia\bar{3}d$ mesoporous silica and HPW-meso-silica composite with different HPW contents.

Figure 4.1 shows the SAXS patterns of pure mesoporous silica and HPW-meso-silica composite materials. All samples show the well-resolved scattering peaks and characteristic SAXS patterns of mesoporous silica. For the pure mesoporous silica, the SAXS curve (solid line) shows four well-resolved scattering peaks, which can be assigned to the 211, 220, 420 and 431 scattering peaks of the $Ia\bar{3}d$ structure, suggesting the successful formation of the $Ia\bar{3}d$ mesoporous silica structure.(Li et al., 2007, Kim et al., 2005) The bicontinus cubic structure (space group $Ia\bar{3}d$) consists of two sets of cylindrical pore channels which are mutually perpendicular and linked by smaller channels with pore size of 1-2 nm between them.(Wan and Zhao, 2007, Chen et al., 2005) After the HPW functionalization, the relative intensities of the 211, 220, 420 and 431 scattering peaks of $Ia\bar{3}d$ structure decrease with increasing HPW content. However, the position of the scattering peaks for HPW-meso-silica composites remains more or less the same as that of the corresponding meso-silica hosts, which implies that the symmetrical and dimensional properties of meso-silica host are well reserved after the HPW impregnation. One possible explanation for the significant decrease in the relative intensity of the scattering peak is that the impregnation of HPW molecules inside the silica mesopores reduces the contrast between the wall and pore of meso-silica, leading to the drop in the scattering intensity of SAXS. The interaction between the siliceous host and impregnated HPW molecules could be detrimental to the structural regularity of the mesoporous silica. Table 4.2 lists the corresponding structural parameters of the HPW-meso-silica nanocomposites with different HPW contents.

Table 4.2 Parameters of meso-silica and HPW-meso-silica nanocomposites with different HPW contents.

Samples	Unit cell α (nm)[a]	S_{BET} (m^2g^{-1})	Pore volume (cm^3g^{-1})	Pore size (nm)	Wall thickness (nm)[b]
Meso-silica	20.5	935	1.084	5.0	5.2 ±0.2
20%HPW-meso-silica	20.5	822	0.928	4.9	5.2 ±0.3
40%HPW-meso-silica	20.5	679	0.643	4.2	5.6 ±0.3
60%HPW-meso-silica	20.6	434	0.282	3.9	6.0 ±0.3

80%HPW-meso-silica	20.8	252	0.153	3.7	6.3±0.4

[a]For cubic Ia3d pore symmetry, the unit cell parameter is obtained by $\alpha_0 = d_{211}\sqrt{6}$.

[b]Estimated from TEM micrographs.

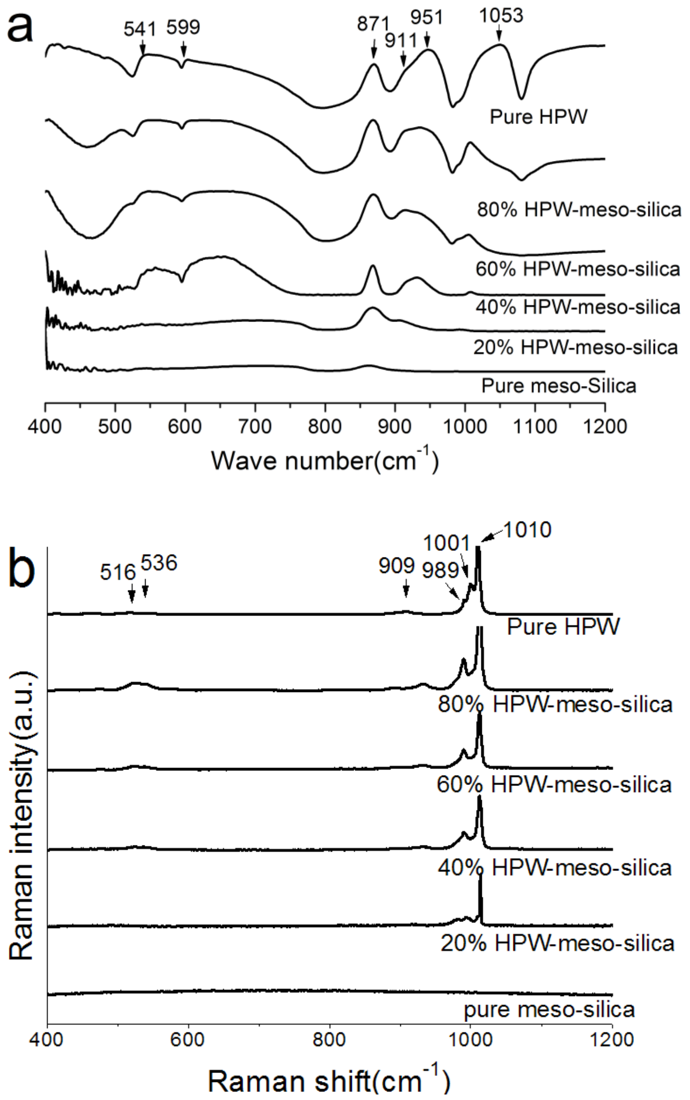

Figure 4.2 (a) FTIR spectra and (b) Raman scattering spectra of HPW, meso-silica and HPW-meso-silica nanocomposites measured at room temperature.

The FTIR spectra of pure HPW, meso-silica and HPW-meso-silica nanocomposites are measured in reflected beam, and the corresponding results are presented in Figure 4.2a. HPW in the dehydrated state or in polar solvents produces stable Keggin type anions such as $PW_{12}O_{40}^{3-}$, which is neutralized by three protons in water. This structure is formed by a central atom of phosphorous tetrahedrically linked to oxygen atoms surrounded by seven other oxygen atoms linked to a tungsten atom.(Yang et al., 2005b) When hydrated water molecules are present in HPW, the terminal oxygen atoms of the Keggin anions are associated with $H_5O_2^+$, generating a secondary structure with characteristic peaks in the FTIR spectroscopy. (Kim et al., 2003) For pure HPW, characteristic bands are observed at 1053 cm^{-1} for $P\text{-}O_a$, 951 cm^{-1} for $W{=}O_d$, 911 cm^{-1} for $W\text{-}O_b\text{-}W$ and 871 cm^{-1} for $W\text{-}O_c\text{-}W$, which is close to that reported in the literature. (Rocchiccioli-Deltcheff et al., 1983) The appearance of the characteristic peaks in the spectra of HPW-meso-silica nanocomposites indicates that the Keggin type anions, $P_4W_{12}O_{40}^{3-}$ remains in the nanocomposite structure; besides, the peaks in the range of 800-100 cm^{-1} are partially overlapped by the δ(Si-O-Si) stretching as well as the OH bending of $O_3Si\text{-}H$ group from the mesoporous silica framework. In the spectra displaying the samples with various HPW contents, one can observe a broadening and progressive shift of the band at 951 cm^{-1} as the HPW contents increase from 20 to 80%, the frequency shift reveals possible interaction between the Keggin anions of HPW with the silanols on the silica surface. Dias et al studied HPW-impregnated mesoporous silica by the ^{31}P solid state NMR and observed the chemical shift of the ^{31}P NMR peak from 15.5 ppm for pure HPW to 15.0 ppm for the HPW-impregnated meso-silica.(Dias et al., 2006) The chemical shift in the ^{31}P NMR spectra is attributed to the formation of

$(\equiv SiOH_2^+)(H_2PW_{12}O_{40}^-)$ species. (Lefebvre, 1992) The increased intensity of the new peak at ~1011 cm^{-1} with increasing HPW contents may be associated with the formation of $(\equiv SiOH_2^+)(H_2PW_{12}O_{40}^-)$ species.

The Raman scattering spectra of pure HPW, meso-silica and HPW/meso-silica nanocomposite are shown in Figure 4.2b. The spectrum of pure HPW is characterized by bands at 1010 and 989, which are assigned to antisymmetric and symmetric stretching modes of W-O octahedral, respectively. (Rocchiccioli-Deltcheff et al., 1983) Both are the signatures of the Keggin structure and are in agreement with the FTIR results. The peak typical of the Keggin structure (i.e. the asymmetric stretching vibration of the central PO_4 tetrahedran) at 1053 cm^{-1} was partially overlaid by the Si-O frame vibrations. The appearance of these characteristic peaks in the spectrum of HPW-meso-silica composite indicates that the skeleton of the heteropolyanions $P_4W_{12}O_{40}^{3-}$ still remains in the composite material.

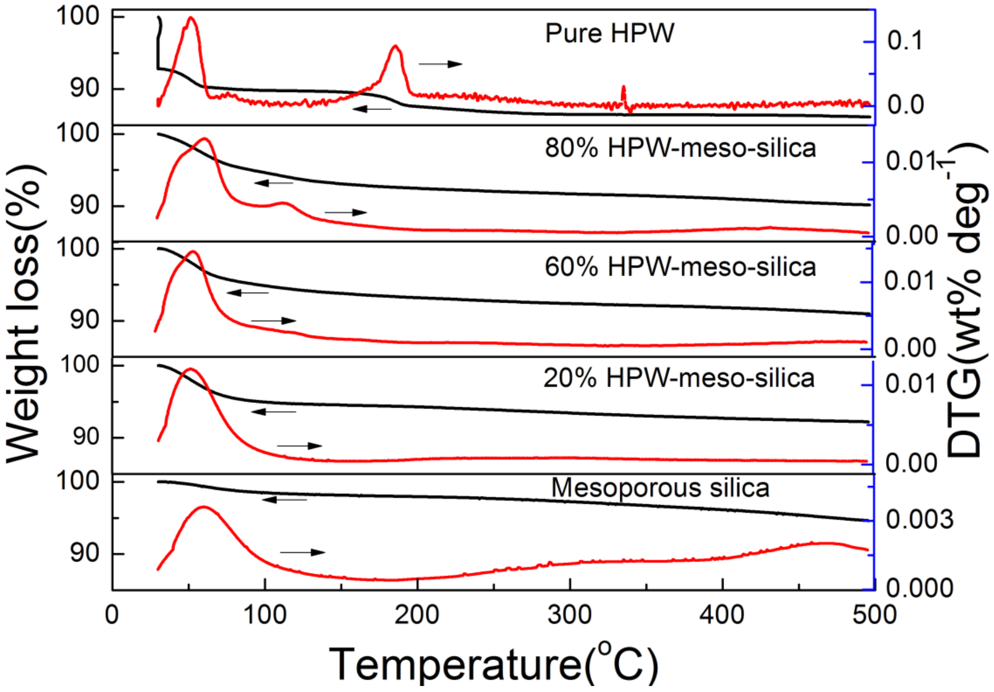

Figure 4.3 TGA spectra of HPW, meso-silica and HPW-meso-silica nnaocomposites with different HPW contents.

Figure 4.3 shows the TGA of the pure HPW, mesoporous silica and HPW-meso-silica measured in the temperature range of 30-500^{o}C. The TGA curve of pure HPW exhibits two weight loss steps at temperatures around 50 and 186 ^{o}C, which is in agreement with that reported in the literature. (Sweikart et al., 2005, Yamada and Honma, 2006) The first weight loss between room temperature and 70 ^{o}C can be attributed to the loss of physically absorbed water while the second one between 160 and 200 ^{o}C can be assigned to the release of structural water from the HPW hydrate. The weight loss of HPW at 200^{o}C was 14.6%. The retention of water molecules by the Keggion-type HPW structure at elevated high temperatures indicates the possibility of proton conductivity at high temperatures. On the other hand, the $Ia\bar{3}d$ meso-silica indicates only one weight loss step at 65^{o}C and weight loss is 1.0% at 200^{o} C, much lower than 14.6 % of pure HPW. The very low weight loss of meso-silica shows that the water retention capability of pure meso-silica is low despite its high pore volume (see sections below). The thermal behavior of HPW-meso-silica nanocomposite is significantly different from that of pure HPW. For example, in the case of the 80%HPW-meso-silica nanocomposite, in the temperature range of 30-500^{o}C the dehydration peak of structural water of pure HPW at 186^{o}C disappears and the weight loss at 200ºC is 7.2% for the 80 wt% HPW-meso-silica, which is lower than 14.6% observed for pure HPW, but significantly higher than 1% for pure meso-silica. The disappearance of the dehydration peak at high temperatures suggests that the homogeneous distribution of HPW in the mesoporous silica host changes the behavior of adsorbed water molecules in the HPW Keggin structure and enhances the stability of water in the HPW-meso-silica system.

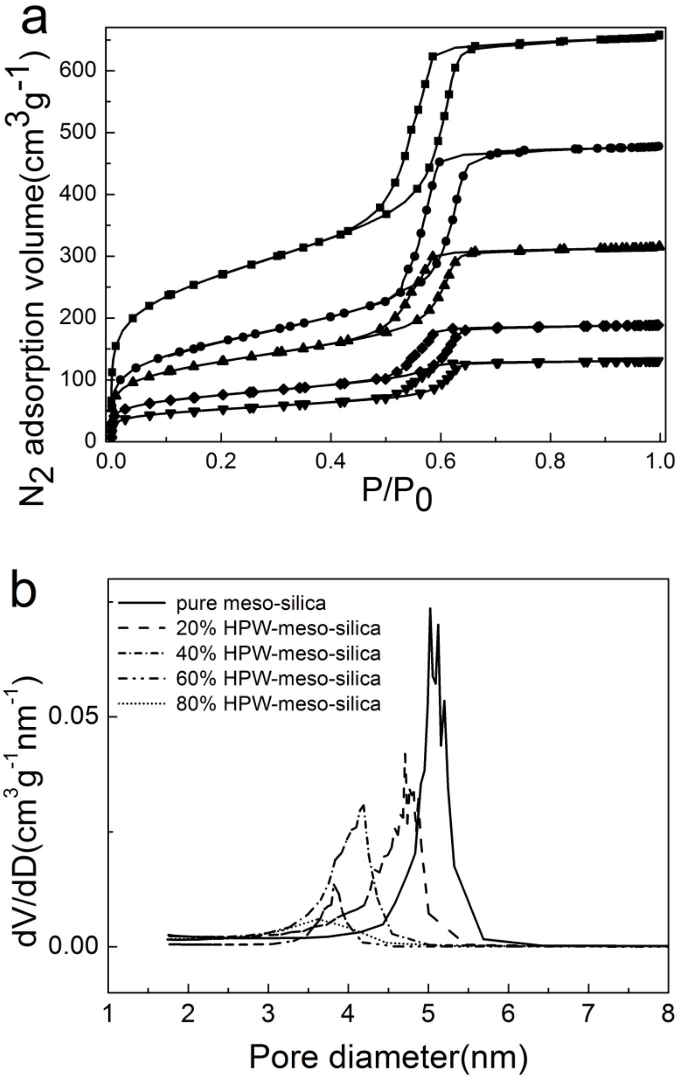

Figure 4.4 (a) N_2 absorption isotherms and (b) pore size distribution of (■) meso-silica, (●) 20%HPW-meso-silica, (▲) 40%HPW-meso-silica, (♦) 60%HPW-meso-silica and (▼) 80%HPW-meso-silica nanocomposites.

The pore size and pore volume of meso-silica and HPW-meso-silica nanocomposites with different HPW contents were evaluated with nitrogen adsorption-desorption isotherm measurements and the results are shown in Figure 4.4. The N_2 sorption isotherms in Figure 4.4a show the typical type-IV characteristics(Gregg and Sing, 1982) associated with a distinct and sharp step at a relative pressure of ~0.58. The sharp step in the adsorption isotherm indicates the capillary condensation because the pore size distribution is very uniform.(Gregg and Sing, 1991) The analysis of the adsorption isotherms with the Brunauer-Emmett-Teller (BET) method gives surface areas in the range of 935 m^2 $g^{-1}$for pure meso-silica, which is larger than 822 m^2 g^{-1} reported for mesoporous SBA-15 silica.(Rao et al., 2005) On the other hand, the surface area and pore volume of the HPW-meso-silica composite are reduced significantly with the impregnation of HPW into the meso-silica matrix. As the impregnated HPW loading increased from 0 to 80 wt%, the surface of the meso-silica host drops from 935 to 252m^2 g^{-1}, while the pore volume decreased from 1.084 to 0.153 cm^3 g^{-1}, indicating the filling of the mesoporous channels of the silica by the impregnated HPW particles.

As compared with the meso-silica hosts, the N_2 sorption isotherms of HPW-meso-silica nanocomposite exhibit a much wider hysteresis loop, suggesting more resistance for the nitrogen diffusion due to the reduced entrance size of HPW-meso-silica porous structure. The impregnated HPW partially blocked the pore entrance of nanochannel structure of meso-silica, similar phenomenon is also observed by other researchers (Xu et al., 2009) Figure 4.4b shows the pore size distribution characterized by the non-linear density function theory (NLDFT), which also indicates a significant drop in the pore diameter from 5.0 to 3.7 nm as the HPW loading increased from 0 to 80wt%, implying that most void space exiting in the original host was occupied by impregnated HPW particles. The pore size, pore volume and BET surface areas of HPW-meso-silica nanocomposites with different HPW contents are listed in Table 4.2.

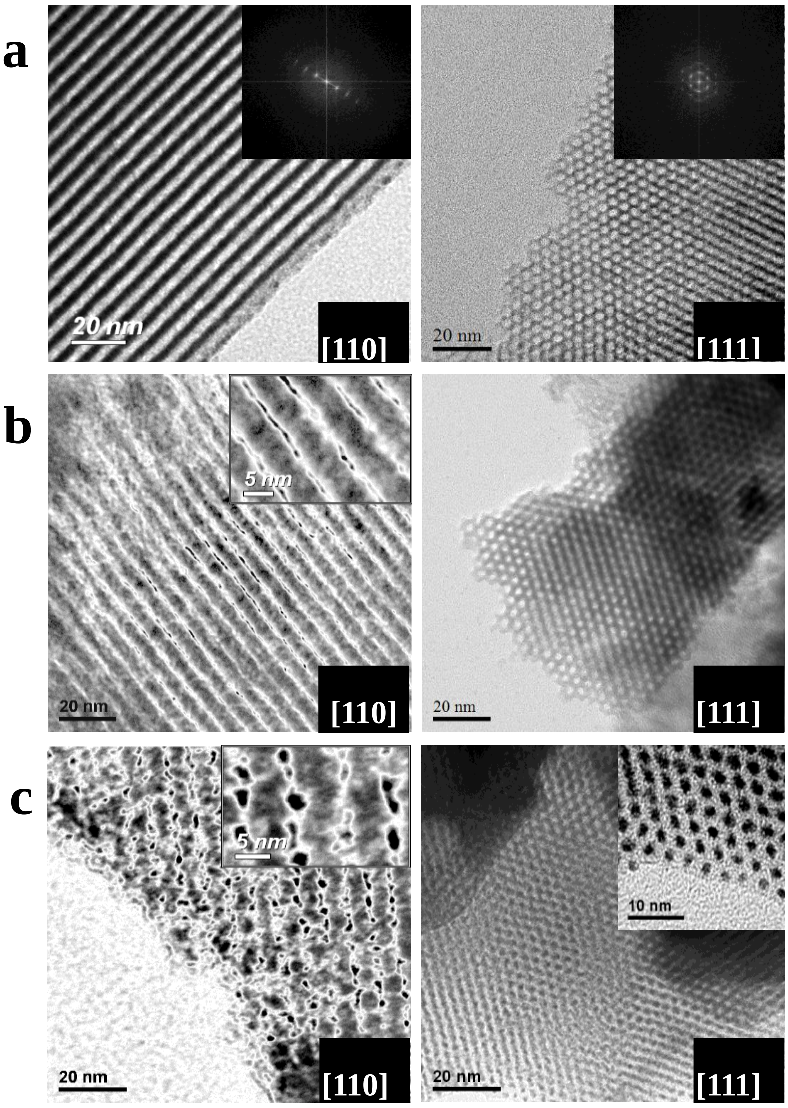

Figure 4.5 TEM images of (a) pure meso-silica; (b) 20%HPW-meso-silica, (c) 80%HPW-meso-silica; the left images were viewed from the [110] direction while the right images were viewed from the [111] direction.

The mesostrucure of mesoporous silica and HPW-meso-silica nanocomposite were studied by TEM and the results are shown in Figure 4.5. The mesoporous silica host was characterized by highly ordered nano-channels as shown in Figure 4.5a. The TEM images (from left to right) of Figure 4.5a were taken from [110] and [111] direction, which can be confirmed by the corresponding Fast Fourier Transform (FFT) images in Figure 4.5a. TEM image taken along the pore axis (i.e., [111] direction) indicates that the channel diameter of mesoporous silica is ~5.2 nm, which is consistent with the pore size obtained from the N_2 absorption isothermal result of 5.0nm.

In the case of HPW-meso-silica nanocomposites, the TEM images provide a direct observation of the morphology and distribution of the impregnated HPW nanoparticles in the mesoporous silica matrix, which are indicated by the ordered but not continuous black dots sandwiched between continuous channels (grey in color, see Figure 4.5b and 4.5c). The belt-like structure in grey color is siliceous pore walls and the color difference between the black dots and grey belt-like channels is due to the phase contrast between HPW and silica (tungsten atoms of HPW are much heavier than silicon atoms of silica). The phase contrast becomes pronounced as the HPW content in the nanocomposite increased to 80% (see the inset, Fig.4.5c). Such phase contrast was also observed in the cesium substituted HPA-meso-silica system.(Rao et al., 2007) As the HPW content in meso-silica increased to 80 wt%, the density of HPW particles (i.e, the black dots, see Figure 4.5c) increases, indicating that the distribution of HPW particles in 80%HPW-meso-silica is much more uniform than that of 20%HPW-meso-silica (Fig.4.5b). The higher intensity of HPW particles inside the meso-silica means shorter pathway of proton transportation, which would lead to high proton conductivity and lower activation energy for the proton conductance in the meso-silica matrix. The average distances between the HPW particles in the HPW-meso-silica nanocomposites vary between 0 to 5 nm, and the shape and diameter of the interconnected channels of HPW-meso-silica nanocomposites are not as regular as that of the pristine meso-silica host (the inset, Fig.6c), probably due to the impregnation and insertion of HPW particles.

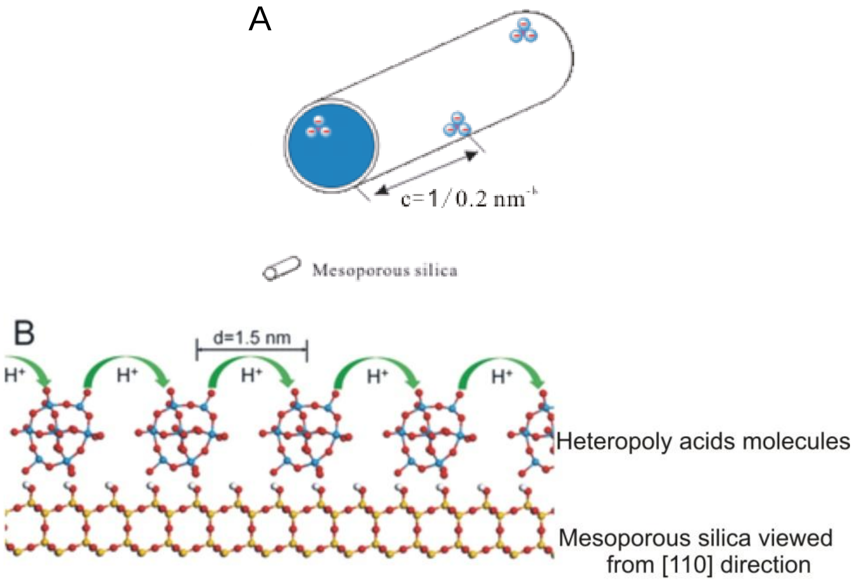

Figure 4.6 (a)concentration of HPW within the mesoporous silica matrix and (b)distance between two nearest HPW molecules calculating from experimental results

With the assumption that the distributions of HPW on silica are uniform, at a given concentration of HPW, *c*, we can get the average distance, *d*, between two nearest HPW molecules in HPW/meso-silica electrolyte by using the followed eq.4.1 and eq.4.2:

$$d = \sqrt{\frac{A \bullet m_{silica}}{\frac{m_{HPW}}{M_{HPW}} \times N_A}} \tag{4.1}$$

$$c = \frac{A \bullet m_{silica}}{\frac{m_{HPW}}{M_{HPW}} \times N_A} \times \frac{1}{\pi R} \tag{4.2}$$

Where M_{HPW} is the molecular weight of $H_3P_4W_{12}O_{40}$, N_A is the Avogadro constant; besides A and D stand for surface area and pore diameter of siliceous host, respectively. For the sample 80 %HPW-meso-silica, $N_A=6.02\times10^{23}$, $m_{HPW}/m_{silica} = 2:1$, $A = 935\ m^2g^{-1}$, $R = R_{nanotube}-R_{HPW}=3.8$ nm, $M_{HPW} = 2808.05g$, thus *d* is calculated to be 1.5 nm according to the model shown in Figure 4.6(a), which is consistent with the value of 1.5 nm from TEM results (Figure 4.5c). The value of *c* is 1/0.2 nm^{-1}, which means that there was one HPW existent every 0.2nm in length inside the nanochannels.

4.3.2 Water uptake and conductivity of the HPW-meso-silica nanocomposites

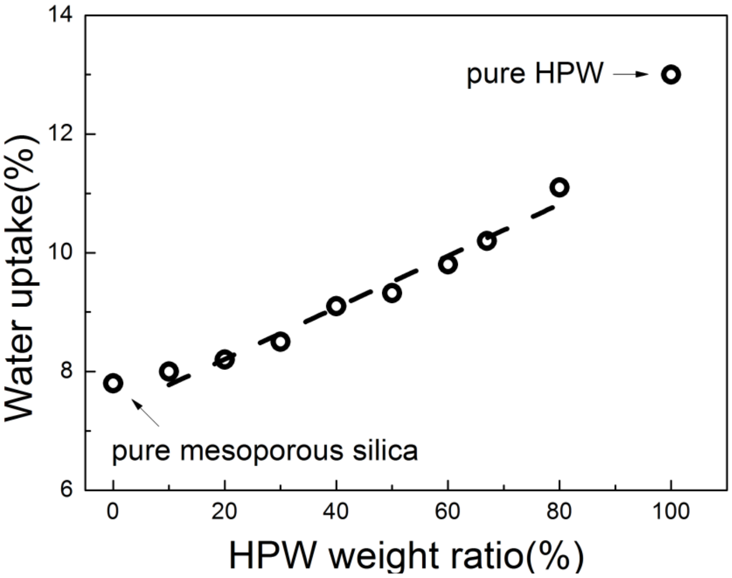

Figure 4.7 Water uptake of pure meso-silica, pure HPW and HPW-meso-silica with various HPW contents.

Figure 4.7 is the water uptake results of HPW-meso-silica nanocomposite as a function of HPW content. The water uptake of meso-silica is ~8% and it increases almost linearly with the impregnated HPW content. As the HPW content increased to 80wt%, the water uptake of the HPW-meso-silica nanocomposite is ~11%, which is slightly low than 13% for pure HPW under the conditions studied. No change in the sample dimension during the water uptake tests was observed and swelling of the HPW-meso-silica nanocomposite was negligible. The high water content in the HPW-meso-silica as compared to that of meso-silica indicates the significantly enhanced water retention ability by the impregnated HPW in the mesoporous silica matrix. In the case of Nafion-based membranes, the water uptake can be as high as 30% with high swelling ratios of 12.8-14% in pure water and 51-53% in 1M methanol/water solution;(Tazi and Savadogo, 2000, Randov et al., 2008, Gebel et al., 1993) the high swelling ratio could seriously jeopardize the membrane's mechanical stability as well as its resistance against fuel crossover, including hydrogen methanol and formic acid.(Jeong et al., 2007, Xu et al., 2010)

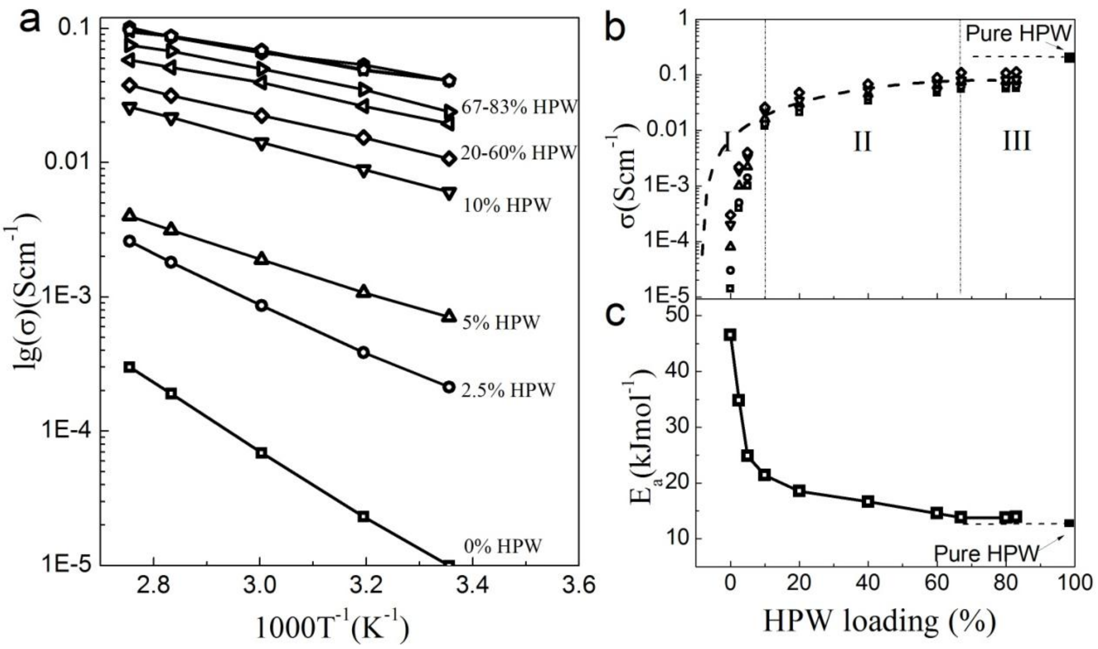

Figure 4.8 (a) Proton conductivity versus temperature for the HPW-meso-silica composite membranes as a function of HPW content, (b) Proton conductivity versus HPW content measured at 25^{o}C, and (c) Activation energy versus HPW content of the HPW-meso-silica membrane. Conductivity and activation energy of pure HPW are obtained from reference. (Osamu Nakamura et al., 1979)

The proton conductivity measurements of HPW-meso-silica were performed by electrochemical impedance method over the frequency range from 1Hz to 1MHz in the temperatures range from 20 to 90 ^{o}C under 100 %RH. The HPW content in meso-silica matrix was varied between 0 to 83%. Figure 4.8a shows the proton conductivity of HPW-meso-silica nanocomposites as a function of HPW content measured at different temperatures. The meso-silica shows a very low proton conductivity of 1.4×10^{-5} S cm^{-1} at 25^{o}C and 3×10^{-4} S cm^{-1} at 90 ^{o}C with a high activation energy of 46.6 kJ mol^{-1}, very close to the results reported in the literature. (Li and Nogami, 2002b) On the other hand, the proton conductivity of mesoporous silica is enhanced significantly with the HPW functionalization and increases dramatically with the HPW content in the meso-silica structure. In the case of the 80%HPW-meso-silica nanocomposite the conductivity is 0.07 S cm^{-1} at 25^{o}C, more than three orders of magnitude higher than 1.4×10^{-5} S cm^{-1} measured on pure meso-silica. The activation energy is 14.5 kJmol^{-1}, also much smaller than 46.6 kJ mol^{-1}for the pure meso-silica.

The dependence of the proton conductivity of HPW-meso-silica nanocomposites on HPW content measured at 25 ^{o}C is shown in Figure 4.8b. The proton conductivity depends strongly on the HPW content and is characterized by three regions: 0-10wt% HPW loading, proton conductivity of the HPW-meso-silica increases rapidly with the HPW content and is an exponential function of HPW loading (region I). The proton conductivity is 1.4×10^{-5} S cm^{-1} for pure meso-silica and increases rapidly to 4.5×10^{-2} S cm^{-1} when 5 wt%HPW was impregnated into meso-silica (5%HPW-meso-silica), which is an increase by 3 orders of magnitude in proton conductivity. When the HPW content increased to 10 wt%, the increase in the proton conductivity of the HPW-meso-silica nanocomposites becomes much slower (region II) and once the HPW content reaches 65-67 wt%, the conductivity of HPW-meso-silica is almost independent of the HPW content and remains a constant value of 0.07 S cm^{-1} (region III). This indicates that threshold of HPW in the meso-silica nanocomposite is about 10%. The highest conductivity of the HPW-meso-silica nanocomposites based on the $Ia\bar{3}d$ structure is ~0.07 S cm^{-1} at 25 ^{o}C under the conditions used in the present study, which is slightly lower than 0.18 S cm^{-1} of fully hydrated HPW. (Osamu Nakamura et al., 1979)

The activation energy (E_a) for proton conductance of HPW-meso-silica nanocomposites also depends strongly on the HPW content. As shown in Figure 4.8c, the dependence of the activation energy on the HPW contents is also characterized by three distinct regions, similar to those observed for the conductivity. When the HPW content increased from 0 to 10%, the activation energy decreases sharply from 46.6 to 21.4 kJ mol^{-1} (region I). Further increase of the HPW content leads to a more moderate decrease of E_a (region II). When the HPW content of the HPW-meso-silica nanocomposites reached 65-67 wt%, the activation energy becomes stable, ~15 kJ mol^{-1}, which is also close to ~14.5 kJmol^{-1} of proton conductivity of fully hydrated HPW. The high proton conductivity and low activation energy indicate the establishment of effective proton transfer paths in the HPW-meso-silica nanocomposites when the HPW contents in the meso-silica reaches the threshold value of ~10%.

4.3.3 Single cell performance

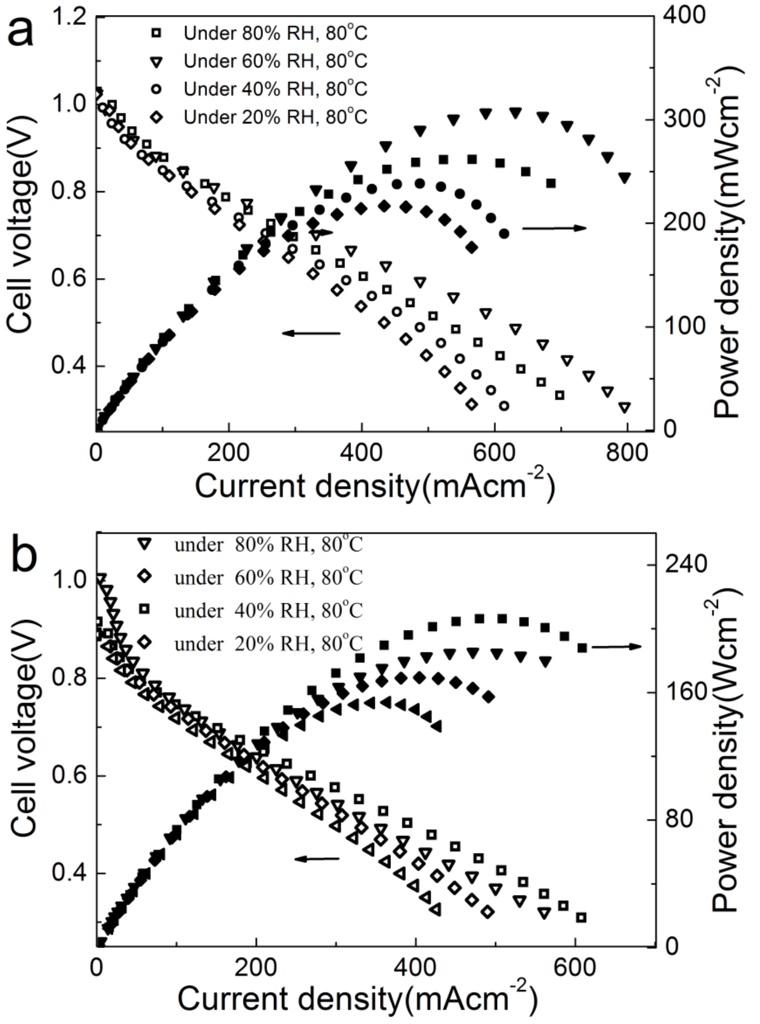

Figure 4.9 Polarization and power density of single cell employing a 80%HPW-meso-silica nanocomposite membrane in (a) H_2/O_2 and at 80°C under different RH and (b) H_2/air at 80°C under different RH.

In order to demonstrate the applicability of the HPW-meso-silica membrane in fuel cells, single cell performance tests were carried out under various operational temperatures and RH conditions in hydrogen and methanol. Figure 4.9 shows the single cell performance of the 80%HPW-meso-silica membrane operating in both H_2/O_2 and H_2/air as a function of RH at 80 °C. For comparison, the cell performance based on Nafion 115 was also measured in H_2/O_2 as a function of RH at 80°C (but the performance curve is not shown). The typical open circuit voltage (OCV) of the cell operated in H_2/O_2 at 80 °C is 1.01 V (Figure 4.9a), close to that of typical single cells assembled with Nafion membranes, suggesting the HPW-meso-silica membrane has a good resistance to hydrogen crossover; The maximum power density is 308 mW cm^{-2} at 80 °C under 80 %RH in H_2/O_2 and 206 mW cm^{-2} in H_2/air, which is quite high as compared to those reported on inorganic membranes such as phosphoric acid doped silica, HPMo or HPW doped glass electrolytes, etc. (Uma and Nogami, 2008c, Nakanishi et al., 2007, Xiong et al., 2008, Uma and Nogami, 2008a, Inoue et al., 2008, Uma and Nogami, 2007b) The good power output of the cell with HPW-meso-silica nanocomposite can be attributed to its high proton conductivity. The significant voltage drop of the cell at low currents in H_2/air (Figure 4.9b) indicates that the performance is limited by the activation loss, particularly on the cathode side probably due to poor and not-optimized interface between the Pt/C catalyst layer and the HPW-meso-silica membrane. This suggests that the performance of the fuel cell can be further enhanced by the optimization of the catalyst and electrolyte interface.

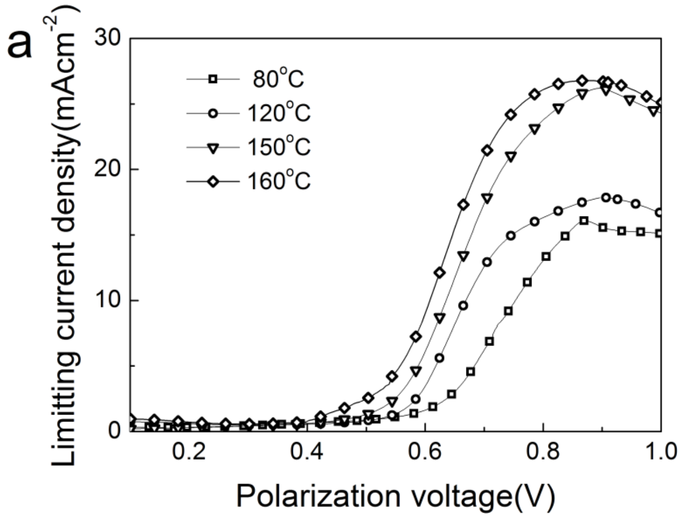

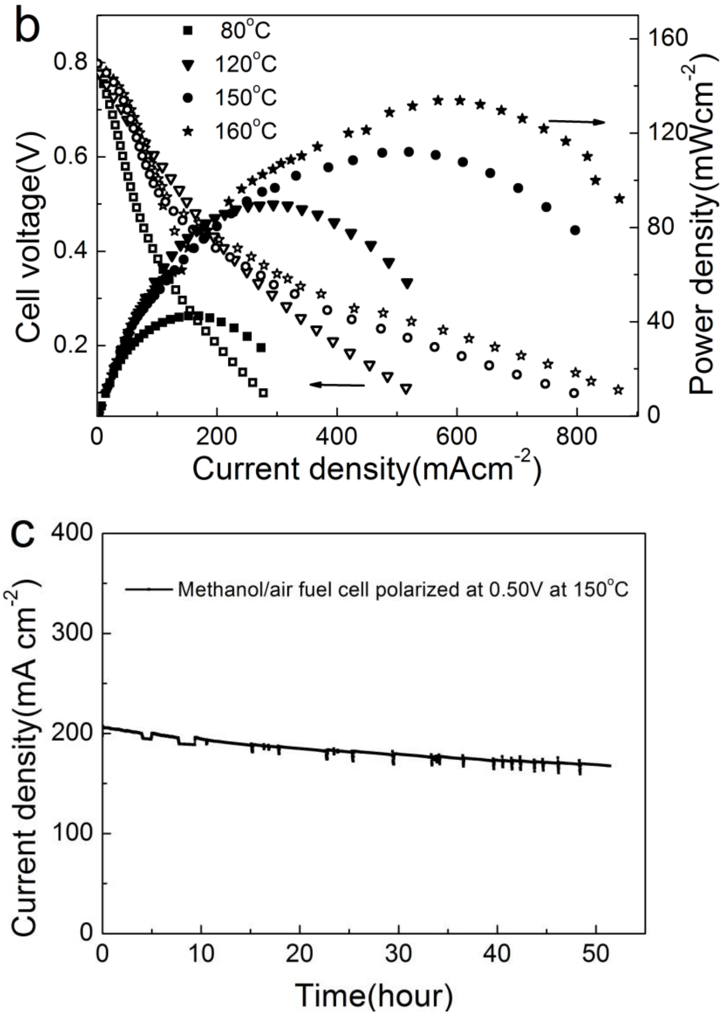

Figure 4.10 (a) Methanol crossover limiting current curves of a 80%HPW-meso-silica nanocomposite membrane measured at different temperatures and (b) polarization and power density of single cells employing a 80%HPW-meso-silica membrane in methanol/air at different temperatures without external humidification, and (c) cell stability measured at a constant cell potential of 0.50 V at 150 ℃ in methanol/air without external humidification.

Figure 4.10a shows the methanol crossover current curves in a 80%HPW-meso-silica membrane. The limiting current of the methanol oxidation with the HPW-meso-silica membrane is 16 mA cm^{-2} at 80 ℃ and increases to 27 mA cm^{-2} at 160 ℃. The methanol crossover limiting currents are significantly lower than that of Nafion membranes. For example, the limiting crossover current is 98 mA cm^{-2} on a Nafion 1135 (89 µm in thickness) measured at room temperature (Jiang et al., 2006b) and 277 mA cm^{-2} on a Nafion 117 (178 μm in thickness) measured at 80 ºC in a 2M methanol solution. (Ren et al., 2000) The much lower methanol crossover current on the HPW-meso-silica membrane could also be related to the gas phase diffusion of methanol and the much thicker HPW-meso-silica membranes (~500 μm in this case). Another important reason is due to the fact the size of the mesopores or channels of HPW-meso-silica nanocomposites is in the range of 3.7-4.9 nm and does not swell with water or humidity like in the case of Nafion membranes. (Tazi and Savadogo, 2000, Randov et al., 2008, Gebel et al., 1993, Divisek et al., 1998)

The performance of cells with a 67%HPW-meso-silica nanocomposite membrane was measured in methanol fuel with no external humidifier at the air side (Figure 4.10b). The OCV of the cell in methanol/air is ~0.80 V, lower than 0.9-1.0 V observed for H_2/air. The low OCV for the cell in methanol as compared with that in hydrogen may be due to the methanol crossover (see Figure 4.10a). The maximum power output is 43 mW cm^{-2} at 80 ^{o}C and increased to 134 mW cm^{-2} as the temperature increased to 160^{o}C. This means that increase in the operation temperature is beneficial for DMFCs. In the case of methanol fuel, the CH_3OH solution (2M) will be gasified after entering the anode chamber and the molar ratio of water to methanol is 9 to 1. The high water/methanol ratio could help to maintain a certain hydration level on the anode of the cell. The decrease in the cell polarization potential in the low current region is substantial in methanol/air as compared to that in H_2/air (Fig 4.10b), indicating the significant activation losses for the methanol oxidation reaction. The performance of DMFCs based on HPW-meso-silica nanocomposite membranes is most likely limited by the methanol oxidation reaction in addition to the oxygen reduction reaction probably due to the not-optimized electrocatalysts for both anode and cathode at elevated high temperatures. However, the cell with the HPW-meso-silica nanocomposite membranes exhibits a reasonable stability, as shown in Figure 4.10b, measured under a constant potential of 0.5 V at 150°C for 51.5 hours. The fuel cell experienced a gradual drop in current density and the degradation rate was 0.6 mA h^{-1} over the test period. Nevertheless, the stability of the cell is reasonable considering that the catalyst and HPW-meso-silica membrane interface was far from optimized. The high power density over the wide range of RH and good stability indicate the applicability of the HPW-meso-silica nanocomposite as high temperature PEM for fuel cells.

4.3.4. Proton transfer in HPW-meso-silica nanocomposites

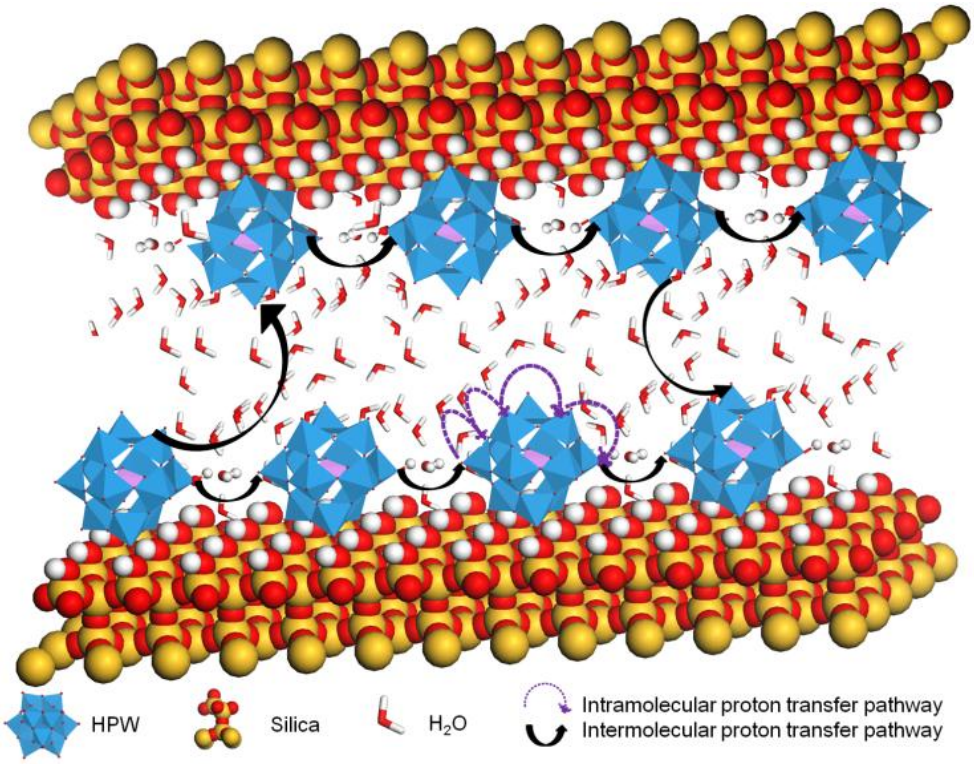

Figure 4.11 The proton transportation was proposed to occur effectively in two ways. One is that protons-hop on isolated phosphotungsitc acid molecules, briefly as an intramolecular proton transfer pathway. The other is called the intermolecular proton transfer pathway, in which the proton transfer process is achieved through a series of “hops” among HPW molecules and water molecules along the hydrogen bond between HPW and water.

The low activation energy and high proton conductivity of HPW-meso-silica nanocomposites in the present study indicate that water plays an important role in protons transfer process because the presence of water significantly reduces the activation barrier to proton movement. The increase of proton mobility enhanced by small amounts of water has been explained by quantum chemical DFT calculations.(Janik et al., 2005) Without the assistance of water molecule, the barrier to the motion of protons on an isolated HPW is significantly high, owing to the larger distance over which transfer must occur between two bridging oxygen atoms. The activation energy for anhydrous proton movement through the individual HPW clusters was calculated to be 103.3 kJ mol^{-1}. (Janik et al., 2005) After water adsorption, a second hydrogen bond would be formed between the hydrogen atom of the water molecule and a terminal oxygen site of the Keggin Unit (KU) in addition to the hydrogen bonding between the proton of the KU and the oxygen atom of the water molecule. Herein, the barrier is greatly reduced by an order of magnitude to ~14.5 kJ mol^{-1} under 100%RH, as shown in the present study. The significantly low activation energy, together with the high conductivity is most likely due to the water-promoted proton hopping pathway which does not require substantial structural rearrangement of the Keggin unit to form the transition state. The much smaller reduction in the performance of HPW-meso-silica nanocomposites with the RH change, in comparison with that of Nafion membranes, clearly demonstrates the high water retention capability of the HPW-meso-silica nanocomposites. The high water retention properties of HPW-meso-silica nanocomposites are also supported by the observed reasonable stability of the cell in methanol/air without external humidification. The high water retention properties of HPW-meso-silica could be attributed to the ordered mesoporous silica structure and the possible interaction between the Keggin anions and meso-silica, leading to the formation of $(\equiv SiOH_2^+)(H_2PW_{12}O_{40}^-)$ species. (Dias et al., 2006) However, the present study would not be sufficient to vertify whether the proton transfer in the HPW-meso-silica nanocomposites occurs by Grotthuss or vehicle mechanisms or combination of both.

More work is needed for fundamental understanding of the proton transfer mechanism in the HPW-meso-silica nanocomposite systems.

4.4 Summary

A novel inorganic proton exchange membrane based on the HPW-meso-silica nanocomposite was characterized in detail. The results prove the formation of ordered three-dimensional mesoporous framework with HPW molecules anchored in mesoporous silica matrix, forming an effective proton conduction pathway. The membrane conductivity increases sharply as the HPW loading was increased from 0-67 wt% and becomes stable as HPW loading was between 67-83 wt%. The highest proton conductivity of 0.07 S cm^{-1} at 25^{o}C with low activation energy of 14.5 kJ mol^{-1} is achieved with the HPW loading of 80% for HPW-meso-silica electrolyte. The single cell based on a HPW-meso-silica membrane produced a peak power of 134 mW cm^{-2} in methanol/air at 160 ^{o}C without humidification, as well as a peak power of 308 mWcm^{-2} in H_2/O_2 and 206 mW cm^{-2} in H_2/air at 80 ^{o}C and 80 %RH, respectively. The high tolerance of HPW-meso-silica nanocomposites towards the RH change, in comparison with that of Nafion membranes, indicates the high water retention capability of the HPW-meso-silica nanocomposites. The present study demonstrates that inorganic proton exchange membranes with high proton conductivities can be realized in the HPW-meso-silica nanocomposite, and can be used as effective proton exchange membrane for high temperature H_2/air fuel cells and DMFCs.

CHAPTER 5. HPW-meso-silica Membrane With Tunable Bicontinuous Mesoporous Structure

In this chapter, the HPW-meso-silica membrane under high temperature and low relative humidity environment has been studied in terms of proton conductivity and fuel cell performance, and the commercial PFSA membrane was used for reference. Besides, the effects of the pore size of meso-silica host on the membrane stability under a water washing condition have been examined. The optimized pore size and testing conditions were determined for further investigation.

5.1 Introduction

Nanoporous or mesoporous silica materials with high structural order, large surface areas and pore volumes, and easy and variable surface functionalization offer great potential as porous frameworks for high temperature PEM applications. (Li and Nogami, 2002b, Athens et al., 2007b, Colomer, 2006b, Yamada et al., 2005b, Daiko et al., 2002, Li and Nogami, 2003b, Uma and Nogami, 2007d, Xiong and Nogami, 2006, Vichi et al., 2000, Halla et al., 2003a) Proton conductivity of pristine mesoporous silica is low, ranging from 10^{-6} S cm^{-1} to 10^{-4} S cm^{-1} under 40% to 90% RH. (Li and Nogami, 2002b) However, the conductivity of mesporous silica can be increased significantly by functionalization such as grafting sulfonic side groups on the external Si-O sites. (Marschall et al., 2009a) Marschall et al.(Marschall et al., 2009b) synthesized imidazole functionalized mesoporous MCM-41 silica by immersing treatment and achieved the highest conductivity of 10^{-4} S cm^{-1} under 140 °C and 100% RH. However, the proton conductivity of sulfonic acid and imidazole functionalized mesoporous silica composites is also very sensitive to RH. (Marschall et al., 2009a, Marschall et al., 2009b) Research indicated that replacing the pure silica with a composite silicate of strong acidity, e.g., the $Cs_3(H_2PO_4)(HSO_4)_2/SiO_2$ (Ponomareva and Shutova, 2005), CsH_2SO_4-SiO_2 (Ponomareva and Shutova, 2007), P_2O_5-SiO_2 (Tung and Hwang, 2005), P_2O_5-TiO_2-SiO_2 (Nogami et al., 1999) or P_2O_5-ZrO_2-SiO_2(Nogami et al., 2001) also improves the proton conductivity. Matsuda et al (Matsushita et al., 1999) used HPW and SiO_2 as basic materials and milled them mechanically to form HPW-SiO_2 composites and achieved a proton conductivity of 3×10^{-3} Scm^{-1} at 30 °C and 60% RH. Nogami et al (Uma and Nogami, 2009, Uma and Nogami, 2008a, Uma and Nogami, 2008b, Inoue et al., 2008, Uma and Nogami, 2007b, Uma and Nogami, 2007c, Uma and Nogami, 2007a) incorporated various heterpolyacids into silicaphosphate porous glass and yielded an electrolyte membrane with proton conductivity of 0.1 S cm^{-1} at 85 ℃ and 85% RH. The fuel cell based on Phosphomolybdic acid (HPM) and HPW incorporated silicaphosphate glass produced a maximum power of 35~42 $mWcm^{-2}$ under 30 °C and 30% RH.

This chapter focus on the influence of structural properties of silica host such as pore size, pore volume and surface area on the proton conductivity and stability properties of HPW-meso-silica nanocomposite has been investigated in detail. The results indicate that the proton conductivity of HPW-meso-silcia nanocomposites depends strongly on the nanostructure of mesoporous silica and the highest proton conductivity was obtained on meso-silica with a nanopore size of 5.0 nm. The dependence of the conductivity, stability and cell performance of HPW-meso-Silica nanocomposites on the mesoporous structure and humidity are discussed. Cubic bicontinuous silica structure ($Ia\bar{3}d$) is chosen because of their high thermal stability (~650 ^{o}C), good chemical stability, high surface area, and well-controlled pore architectures.(Wan and Zhao, 2007) On the other hand, HPW has the highest stability and strongest acidity among the Keggin-type heteropolyacids. HPW is soluble in water, forming negatively charged $PW_{12}O_{40}^{3-}$ ions. A combined study of solid-state NMR and quantum chemical DFT indicates that the isolated acidic protons are immobile, but hydrated acidic protons are highly mobile in HPW Keggin units.(Yang et al., 2005b) Under normal conditions, the proton adsorption on the SiOH surface groups of the meso-silica is very low. However, the presence of highly acidic HPW would significantly increase the proton adsorption of SiOH groups, forming positively charged $SiOH_2^{+1}$.(Pettersson and Rosenholm, 2002) With a large amount of silanol groups on its ordered mesoporous surface, the electrostatic interaction between the positively charged $SiOH_2^{+1}$ groups and the negatively charged $PW_{12}O_{40}^{3-}$ ions would anchor and immobilize HPW molecules in the ordered mesoporous silica structure, forming an effective transportation pathway for proton conduction via HPW Keggin units. The initial results show that HPW can be impregnated into mesoporous silica, MCM-41, forming an HPW-meso-silica nanocomposite with a proton conductivity of 0.018 S cm^{-1} at 25 ^{o}C and 100% RH.(Lu et al., 2010)

5.2 Experimental

5.2.1 Powder and cell preparation

Matrix material-bicontinuous cubic Ia3d mesoporous silica was synthesized as described in section 3.2. The calcinated samples were denoted as Ia3d-x (x is the hydrothermal treatment temperature, ranging from 60^{o}C to 160^{o}C). Table 5.1 shows the experimental conditions of the synthesis process.

Table 5.1 Experimental conditions for fabrication of HPW-meso-silica electrolyte

Samples	Heat treatment temperature of host materials	Composition (in weight ratio)
Ia3d-60	60^{o}C	100% silica
Ia3d-60-80	60^{o}C	20% silica + 80%HPW
Ia3d-100	100^{o}C	100% silica
Ia3d-100-80	100^{o}C	20% silica + 80%HPW
Ia3d-160	160^{o}C	100% silica
Ia3d-160-80	160^{o}C	20% silica + 80%HPW

5.2.2 Characterization

For the cell performance measurement, the 80 wt% HPW-meso-60 nanocomposite was used as electrolyte membrane for PEMFC. A Greenlight PEMFC station was used to control the single cell's temperature and humidity. The relative humidity of the cell was calculated from the humidifier temperature against the cell temperature. All the measurements were conducted at ambient pressure. Hydrogen and oxygen flow rates were controlled at 30 ml min^{-1}. The membrane electrode assemblies (MEAs) were prepared according to the following procedures: Pt/C (20 wt% Pt/C, E-TEC) was used as catalysts for both of anode and cathode, Nafion emulsion (5 wt % in a mixture of aliphatic alcohols, Sigma Aldrich), and isopropyl alcohol (+99.5%, Sigma Aldrich) were sprayed onto a carbon gas diffusion layer (Toray Graphite Paper, TGPH-120, 40% wet-proofed, E-TEK) by airbrushing until a platinum loading of 0.4 mg cm^{-2} was achieved for both the anode and cathode. Once the catalyst layers had been deposited, an additional amount of Nafion (1 mg cm^{-2}) was added to improve the adhesion of the electrodes to the membrane and reduce the contact resistance between them. The electrodes (4.0 cm^{2}) were assembled with the 80 wt% HPW-meso-silica-60 membrane (~0.5 mm thick) by hot-pressing at 140 ℃ and 100 kg cm^{-2} for 3 min. The Nafion 115 membrane (~125 μm, DuPont) based MEA was fabricated through the same procedures and the Pt loading was controlled to be 0.4 mg cm^{-2}. The MEAs assembled by this procedure were stored in sealed bags until further use.

5.3 Results and discussion

5.3.1 Structural properties and thermal stability of HPW-meso-silica nanocomposite measured through SAXS, N_2 absorption isotherms, TGA and TEM

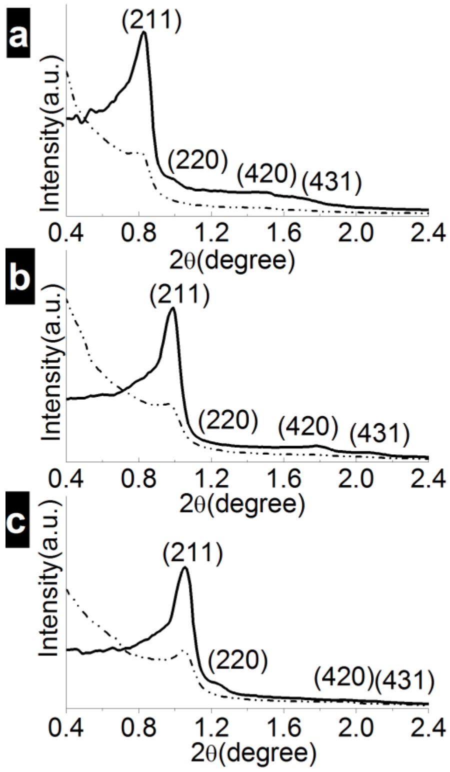

Figure 5.1 Small-Angle X-ray Scattering spectra of mesoporous silica (solid line) and 80wt%HPW-meso-silica nanocomposites (dotted lines) synthesized at hydrothermal treatment temperatures: (a) 60 °C; (b) 100 °C and (c) 160 °C.

Figure 5.1 shows the SAXS spectra of pure mesoporous silica (solid lines) and 80 wt% HPW-meso-silica nanocomposites (dotted lines) prepared at different hydrothermal temperatures. All samples show well-resolved scattering peaks and characteristic SAXS patterns of $Ia\bar{3}d$ symmetry,(Wan and Zhao, 2007) suggesting the formation of the $Ia\bar{3}d$ mesoporous structure. The increase of hydrothermal temperature from 60 °C to 160 °C caused a pronounced shift of the characteristic

SAXS peaks towards lower angles, an evidence for the enlargement of unit cell parameter (α) of the mesoporous silica from 20.5 nm to 26.2 nm. It is noted that the major SAXS peaks are enhanced for meso-silica treated at higher temperatures. This indicates that increasing hydrothermal temperature results in the shrinkage of meso-silica wall thickness and expansion of pore sizes. Moreover, the corresponding SAXS spectra of HPW-meso-silica composite materials (dotted lines) indicate a dramatic drop of the relative intensity of scattering peaks. The reason could be due to the high loading of HPW (80 wt%) being impregnated or anchored inside the silica matrix, which reduces the wall-pore contrast of the $Ia\bar{3}d$ meso-silica, leading to the decrease of scattering intensity. Another possible explanation for the reduced intensity is that the interaction between the siliceous host and HPW could be detrimental to the structural regularity of the mesoporous silica.

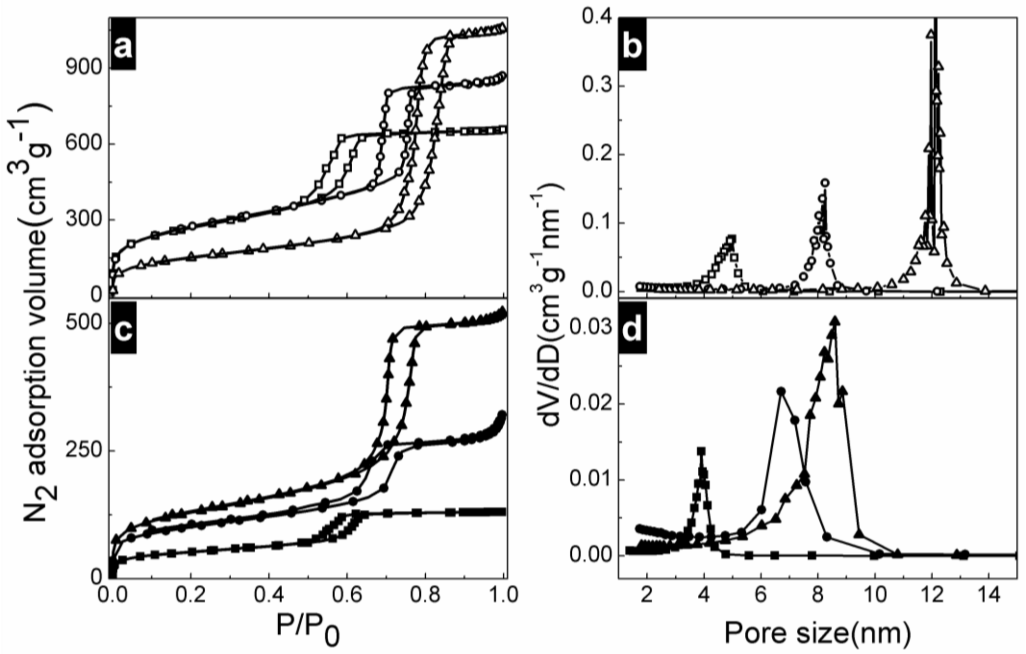

Figure 5.2 N_2 absorption isotherms and pore size distribution of (a, b) mesoporous silica synthesized with hydrothermal treatment temperatures of 60 °C, meso-silica-60 (□); 100 °C,

meso-silica-100 (○); and 160 °C, meso-silica-160 (△); and of (c, d) HPW-meso-silica-60 (■); HPW-meso-silica-100 (●); and HPW-meso-silica-160 (▲).

Table 5.2 Topological properties of $Ia\bar{3}d$ meso-silica and 80wt% HPW-functionalized meso-silica.

Sample	Hydrothermal temperature ^{o}C	Unit cell α (nm)^{a}	S_{BET} (m^2g^{-1})	Pore vol (cm^3g^{-1})^{b}	Pore size (nm)	Wall thickness (nm)^{d}
meso-silica-60	60	20.5	935	1.08	5.0^{c} (5.2)^{d}	5.0
HPW-meso-silica-60	100	21.9	952	1.34	8.2^{c} (8.3)^{d}	4.5
meso-silica -100	160	26.2	979	1.64	12.1^{c}(11.6)^{d}	4.0
HPW-meso-silica-100	60	20.6	252	0.15	3.7^{c}	7.0
meso-silica -160	100	22.1	377	0.39	6.6^{c}	6.5
HPW-meso-silica-160	160	26.5	451	0.71	8.6^{c}	5.5

[a] For cubic $Ia\bar{3}d$ pore symmetry, the unit cell parameter is obtained by $\alpha = d_{211}\sqrt{6}$

[b] Cumulative pore volume at P/P_0=0.99.

[c] Calculated from the adsorption branch of the isotherms based on the NLDFT method.

[d] Estimated from TEM experiments.

The pore and pore size distribution of mesoporous silica and HPW-meso-silica composite were examined with nitrogen adsorption measurements (Figure 5.2), and the structural parameters are given in Table 5.2. Both pure meso-silica and HPW-meso-silica nanocomposites are characterized by typical type-IV N_2 adsorption isotherms associated with a distinct step at a narrow relative pressure (p/p_o is in the range ~0.6 to 0.75)(Kleitz et al., 2003, Yang et al., 2005a). In mesoporous materials the adsorption isotherm exhibits a sharp and distinct step whenever the capillary condensation occurs because of the narrowly distributed pore size of mesostructure.(Gregg and Sing, 1991, Wan and Zhao, 2007) The analysis of the adsorption isotherms with the Brunauer-Emmett-Teller method gives surface areas in the range of 935-979$m^2g^{-1}$for pure meso-silica hosts. The porous structure of meso-silica hosts is significantly affected by the hydrothermal temperature. As the hydrothermal temperature was increased from 60, 100 to 160 ^{o}C, the pore size of the meso-silica hosts increased from 5.0, 8.2 to 12.1 nm (Figure 5.2b), respectively. The effect of hydrothermal temperature on the nanostructure of meso-silica is in agreement with that reported in the literature.(Gobin et al., 2007b) The pore volume also increased from 1.08, 1.34 to 1.64 cm^{3} g^{-1}, respectively. With the impregnation of 80wt% HPW, the corresponding pore size is reduced to 3.7, 6.6 and 8.6 nm, respectively (Figure 5.2d), implying that the average thickness of anchored HPW layer inside the meso-silica would be 1.3, 1.6 and 3.5 nm, respectively, for meso-silica host heated treated at 60, 100 and 160 ^{o}C. As compared with that of pure meso-silica, HPW-meso-silica nanocomposites exhibit a wider hysteresis loop, suggesting a smaller pore entrance for the HPW-meso-silica nanocomposites. As shown early, HPW may block some pore entrance of meso-silica framework during the HPW impregnation treatment.(Lu et al., 2010) The pore volume of the 80 wt% HPW-meso-silica heat-treated at 60, 100 and 160 ^{o}C is 0.15, 0.39 and 0.71 cm^{3} g^{-1}, significantly smaller than that of pristine meso-silica. The reduction in pore size and pore volume of the HPW-meso-silica indicates the successful functionalization of HPW inside the mesoporous structure of host silica. Table 5.2 lists the topological parameters of meso-silica and HPW-meso-silica hydrothermally treated at different temperatures.

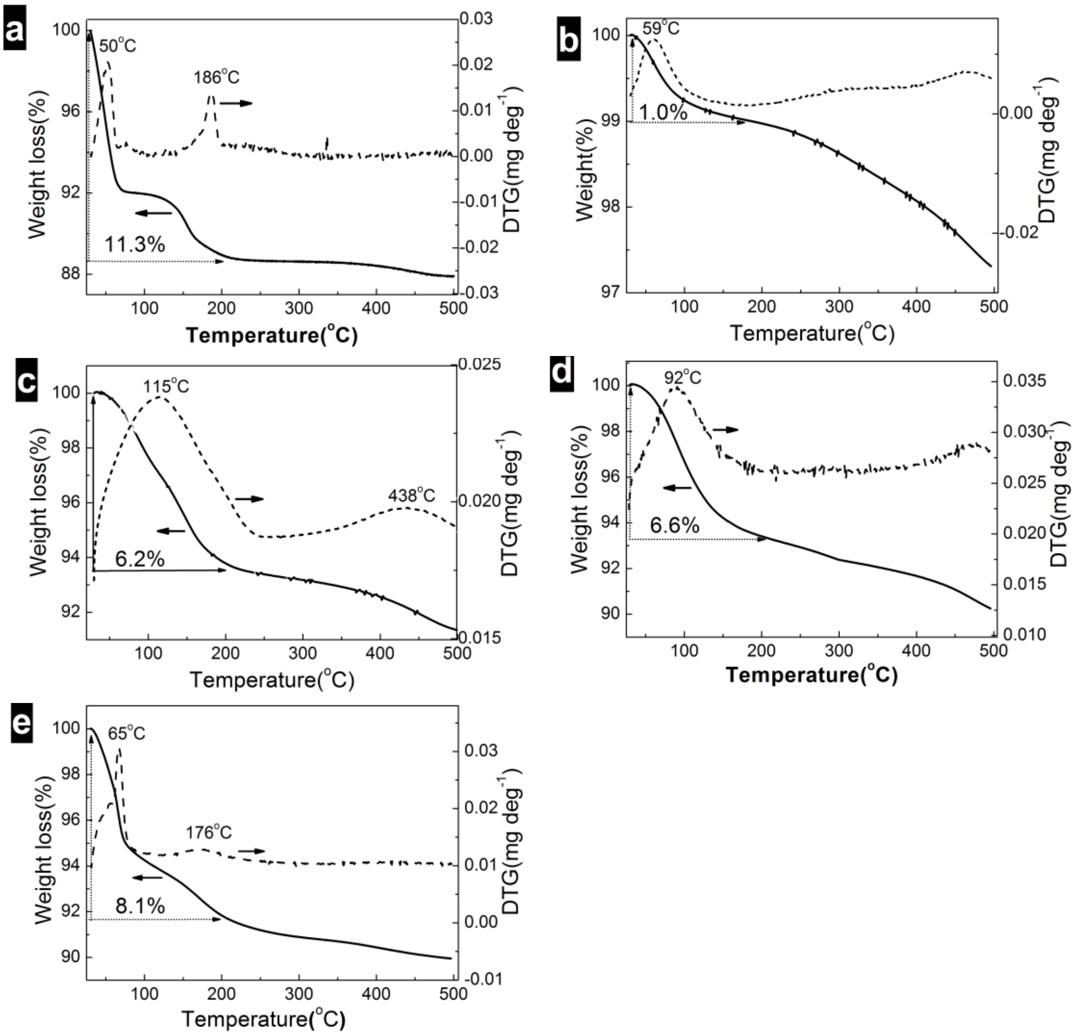

Figure 5.3 TGA spectra of (a) HPW, (b) meso-silica, (c) HPW-meso-silica-60, (d) HPW-meso-silica-100, and (e) HPW-meso-silica-160 nanocomposites.

Figure 5.3 shows TG thermograms of the pure HPW, meso-silica and HPW-meso-silica nanocomposite heat-treated at different temperatures. TGA was measured in the temperature range of 30-500°C. The weight loss measured at 200°C is also given in Figure 5.3. The pure HPW exhibits two hydrate loss steps at temperatures around 50 and 186 °C (Fig.5.3a), which are consistent with that reported in the literature. (Sweikart et al., 2005, Yamada and Honma, 2006) The first water loss can be attributed to desorption of physically absorbed water while the second step in the water loss, which occurred between 160 and 200^{o}C, could be assigned to the release of structural water from the HPW hydrate. On the other hand, the meso-silica is thermally stable in the temperature range of 30-500^{o}C and shows only 1.0% weight loss at 200^{o}C (Fig.5.3b), much lower than 11.3% of pure HPW.

The thermal behavior of HPW-meso-silica nanocomposite is very different from that of pure HPW. Knowing from the TGA spectra in temperature range of 30-500^{o}C the dehydration of HPW-meso-silica hydrothermally treated at different temperatures occurred in one single step, rather than two steps as observed in the dehydration of pure HPW. Moreover, the weight loss at 200ºC is 6.2% for HPW-meso-silica-60, 6.6% for HPW-meso-silica-100 and 8.1% for HPW-meso-silica-160, respectively, which are lower than 11.3% of pure HPW, suggesting probably the higher thermal stability of water in the HPW-meso-silica nanocomposites as compared with the isolated HPW Keggin structure. The results also indicate that the meso-silica host materials with smaller pore size seem to be able to retain more structural water in HPW-meso-silica nanocomposites. This shows that HPW-meso-silica hydrothermally treated at 60^{o}C could be a promising candidate for electrolyte membranes used for fuel cell applications.

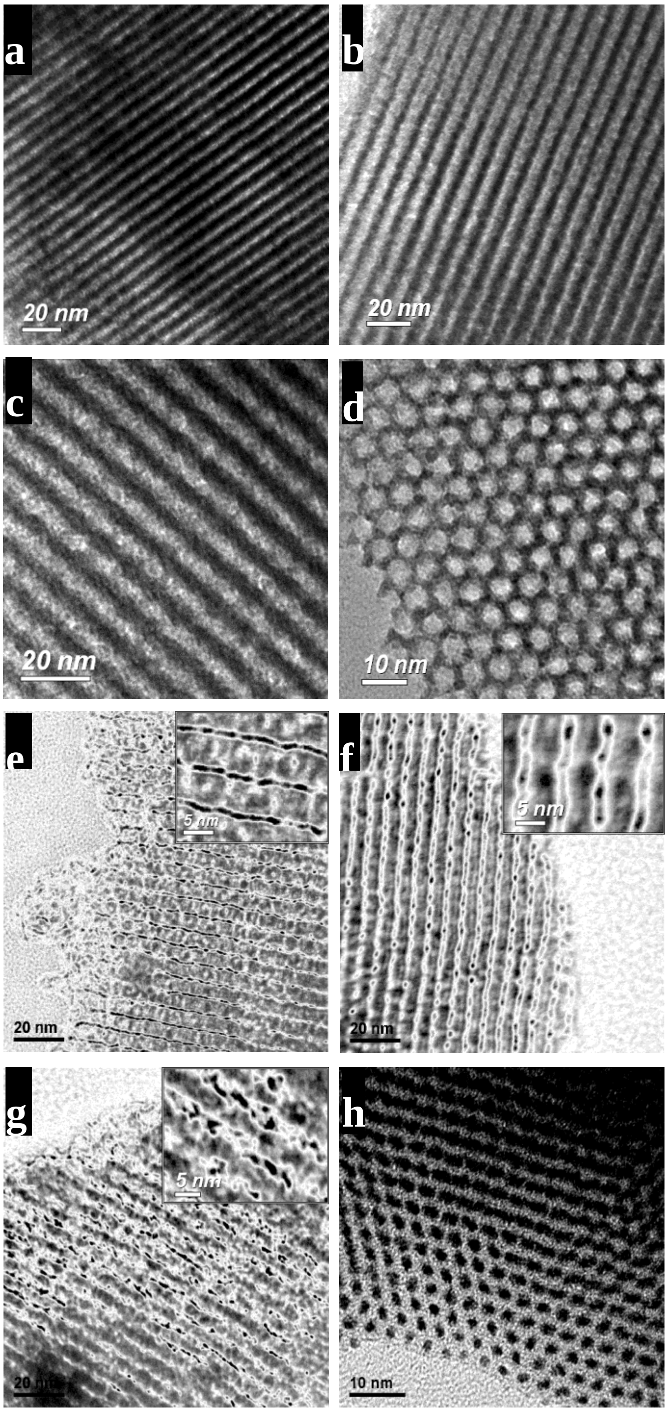

Figure 5.4 TEM images of pristine meso-silica and 80wt% HPW-meso-silica nanocomposites synthesized at different hydrothermal treatment temperatures; (a) meso-silica-60; (b) meso-silica-100; (c) meso-silica-160, (d) meso-silica-60 viewed along the pore axis (e) HPW-meso-silica-60; (f) HPW-meso-silica-100; (g) HPW-meso-silica-160; and (h) HPW-meso-silica-60 viewed along the pore axis.

The microstructures of meso-silica before and after HPW functionalization were studied by TEM and the results are shown in Figure 5.4. All specimens were characterized by highly ordered nano-channels, as viewing from [110] and [111] directions. $Ia\bar{3}d$ meso-silica is characterized by highly ordered 2D nanochannels with wall thickness of 5.0, 4.5 and 4.0 nm (the thick black lines in Figure 5.4a, b, and c) for meso-silica heat-treated at 60, 100 and 160 ^{o}C, respectively. On the other hand, the pore diameter increases with the increase in the hydrothermal temperature of meso-silica host (see Table 1). TEM image taken along the pore axis indicates that the channel diameter of meso-silica-100 is ~8.3 nm (Figure 5.4d), which is consistent with that obtained by the N_2 absorption isothermal analysis. The TEM results clearly demonstrate that the mesoporous structure of $Ia\bar{3}d$ meso-silica can be easily tuned by the control of hydrothermal temperature. In the case of HPW-functionalized meso-silica, the TEM images provide a direct observation of the morphology and distribution of HPW nanoparticles in the $Ia\bar{3}d$ meso-silica hosts, indicated by the ordered, but not continuous black dots sandwiched between continuous siliceous pore walls (grey or white in color, see Figure 5.4e, f, and g). The distances between HPW nanoparticles (i.e., the black dots) vary between 0 to 4 nm, indicating the highly dispersed HPW nanoparticles inside the mesopores or nanochannels of silica. The density of HPW nanoparticles appears to depend on the nanostructure of meso-silica hosts, e.g., the hydrothermal temperature. Local aggregation of HPW nanoparticles was observed for the sample with larger pore volume (Figure 5.4g). The shape and diameter of the hexagonal channels of HPW-functionalized meso-silica are not as regular as that of the pristine $Ia\bar{3}d$ meso-silica (compare Figure 5.4d and h). This is most likely due to the impregnation and insertion of HPW into the mesoporous channels of meso-silica. Due to the phase contrast between tungsten in HPW and silica in meso-silica host, the mesoporous channels of HPW-meso-silica viewing along the pore axis of meso-silica become black in color (Figure 5.4h).

5.3.2 Conductivity, stability and water uptake

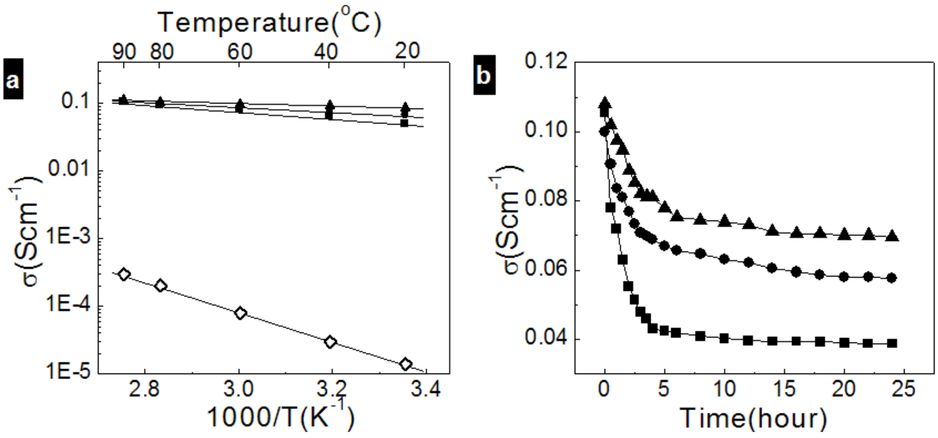

Figure 5.5 (a) Arrhenius plots of (◊) pristine meso-silica-60, (▲) HPW-meso-silica-60, (●) HPW-meso-silica-100 and (■) HPW-meso-silica-160, measured under 100%RH. (b**)** Proton conductivity stability of the (▲) HPW-meso-silica-60, (●) HPW-meso-silica-100, and (■) HPW-meso-silica-160, measured at 80°C under a constant water flow at 50 ml min^{-1}.

Figure 5.5a shows the plots of the proton conductivity versus temperature for pristine meso-silica heat-treated at 60 °C and HPW-meso-silica treated at different temperatures. The proton conductivity of meso-silica heat-treated at different temperatures is similar, ~3×10^{-4} S cm^{-1} at 90°C and 100% RH and the activation energy of conductivity is ~47 kJ mol^{-1}, very close to the results reported in the literature. (Li and Nogami, 2002b) On the other hand, the proton conductivity of $Ia\bar{3}d$ structured silica increases significantly after functionalization with 80 wt% HPW. The conductivity of HPW-meso-silica-60 is 0.11 S cm^{-1} at 90^{o}C and 100% RH, which is close to 0.18 S cm^{-1} of fully hydrated HPW. (Osamu Nakamura et al., 1979) The activation energy of HPW-meso-silica-60 is 14.5 kJ mol^{-1}, and in the case of HPW-meso-silica-100 and HPW-meso-silica-160, the activation energy is 14.8 kJ mol^{-1} and 15.6 kJ mol^{-1}, respectively, much smaller than that of the pristine meso-silica.

The stability of the proton conductivity of HPW-meso-silica was investigated under an accelerated durability test at 80 ^{o}C with a constant water flow rate (Figure 5.5b). The conductivity value of the HPW-meso-silica membranes drops rather rapidly during the first few hours and reaches a constant value after tested for 6 h. The decrease in conductivity depends strongly on the microstructure of the meso-silica framework; in the case of 80 wt% HPW-meso-silica-60, the conductivity was stabilized after 6h test and the proton conductivity decreased from 0.108 to 0.075 S cm^{-1}, a loss of 29%. The stabilized conductivity indicates the successful immobilization of water soluble HPW in mesoporous silica framework. For 80 wt% HPW-meso-silica-100, the stabilized conductivity is 0.064 S cm^{-1} and the decrease in conductivity is 38%, while for 80 wt% HPW-meso-silica-160 the stabilized conductivity is 0.041 S cm^{-1} and the overall loss in conductivity is 58%. The diameter of mesopores of meso-silica-60 is 5.0 nm, 8.2 nm for meso-silcia-100 and 12.1 nm for meso-silica-160. The loss in proton conductivity for the HPW-meso-silica nanocomposites increases with the increase in the pore size of $Ia\bar{3}d$ meso-silica hosts. The best stability and high conductivity were obtained on HPW-functionalized meso-silica with smaller pore size, meso-silica-60 in the present study. The results suggest that large pore size of the host meso-silica would lead to a high loss of the conductivity, though their initial conductivities are close (see Figure 5.5a). The decay in the conductivity is most likely due to the leaching of HPW during the flushing of DI-water: the membranes suffered a weight loss of 1.2-5.4 wt% after the stability test. It should be pointed out here that the stability test conditions under continuous flow of DI-water are much more severe than the normal fuel cell operating conditions. The results demonstrate that both high level of proton conductivity and stability for HPW-meso-silica nanocomposite membranes can be achieved by optimization of the pore structure of mesoporous silica host.

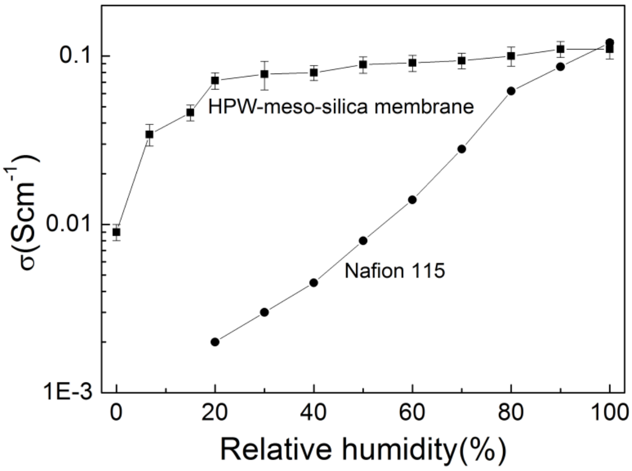

Figure 5.6 The conductivity of HPW-meso-silica-60 nanocomposite (■) as a function of humidity, measured at 80^{o}C. The conductivity data of Nafion 115 membrane (●) measured at 30 ℃ as a function of RH were taken from references.(Zhang et al., 2008)

The effect of relative humidity on the conductivity of HPW-functionalized meso-silica was studied on the best performed nanocomposite, 80 wt% HPW-meso-silica-60. Figure 5.6 shows the RH dependence of the conductivity of 80 wt% HPW-meso-silica-60 nanocomposite under 0-100 %RH and 80 ℃. For the purpose of comparison, the proton conductivity of Nafion 115 membrane measured at 30 ℃ as a function of RH (Ma et al., 2003, Ye et al., 2010, Casciola et al., 2009) is also given in the figure. The proton conductivity of HPW-functionalized meso-silica increases with the RH, indicating that water also plays an important role in the proton transfer and conduction in the HPW-meso-silica nanocomposites. However, the dependence of the conductivity on RH is far less sensitive as compared to that of the state-of-the-art PFSA electrolyte membranes such as Nafion. For example, the conductivity of Nafion 115 increases from 0.07 to 0.15 S cm^{-1} when the temperature is raised from 30 to 85 ^{o}C at 100 % RH but at 30 ^{o}C it decreases substantially from 0.066 to 0.002 Scm^{-1} as RH decreases from 100% to 20%,(Hyun and Kim, 2004) a loss of more than one order of magnitude in the conductivity. In the case of 80 wt% HPW-meso-silica nanocomposites, the conductivity decreases from 0.11 S cm^{-1} to 0.077 S cm^{-1} when the RH decreases from 100% to 30% at 80 ℃, a reduction in the conductivity by only 23%. The much lower denpendence of the proton conductivity on the RH indicates the high water retention ability of the HPW Keggin-type molecules anchored in the ordered meso-silica structure.

The high tolerance of the HPW-meso-silica nanocomposites towards the RH fluctuation is also supported by the water uptake test. The water uptake contents of meso-silica and HPW-meso-silica are 42.8% and 16.2%, respectively before drying treatment at 40 ^{o}C. After drying at 40 ℃ with N_2 flow overnight, the water uptake is 2 and 12.3%, respectively for meso-silica and HPW-meso-silica. The significant change in water uptake for meso-silica before and after drying treatment at 40^{o}C indicates that majority of water in the case of mesoporous silica is physically adsorbed surface water. The much higher water uptake of HPW-meso-silica after the drying treatment means that the presence of HPW in the nanochannels of meso-silica enhances substantially the water retention ability of meso-silica. The dimension of the HPW-meso-silica nanocompsoite membrane discs did not change before and after the water uptake experiment, indicating that the swelling of the nanocomposite membranes is negligible. In the case of PFSA membranes such as Nafion, the volume of the Nafion membrane changes siginficantly with water uptake and swelling ratios of Nafion membrane were reported as high as 12.8-14% in pure water and 51-53% in 1M methanol/water solution (Tazi and Savadogo, 2000, Randov et al., 2008, Gebel et al., 1993). The high swelling ratios of Nafion-based membranes seriously jeopardise the membrane mechanical stability as well as their resistance against fuel crossover, including hydrogen, methanol and formic acid (Jeong et al., 2007, Xu et al., 2010).

The conductivity of HPW-meso-silica nanocomposites indicates that the highly dispersed HPW molecules in the mesoporous silica nanochannels significantly reduce the conduction barrier for proton mobility. The dependence of conductivity on RH indicates that water also plays an important role in this process because the presence of water significantly reduces the activation barrier to proton movement. The increase of proton mobility enhanced by small amounts of water has been explained by quantum chemical density function theory (DFT) calculations. (Janik et al., 2005) Without water molecule consideration, the motion of protons on an isolated HPW is unfavorable, and the barrier would be significantly high, owing to the larger distance over which proton transfer must occur between two neighbor oxygen bridged by water. The activation energy for anhydrous proton movement through the individual HPW clusters was calculated to be 103.3 kJ mol^{-1}. (Janik et al., 2005) After water adsorption, a second hydrogen bond would be formed between the hydrogen atom of the water molecule and a terminal oxygen atom site of the Keggin unit in addition to the initial one between the proton of the KU and the oxygen atom of the water molecule. Herein, the barrier would be greatly reduced by an order of magnitude to ~11 kJ mol^{-1}. The significant low activation energy, together with the high conductivity is most likely attributed to the water-promoted proton hopping pathway which does not require substantial structural rearrangement of the Keggin unit to form the transition state. Moreover, the proton transport could also take place via the vehicle mechanism, in which the highly dispersed HPW acts as proton donor and acceptor simultaneously, and water assists proton movement by facilitating transport via the transition state with a separated hydronium ion H_3O^+.

5.3.3 Influence of relative humidity on cell performance

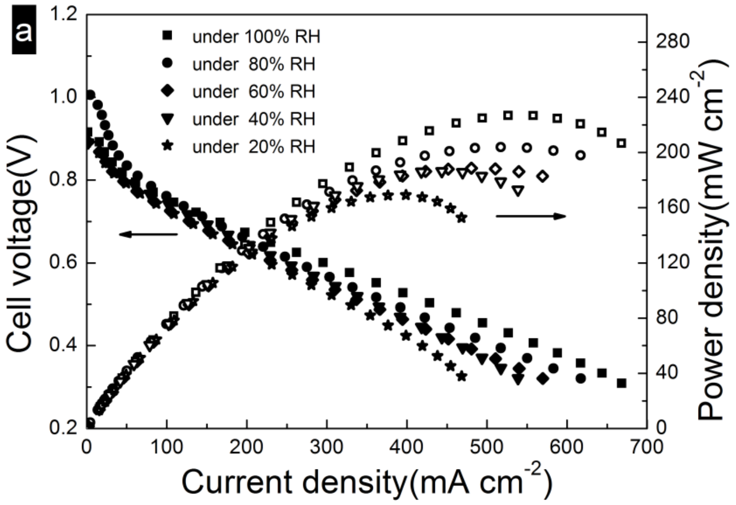

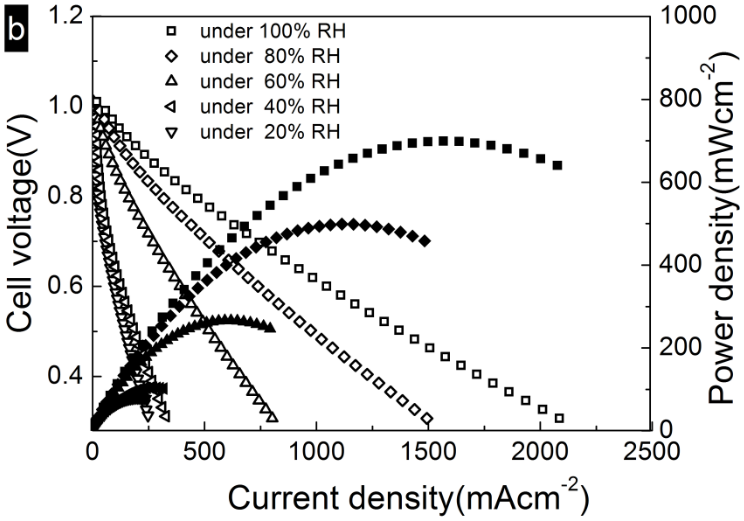

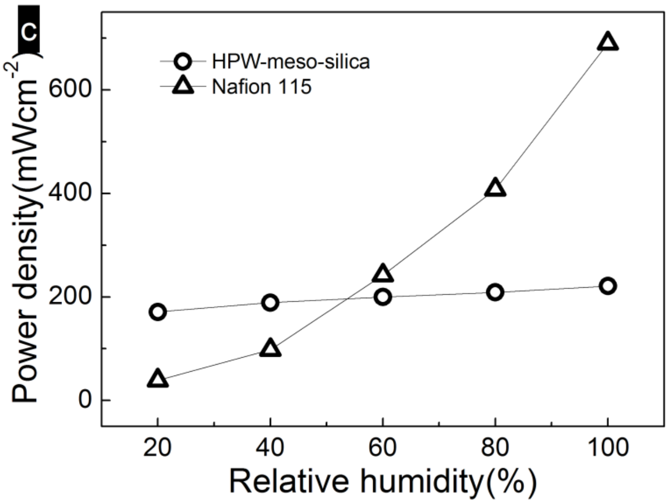

Figure 5. 7 (a) Performance of single cells with HPW-meso-silica-60 nanocomposite membrane, measured in H_2/O_2 at 80°C and different RH, and (b) performance of single cells with Nafion 115 membranes measured in H_2/O_2 and at 80°C and different RH; (c) maximum power density of cells with HPW-meso-silica nanocomposite and Nafion 115 membranes as a function of RH; and

To demonstrate the applicability of the HPW-meso-silica nanocomposite as PEMs for fuel cells, cells with 80wt%HPW-meso-silica nanocomposite membranes were fabricated and tested in H_2/O_2 at 80 °C and different RH and the results are shown in Figure 5.7a. The meso-silica hosts were synthesized at a hydrothermal temperature of 60°C. For the purpose of comparison, cell performance of Nafion 115 membranes was also measured under identical experimental conditions (see Figure 5.7b). The maximum power density of cells with HPW-meso-silica nanoconposites and Nafion 115 membranes as a function of RH is compared in Figure 5.7c. At 100 % RH, the maximum power density of the cell with HPW-meso-silica membrance is 221 mW cm^{-2} and when RH is reduced to 20 %, the maximum power density is 171 mW cm^{-2}. This corresponds to a power loss of ~22% when the RH is reduced from 100% to 20%. The cell performance as a fuction of RH is consistent with the proton conductivity as shown in Figure 5.6. This clearly demonstrates again the high tolerance of HPW-meso-silica nanocomposite membranes towards the fluctuation in relative humidity, suggesting the extremely high water retention ability of HPW-meso-silica nanocomposites studied here. In contrast, cells with conventional Nafion membranes show a significant performance drop as the RH decreases (Figure 5.7c). At 100% RH and 80^{o}C, the maximum power density is 706 mW cm^{-2} and as the RH is reduced to 20%, the maximum power density decreases substantially to 33 mWcm^{-2}, a 95% reduction in power density. It is well known that proton conductivity and cell performance of Nafion PFSA membranes are very sensitive to the change and flunctuation in relative humidity. (Jeon et al., 2010, Zawodzinski et al., 1993, Buchi and Scherer, 2001) Zhang et al studied the cell performance of Nafion 112 membrane as a function of RH in H_2/O_2 and found that as RH decreased from 100% to 70%, the peak power density decreased dramatically from 572 mW cm^{-2} to 218 mW cm^{-2}.(Zhang et al., 2008) Such significant dependence of the Nafion membrane cells on the relative humidity was also reported by Hyun and Kim.(Hyun and Kim, 2004)

Figure 5.7c is the comparison of the peak power density of cells with HPW-meso-silica and Nafion 115 as a function of RH, measured at 80^{o}C. The power density of cell with Nafion 115 is ~400 mW cm^{-2} under 80 %RH and drops significantly to ~38 mW cm^{-2} when RH is decreased to 20%, a reduction in power output by 90%. The substantial reduction in power output of Nafion 115 with the decrease in RH is clear due to the fact that the proton conductivity of Nafion membranes decreases significantly with the decrease of RH. (Zawodzinski et al., 1993, Buchi and Scherer, 2001, Yan et al., 2009) In contrast to the Nafion 115 membrane, cells with HPW-meso-silica nanocomposite membranes show a much smaller change with RH. Under 80 %RH, the power density of HPW-meso-silica membrane is 308 mW cm^{-2} in H_2/O_2 and it is 215 mWcm^{-2} as the RH decreases to 20%. The decrease in power output is 30%, which is three times smaller as compared to the cell with Nafion 115 membranes. Similar dependence of the power output on the RH was also observed for the HPW-meso-silica cells operated in H_2/air. The stable performance of HPW-meso-silica nanocomposites indicates that the proton conductivity of the HPW-meso-silica nanocomposites does not change significantly with the change in RH, clearly demonstrating the high water retention capability of the HPW-meso-silica nanocomposites. The lower performance of HPW-meso-silica nanocomposites as comapred to that of Nafion 115 in the high RH region may also be due to the fact HPW-meso-silica nanocomposite membranes are significantly thicker than Nafion 115 used in this study (500 μm verse 125 μm).

5.4 Summary

A novel inorganic proton exchange membrane based on the HPW-functionalized mesoporous silica nanocomposites was successfully developed. The structure of mesoporous silica host can be controlled by the hydrothermal temperature and the functionalization of the meso-silica by HPW impregnation leads to the formation of highly ordered mesoporous framework with HPW molecules anchored in the mesoporous silica matrix, forming an effective proton conduction pathway. The HPW loading of the HPW-meso-silica composite has been optimized in Chapter 4 and is set to be 80 wt%. The best conductivity was obtained on the HPW-meso-silica nanocomposites synthesized at a hydrothermal temperature of 60 ^{o}C, achieving a high proton conductivity of 0.07~0.11 S cm^{-1} at 25~90 ^{o}C and a low activation energy of 14.5 kJ mol^{-1}. The proton conductivity is also stable, indicating the immobilization of the impregnated HPW in the mesoporous silica structure. As compared to conventional Nafion membranes, the proton conductivity and cell performance of HPW-meso-silica nanocomposites are much less sensitive to the change in RH. In the case of the HPW-meso-silica membrane based PEMFC, a decrease of 22% in power density was observed when the relative humidity was reduced from 100% to 20%, as compared to a much severe decrease of 95% in power density for Nafion 115 membrane under the same condition. The present study demonstrates that inorganic proton exchange membranes with high proton conductivities and stability can be realized through the functionalization of the HPW-meso-silica nanocomposite.

CHAPTER 6. Correlation of Proton Conductivity, Thermal Stability and Structure Symmetries

In this chapter, HPW-meso-silica nanocomposites based on mesoporous silica host of four symmetries were prepared via a vacuum impregnation method. The effect of different structural symmetries of meso-silica on the membrane conductivity at various temperatures and different relative humidity were studied systematically. The long-term durability of DMFC based a HPW-meso-silica membrane was measured on a home-made vapor-fed DMFC testing system.

6.1 Introduction

The engineering of porosity and porous structure in common materials such as silica and carbon is emerging as a new area with scientific and technological interest and importance.(Fan et al., 2008, Armatas et al., 2003, Lin et al., 2008, Lu et al., 1999, Tang and Jiang, 2008, Wan and Zhao, 2007, Dias et al., 2006, Yang et al., 2009) In particular, materials with high specific surface area, nano or meso-sized channels or frameworks with an ordered and connected internal structure, and high structural stability offer great potential in applications as proton exchange membranes for fuel cells operating at elevated temperatures.(Hogarth et al., 2005b) The proton conductivity of inorganic framework materials such as mesoporous silica or aluminosilica is in the range of 10^{-5}~10^{-4} S cm^{-1} under fully hydrated conditions (Li and Nogami, 2002b, Sharifi et al., 2010) and is too low for the practical fuel cell applications. However, incorporation of a proton carrier into mesoporous structure is approved to be effective to increase the proton conductivity. (Li and Nogami, 2002b, Athens et al., 2007b, Colomer, 2006b, Yamada et al., 2005b, Daiko et al., 2002, Uma and Nogami, 2007d, Xiong and Nogami, 2006, Halla et al., 2003a, Athens et al., 2007a) Marschall et al.(Marschall et al., 2009b) used imidazole to functionalize mesoporous MCM-41 silica by immersing treatment and the highest conductivity was ~10^{-4} S cm^{-1} at 140 ^{o}C and 100% RH. Jin et al (Jin et al., 2009) functionalized silica gel with phosphonic acid and found that at 150^{o}C the proton conductivity of phosphonic acid silica gel increased from $4.4x10^{-4}$ Scm^{-1} at 20%RH to 0.031 Scm^{-1} when RH incrased to 100%RH, indicating the sensitivity of the conductivity to the humidity. The proton conductivity of sulfonic acid functionalized meso-silica is also found to be very sensitive to RH.(Marschall et al., 2009a) In th case of acid catalysts (CF_3SO_3H) and surfactant ($C_{12}EO_{10}OH$) functionalized meso-silica, proton conductivity only started to increase and reach ~10^{-3} Scm^{-1} at a 90% RH and at room temperature. (Halla et al., 2003a)

In this work, we explore the intrinsic relationship between the structure symmetries of 2D and 3D *meso*-silica (*p6mm*, $Fm\bar{3}m$, $Im\bar{3}m$ and $Ia\bar{3}d$), thermal stability, and proton conductivity for the applications as inorganic proton exchange membranes for fuel cells. The HPW-*meso*-silica with 3D structural symmetries ($Im\bar{3}m$) showed an impressive proton conductivity of 0.140 S cm^{-1} at 150 ℃, which is significantly higher than 0.08 S cm^{-1} for the HPW-*meso*-silica with 2D structural symmetries (*p6mm*). The HPW-*meso*-silica nanocomposites with 3D structural symmetries ($Im\bar{3}m$ and $Ia\bar{3}d$) also show a high tolerance toward the change in RH, which is a very important property for the design of fuel cells operated at elevated high temperatures and reduced humidities.

6.2 Experimental

6.2.1 Synthesis of meso-silica and HPW-meso-silica nanocomposites

Various structures of mesoporous silica, including P6mm, Fm3m, Im3m and Ia3d were synthesized as described in Section 3.2. The experimental conditions of the synthesis process are given in Table 6.1. The HPW-meso-silica nanocomposites are prepared with a constant HPW loading of 80 wt% for concerns of both proton conductivity and mechanical stability, the optimization work is detailed in Chapter 4. The influence of HPW loading on membrane performance was detailed in Figure 4.8, Page 104.

Table 6.1 Synthesis conditions for Ia3d, Im3m, and Fm3m structure

Meso-structure	Butanol(g)	Surfacant(g)	TEOS(g)	HCl(g)	H_2O(g)
2D Hexagonal (P6mm)	0	4(P123)*	8.6	7.9	144
3D Face-center (Fm3m)	0	3(F127)*	14.4	6.3	144
3D Cubic-center (Im3m)	9	3(F127)*	14.2	5.94	144
3D Bicontinuous (Ia3d)	4	4(P123)*	8.6	7.9	144

6.2.2 Measurements of conductivity, cell performance, methanol crossover

The proton conductivity measurements of HPW-*meso*-silica nanocomposites with different structural symmetries were performed by a four-probe method, using electrochemical impedance spectroscopy (PGSTAT30/FRA, Autolab, Netherlands) over the frequency range from 1Hz to 1MHz in the temperature range from 25 to 150 ^{o}C. The relative RH of the measurements was controlled by a PEMFC test station (FCATS-G050, Greenlight, Canada) and measured in situ using a HM141 humidity indicator (Vaisala, US). The cell performance was measured with a methanol flow rate of 2 mL min^{-1} and an O_2 flow rate of 40mL min^{-1}. No back pressure control of both sides was applied in this work.

Limiting methanol permeation currents through the membranes were measured using electrochemical oxidation technique. (Jiang et al., 2006b) This method consists of inverting the cell polarity with respect to that used in the single cell. Given that the fuel cell is fed with inert N_2, the limiting current density is measured based on the assumption that the entire crossover methanol was oxidized at the cathode during transport-controlled process. At the anode of fuel cell, hydrogen evolution takes place, serving as a counter and reference electrode. The limiting methanol crossover current was obtained from the methanol oxidation current curves.

6.3 Results and discussion

6.3.1. SAXS, TGA, TEM of HPW-meso-silica nanocomposites

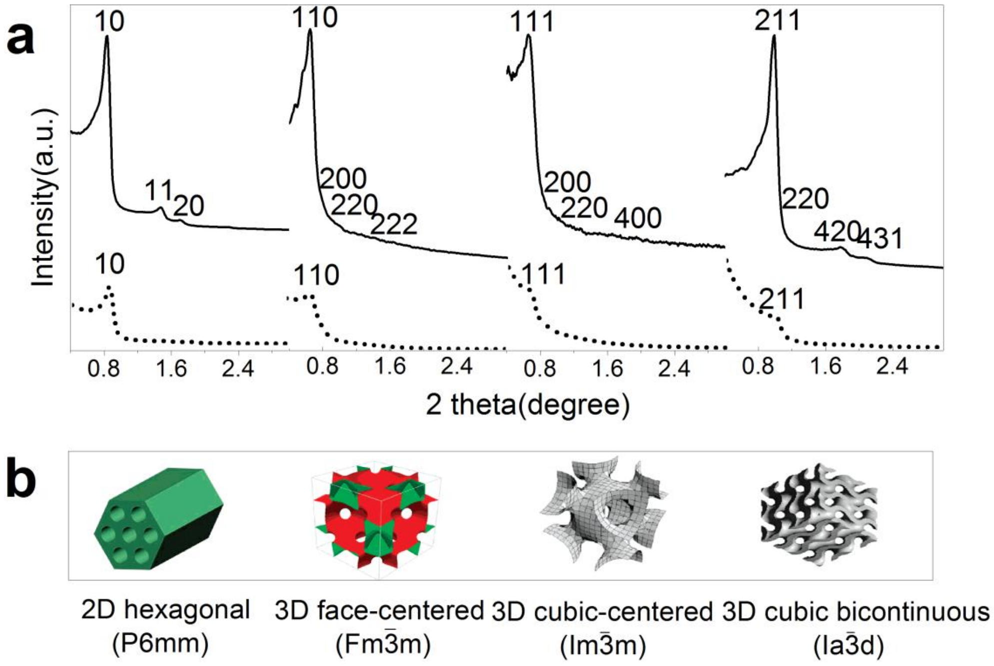

Figure 6.1 a) SAXS patterns of mesoporous silica with $P6mm$, $Fm\bar{3}m$, $Im\bar{3}m$ and $Ia\bar{3}d$ symmetries arranging from left to right (solid line); and the corresponding HPW-meso-silica nanocomposite: HPW-$P6mm$, HPW-$Fm\bar{3}m$, HPW-$Im\bar{3}m$ and HPW-$Ia\bar{3}d$ arranging from left to right (dotted line) and b) The schematic structures of $P6mm$, $Fm\bar{3}m$, $Im\bar{3}m$ and $Ia\bar{3}d$ mesoporous silica from reference.(Wan and Zhao, 2007)

Figure 6.1 shows the small-angle X-ray scattering (SAXS) patterns of mesoporous silica with different structural symmetries before and after HPW functionalization. All samples show the well-resolved scattering peaks, and the major peaks are considered to be the ‘fingerprint’ scattering patterns of hexagonal $P6mm$, face-centered $Fm\bar{3}m$, body-centered $Im\bar{3}m$ and cubic bicontinuous $Ia\bar{3}d$ symmetries of mesoporous silica (see Figure 4.1a)(Wan and Zhao, 2007), suggesting the successful formation of well ordered mesoporous silica with different structures. On the basis of pore symmetry and SAXS data, the unit cell parameter, α, of mesoporous silica can be calculated from the *d*-spacing of the main scattering peak (The calculation process is detailed in Page 82, Chapter 3). For *meso*-silica with the *p6mm* symmetry, α is 4.6 nm, significantly smaller than 18.9 nm for $Fm\bar{3}m$, 19.6 nm for $Im\bar{3}m$, and 21.9 nm for $Ia\bar{3}d$. The unit cell parameters of *meso*-silica and HPW-*meso*-silica nanocomposite are given in Table 6.2.

Table 6.2 Textural parameters of *meso*-silica and HPW-*meso*-silica nanocomposites with different structural symmetries

Sample	Unit cell α (nm)[a]	S_{BET} (m^2g^{-1})	Pore vol (cm^3g^{-1})[b]	Pore size (nm)[c]	Wall thickness (nm)[d]
$P6mm$	4.6	946	0.678	2.4	2.1
$Fm\bar{3}m$	18.9	893	0.386	4.6	8.8
$Im\bar{3}m$	19.6	900	0.517	6.5	7.4
$Ia\bar{3}d$	21.9	952	1.335	8.2	7.3
HPW-$P6mm$	4.6	135	0.266	1.4	
HPW-$Fm\bar{3}m$	18.9	323	0.198	3.5	
HPW-$Im\bar{3}m$	19.6	360	0.212	5.5	
HPW-$Ia\bar{3}d$	21.9	377	0.391	6.6	

[a] Calculated from SAXS results, detailed in Page 82, Chapter 3

[b] Cumulative pore volume

[c] Calculated from the adsorption branch of the isotherms based on the NLDFT method

[d] Estimated from SAXS and BET results

After the HPW functionalization, the major scattering peaks of meso-silica experienced a significant drop in intensity. However, the position of the scattering peaks for HPW-*meso*-silica nanocomposites remains more or less the same as that of the corresponding *meso*-silica hosts, and this is also indicated by the same unit cell parameters for HPW-*meso*-silica as comapred to that of *meso*-silica hosts (Table 6.2).

This implies that the symmetrical and dimensional properties of the *meso*-silica hosts are well preserved after the HPW impregnation. The significant decrease in the relative intensity of the scattering peak could be due to the reduced contrast between the wall and pore of *meso*-silica as the result of the impregnation of HPW molecules inside the silica mesopores. The interaction between the siliceous host and impregnated HPW molecules could be detrimental to the structural regularity of the mesoporous silica.

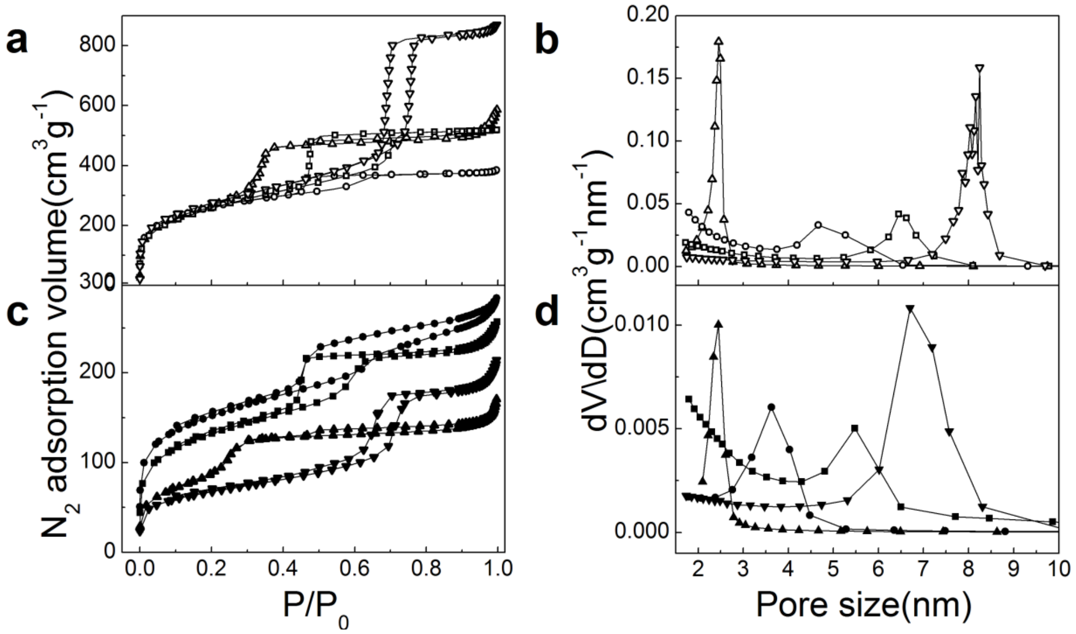

Figure 6.2 N_2 sorption isotherms and pore size distribution of *meso*-silica (empty symbols) and HPW-*meso*-silica nanocomposites (filled symbols) with $P6mm$, $Fm\bar{3}m$, $Im\bar{3}m$, $Ia\bar{3}d$ symmetries; a, c) N_2 sorption isotherms; b, d) pore size distribution; Symbols in a-d: triangles, $P6mm$ and HPW-$P6mm$; circles, $Fm\bar{3}m$ and HPW-$Fm\bar{3}m$; squares, $Im\bar{3}m$ and HPW-$Im\bar{3}m$; and inverted triangles, $Ia\bar{3}d$ and HPW-$Ia\bar{3}d$

The porosity of *meso*-silica and HPW-*meso*-silica nanocomposites with different symmetries was probed with N_2 absorption/desorption isotherm measurements and the results are shown in Figure 6.2. The N_2 sorption curves show the typical type-IV isotherms associated with a distinct step at certain relative pressures (~0.3 for *P6mm*, ~0.5 for $Fm\bar{3}m$ and $Im\bar{3}m$ and ~0.7 for $Ia\bar{3}d$) (Figure 6.2a). The distinct step in the absorption isotherm is attributed to capillary condensation in narrowly distributed mesopores. As compared with that of pure *meso*-silica, it appears that the HPW-*meso*-silica nanocomposites exhibit much wider hysteresis loops, suggesting a smaller entrance size for the mesoporous structure probably due to the filling of adsorbent in the *meso*-silica host, similar to the wider hysteresis loop of boronic acid-functionalized *meso*-silica after enrichment of glycopeptides.(Xu et al., 2009) Further analysis indicates a H1 hysteresis loops for *P6mm* and $Ia\bar{3}d$ structure, suggesting a cylindrical pore shape for their textural structure, while in the case of *meso*-silica with the $Fm\bar{3}m$ and $Im\bar{3}m$ structural symmetries, a H2 hysteresis loop is prevailed, which means that the textural structure is an ink-bottle pore shape.(Ravikovitch and Neimark, 2002, Morishige and Tateishi, 2003) The analysis of the adsorption isotherms with the Brunauer-Emmett-Teller (BET) method gives surface areas in the range of 893-952 m^{2} g^{-1} for *meso*-silica. The specific surface areas of *meso*-silica with different structural symmetries are rather similar. However, after functionalized with 67wt% HPW, the specific surface of *meso*-silica with 2D mesostructure of *p6mm* is 135 m^{2} g^{-1}, which is an 86% reduction in surface area. On the other hand, the reduction of specific areas for the 67wt% HPW-fucntionalized *meso*-silica with 3D mesostructures is in the range of 60-64%, which is considerably smaller than HPW-*meso*-silica with 2D *p6mm* symmetry. Similar phenomenon can be observed for the pore volume and pore size of the *meso*-silica/HPW composite. This indicates that the differences in pore shape and textures of the mesostructures would have influence on the distribution of impregnated HPW. The cylindrical and straight pores of 2D mesostructure with space group *p6mm* favor more uniform HPW impregnation and distribution, as compared to more complex and ink-bottle shaped pores of 3D mesostructures with space groups $Im\bar{3}m$, $Fm\bar{3}m$ and $Ia\bar{3}d$. The high specific areas of HPW-*meso*-silica with 3D mesostructures also imply the high pore interconnectivity.(Armatas et al., 2003) The pore volume of *P6mm* and $Ia\bar{3}d$ *meso*-silica was reduced by 0.412 cm^3 g^{-1} and 0.944 cm^3 g^{-1} after HPW impregnation, respectively; the reduced values for $Fm\bar{3}m$ and $Im\bar{3}m$ were 0.188 cm^3 g^{-1} and 0.305 cm^3 g^{-1}, respectively. The BET specific surface area, pore volume, and pore size of *meso*-silica and HPW-*meso*-silica are also given in Table 6.2.

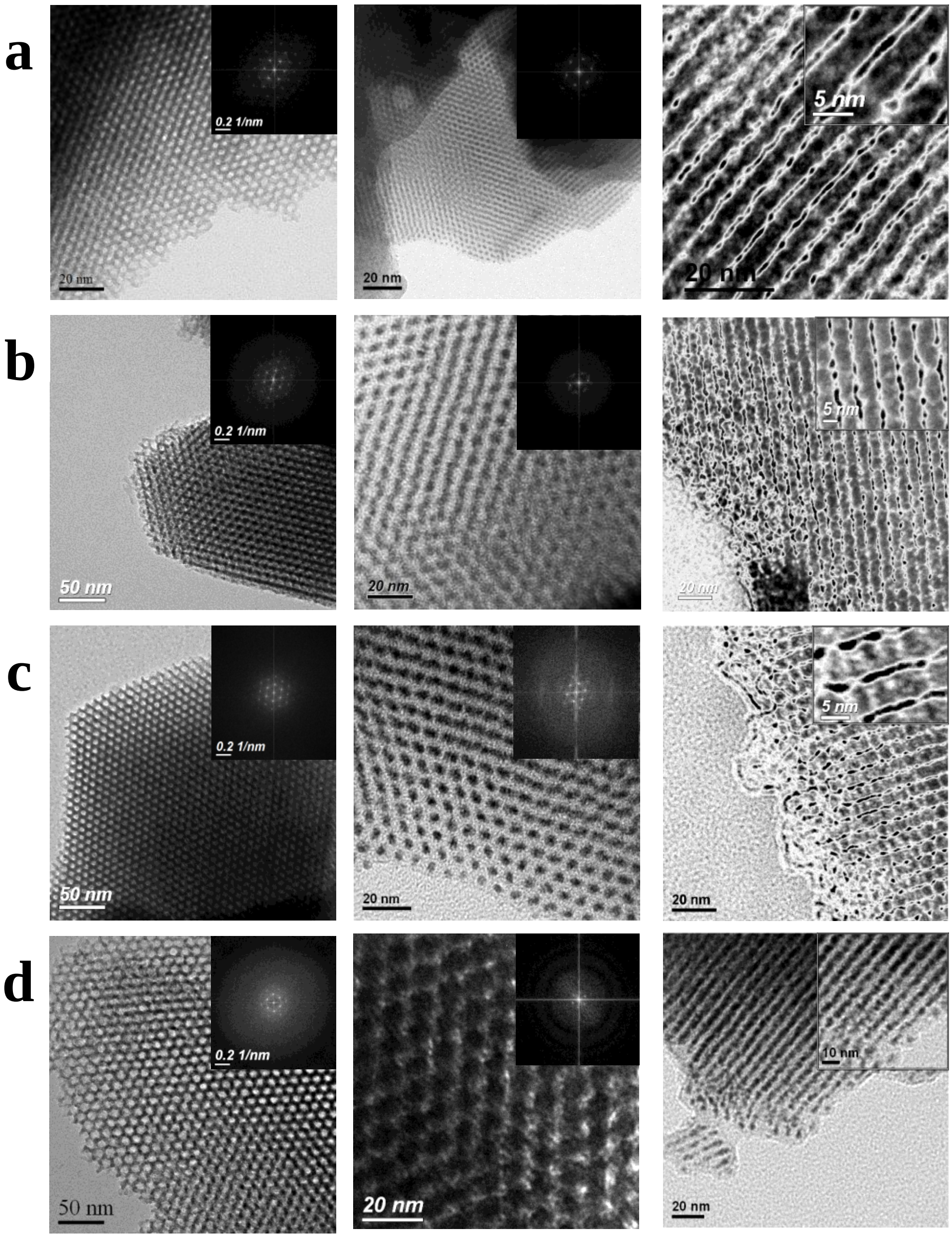

Figure 6.3 TEM images of *meso*-silica (left micrograph) and HPW-*meso*-silica nanocomposites (middle and right micrographs); a) $P6mm$ and HPW-$P6mm$; b) $Fm\bar{3}m$ and HPW-$Fm\bar{3}m$; c) $Im\bar{3}m$ and HPW-$Im\bar{3}m$; d) $Ia\bar{3}d$ and HPW-$Ia\bar{3}d$. The left and middle images of each sets are viewed from [111] direction while the right images are viewed from [110] direction.

Figure 6.3 shows TEM images and the corresponding fast-Fourier transform (FFT) patterns of *meso*-silica and the HPW-*meso*-silica nanocomposites. *Meso*-silica structure is characterized by a hexagonal arrangement of parallel or inter-connected pore channels, where the mesoporous channels are white in color and the siliceous walls are in grey color. The TEM images of the mesoporous silica family show regular arrays of mesopores, which can be assigned to [111] direction of the $P6mm$, $Fm\bar{3}m$, $Im\bar{3}m$ and $Ia\bar{3}d$ symmetries according to the coresponding FFT patterns, respectively. For example, in the case of the mesostructure with p6mm space group, the TEM images are characterized by hexagonal structures along the channel direction and parallel strips viewed perpendicular to the channel directions (Figure 6.3a). The HPW-*meso*-silica nanocomposites show ordered but not continuous black dots sandwiched between continuous siliceous walls, where the color difference is due to the much heavier tungsten ion of HPWs as compared to silicon ion of the *meso*-silica hosts. The distances between the HPW nanoparticles inside the mesoporous channels are in the range of 1-2 nm, indicating the formation of continuous HPW paths for the HPW-*meso*-silica nanocomposites with different structural symmetries.

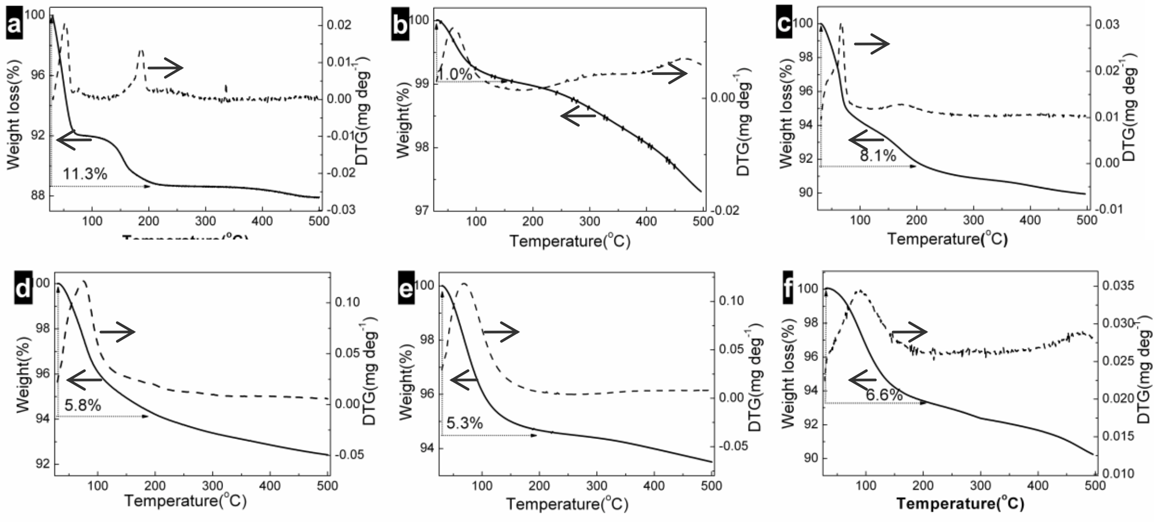

Figure 6.4 TGA curves of HPW, meso-silica and HPW-meso-silica nanocomposites; a) pure HPW; b) $Im\bar{3}m$ silica; c) HPW-$P6mm$; d) HPW- $Fm\bar{3}m$; e) HPW- $Im\bar{3}m$; f) HPW- $Ia\bar{3}d$. The numbers shown in the figures are the weight loss percentage at 200 ℃.

The thermogravimetic behaviors of HPW, *meso*-silica and HPW-*meso*-silica nanocomposites with different structural symmertries are shown in Figure 6.4. In the case of HPW, the TGA curve exhibited two sharp weight loss peaks at 53 ℃ and 185℃ (Figure 6.4a), which is in agreement with the results reported in the literature.(Sweikart et al., 2005) The peak at 53^{o}C is most likely due to the initial loss of physically absorbed water, followed by the loss of structural water from HPW Keggin structure at 185^{o}C. The overall weight loss (i.e., the water content) of HPW at 200^{o}C is 11.3%. All molecular water can be fully recovered by placing HPW in a humid environment. The irreversible decomposition temperature of HPW is 588 ^{o}C. (Nakamura et al., 1981) In the case of *meso*-silica with the structure symmetry of $Im\bar{3}m$, the dehydration occurs at around 60^{o}C and the weight loss is 1% at 200^{o}C (Figure 6.4b), significantly smaller than that of HPW. The low weight loss of pure *meso*-silica indicates the poor water retention ability of mesoporous silica. The relatively high dehydration loss of HPW comes from the adsorbed and structural water in the polyhydrate HPW ($H_3PW_{12}O_{40}$• nH_2O, n=6~29). Based on the thermal behavior of HPW discussed above, HPW may exist as $H_3PW_{12}O_{40}$•$13H_2O$ in the temperature range of 120-200 ^{o}C.(G. M. Brown et al., 1977) According to the results reported by Nakamura et al., (Nakamura et al., 1981) the $H_3P_4W_{12}O_{40}$• $13H_2O$ in the bulk state is stable at 30% RH.

On the other hand, the thermal behavior of HPW-*meso*-silica nanocomposites with different structural symmetries is very much different from that of HPW and *meso*-silica. Two dehydration peaks at 65 and 188 ℃ were also observed for the HPW-*meso*-silica nanocomposites with p6mm symmetry, HPW-*p6mm*, similar to that of pure HPW (Figure 6.4c). However, the weight loss of HPW-*p6mm* nanocomposites is 8.1%, significantly higher than 1% for pure *meso*-silica. This clearly shows that impregnation of HPW considerably enhances the water retention ability of *meso*-silica. The water retention properties of HPW-meso-silica nanocomposites also depend strongly on the structural symmetries of the meso-silica hosts. Very different from that of HPW-*p6mm* nanocomposites, the thermal behavior of HPW-*meso*-silica nanocomposites with 3D symmetries of $Fm\bar{3}m$, $Im\bar{3}m$ and $Ia\bar{3}d$, HPW-$Fm\bar{3}m$, HPW-$Im\bar{3}m$ and HPW-$Ia\bar{3}d$ is characterized by one but broad dehydration peak, at 72, 75 and 95 °C, respectively (Figure 6.4d-f). The dehydration temperatures for HPW-*meso*-silica nanocomposites are higher than the first dehydration peak of HPW and HPW-*p6mm* nanocomposites. The dehydration of HPW-*meso*-silica nanocomposites with 3D symmetries takes place in a temperature range of 25-200°C and experiences a more gradual dehydration step as compared with that of HPW-*meso*-silica with 2D symmetry of p6mm. The differences in the thermal behavior of the HPW-*meso*-silica nanocomposites with different structural symmetries may indicate the important role of the mesoporous structure in water retention. The higher and broader dehydration peak of the HPW-meso-silica nanocomposites with 3D symmetries demonstrate that the more complicated and connected three-dimensional mesoporous frameworks is beneficial for the retention of water particularly at high temperatures. The weight loss of HPW-$Fm\bar{3}m$, HPW-$Im\bar{3}m$ and HPW-$Ia\bar{3}d$ is in the range of 5.3 to 6.6%, also considerably higher than that of pure *meso*-silica.

6.3.2. Proton conductivity and cell performance

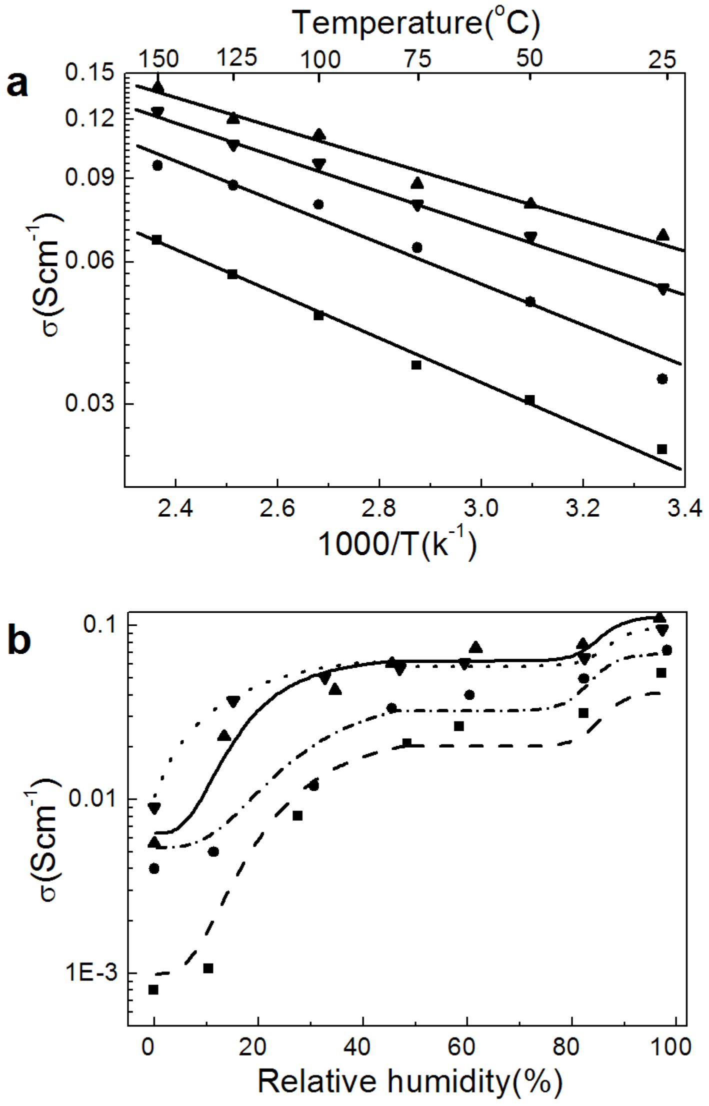

Figure 6.5 a) Conductivity as a function of (inverse) test temperature; b) conductivity as a function of RH measured at 80 °C. Triangles, HPW-$Ia\bar{3}d$; Inverted triangles, HPW-$Im\bar{3}m$;

circles, HPW-$Fm\bar{3}m$ and squares, HPW-$P6mm$. The content of HPW in the HPW-meso-silica nanocomposites was 67 %HPW.

Figure 6.5a shows the proton conductivity for the HPW-*meso*-silica nanocomposites measured at different temperatures under 100% RH. The conductivity ranged from 0.02 to 0.140 S cm^{-1} for the HPW-*meso*-silica nanocomposite membranes and the significant differences in conductivity in the temperature ranges used can be attributed to the differences in the morphology and structural symmetries of the *meso*-silica hosts. Among the HPW-meso-silica nanocomposites, the highest proton conductivity was obtained on the HPW-meso-silica nanocomposite with $Im\bar{3}m$ symmetry, HPW-$Im\bar{3}m$ which was 0.140 S cm^{-1} at 150 ^{o}C and 0.068 S cm^{-1} at 25 ^{o}C, respectively. In the case of HPW-$Ia\bar{3}d$, HPW-$Fm\bar{3}m$ and HPW-*p6mm* nanocomposites, the conductivity values are 0.111, 0.084 and 0.059 S cm^{-1}, respectively. The HPW-*meso*-silica with a 2D symmetry of *p6mm* has the lowest proton conductivity. The activation energy for the proton conductivity also depends on the structural symmetries of the *meso*-silica. The activation energy, E_a, of the membranes was calculated by linear regression of Arrhenius plots in the temperature range of 25-150 ℃. E_a is 10.0 kJ mol^{-1} for the proton conduction on the HPW-$Im\bar{3}m$ nanocomposite membrane, 11.2 kJ mol^{-1} on HPW-$Ia\bar{3}d$, 13.5 kJ mol^{-1} on HPW-$Fm\bar{3}m$ and 14.5 kJ mol^{-1} for HPW-*p6mm*. The lowest E_a value was obtained on the nanocomposite with 3D symmetry of $Im\bar{3}m$ and the highest E_a was obtained on the nancomposites with 2D symmetry of *p6mm*. Nevertheless, the activation energy of HPW-*meso*-silica nanocomposite membranes is compatible with the value of ~13 kJ mol^{-1} for the Nafion membranes.(Lu et al., 2011) The high conductivity and low activation energies suggest the presence of continuous proton transport pathways through Keggin-type HPW nanoparticles/clusters in the ordered mesoporous silica framework. Sayler et al. (Sayler et al., 2010) studied the electrical conductivity and pore interconnectivity of mesoporous silica monoliths as a function of RH value and reported that the conductivity of mesoporous silica monolith largely depends on its pore size and mesopore interconnectivity throughout the monoliths. The interconnectivity of the mesopores is essential for the high conductivity. Thus, the high interconnectivity of mesoporous silica hosts with 3D structural symmetries such as $Im\bar{3}m$, $Fm\bar{3}m$ and $Ia\bar{3}d$ is beneficial for the proton migration and conductance via Keggin unit of HPW, as shown in the present study.

Figure 6.5b is the proton conductivities of HPW-*meso*-silica nanocomposite membranes with different structural symmetries measured at 80 ^{o}C as a function of RH. The conductivity values of the composite membranes increases rather rapidly initially, and then stabilizes in the RH range of 20-80%, followed by another small rise as RH goes beyond 90%. The initially rapid rise in the conductivity comes from the change in the hydration state of HPW as the conductivity of HPW is strongly dependent on the number of molecular water contained in hydrated HPW (noted as $H_3PW_{12}O_{40}\cdot nH_2O$, n=4~29). The dependence of the conductivity on RH indicates that the proton conductivity of HPW-*meso*-silica nanocomposites also requires the presence of water. However, being very different from the perfluorosulfonic acid membranes such as Nafion, the proton conductivity of HPW-*meso*-silica nanocomposites shows a much less sensitivity toward RH. Most interestingly, for the HPW-*meso*-silica nanocomposites with $Im\bar{3}m$ and $Ia\bar{3}d$ symmetries, the proton conductivity remains more or less the same in the RH range of 20-80%. The high tolerance of proton conductivity toward the RH change is an important property of PEMs for a stable operation of fuel cells. In the case of Nafion membranes, the proton conductivity decreases dramatically with the decrease in RH.(Ye et al., 2010, Yan et al., 2009) For example, in the case of Nafion115 membranes, the conductivity is 0.1 S cm^{-1} at $30^{o}C$ and 100%RH and drops to 0.0046 S cm^{-1} as RH decreases to 40%. (Zeng et al., 2011b)The high stability of proton conductivity of HPW-*meso*-silica nanocomposites with $Im\bar{3}m$ and $Ia\bar{3}d$ 3D symmetries indicates that highly interconnected mesoporous networks promote the water retention ability of the mesoporous silica, which is consistent with the TGA results. Moreover, the dependence of relative humidity on the conductivity of HPW-*meso*-silica membranes showed in Figure 6.5b gives further insight into the pore interconnectivity and water retention properties of HPW-*meso*-silica. As pointed out by Sayler et al. (Sayler et al., 2010) for a given RH, the better the overall interconnectivity of mesopores, the higher the conductivity expected. The high conductivity of HPW-meso-silica with 3D mesostructures demonstrates the high pore interconnectivity 3D mesostructure symmetries as compared to a 2D mesostructure symmetry. As RH rises, an unobstructed path for proton migration is established between the impregnated HPW nanopartilces inside the mesochannels and this is indicated by the significant increase of the proton conductivity as the RH increases from 0% to 20-40% (Figure 6.5b). The rather stable conductivity particularly for HPW-*meso*-silica with $Im\bar{3}m$ and $Ia\bar{3}d$ 3D symmetries in the RH range of 20-80% clearly shows the extraordinarily high water retention capability of the HPW-$Im\bar{3}m$ and HPW-$Ia\bar{3}d$ nanocomposites. The high water retention capability is clearly due to the combination of high interconnectivity of cubic 3D mesostructures and the high proton conductivity of HPW nanoparticles along the mesochannels. The contents as presented in Chapter 4 and Chapter 5 have addressed the influence of the pore size of meso-silica framework on the membrane conductivity, by reducing the pore size of mesoporous silica host from 12.1 nm to 5.0 nm, the conductivity of mesoporouss silica/HPW composite membrane was enhanced from 4.9×10^{-2} S cm^{-1} to 6.8×10^{-2} S cm^{-1} at room temperature. (Zeng et al., 2011a) The similar tendency was also reported by Munakata et al., (Munakata et al., 2007): the proton conductivity of macroporous silica/AMPS composite membrane was improved from 1×10^{-2} S cm^{-1} to 2.6×10^{-2} S cm^{-1} when silica host with smaller pore size was used.

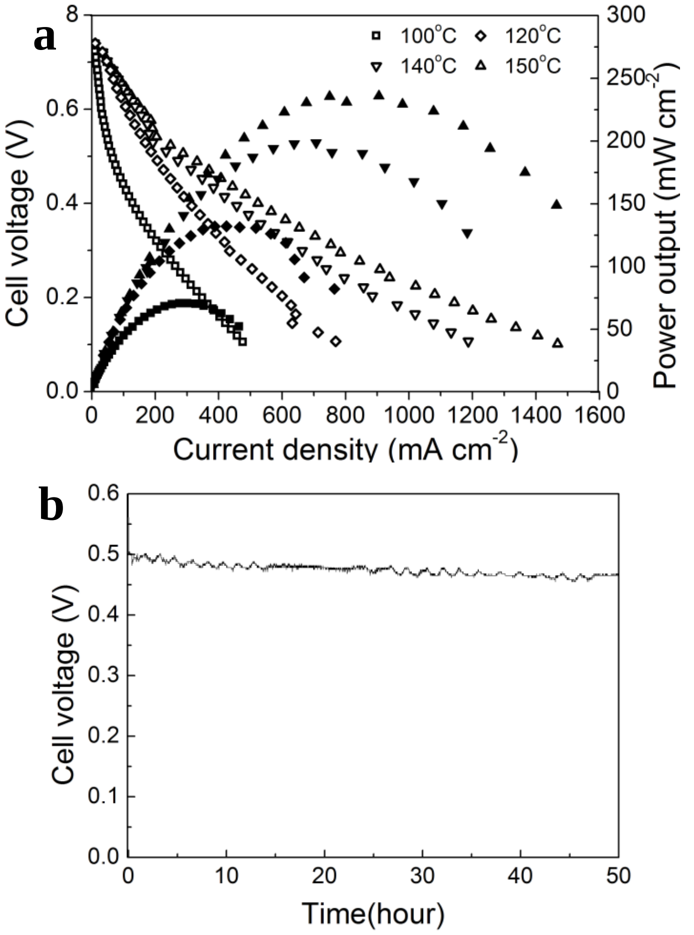

Figure 6.6 a)Polarization and power density of single cell employing a meso-silica/PA membrane in methanol/O_2 at 100-150 ℃; b) Evolution of the cell voltage during the durability test (the single cell polarized at 200 mA cm^{-2}, T=150 ℃, methanol/O_2=1 atm/1 atm)

The applicability of the HPW-*meso*-silica nanocomposite membranes was demonstrated in DMFC with one of the best performed HPW-meso-silica membranes (HPW-$Ia\bar{3}d$). The membrane thickness was ~0.5 mm. Figure 6.6 shows the cell performance and the corresponding methanol crossover current measured at different temperatures. From Figure 6.6a it is kown that the cell performance for methanol increases significantly as the temperature increases. The increase in the performance with temperature can be explained in terms of the enhancement of the electrode kinetics and the decrease in the membrane resistance. This is also reflected in the power output curves (solid symbols). The maximum power density is 71.1 mW cm^{-2} at 100 ℃, 132.3 mW cm^{-2} at 120 ℃, 199.5 mW cm^{-2} at 140 ℃, and 236.4 mW cm^{-2} at 150 ℃. It is well known that the proton conductivity of HPW alone is a strong function of number of molecular water contained in hydrated HPW. The proton conductivity of fully hydrated HPW is 0.18 Scm^{-1}.(Nakamura et al., 1979) In the case of $H_3PW_{12}O_{40}$•$11H_2O$ (this may be the states of pure HPW in the temperature range of 120-200 ^oC, see TGA results in Figure 6.4), the proton conductivity is 0.0013 Scm^{-1},(Ukshe et al., 1989) two orders of magnitudes lower than that under the fully hydrated state. The increased power output with the increased temperature indicates that the high proton conductivity of HPW-meso-silica nanocomposites is maintained at high temperatures, most likely due to the high water retention ability of HPW in the mesoporous silica.

6.3.3 The on/off durability test on DMFC

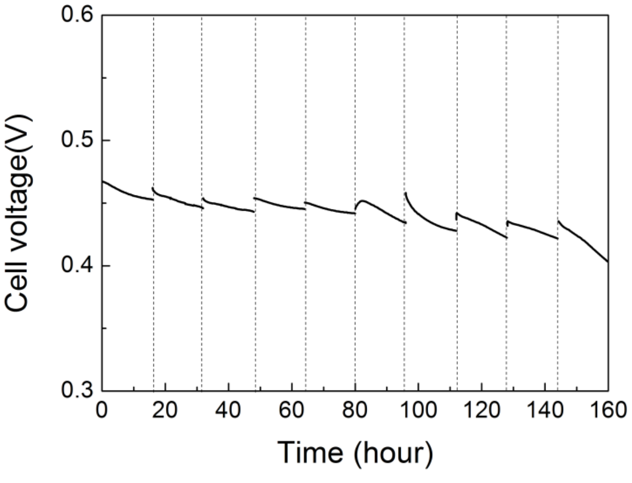

Figure 6.7 Evolution of the cell voltage during the intermittent durability test (10 days for 16h

at 200 mA cm^{-2}; T=80 ℃; methanol/O_2=1 atm/1 atm), only running hours are shown. Dashed lines indicate the overnight break.

The stability is of key importance in fuel cell operation. Because the HPW is water soluble, the HPW-meso-silica membrane can only be used in a vapor-fed system, such as a PEMFC or a DMFC operated at >100 ℃, to avoid the washing out of HPW by the liquid fuel. Even in a PEMFC system, the condensation of vapor water in the cell is also detrimental to the HPW-meso-silica membrane based fuel cell performance. In order to measure the detrimental effect of condensed water, a durability test was performed intermittently on the cell for 16 h daily during 10 days and the results are shown in Figure 6.7. The experiments were carried out with methanol/O_2 at 80 ℃ without humidity or pressure control during the test. The applied load was 200 mA cm^{-2}. Prior to the daily measurement, a short time around 10 min was allowed to elapse for a stable potential value to be reached. From Figure 6.7, it can be seen how the cell performance is rather stable over the 10 days. If we compare the curves obtained for each day, we can see that they follow a similar pattern. There is an initial recovery in the cell voltage at the beginning of each daily test, followed by a steady polarization in the subsequent time. The cell voltage profile observed at each day can be explained as follows. The protocol for this experiment stipulated that the cell should be stopped overnight. As the temperature of the whole system decreased to ambient temperature, the condensed water from the remaining vapor in the cell ‘flood’ the catalyst layers and the HPW-meso-silica membrane, causing two effects: The catalyst layer, which was formed from the catalyst itself and a certain amount of electrolyte to provide a pathway for the protons, was re-hydrated and resulted in an increase in its conductivity, and, as a consequence, the catalyst activity was enhanced. On the other hand, the condensed water was absorbed by the HPW-meos-silica membrane and caused leaching of HPW, leading to a decrease in the membrane conductivity, which explains the increase in the decay rate of cell performance in the last day of test. In any case, as mentioned above, the most outstanding feature is that, during those 10 days of operation, the cell voltage did not decrease significantly, indicating that the cell (including all of its elements such as the catalyst, HPW-meso-silica membrane, and gas diffusion support) behavior was relatively stable.

6.4 Summary

In summary, we have successfully prepared the novel inorganic proton exchange membranes (PEMs) based on HPW-functionalized *meso*-silica nanocomposites with 2D symmetry of *p6mm* and 3D symmetries of $Fm\bar{3}m$, $Im\bar{3}m$ and $Ia\bar{3}d$. The HPW loading is set to be 80 wt% according to the optimization work done in Chapter 4. The HPW-meso-silica nanocomposites with 3D mesostructures showed high proton conductivity and high stability as a function of RH, as compared to that with a 2D mesostructure. The best results were obtained on HPW-*meso*-silica with body-centered cubic ($Im\bar{3}m$) and cubic bicontinuous $Ia\bar{3}d$. HPW- $Im\bar{3}m$ nanocomposites achieved a high proton conductivity of 0.061 and 0.140 S cm^{-1} at 25 and 150 ^{o}C, respectively, with activation energy of 10.0 kJ mol^{-1}. The HPW-functionalized 3D mesoporous silica framework with well ordered and connected mesoporous structures shows high proton conductivity at elevated high temperatures and low humidity environment. The good performance of the DMFCs with HPW-*meso*-silica nanocomposite membranes in the present study demonstrates that inorganic proton exchange membranes with high proton conductivity can be realized in the HPW-*meso*-silica nanocomposites with 3D mesostructures. The DMFC equipped with a HPW-*meso*-silica nanocomposite membrane produced a steady power output of 94 mW at 150 ℃ for 50h without humidification control at the cathode side.

CHAPTER 7. Various Heteropoly Acids Functionalized Silica Nanocomposites as Proton Conductors

In this chapter, HPA-meso-silica nanocomposites based on various types of heteropoly acids as functional reagents were sudied in terms of thermal stability, wettability and proton codncutivity. The influence of temperature and the methanol concentration on the methanol crossover, open circuit voltage (OCV) and cell performance also carefully investigated in order to optimize the fuel cell operational conditions.

7.1 Introduction

It has been well known that heteropolyacid (HPA) is superionic conductor in their fully hydrated states.(Kozhevnikov, 1998, Misono, 1987) HPAs are solid crystalline materials with a polyoxometalate inorganic cage structures, which may adopt the Keggin form with general formula $H_3MX_{12}O_{40}$, where typically M = P or Si, and X = W or Mo. The highest stability and strongest acidity is observed for phosphotungstic acid ($H_3PW_{12}O_{40}$, abbreviated as HPW or PWA). Because of their high acidity, stability and high proton conductivity, HPA and HPA mixed or embedded with silica supports have been extensively studied as acid and redox catalysts in homogeneous and heterogeneous reactions.(Garcia et al., 2007, Kim et al., 2006, Blasco et al., 1998, Micek-Ilnicka, 2009, Wee et al., 2010, Zhu and Yang, 2009, Kumar et al., 2006) HPA is also used as additives to promote the electrocatalytic activities of electrocatalysts for methanol oxidation reaction(Cui et al., 2010, Kulesza et al., 2004, Barczuk et al., 2006) and oxygen reduction.(Wlodarczyk et al., 2006, Wlodarczyk et al., 2007, Wang et al., 2010, Stanis et al., 2008) However, the application of HPAs as proton exchange membranes in fuel cells is limited due to the sensitivity of their conductivity to the relative humidity of the surrounding environment in addition to their solubility in water. The risk of the leakage of HPAs during cell operation is thus high. Various attempts have been made to immobilize the HPAs in silica gel, (Tatsumisago et al., 1994, Rao et al., 2005, Rao et al., 2004) ammonium salt,(Mikhailenko et al., 1997) P_2O_5-SiO_2 glasses (Uma and Nogami, 2007d, Uma and Nogami, 2008c), to form HPW composite with room temperature ionic liquid,(Li et al., 2006) and to form hybrid organic/inorganic membranes.(Yamada and Honma, 2006, Staiti et al., 2001, Celso et al., 2009, Cui et al., 2009, Oh et al., 2010) Lakshminarayana and Nogami mixed phosphotungstic acid (HPW) and phosphomolybdic acid (HPMo) with 3-glycidoxypropyltrimethoxysilane (GPTMS), 3-aminopropyltriethoxysilane (APTES), phosphoric acid, and tetraethoxysilane (TEOS) by a sol-gel process and reported a proton conductivity of 3×10^{-2} Scm^{-1} with a composition of 50TEOS-25GPTMS-20H_3PO_4-5APTES-3HPMo-6HPW at 120^{o}C under 90% RH. (Lakshminarayana and Nogami, 2009) Sweikart et al mechanically mixed HPW and commercially available high temperature epoxy (Duralco 4538N) and reported a conductivity of $6x10^{-5}$ Scm^{-1} at 165^{o}C without humidification for a HPW-doped sulfonated epoxy.(Sweikart et al., 2005) The conductivity of mixed HPW/epoxy hybrid membranes is too low for practical fuel cell applications. Tan et al synthesized composite membranes containing sulfonated poly(arylene ether sulfone (SPSU), benzimidazole derivatives (BIzD) and HPW.(Tan et al., 2005) Adding BIzD helps to retain HPW particles and good conductivity was reported for the SPSU-BIzD-HPW hybrid membranes (0.084-0.159 Scm^{-1}) at 110°C under fully hydrated conditions. High proton conductivity and excellent cell performance of 510 $mWcm^{-2}$ at 120°C was also reported on Nafion-HPW/meso-silica hybrid membranes.(Yan et al., 2009) However high swelling ratios associated with polymeric materials are detrimental to structural stability of the membranes.

7.2 Experimental

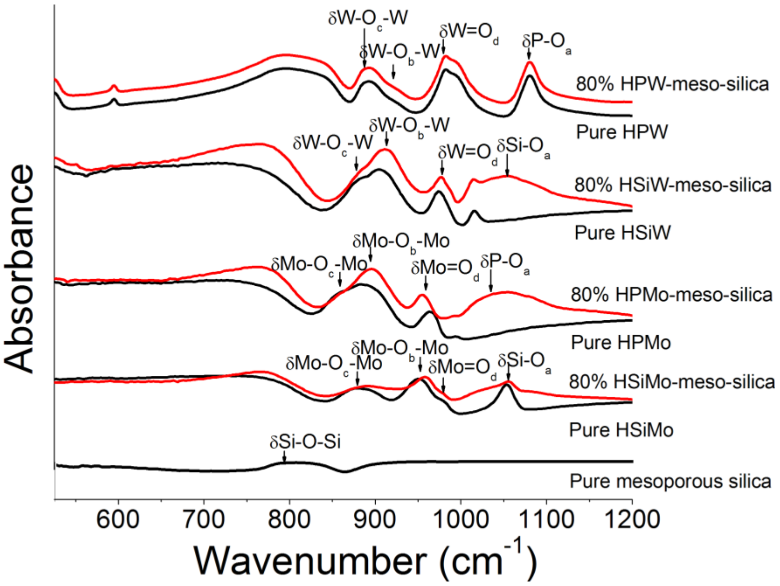

Figure 7.1 FTIR spectra of mesoporous silica, 4 types of HPAs (HPW, HSiW, HPMo and HSiMo) and the coresponding 80% HPA-meso-silica nanocomposites measured at room temperature.

The FTIR spectra of pure HPAs, meso-silica and 80%HPA-meso-silica nanocomposites are presented in Figure 7.1. A weak, broad band at 801 cm^{-1} is observed, which is the characteristic of the vibrations of Si-O-Si. (Liang et al., 2006) HPAs in the dehydrated state or in polar solvents produces stable Keggin type anions such as $AB_{12}O_{40}^{3-}$(A=P or Si; B=W or Mo), which is neutralized by three protons in water. This structure is formed by a central atom of phosphorous tetrahedrically linked to oxygen atoms surrounded by seven other oxygen atoms linked to a tungsten atom. (Yang et al., 2005b) When hydrated water molecules are present in HPW, the terminal oxygen atoms of the Keggin anions are associated with $H_5O_2^+$, generating a secondary structure with characteristic peaks in the FTIR spectra. (Kim et al., 2003) Taking the HPW as an example, characteristic bands are observed at 1053 cm^{-1} for P-O_a, 951 cm^{-1} for W=O_d, 911 cm^{-1} for W-O_b-W and 871 cm^{-1} for W-O_c-W, which are close to that reported in the literature. (Rocchiccioli-Deltcheff et al., 1983) The appearance of the characteristic peaks in the FTIR spectra of HPW-meso-silica nanocomposites indicates that the Keggin type anions, $P_4W_{12}O_{40}^{3-}$ remains in the nanocomposite structure; besides, the peaks in the range of 800-100 cm^{-1} are partially overlapped by the δ(Si-O-Si) stretching as well as the OH bending of O_3Si-H group from the mesoporous silica framework. Dias et al studied HPW-impregnated mesoporous silica by the ^{31}P solid state NMR and observed the chemical shift of the ^{31}P NMR peak from 15.5 ppm for pure HPW to 15.0 ppm for the HPW-impregnated meso-silica.(Dias et al., 2006) The chemical shift in the ^{31}P NMR spectra has been attributed to the formation of $(\equiv SiOH_2^+)(H_2PW_{12}O_{40}^-)$ species.(Lefebvre, 1992) The increased intensity of the new peak at ~1011 cm^{-1} with increase of the HPW content may be associated with the formation of $(\equiv SiOH_2^+)(H_2PW_{12}O_{40}^-)$ species.

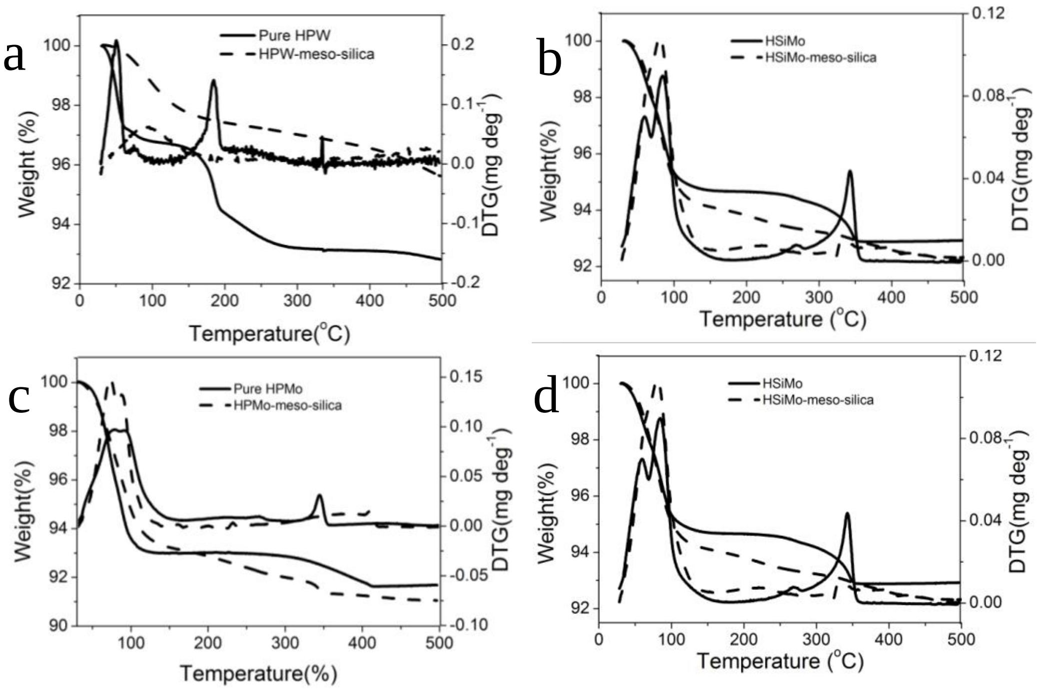

Figure 7.2 TGA spectra of 4 types of HPAs [(a)HPW, (b) HSiW, (c) HPMo, and (d) HSiMo], meso-silica and the coresponding 80%HPA-meso-silica nnaocomposites

Figure 7.2 shows the TG thermograms of 4 types of pure HPAs, mesoporous silica and HPA-meso-silica measured in the temperature range of 30-500 ^{o}C. The TGA curves of pure HPW and HSiW exhibits two weight loss steps at temperatures around 50 and 186 ^{o}C, which is in agreement with the literature. (Sweikart et al., 2005, Yamada and Honma, 2006) The first weight loss between room temperature and 70 ^{o}C can be attributed to the loss of physically absorbed water while the second one between 160 and 200 ^{o}C can be assigned to the release of structural water from HPW hydrate. The weight loss of HPW at 200 ^{o}C was 14.6%. The retention of water molecules by the Keggion-type HPW structure at elevated high temperatures indicates the possibility of proton conductivity at high temperatures. On the other hand, the $Ia\bar{3}d$ meso-silica shows only one weight loss step at ~65 ^{o}C and the weight loss is ~1.0% at 200 ^{o}C, much lower than 14.6 % of pure HPW. The very low weight loss of the meso-silica shows that the water retention capability of pure meso-silica is low despite its high pore volume (see sections below). The thermal behavior of HPW-meso-silica nanocomposite is significantly different from that of pure HPW. For example, in the case of 80%HPW-meso-silica nanocomposite, in the temperature range of 30-500 ^{o}C the dehydration peak of structural water of pure HPW at 186^{o}C disappears and the weight loss at 200℃ is 7.2% for 80 wt% HPW-meso-silica, which is lower than 14.6% observed for pure HPW, but significantly higher than 1% for pure meso-silica. The disappearance of the dehydration peak at high temperatures suggests that the homogeneous distribution of HPW in the mesoporous silica host changes the behavior of adsorbed water molecules in the HPW Keggin structure and enhances the stability of water in the HPW-meso-silica system.

7.3.2 Membrane wettability and conductivity

Figure 7.3 Water contact angle on the surface of Nafion 117, HPW-meso-silica, HSiW-meso-silica, HPMo-meso-silica and HSiMo-meso-silica membrane

Table 7.1 Water contact angle, water uptake and swelling ratio for several membranes of Nafion 117 membrane and 4 types of HPA-meso-silica membranes

Various proton conductive membrane	Contact angle degree (left)	Contact angle degree (right)	Contact angle degree (mean)	Water uptake (wt %)	Swelling ratio in thickness (%)

Nafion 117	57.81	52.54	54.62	30±2.0	18
Meso-silica				28.2	Neglectable
PBI/Phosphoric acid				30-140*	50-700*
HPW-meso-silica	43.66	33.34	40.05	26.6±1.8	Neglectable
HSiW-meso-silica	54.10	51.34	52.72	20.4±1.2	Neglectable
HPMo-meso-silica	44.74	44.76	44.75	30.6±2.3	Neglectable
HSiMo-meso-silica	54.84	57.25	56.05	24.2±1.4	Neglectable

*this value cited from reference (Kumbharkar et al., 2009)

The HPA-meso-silica discs have a diameter of 3.8 cm and thickness of around 500 µm. In order to study the wettability of HPA-meso-silica memrbrane, the water contact angles were measured and given in Fig.7.3. The Nafion 117 membrane, which is noted as a typical hydrophilic material, was also measured for comparion. The incorporation of heteropoly acid into the interior pore walls of mesoporous silica results in more -OH groups grafted on the silica surface, leading to an imroved wettability, which is also confirmed by the FTIR and Raman scattering as presented in Chapter 1. After functionalization by the strong acidic HPAs, the water contact angles observed from the surface of HPA-meso-silica are very close to or even smaller that the value of Nafion 117 membrane, suggesting that both the inner and outside surface of the mesoporous framework become more hydrophilic.

The water uptake and the water swollen ratio for various proton exchange membranes are also shown in Table 7.1. The structure of Nafion membrane has interconnected hydrophilic domains that make it quite permeable to water and methanol. The swelling ratio of Nafion membrane in water is measured to be ~18%; a more detrimental factor is the proton movement, which occurs by the so-called "vehicle mechanism", which involves the protons travelling along the membrane with water moleculars with electro-osmotic drag coefficient of 2-3. As a consequence, in a Nafion-based DMFC, unacceptable amounts of methanol penetrate through the membrane from the anode to the cathode. The PBI/phosphoric acid membrane also suffers from a swollen problem in phosphoric acid, which lead to degradation in the membrane's mechanical stability. The measurement carried out by Kumbharkar et al. indicated that the swelling ratio in volume reached up to 200-700% as acid loading kept increasing to 20 mol per repeat unit. (Kumbharkar et al., 2009)

On ther other hand, the HPA-meso-silica families also show high water uptake in comparison with the Nafion 117 membrane, which may benefit the proton conductance by reducing the activation energy requited for proton "hoping" from one conductive site to another. Most importantly, the HPA-meso-silica families are immune to water swollen problem faced by the Nafion 117 and PBI/phosphoric acid membrane. No dimentional change in membrane size or membrane thickness can be dectected during the measurement, and this unique peroperty can be attributed to the dimension-stable mesoporou silica host materials.

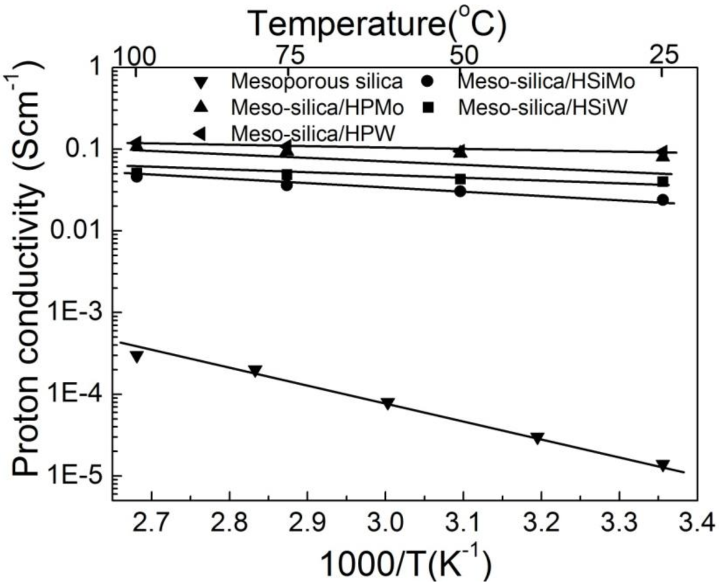

Figure 7.4 Arrhenius plots of (▼) pristine meso-silica, (●) 80%HSiMo-meso-silica, (▲) 80%HPMo-meso-silica (■) 80%HSiW-meso-silica and (◀)80%HPW-meso-silica, measured under 90 %RH.

Figure 7.4 shows the plots of the conductivity versus temperature for pristine meso-silica heat-treated at 60 °C and HPW-meso-silica treated at different hydrothermal temperatures. The proton conductivity of meso-silica heat-treated at different temperatures is similar, ~3×10^{-4} S cm^{-1} at 90 °C and 100% RH and the activation energy of the conductivity is ~47 kJ mol^{-1}, very close to the results reported in the literature.(Li and Nogami, 2002b) On the other hand, the proton conductivity of $Ia\bar{3}d$ structured silica increases significantly after functionalization with 80 wt% HPAs. Taking the HPW-meso-silica membrane as an example, the conductivity of 80%HPW-meso-silica is 0.14 S cm^{-1} at 100 °C and 90% RH, which is close to 0.18 S cm^{-1} of fully hydrated HPW.(Osamu Nakamura et al., 1979) The activation energy of 80%HPW-meso-silica is 13.5 kJ mol^{-1}, and in the case of 80%HSiW-meso-silica, 80%HPMo-meso-silica and 80%HSiMo-meso-silica, the coresponding activation energies are 14.8 kJ mol^{-1}, 15.6 kJ mol^{-1} and 15.8 kJ mol^{-1}, respectively; which are all much smaller than that of the pristine meso-silica.

7.3.3 Influence of temperature on direct methanol fuel cell peroformance

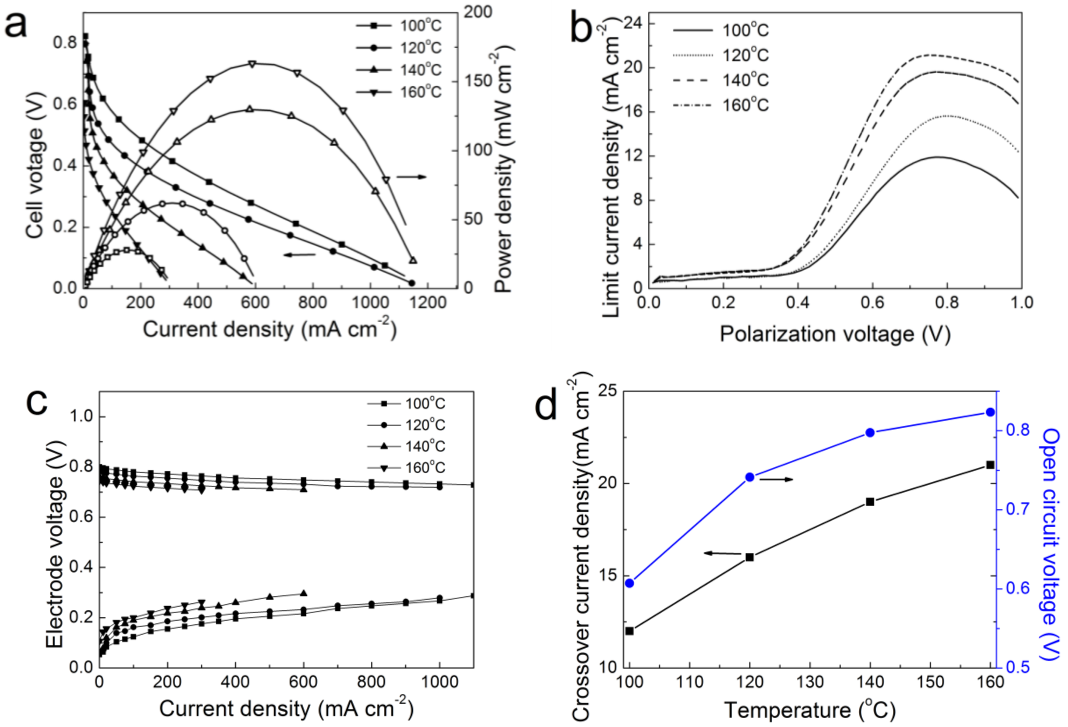

Figure 7.5 Influence of temperatures on (a) cell performance (b) methanol limit current density (c) electrode overvoltage and (d) open circuit voltage and methanol crossover current of a vapor-fed meso-silica/HPW membrane based DMFC

To demonstrate the applicability of the HPW-meso-silica membrane in DMFC, a single cell was assembled with a HPW-meso-silica membrane with a thickness of about 0.5 mm. The open circuit voltage (OCV) of the cell was 0.82 V at 160 ℃, slightly higher than that of DMFC assembled with a Nafion 117 membrane at 80 ℃. (Wu et al., 2010) The influence of the operational temperature (100-160 ℃) on the cell performance was shown in Figure 7.5a; the corresponding crossover current and electrode potential measured were also shown in Figure 7.5b and Figure 7.5c, respectively. The variation of the OCV and crossover currents in this temperature range is shown in Figure 7.5d. The cell was operated with pure oxygen at atmospheric pressure. The methanol concentration in its water solution was 6.0 M. In Figure 6a it is known that an increase in the cell performance occurs as the temperature increases. The ohmic polarization regions of the polarization curves (filled symbols), which is also considered to be the operation regions of fuel cells, are 50-275 mA cm^{-2} at 100 ℃, 150-575 mA cm^{-2} at 120 ℃, 200-1100 mA cm^{-2} at 140 ℃, and 150-1100 mA cm^{-2} at 160 ℃, respectively. The increase in the performance with temperature can be explained in terms of the enhancement of the electrode kinetics and the decrease in the membrane resistance. This is also reflected in the power output curves (empty symbols). Power peaks are 28.2 mW cm^{-2} at 100 ℃, 61.9 mW cm^{-2} at 120 ℃, 130.0 mW cm^{-2} at 140 ℃, and 163.2 mW cm^{-2} at 160 ℃.

The change in the methanol crossover current is shown in Figure 7.5b. The methanol from the anode side penetrated through the membrane was directly oxidized in the cathode compartment, and brought two negative effects: lowering the cathodic potential and wasting a proportion of the fuel. The crossover current is 12-21 mA cm^{-2} in the temperature range of 100-160 ℃, which is relatively lower comparing with the perfluorinated systems. Using Nafion117 (178 μm in thickness) membrane as an example, a crossover current of 70 mA cm^{-2} is measured with 1M methanol at ambient temperature (Jiang et al., 2006b) and another crossover current of 277 mA cm^{-2} is measured at 80 ℃ in 2M methanol.(Ren et al., 2000) The much lower methanol crossover current on the HPW-meso-silica membrane could also be related to the gas phase diffusion of methanol and the much thicker HPW-meso-silica membranes

(~500 µm in this case). Another reason is that the the mesopores or channels of HPW-meso-silica nanocomposites do not swell with the water content or humidity like in the case of Nafion membranes. (Tazi and Savadogo, 2000, Randov et al., 2008, Gebel et al., 1993, Divisek et al., 1998) The process occurring in the system is represented in Figure 7.5c. Both the anode and cathode performances increase with temperature, which can be attributed to the improved kinetics of the methanol oxidation and oxygen reduction processes. In the previous study as reported(Zawodzinski Jr et al., 1993) the open circuit voltage is used as an indirect measurement of the methanol crossover effects. The change in the methanol crossover current and OCV is shown in Figure 7.5d. It can be seen that the OCV was enhanced as the temperature increases, thus confirming the less detrimental effects of methanol crossover at the highest temperatures. Despite the increase in methanol crossover from anode side, significant enhancement can also be observed for the cathode potential as higher temperature was applied; except the kinetic improvement reason as mentioned above, this also suggested a higher tolerance of the Pt/C catalyst to the catalyst poisoning effect of methanol following the rise of temperature.

7.3.4 Influence of methanol concentration on cell performance.

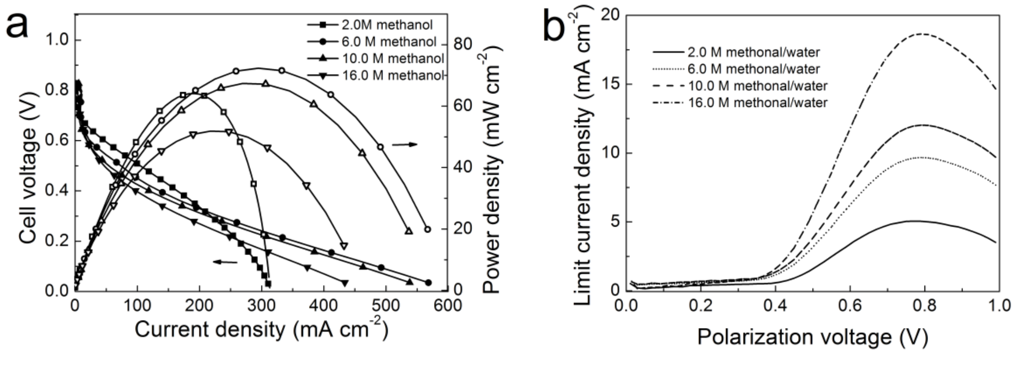

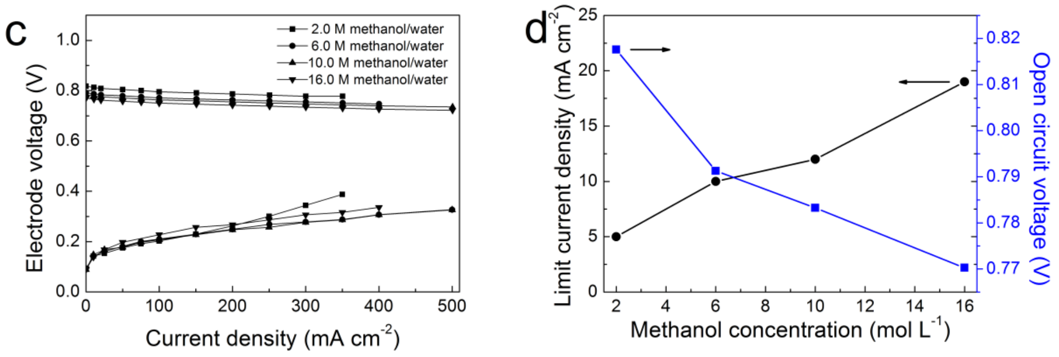

Figure 7.6 Influence of methanol concentration on (a) cell performance (b) methanol limit current density (c) electrode overvoltage and (d) open circuit voltage and methanol crossover current of a vapor-fed HPW-meso-silica membrane based DMFC

The influence of the methanol concentration on the cell voltage and the power output (a), methanol crossover current (b), potentials of anode and cathode (c) are shown in Figure 7.6. The methanol/water solutions with methanol concentration of 6-16 M were used as fuel feeding to anode side and the fuel cell was run at 120 ℃. The variation of the OCV and crossover currents with the various methanol concentrations is shown in Figure 7.6d. The polarization curves in Figure 7.6a (filled symbols) of various methanol concentrations are measured, especially at low and high current densities, and showed in Figure 7.6a. At low current density, which is the region of activation polarization where the kinetics of the electrochemical processes governs the performance, the cell shows a better performance with larger amounts of water. Higher water availability increases the tendency to form OH species, which is crucial for complete methanol oxidation, and leads to faster reaction speed. At high current density, where the mass-transfer processes dominate the performance, the best performance is achieved at the methanol concentration of 6M. A lower methanol concentration reduces the cell performance in this region, probably because of the reduced availability of methanol. On the other hand, the higher methanol concentration of 10M and 16M give rise to worse performance. An increase in the methanol vapor pressure leads to an increase in the methanol crossover (see Figure 7.6b). Besides, a proportion of the methanol feed is not completely oxidized as the concentration of methanol exceeds 20M (methanol/water molar ratio of 0.5) as reported by Lin et al. (Lin et al., 1997), which brings down the efficiency of the system and the cell performance overall. Moreover, low water content causes drop in the membrane conductivity, which also accounts for the drop in cell performance. The power output curves in Figure 7.6a (empty symbols) showed the peak power density of 64.0 mW cm^{-2} for 2M methanol, 72.3 mW cm^{-2} for 6M methanol, 67.6 mW cm^{-2} for 10M methanol and 51.8 mW cm^{-2} for 16M methanol; this suggests that 6M methanol an optimized concentration for fuel cell operation. The cell performance is less influenced by methanol concentration than by operational temperature.

The potential of each electrode is shown in Figure 7.6b, and this helps us to understand the cell performance further. High water content is beneficial for the anodic reaction, except at high current density, where a large amount of methanol is required. This explains the significant increase in potential with 2M methanol. A high methanol concentration also impairs the anodic performance by the low water availability, and reduces the efficiency of the methanol oxidation and the electrolyte conductivity. In the case of the cathode, there is a steady increase in performance as the methanol concentration decreases. The drop in the methanol crossover accounts for this change. Nevertheless, despite the improvements in the cathode performance, the overall performance decays at low methanol/water ratio, thus demonstrating the significant influence of the anodic process on the overall cell performance. The changes in the OCV and in the methanol crossover currents are represented in Figure 7.6d. A decrease in the OCV is observed as the methanol concentration increases, which can be attribute to the higher methanol permeation rate. The crossover current increases with the methanol concentration, as expected from the higher methanol partial pressure in the anode compartment.

7.4 Summary

In summary, we have successfully prepared novel inorganic proton conductors based on mesoporous silica host materials functionalized by heteropoly acids including HPW, HSiW, HPMo and HSiMo. The HPW, HSiW can form more stable nanocomposites with meso-silica host materials which leads to higher thermal stability and proton conductivity for the HPA-meso-silica membranes. Additionally, the HPA-meso-silica membranes show considerable high water uptake in comparion with the commercial Nafion membrane as well as the PBI/Phosphoric membrane, but are free of water swollen caused by high water uptake as Nafion 117 and PBI/Phosphoric membranes. The DMFC performance using a HPW-*meso*-silica nanocomposite membrane was that the power output incrased as operational temperature was raised from 100 to 160 ℃ despite slight increased in the methanol crossover rate. Further analysis indicated that the methanol crossover rate increase when the higher concentration of methanol was used and the best cell performance was achieved with a 6M methanol/water fuel at 120 ℃.

CHAPTER 8. CONCLUSIONS

This object of this projet is to develop novel proton-exchange-membranes based on heteropolyacid functionalized mesoporous silica composite materials that can be operated at elevated high temperature and low humidity conditions. The experimental findings and fundamental understandings obtained through this study are summarized in this chapter.

8.1 Conclusions

1. A hydrothermal method was developed to synthesize silica powders with well ordered mesoporous structure as matrix materials. The synthesis process were studied in details. Structural symmetries of mesoporous silica can be altered by changing the surfactants used during the hydrothermal synthesis process; the pore size of mesoporous silica can also be effectively controlled by carefully controlling the heat treatment temperature or heat treatment time. Mesoporous silica matrix material with tailored structural properties, i.e. surface area, pore volume, pore symmetries and pore sizes were successfully synthesized.
2. Mesoporous silica with interconnected pore structure as well as large pore volume was used for heteropoly acid impregnation. The threshold for proton conductivity for the HPW-meso-silica nanocomposite is ~10 wt% of HPW. The best proton conductivity is 0.07 Scm^{-1} at 25 ^{o}C under 100 %RH with activation energy of ~13.5 kJ mol^{-1}, obtained on 67-83% HPW-meso-silica nanocomposites. The impregnation of heteropoly acids into the pore structure of mesoporous

silica leads to protonation of its surface silicon dioxide molecules; the interaction between the Keggin anions of HPW and meso-silica has been confirmed by the formation of $(\equiv SiOH_2^+)(H_2P_4W_{12}O_{40}^-)$ species. The proton conductivity and performance of HPW-meso-silica nanocomposites also increase with the RH, but it is far less sensitive to RH changes as compared to conventional perfluorosulfonic acid (PFSA) polymers such as Nafion. These properties make HPW-meso-silica nanocomposite a promising proton conductor.

3. The relationship among the proton conductivity, thermal stability and structural symmetries of HPW-functionalized mesoporous silica membrane was investigated with different mesostructures of HPW-meso-silica. The HPW-meso-silica nanocomposites with 3D mesostructures show significantly high proton conductivity and high stability as a function of RH in comparison to 2D mesostructure, due to the higher interconnectivity of the $Fm\bar{3}m$, $Im\bar{3}m$ and $Ia\bar{3}d$ structures. The best result was obtained with the body-centered cubic ($Im\bar{3}m$)-composed HPW-meso-silica, showing proton conductivities of 0.061 and 0.140 S cm^{-1} at 25 and 150 ℃, respectively, and an activation energy of 10.0 kJ mol^{-1}. The effects of pore size on the HPW leakage under water or fuel washing were also investigated. The 24hrs speed tests indicated that smaller pore size leads to reduced leakage of HPW and so more stable membrane conductivity. The HPW-meso-silica membrane with pore size of ~5.0 nm showed both the highest proton conductivity and best stability upon water waching.

4. The HPW-meso-silica membrane was measured in PEMFC and DMFC for its blocking of methanol crossover in DMFC. It was showed that the HPW-meso-silica membrane can effectively reduce the mechanol crossover and enhance the power output of DMFCs by as much as 214% as compared to the best performance of the DMFC based on a Nafion 117 membrane. The methanol crossover for the HPW-meso-silica membrane with a thickness of ~500 μm is much lower compared to the Nafion 117 memrbrane under the same conditions; The HPW-meso-silica membrane was proved to be of great potential in the development of high temperature DMFC.

8.2 Major achievements

1. Developed a new concept, and demonstrated the feasibility of the high temperature proton exchange membrane based on mesoporous silica host and HPA proton carrier for high temperature PEM fuel cells
2. The synthesis and operational conditions of PEMFC and DMFC systems based on the novel HPW-meso-silica proton exchange membranes were evaluated and the best single cell performance on the PEMFC employing a HPW/meso-silica membrane was achieced with a peak power density of 308 mW cm^{-2} in H_2/O_2 and 206 mW cm^{-2} in H_2/air under 80 ^oC and 80 %RH, respectively.

LIST OF PUBLICATIONS

Journal Paper

1. Jie Zeng, Yuhua Zhou, Lin Li, San Ping Jiang. (2011). *Phosphotungstic acid functionalized silica nanocomposites with tunable bicontinuous mesoporous structure and superior proton conductivity and stability for fuel cells.* Physical Chemistry Chemical Physics, **13**(21): 10249-10257.
2. Jie Zeng, San Ping Jiang. (2011). *Characterization of High-Temperature Proton-Exchange Membranes Based on Phosphotungstic Acid Functionalized Mesoporous Silica Nanoconnposites for Fuel Cells*. Journal of Physical Chemistry C. **115**(23): 11854-11863.
3. Jie Zeng, San Ping Jiang, Lin Li. (2011). *High Temperature Proton Exchange Membranes Based on Various Heteropoly Acids (HPW, HSiW, HPMo or HSiMo) Functionalized Silica Nanocomposites with Tunable Mesoporous Structure and Superior Proton Conductivity for Fuel Cells.* ECS Transactions. **41**(1): 1603-1613.
4. Jie Zeng, Lin Li, Yan Xiang, Shanfu Lu, Changming Li, San Ping Jiang. *Correlation between proton conductivity, thermal stability and structure symmetries in novel HPW-meso-silica nanocomposite membranes and its performance in DMFC.* Accept by Journal of membrane science, available online from 18/01/2012. ISSN (0376-7388)
5. Jie Zeng and San Ping Jiang, *Anhydrous proton conducting membrane based on mesoporous silica monolith/phosphoric acid composite for intermediate temperature fuel cells.* Under preparation.
6. Jie Zeng and San Ping Jiang, *A novel high temperature orgnaic-inorganic hybrid conductor based on various heteropoly acids functionalized silica nanocomposites for fuel cells.* Under preparation.
7. Yuhua Zhou, Jie Zeng, San Ping Jiang, Haibin Su, *Theoretical investigation on the mechanism of proton transfer within HPW-based membrane.* Submitted to Journal of American Chemistry Society.

8. Sanfu Lu, Deli Wang, San Ping Jiang, Yan Xiang, Jinlin Lu, Jie Zeng, *HPW/MCM-41 Phosphotungstic Acid/Mesoporous Silica Composites as Novel Proton-Exchange Membranes for Elevated-Temperature Fuel Cells.* Advanced Materials, 2010. **22**(9): 971.
9. Xiaoming Ge, Lan Zhang, Yannan Fang, Jie Zeng, Siew Hwa Chan, *Robust solid oxide cells for alternate power generation and carbon conversion*, in *Rsc Advances*. 715-724.
10. Shanfu Lu, Deli Wang, Jinlin Lu, Jie Zeng, San Ping Jiang, *HPW/MCM-41 mesoporous silica composites as novel proton exchange membranes for elevated temperature fuel cells*, ECS Transactions, 25 (2009) 1927-1933.

Conference Paper:

11. Jie Zeng, San Ping Jiang, *HPW/Silica inorganic membranes based on mesoporous silica for fuel cells*, in *the 1st international Fuel Cell Summer Seminar*. 2010: Yamanashi, Japan. 176

REFERENCE

ADJEMIAN, K. T., LEE, S. J., SRINIVASAN, S., BENZIGER, J. & BOCARSLY, A. B. 2002. Silicon oxide Nafion composite membranes for proton-exchange membrane fuel cell operation at 80-140 degrees C. *Journal of The Electrochemical Society,* 149**,** A256-A261.

AHMAD, H., KAMARUDIN, S. K., HASRAN, U. A. & DAUD, W. R. W. 2010. Overview of hybrid membranes for direct-methanol fuel-cell applications. *International Journal of Hydrogen Energy,* 35**,** 2160-2175.

ALABI, C. A. & DAVIS, M. E. 2006. Proton-Conducting Solid Electrolyte via Ozonolysis of Cationic Ammonium Organoalkoxysilane Surfactant-Templated MCM-41. *Chemistry of Materials,* 18**,** 5634-5636.

ALBERTI, G. & CASCIOLA, M. 2001. Solid state protonic conductors, present main applications and future prospects. *Solid State Ionics,* 145**,** 3-16.

ANANTARAMAN, A. V. & GARDNER, C. L. 1996. Studies on ion-exchange membranes .1. Effect of humidity on the conductivity of Nafion(R). *Journal of Electroanalytical Chemistry,* 414**,** 115-120.

ANDERSON, A. B. & ALBU, T. V. 2000. Catalytic Effect of Platinum on Oxygen Reduction An Ab Initio Model Including Electrode Potential Dependence. *Journal of The Electrochemical Society,* 147**,** 4229-4238.

APPLEBY, A. J. & YEAGER, E. B. 1986. *Energy (oxford),* 11**,** 137.

ARGYROPOULOS, P., SCOTT, K., SHUKLA, A. K. & JACKSON, C. 2003. A semi-empirical model of the direct methanol fuel cell performance: Part I.

Model development and verification. *Journal of Power Sources,* 123**,** 190-199.

ARMATAS, G. S., SALMAS, C. E., LOULOUDI, M., ANDROUTSOPOULOS, G. P. & POMONIS, P. J. 2003. Relationships among pore size, connectivity, dimensionality of capillary condensation, and pore structure tortuosity of functionalized mesoporous silica. *Langmuir,* 19**,** 3128-3136.

ATHENS, G. L., EIN-ELI, Y. & CHMELKA, B. F. 2007a. Acid-Functionalized Mesostructured Aluminosilica for Hydrophilic Proton Conduction Membranes. *Advanced Materials,* 19**,** 2580-2587.

ATHENS, G. L., EIN-ELI, Y. & CHMELKA, B. F. 2007b. Acid-functionalized mesostructured aluminosilica for hydrophilic proton conduction membranes. *Advanced Materials,* 19**,** 2580-+.

BARCZUK, P. J., TSUCHIYA, H., MACAK, J. M., SCHMUKI, P., SZYMANSKA, D., MAKOWSKI, O., MIECZNIKOWSKI, K. & KULESZA, P. J. 2006. Enhancement of the electrocatalytic oxidation of methanol at Pt/Ru nanoparticles immobilized in different WO3 matrices. *Electrochemical and Solid State Letters,* 9**,** E13-E16.

BARRETT, E. P., JOYNER, L. G. & HALENDA, P. P. 1951. *J. Am. Chem. Soc.,* 73**,** 373.

BARTON, S. C., PATTERSON, T., WANG, E., FULLER, T. F. & WEST, A. C. 2001. Mixed-reactant, strip-cell direct methanol fuel cells. *Journal of Power Sources,* 96**,** 329-336.

BAUEN, A. & HART, D. 2000. Assessment of the environmental benefits of transport and stationary fuel cells. *Journal of Power Sources,* 86**,** 482-494.

BEATTIE, P. D., BASURA, V. I. & HOLDCROFT, S. 1999. Temperature and pressure dependence of O-2 reduction at Pt vertical bar Nafion((R)) 117 and Pt vertical bar BAM((R)) 407 interfaces. *Journal of Electroanalytical Chemistry,* 468**,** 180-192.

BIRGERSSON, E., NORDLUND, J., EKSTROM, H., VYNNYCKY, M. & LINDBERGH, G. 2003. Reduced two-dimensional one-phase model for analysis of the anode of a DMFC. *Journal of The Electrochemical Society,* 150**,** A1368-A1376.

BLASCO, T., CORMA, A., MARTINEZ, A. & MARTINEZ-ESCOLANO, P. 1998. Supported heteropolyacid (HPW) catalysts for the continuous alkylation of isobutane with 2-butene: The benefit of using MCM-41 with larger pore diameters. *Journal of Catalysis,* 177**,** 306-313.

BOCKRIS, J. O. M. & SRINIVASAN, S. 1969. *Fuel cells: their electrochemistry,* New York, McGraw-Hill.

BOCQUET, L., CHARLAIX, E., CILIBERTO, S. & CRASSOUS, J. 1998. *Nature,* 396**,** 735-737.

BUCHI, F. N., GUPTA, B., HAAS, O. & SCHERER, G. G. 1995. Study of radiation-grafted FEP-G-polystyrene membranes as polymer electrolytes in fuel cells. *Electrochimica Acta,* 40**,** 345-353.

BUCHI, F. N. & SCHERER, G. G. 2001. Investigation of the transversal water profile in nafion membranes in polymer electrolyte fuel cells. *Journal of The Electrochemical Society,* 148**,** A183-A188.

BUREEKAEW, S., HORIKE, S., HIGUCHI, M., MIZUNO, M., KAWAMURA, T., TANAKA, D., YANAI, N. & KITAGAWA, S. 2009. One-dimensional imidazole aggregate in aluminium porous coordination polymers with high proton conductivity. *Nat Mater,* 8**,** 831-836.

CASCIOLA, M., CAPITANI, D., DONNADIO, A., FRITTELLA, V., PICA, M. & SGANAPPA, M. 2009. Preparation, Proton Conductivity and Mechanical Properties of Nafion 117-Zirconium Phosphate Sulphophenylphosphonate Composite Membranes. *Fuel Cells,* 9**,** 381-386.

CELSO, F., MIKHAILENKO, S. D., KALIAGUINE, S., DUARTE, U. L., MAULER, R. S. & GOMES, A. S. 2009. SPEEK based composite PEMs containing tungstophosphoric acid and modified with benzimidazole derivatives. *Journal of Membrane Science,* 336**,** 118-127.

CHEN, D., LI, Z., YU, C., SHI, Y., ZHANG, Z., TU, B. & ZHAO, D. 2005. Nonionic Block Copolymer and Anionic Mixed Surfactants Directed Synthesis of Highly Ordered Mesoporous Silica with Bicontinuous Cubic Structure. *Chemistry of Materials,* 17**,** 3228-3234.

CHU, D., GERVASIO, D., RAZAQ, M. & YEAGER, E. B. 1990. Infrared reflectance absorption spectroscopy (IRRAS). Study of the thermal stability of perfluorinated sulphonic acid ionomers on Pt. *Journal of Applied Electrochemistry,* 20**,** 157-162.

CIUREANU, M. 2004. Effects of Nafion (R) dehydration in PEM fuel cells. *Journal of Applied Electrochemistry,* 34**,** 705-714.

COLOMER, M. T. 2006a. Nanoporous Anatase Thin Films as Fast Proton-Conducting Materials. *Advanced Materials,* 18**,** 371-374.

COLOMER, M. T. 2006b. Nanoporuous anatase thin films as fast proton-conducting materials. *Advanced Materials,* 18**,** 371-+.

COSTAMAGNA, P. & SRINIVASAN, S. 2001. Quantum jumps in the PEMFC science and technology from the 1960s to the year 2000: Part I. Fundamental scientific aspects. *Journal of Power Sources*, 102**,** 242-252.

CUI, Z. M., XING, W., LIU, C. P., LIAO, J. H. & ZHANG, H. 2009. Chitosan/heteropolyacid composite membranes for direct methanol fuel cell. *Journal of Power Sources*, 188**,** 24-29.

CUI, Z. M., XING, W., LIU, C. P., TIAN, D. & ZHANG, H. 2010. Synthesis and characterization of H5PMo10V2O40 deposited Pt/C nanocatalysts for methanol electrooxidation. *Journal of Power Sources,* 195**,** 1619-1623.

DAI, H., ZHANG, H., ZHONG, H., JIN, H., LI, X., XIAO, S. & MAI, Z. 2010. Properties of Polymer Electrolyte Membranes Based on Poly(Aryl Ether Benzimidazole) and Sulphonated Poly(Aryl Ether Benzimidazole) for High Temperature PEMFCs. *Fuel Cells,* 10**,** 754-761.

DAIKO, Y., KASUGA, T. & NOGAMI, M. 2002. Proton conduction and pore structure in sol-gel glasses. *Chemistry of Materials,* 14**,** 4624-4627.

DHAR, H. P., CHRISTNER, L. G. & KUSH, A. K. 1987. Nature of CO Adsorption during H[sub 2] Oxidation in Relation to Modeling for CO Poisoning of a Fuel Cell Anode. *Journal of The Electrochemical Society,* 134**,** 3021-3026.

DHAR, H. P., CHRISTNER, L. G., KUSH, A. K. & MARU, H. C. 1986. Performance Study of a Fuel Cell Pt-on-C Anode in Presence of CO and CO[sub 2], and Calculation of Adsorption Parameters for CO Poisoning. *Journal of The Electrochemical Society,* 133**,** 1574-1582.

DIAS, A. S., PILLINGER, M. & VALENTE, A. A. 2006. Mesoporous silica-supported 12-tungstophosphoric acid catalysts for the liquid phase dehydration of D-xylose. *Microporous and Mesoporous Materials,* 94**,** 214-225.

DIVISEK, J., EIKERLING, M., MAZIN, V., SCHMITZ, H., STIMMING, U. & VOLFKOVICH, Y. M. 1998. A study of capillary porous structure and sorption properties of Nafion proton-exchange membranes swollen in water. *Journal of The Electrochemical Society,* 145**,** 2677-2683.

ECHIGO, M., SHINKE, N., TAKAMI, S., HIGASHIGUCHI, S., HIRAI, K. & TABATA, T. 2003. Development of residential PEFC cogeneration systems: Ru catalyst for CO preferential oxidation in reformed gas. *Catalysis Today,* 84**,** 209-215.

ELABD, Y. A., NAPADENSKY, E., SLOAN, J. M., CRAWFORD, D. M. & WALKER, C. W. 2003. Triblock copolymer ionomer membranes: Part I. Methanol and proton transport. *Journal of Membrane Science,* 217**,** 227-242.

FAN, R., HUH, S., YAN, R., ARNOLD, J. & YANG, P. D. 2008. Gated proton transport in aligned mesoporous silica films. *Nature Materials,* 7**,** 303-307.

FEINDEL, K. W., BERGENS, S. H. & WASYLISHEN, R. E. 2007. The influence of membrane electrode assembly water content on the performance of a polymer electrolyte membrane fuel cell as investigated by H-1 NMR microscopy. *Physical Chemistry Chemical Physics,* 9**,** 1850-1857.

FIRESTONE, B. A. & SIEGEL, R. A. 1991. Kinetics and mechanisms of water sorption in hydrophobic, ionizable copolymer gels. *Journal of Applied Polymer Science,* 43**,** 901-914.

G. M. BROWN, M.-R. NOE-SPIRLET, W. R. BUSING & LEVY, H. A. 1977. Dodecatungstophosphoric acid hexahydrate, $(H_5O^{2+})_3(PW_{12}O_{40}{}^{3-})$. The true structure of Keggin's `pentahydrate' from single-crystal X-ray and neutron diffraction data. *Acta Cryst.,* B33**,** 1038-1046

GARCIA, M. A. G., THOMAS, S., PITCHON, V. & KIENNEMANN, A. 2007. Selective reduction of NOx by liquid hydrocarbons with supported HPW-metal catalysts. *Catalysis Today,* 119**,** 52-58.

GE, S., LI, X. & HSING, I. M. 2005. Internally humidified polymer electrolyte fuel cells using water absorbing sponge. *Electrochimica Acta,* 50**,** 1909-1916.

GEBEL, G. 2000. Structural evolution of water swollen perfluorosulfonated ionomers from dry membrane to solution. *Polymer,* 41**,** 5829-5838.

GEBEL, G., ALDEBERT, P. & PINERI, M. 1993. Swelling study of perfluorosulphonated ionomer membranes. *Polymer,* 34**,** 333-339.

GILLESPIE, R. J. & ROBINSON, E. A. 1965. *In nonaqueous solvent systems,* New

York, Academic Press.

GOBIN, O. C., WAN, Y., ZHAO, D., KLEITZ, F. & KALIAGUINE, S. 2007a. Mesostructured Silica SBA-16 with Tailored Intrawall Porosity Part 1: Synthesis and Characterization. *The Journal of Physical Chemistry C,* 111**,** 3053-3058.

GOBIN, O. C., WAN, Y., ZHAO, D. Y., KLEITZ, F. & KALIAGUINE, S. 2007b. Mesostructured silica SBA-16 with tailored intrawall porosity part 1: Synthesis and characterization. *Journal of Physical Chemistry C,* 111**,** 3053-3058.

GREGG, S. J. & SING, K. S. W. 1982. Adsorption, Surface Area and Porosity. *Academic.* London.

GREGG, S. J. & SING, K. S. W. 1991. *Adsorption, Surface Area and Porosity,* London, Academic.

HALLA, J. D., MAMAK, M., WILLIAMS, D. E. & OZIN, G. A. 2003a. Meso-SiO2-C12EO10OH-CF3SO3H - A novel proton-conducting solid electrolyte. *Advanced Functional Materials,* 13**,** 133-138.

HALLA, J. D., MAMAK, M., WILLIAMS, D. E. & OZIN, G. A. 2003b. Meso-SiO2–C12EO10OH–CF3SO3H—A Novel Proton-Conducting Solid Electrolyte. *Advanced Functional Materials,* 13**,** 133-138.

HE, R., LI, Q., XIAO, G. & BJERRUM, N. J. 2003. Proton conductivity of phosphoric acid doped polybenzimidazole and its composites with inorganic proton conductors. *Journal of Membrane Science,* 226**,** 169-184.

HEO, P., NAGAO, M., KAMIYA, T., SANO, M., TOMITA, A. & HIBINO, T. 2007a. Sn0.9In0.1P_2O_7-based organic/inorganic composite membranes application to intermediate-temperature fuel cells. *Journal of The Electrochemical Society,* 154**,** B63-B67.

HEO, P., NAGAO, M., SANO, M. & HIBINO, T. 2007b. A high-performance Mo2C-ZrO2 anode catalyst for intermediate-temperature fuel cells. *Journal of The Electrochemical Society,* 154**,** B53-B56.

HICKNER, M. A., GHASSEMI, H., KIM, Y. S., EINSLA, B. R. & MCGRATH, J. E. 2004. Alternative polymer systems for proton exchange membranes (PEMs). *Chemical Reviews,* 104**,** 4587-4611.

HOGARTH, W. H. J., DA COSTA, J. C. D., DRENNAN, J. & LU, G. Q. 2005a. Proton conductivity of mesoporous sol-gel zirconium phosphates for fuel cell applications. *Journal of Materials Chemistry,* 15**,** 754-758.

HOGARTH, W. H. J., DA COSTA, J. C. D. & LU, G. Q. 2005b. Solid acid membranes for high temperature (> 140 degrees C) proton exchange membrane fuel cells. *Journal of Power Sources,* 142**,** 223-237.

HOGARTH, W. H. J., DINIZ DA COSTA, J. C. & LU, G. Q. 2005c. Solid acid membranes for high temperature (>140 ^{o}C) proton exchange membrane fuel cells. *Journal of Power Sources,* 142**,** 223-237.

HOLMBERG, B. A., HWANG, S.-J., DAVIS, M. E. & YAN, Y. 2005a. Synthesis and proton conductivity of sulfonic acid functionalized zeolite BEA nanocrystals. *Microporous and Mesoporous Materials,* 80**,** 347-356.

HOLMBERG, B. A., HWANG, S. J., DAVIS, M. E. & YAN, Y. S. 2005b. Synthesis and proton conductivity of sulfonic acid functionalized zeolite BEA nanocrystals. *Microporous and Mesoporous Materials,* 80**,** 347-356.

HYUN, D. & KIM, J. 2004. Study of external humidification method in proton exchange membrane fuel cell. *Journal of Power Sources,* 126**,** 98-103.

INOUE, T., UMA, T. & NOGAMI, M. 2008. Performance of H-2/O-2 fuel cell using membrane electrolyte of phosphotungstic acid-modified 3-glycidoxypropyl-trimethoxysilanes. *Journal of Membrane Science,* 323**,** 148-152.

JANIK, M. J., DAVIS, R. J. & NEUROCK, M. 2005. Anhydrous and Water-Assisted Proton Mobility in Phosphotungstic Acid. *J. Am. Chem. Soc.,* 127**,** 5238-5245.

JEON, S., LEE, J., RIOS, G. M., KIM, H.-J., LEE, S.-Y., CHO, E., LIM, T.-H. & HYUN JANG, J. 2010. Effect of ionomer content and relative humidity on polymer electrolyte membrane fuel cell (PEMFC) performance of membrane-electrode assemblies (MEAs) prepared by decal transfer method. *International Journal of Hydrogen Energy,* 35**,** 9678-9686.

JEONG, K.-J., MIESSE, C. M., CHOI, J.-H., LEE, J., HAN, J., YOON, S. P., NAM, S. W., LIM, T.-H. & LEE, T. G. 2007. Fuel crossover in direct formic acid fuel cells. *Journal of Power Sources,* 168**,** 119-125.

JIANG, J. & KUCERNAK, A. 2004. Investigations of fuel cell reactions at the composite microelectrodesolid polymer electrolyte interface. I. Hydrogen oxidation at the nanostructured PtNafion?membrane interface. *Journal of*

Electroanalytical Chemistry, 567**,** 123-137.

JIANG, S. P., LIU, Z. & TIAN, Z. Q. 2006a. Layer-by-Layer Self-Assembly of Composite Polyelectrolyte–Nafion Membranes for Direct Methanol Fuel Cells. *Advanced Materials,* 18**,** 1068-1072.

JIANG, S. P., LIU, Z. C. & TIAN, Z. Q. 2006b. Layer-by-layer self-assembly of composite polyelectrolyte-nafion membranes for direct methanol fuel cells. *Advanced Materials,* 18**,** 1068-+.

JIAO, K. & LI, X. 2010. Effect of surface dynamic wettability in proton exchange membrane fuel cells. *International Journal of Hydrogen Energy,* 35**,** 9095-9103.

JIN, Y. G., QIAO, S. Z., XU, Z. P., YAN, Z. M., HUANG, Y. N., DA COSTA, J. C. D. & LU, G. Q. 2009. Phosphonic acid functionalized silicas for intermediate temperature proton conduction. *Journal of Materials Chemistry,* 19**,** 2363-2372.

JIN, Z. X., YONG, G. P., SHENG, L. Q., TONG, H. W., SU, Q. D. & LIU, S. M. 2006. Spectroscopic characterization of structure of cerium incorporated MCM-48 mesoporous molecular sieve. *Spectroscopy and Spectral Analysis,* 26**,** 484-487.

JUNG, E. H., JUNG, U. H., YANG, T. H., PEAK, D. H., JUNG, D. H. & KIM, S. H. 2007. Methanol crossover through PtRu/Nafion composite membrane for a direct methanol fuel cell. *International Journal of Hydrogen Energy,* 32**,** 903-907.

KIM, H. J., SHUL, Y. G. & HAN, H. 2006. Synthesis of heteropolyacid (H3PW12O40)/SiO2 nanoparticles and their catalytic properties. *Applied Catalysis a-General,* 299**,** 46-51.

KIM, J. D. & HONMA, I. 2004. Synthesis and proton conducting properties of zirconia bridged hydrocarbon/phosphotungstic acid hybrid materials. *Electrochimica Acta,* 49**,** 3179-3183.

KIM, J. M., KIM, S. K. & RYOO, R. 1998. Synthesis of MCM-48 single crystals. *Chemical Communications***,** 259-260.

KIM, T. W., KLEITZ, F., PAUL, B. & RYOO, R. 2005. MCM-48-like large mesoporous silicas with tailored pore structure: Facile synthesis domain in a ternary triblock copolymer-butanol-water system. *Journal of the American Chemical Society,* 127**,** 7601-7610.

KIM, Y. S., WANG, F., HICKNER, M., ZAWODZINSKI, T. A. & MCGRATH, J. E. 2003. Fabrication and characterization of heteropolyacid (H3PW12O40)/directly polymerized sulfonated poly(arylene ether sulfone) copolymer composite membranes for higher temperature fuel cell applications. *Journal of Membrane Science,* 212**,** 263-282.

KLEITZ, F., CHOI, S. H. & RYOO, R. 2003. Cubic Ia3d large mesoporous silica: synthesis and replication to platinum nanowires, carbon nanorods and carbon nanotubes. *Chemical Communications***,** 2136-2137.

KORDESCH, K. & SIMANDER, G. 1996. *Fuel Cells and their Applications,* Germany, VCH Publishers.

KOZHEVNIKOV, I. V. 1998. Catalysis by heteropoly acids and multicomponent polyoxometalates in liquid-phase reactions. *Chemical Reviews,* 98**,** 171-198.

KREUER, K.-D. 1988. Fast proton transport in solids. *Journal of Molecular Structure,* 177**,** 265-276.

KREUER, K.-D., PADDISON, S. J., SPOHR, E. & SCHUSTER, M. 2004. Transport in Proton Conductors for Fuel-Cell Applications:Simulations, Elementary Reactions, and Phenomenology. *Chemical Reviews,* 104**,** 4637-4678.

KREUER, K. D. 1996. *Chemistry of Materials,* 8**,** 610.

KREUER, K. D. 1997. *Solid State Ionics,* 94**,** 55.

KUKINO, T., KIKUCHI, R., TAKEGUCHI, T., MATSUI, T. & EGUCHI, K. 2005. Proton conductivity and stability of $Cs_2HPW_{12}O_{40}$ electrolyte at intermediate temperatures. *Solid State Ionics,* 176**,** 1845-1848.

KULESZA, P. J., CHOJAK, M., KARNICKA, K., MIECZNIKOWSKI, K., PALYS, B., LEWERA, A. & WIECKOWSKI, A. 2004. Network films composed of conducting polymer-linked and polyoxometalate-stabilized platinum nanoparticles. *Chemistry of Materials,* 16**,** 4128-4134.

KUMAR, G. S., VISHNUVARTHAN, M., PALANICHAMY, M. & MURUGESAN, V. 2006. SBA-15 supported HPW: Effective catalytic performance in the alkylation of phenol. *Journal of Molecular Catalysis a-Chemical,* 260**,** 49-55.

KUMBHARKAR, S. C., ISLAM, M. N., POTREKAR, R. A. & KHARUL, U. K. 2009. Variation in acid moiety of polybenzimidazoles: Investigation of physico-chemical properties towards their applicability as proton exchange and gas separation membrane materials. *Polymer,* 50**,** 1403-1413.

KUVER, A. & VIELSTICH, W. 1998. Investigation of methanol crossover and single electrode performance during PEMDMFC operation: A study using a solid polymer electrolyte membrane fuel cell system. *Journal of Power Sources,* 74**,** 211-218.

LABERTY-ROBERT, C., VALLE, K., PEREIRA, F. & SANCHEZ, C. 2011. Design and properties of functional hybrid organic-inorganic membranes for fuel cells. *Chemical Society Reviews,* 40**,** 961-1005.

LAKSHMINARAYANA, G. & NOGAMI, M. 2009. Synthesis and Characterization of Proton Conducting Inorganic-Organic Hybrid Nanocomposite Membranes Based on mixed PWA-PMA-TEOS-GPTMS-H3PO4-APTES for H-2/O-2 Fuel Cells. *Journal of Physical Chemistry C,* 113**,** 14540-14550.

LARMINIE, J., DICKS, A. & (FIRM), K. 2003. *Fuel cell systems explained,* West Sussex, J. Wiley, Chichester,.

LEFEBVRE, F. 1992. P-31 MAS NMR-STUDY OF H3PW12O40 SUPPORTED ON SILICA - FORMATION OF (EQUIVALENT-TO-SIOH2+)(H2PW12O40-). *Journal of the Chemical Society-Chemical Communications***,** 756-757.

LI, H. & NOGAMI, M. 2002a. Pore-Controlled Proton Conducting Silica Films. *Advanced Materials,* 14**,** 912-914.

LI, H. & NOGAMI, M. 2003a. Ordered mesoporous phosphosilicate glass electrolyte film with low area specific resistivity. *Chemical Communications***,** 236-237.

LI, H. B. & NOGAMI, M. 2002b. Pore-controlled proton conducting silica films.

Advanced Materials, 14**,** 912-914.

LI, H. B. & NOGAMI, M. 2003b. Ordered mesoporous phosphosilicate glass electrolyte film with low area specific resistivity. *Chemical Communications***,** 236-237.

LI, Q., HE, R., GAO, J.-A., JENSEN, J. O. & BJERRUM, N. J. 2003a. The CO Poisoning Effect in PEMFCs Operational at Temperatures up to 200[degree]C. *Journal of The Electrochemical Society,* 150**,** A1599-A1605.

LI, Q. F., HE, R. H., JENSEN, J. O. & BJERRUM, N. J. 2003b. Approaches and recent development of polymer electrolyte membranes for fuel cells operating above 100 degrees C. *Chemistry of Materials,* 15**,** 4896-4915.

LI, Z., CHEN, D. H., TU, B. & ZHAO, D. Y. 2007. Synthesis and phase behaviors of bicontinuous cubic mesoporous silica from triblock copolymer mixed anionic surfactant. *Microporous and Mesoporous Materials,* 105**,** 34-40.

LI, Z. Y., ZHANG, Q., LIU, H. T., HE, P., XU, X. D. & LI, J. H. 2006. Organic-inorganic composites based on room temperature ionic liquid and 12-phosphotungstic acid salt with high assistant catalysis and proton conductivity. *Journal of Power Sources,* 158**,** 103-109.

LIANG, W. J., HSIEH, S. J., HSU, C. Y., CHEN, W. F. & KUO, P. L. 2006. Microstructure and protonic conductivity of H3PO4-doped polyethylenimine-siloxane chemically covalently organic-inorganic hybrids. *Journal of Polymer Science Part B-Polymer Physics,* 44**,** 2135-2144.

LIN, M. L., HUANG, C. C., LO, M. Y. & MOU, C. Y. 2008. Well-ordered mesoporous carbon thin film with perpendicular channels: Application to direct methanol fuel cell. *Journal of Physical Chemistry C,* 112**,** 867-873.

LIN, W. F., WANG, J. T. & SAVINELL, R. F. 1997. On-line FTIR spectroscopic investigations of methanol oxidation in a direct methanol fuel cell. *Journal of The Electrochemical Society,* 144**,** 1917-1922.

LIN, Y.-F., YEN, C.-Y., MA, C.-C. M., LIAO, S.-H., LEE, C.-H., HSIAO, Y.-H. & LIN, H.-P. 2007. High proton-conducting Nafion-SO_3H functionalized mesoporous silica composite membranes. *Journal of Power Sources,* 171**,** 388-395.

LOBATO, J., CANIZARES, P., RODRIGO, M. A., LINARES, J. J. & LOPEZ-VIZCAINO, R. 2008. Performance of a Vapor-Fed Polybenzimidazole (PBI)-Based Direct Methanol Fuel Cell. *Energy & Fuels,* 22**,** 3335-3345.

LU, J. L., LU, S. F. & JIANG, S. P. 2011. Highly ordered mesoporous Nafion membranes for fuel cells. *Chemical Communications,* 47**,** 3216-3218.

LU, S. F., WANG, D. L., JIANG, S. P., XIANG, Y., LU, J. L. & ZENG, J. 2010. HPW/MCM-41 Phosphotungstic Acid/Mesoporous Silica Composites as Novel Proton-Exchange Membranes for Elevated-Temperature Fuel Cells. *Advanced Materials,* 22**,** 971-976.

LU, Y. F., CAO, G. Z., KALE, R. P., PRABAKAR, S., LOPEZ, G. P. & BRINKER, C. J. 1999. Microporous silica prepared by organic templating: Relationship between the molecular template and pore structure. *Chemistry of Materials,* 11**,** 1223-1229.

MA, C. S., ZHANG, L., MUKERJEE, S., OFER, D. & NAIR, B. D. 2003. An investigation of proton conduction in select PEM's and reaction layer interfaces-designed for elevated temperature operation. *Journal of Membrane Science,* 219**,** 123-136.

MALHOTRA, S. & DATTA, R. 1997. Membrane-Supported Nonvolatile Acidic Electrolytes Allow Higher Temperature Operation of Proton-Exchange Membrane Fuel Cells. *Journal of The Electrochemical Society,* 144**,** L23-L26.

MARSCHALL, R., BANNAT, I., FELDHOFF, A., WANG, L. Z., LU, G. Q. & WARK, M. 2009a. Nanoparticles of Mesoporous SO3H-Functionalized Si-MCM-41 with Superior Proton Conductivity. *Small,* 5**,** 854-859.

MARSCHALL, R., SHARIFI, M. & WARK, M. 2009b. Proton conductivity of imidazole functionalized ordered mesoporous silica: Influence of type of anchorage, chain length and humidity. *Microporous and Mesoporous Materials,* 123**,** 21-29.

MATSUDA, A., KANZAKI, T., TADANAGA, K., TATSUMISAGO, M. & MINAMI, T. 2001. Medium temperature range characterization as a proton conductor for phosphosilicate dry gels containing large amounts of phosphorus. *Electrochimica Acta,* 47**,** 939-944.

MATSUDA, A., KANZAKI, T., TADANAGA, K., TATSUMISAGO, M. & MINAMI, T. 2002a. Phosphosilicate gels as a solid state proton conductor at medium temperature and low humidity. *Journal of the Ceramic Society of*

Japan, 110**,** 131-134.

MATSUDA, A., KANZAKI, T., TADANAGA, K., TATSUMISAGO, M. & MINAMI, T. 2002b. Proton conductivities of sol-gel derived phosphosilicate gels in medium temperature range with low humidity. *Solid State Ionics,* 154-155**,** 687-692.

MATSUDA, A., NAKAMOTO, N., TADANAGA, K., MINAMI, T. & TATSUMISAGO, M. 2003. Preparation and characterization of thermally stable proton-conducting composite sheets composed of phosphosilicate gel and polyimide. *Solid State Ionics,* 162**,** 247-252.

MATSUDA, A., NAKAMOTO, N., TADANAGA, K., MINAMI, T. & TATSUMISAGO, M. 2006. Operation of PEFC using composite sheets composed of phosphosilicate gels and thermally stable organic polymers. *Solid State Ionics,* 177**,** 2437-2441.

MATSUDA, A., TEZUKA, T., NONO, Y., TADANAGA, K., MINAMI, T. & TATSUMISAGO, M. 2005. Preparation of proton conducting composites by mechanical milling for phosphorus-containing solid acids. *Solid State Ionics,* 176**,** 2899-2904.

MATSUMOTO, Y., YOKOYAMA, R. & ITO, K. 1994. Engineering-Economic Optimization of a Fuel Cell Cogeneration Plant. *Journal of Engineering for Gas Turbines and Power,* 116**,** 8-14.

MATSUSHITA, H., NAGAO, R., NOGAMI, M., KASUGA, T. & HAYAKAWA, T. Hydrogen gas sensing of high electrical conducting-P2O5-SiO2 glasses prepared by sol-gel process. 10th International Workshop on Glasses, Ceramics, Hybrids, and Nanocomposites from Gels, Sep 19-24 1999 Yokohama, Japan. 559-562.

MAURITZ, K. A. & MOORE, R. B. 2004. State of understanding of Nafion. *Chemical Reviews,* 104**,** 4535-4585.

MCKEEN, J. C., YAN, Y. S. & DAVIS, M. E. 2008a. Proton Conductivity in Sulfonic Acid-Functionalized Zeolite Beta: Effect of Hydroxyl Group. *Chemistry of Materials,* 20**,** 3791-3793.

MCKEEN, J. C., YAN, Y. S. & DAVIS, M. E. 2008b. Proton Conductivity of Acid-Functionalized Zeolite Beta, MCM-41, and MCM-48: Effect of Acid Strength. *Chemistry of Materials,* 20**,** 5122-5124.

MICEK-ILNICKA, A. 2009. The role of water in the catalysis on solid heteropolyacids. *Journal of Molecular Catalysis a-Chemical,* 308**,** 1-14.

MIKHAILENKO, S. D., KALIAGUINE, S. & MOFFAT, J. B. 1997. Electrical impedance studies of the ammonium salt of 12-tungstophosphoric acid in the presence of liquid water. *Solid State Ionics,* 99**,** 281-286.

MISONO, M. 1987. Heterogeneous Catalysis by Heteropoly Compounds of Molybdenum and Tungsten. *Catalysis Reviews-Science and Engineering,* 29**,** 269-321.

MOND, L. & LANGER, C. 1889. A New Form of Gas Battery. *Proceedings of the Royal Society of London,* 46**,** 296-304.

MORISHIGE, K. & TATEISHI, N. 2003. Adsorption hysteresis in ink-bottle pore.

Journal of Chemical Physics, 119**,** 2301-2306.

MUNAKATA, H., OCHIAI, S. & KANAMURA, K. 2007. Pore size effect on improvement of surface proton conductivity for three-dimensionally ordered macroporous silica composite membrane. *Journal of The Electrochemical Society,* 154**,** B871-B875.

NAGAO, M., TAKEUCHI, A., HEO, P., HIBINO, T., SANO, M. & TOMITAB, A. 2006. A proton-conducting In^{3+}-doped SnP_2O_7 electrolyte for intermediate-temperature fuel cells. *Electrochemical and Solid State Letters,* 9**,** A105-A109.

NAKAMURA, O., KODAMA, T., OGINO, I. & MIYAKE, Y. 1979. HIGH-CONDUCTIVITY SOLID PROTON CONDUCTORS - DODECAMOLYBDOPHOSPHORIC ACID AND DODECATUNGSTOPHOSPHORIC ACID CRYSTALS. *Chemistry Letters***,** 17-18.

NAKAMURA, O., OGINO, I. & KODAMA, T. 1981. Temperature and humidity ranges of some hydrates of high-proton-conductive dodecamolybdophosphoric acid and dodecatungstophosphoric acid crystals under an atmosphere of hydrogen or either oxygen or air. *Solid State Ionics,* 3-4**,** 347-351.

NAKANISHI, T., NORISUYE, T., SATO, H., TAKEMORI, T., TRAN-CONG-MIYATA, Q., SUGIMOTO, T. & NOMURA, S. 2007. Studies on microscopic structure of sol-gel derived nanohybrids containing heteropolyacid. *Macromolecules,* 40**,** 4165-4172.

NEBURCHILOV, V., MARTIN, J., WANG, H. J. & ZHANG, J. J. 2007. A review of polymer electrolyte membranes for direct methanol fuel cells. *Journal of Power Sources,* 169**,** 221-238.

NOGAMI, M., DAIKO, Y., AKAI, T. & KASUGA, T. 2001. Dynamics of Proton Transfer in the Sol-Gel-Derived P2O5-SiO2 Glasses. *J. Phys. Chem. B,* 105**,** 4653-4656.

NOGAMI, M., NAGAO, R., WONG, C., KASUGA, T. & HAYAKAWA, T. 1999. High Proton Conductivity in Porous P_2O_5-SiO_2 Glasses. *The Journal of Physical Chemistry B,* 103**,** 9468-9472.

OH, S. Y., YOSHIDA, T., KAWAMURA, G., MUTO, H., SAKAI, M. & MATSUDA, A. 2010. Inorganic-organic composite electrolytes consisting of polybenzimidazole and Cs-substituted heteropoly acids and their application for medium temperature fuel cells. *Journal of Materials Chemistry,* 20**,** 6359-6366.

OSAMU NAKAMURA, TERUO KODAMA & OGINO, I. 1979. High-conductivity solid proton conductors: dodecamolybdophoric acid and dodecatungstophosphoric acid crystals. *Chemistry Letters***,** 17-18.

OTOMO, J., SHIGEOKA, H., NAGAMOTO, H. & TAKAHASHI, H. 2005. Phase transition behavior and proton conduction mechanism in cesium hydrogen sulfate/silica composite. *Journal of Physics and Chemistry of Solids,* 66**,** 21-30.

PARK, C. H., LEE, C. H., GUIVER, M. D. & LEE, Y. M. Sulfonated hydrocarbon membranes for medium-temperature and low-humidity proton exchange membrane fuel cells (PEMFCs). *Progress in Polymer Science,* 36**,** 1443-1498.

PARTHASARATHY, A., SRINIVASAN, S., APPLEBY, A. J. & MARTIN, C. R. 1992. Temperature Dependence of the Electrode Kinetics of Oxygen Reduction at the Platinum/Nafion[registered sign] Interface---A Microelectrode Investigation. *Journal of The Electrochemical Society,* 139**,** 2530-2537.

PERRY, M. L. & FULLER, T. F. 2002. A Historical Perspective of Fuel Cell Technology in the 20th Century. *Journal of The Electrochemical Society,* 149**,** S59-S67.

PETTERSSON, A. & ROSENHOLM, J. B. 2002. Streaming potential studies on the adsorption of amphoteric alkyldimethylamine and alkyldimethylphosphine oxides on mesoporous silica from aqueous solution. *Langmuir,* 18**,** 8447-8454.

PONOMAREVA, V. G. & SHUTOVA, E. S. 2005. Composite electrolytes Cs-3(H2PO4)(HSO4)(2)/SiO2 with high proton conductivity. *Solid State Ionics,* 176**,** 2905-2908.

PONOMAREVA, V. G. & SHUTOVA, E. S. 2007. High-temperature behavior of CsH2PO4 and CsH2PO4-SiO2 composites. *Solid State Ionics,* 178**,** 729-734.

QI, Z. & KAUFMAN, A. 2002. Improvement of water management by a microporous sublayer for PEM fuel cells. *Journal of Power Sources,* 109**,** 38-46.

RAMAN, R. K., MURGIA, G. & SHUKLA, A. K. 2004. A solid-polymer electrolyte direct methanol fuel cell with a methanol-tolerant cathode and its mathematical modelling. *Journal of Applied Electrochemistry,* 34**,** 1029-1038.

RANDOV, A., HOVORKA, S., IZAK, P. & BARTOVSK, L. 2008. Swelling of Nafion in methanol-water-inorganic salt ternary mixtures. *Journal of Electroanalytical Chemistry,* 616**,** 117-121.

RAO, P. M., GOLDBERG-OPPENHEIMER, P., KABABYA, S., VEGA, S. & LANDAU, M. 2007. Proton enriched high-surface-area cesium salt of phosphotungstic heteropolyacid with enhanced catalytic activity fabricated by nanocasting strategy. *Journal of Molecular Catalysis a-Chemical,* 275**,** 214-227.

RAO, P. M., WOLFSON, A., KABABYA, S., VEGA, S. & LANDAU, M. V. 2005. Immobilization of molecular H3PW12O40 heteropolyacid catalyst in alumina-grafted silica-gel and mesostructured SBA-15 silica matrices. *Journal of Catalysis,* 232**,** 210-225.

RAO, P. M., WOLFSON, A., LANDAU, M. V. & HERSKOWITZ, M. 2004. Efficient immobilization of 12-tungstophosphoric acid catalyst at the surface of silica support grafted with alumina. *Catalysis Communications,* 5**,** 327-331.

RAVIKOVITCH, P. I. & NEIMARK, A. V. 2002. Experimental confirmation of different mechanisms of evaporation from ink-bottle type pores: Equilibrium, pore blocking, and cavitation. *Langmuir,* 18**,** 9830-9837.

REN, X., SPRINGER, T. E. & GOTTESFELD, S. 2000. Water and methanol uptakes in nafion membranes and membrane effects on direct methanol cell performance. *Journal of the Electrochemical Society,* 147**,** 92-98.

ROCCHICCIOLI-DELTCHEFF, C., FOURNIER, M., FRANCK, R. & THOUVENOT, R. 1983. Vibrational investigations of polyoxometalates. 2. Evidence for anion-anion interactions in molybdenum(VI) and tungsten(VI) compounds related to the Keggin structure. *Inorganic Chemistry,* 22**,** 207-216.

SADAKIYO, M., YAMADA, T. & KITAGAWA, H. 2009. Rational Designs for Highly Proton-Conductive Metal-Organic Frameworks. *Journal of the American Chemical Society,* 131**,** 9906-+.

SAKAMOTO, Y., DIAZ, I., TERASAKI, O., ZHAO, D., PEREZ-PARIENTE, J., KIM, J. M. & STUCKY, G. D. 2002. Three-Dimensional Cubic Mesoporous Structures of SBA-12 and Related Materials by Electron Crystallography. *The Journal of Physical Chemistry B,* 106**,** 3118-3123.

SAMMS, S. R., WASMUS, S. & SAVINELL, R. F. 1996. Thermal Stability of Proton Conducting Acid Doped Polybenzimidazole in Simulated Fuel Cell Environments. *Journal of The Electrochemical Society,* 143**,** 1225-1232.

SAYLER, F. M., BAKKER, M. G., SMATT, J. H. & LINDEN, M. 2010. Correlation between Electrical Conductivity, Relative Humidity, and Pore Connectivity in Mesoporous Silica Monoliths. *Journal of Physical Chemistry C,* 114**,** 8710-8716.

SHAIR, C., LERNER, S., JOYNER, P. & EVANS, G. E. 1967. A review of batteries and fuel cells for space power systems. *Journal of Spacecrafts and Rockets,* 4**,** 833-838.

SHAO, Z. G., XU, H. F., LI, M. Q. & HSING, I. M. 2006. Hybrid Nafion-inorganic oxides membrane doped with heteropolyacids for high temperature operation of proton exchange membrane fuel cell. *Solid State Ionics,* 177**,** 779-785.

SHARIFI, M., MARSCHALL, R., WILKENING, M. & WARK, M. 2010. Proton conductivity of ordered mesoporous materials containing aluminium. *Journal of Power Sources,* 195**,** 7781-7786.

SONE, Y., EKDUNGE, P. & SIMONSSON, D. 1996. Proton conductivity of Nafion 117 as measured by a four-electrode AC impedance method. *Journal of The Electrochemical Society,* 143**,** 1254-1259.

SRINIVASAN, S., TICIANELLI, E. A., DEROUIN, C. R. & REDONDO, A. Advances in solid polymer electrolyte fuel cell technology with low platinum loading electrodes. *Journal of Power Sources,* 22**,** 359-375.

STAITI, P., ARICO, A. S., BAGLIO, V., LUFRANO, F., PASSALACQUA, E. & ANTONUCCI, V. 2001. Hybrid Nafion-silica membranes doped with heteropolyacids for application in direct methanol fuel cells. *Solid State Ionics,* 145**,** 101-107.

STANIS, R. J., KUO, M. C., RICKETT, A. J., TURNER, J. A. & HERRING, A. M. 2008. Investigation into the activity of heteropolyacids towards the oxygen reduction reaction on PEMFC cathodes. *Electrochimica Acta,* 53**,** 8277-8286.

STEELE, B. C. H. & HEINZEL, A. 2001. Materials for fuel-cell technologies. *Nature,* 414**,** 345-352.

STEVENS, J. R., WIECZOREK, W., RADUCHA, D. & JEFFREY, K. R. 1997.

Proton conducting gel/H_3PO_4 electrolytes. *Solid State Ionics,* 97**,** 347-358.

SUROWIEC, J. & BOGOCZEK, R. 1988. Studies on the thermal stability of the perfluorinated cation-exchange membrane Nafion-417. *Journal of Thermal Analysis and Calorimetry,* 33**,** 1097-1102.

SWEIKART, M. A., HERRING, A. M., TURNER, J. A., WILLIAMSON, D. L., MCCLOSKEY, B. D., BOONRUENG, S. R. & SANCHEZ, M. 2005. 12-tungstophosphoric acid composites with sulfonated or unsulfonated epoxies for high-temperature PEMFCs. *Journal of The Electrochemical Society,* 152**,** A98-A103.

TAN, A. R., DE CARVALHO, L. M. & GOMES, A. D. 2005. Nanostructured proton-conducting membranes for fuel cell applications. *Macromolecular Symposia,* 229**,** 168-178.

TANG, H. & JIANG, S. P. 2008. Self-Assembled Pt/Mesoporous Silica-Carbon Electrocatalysts for Elevated-Temperature Polymer Electrolyte Membrane Fuel Cells. *Journal of Physical Chemistry C,* 112**,** 19748-19755.

TANG, H. L., PAN, M., LU, S. F., LU, J. L. & JIANG, S. P. 2010. One-step synthesized HPW/meso-silica inorganic proton exchange membranes for fuel cells. *Chemical Communications,* 46**,** 4351-4353.

TATSUMISAGO, M., HONJO, H., SAKAI, Y. & MINAMI, T. 1994. PROTON-CONDUCTING SILICA-GEL FILMS DOPED WITH A VARIETY OF ELECTROLYTES. *Solid State Ionics,* 74**,** 105-108.

TAZI, B. & SAVADOGO, O. 2000. Parameters of PEM fuel-cells based on new membranes fabricated from Nafion? silicotungstic acid and thiophene. *Electrochimica Acta,* 45**,** 4329-4339.

THAMPAN, T., MALHOTRA, S., TANG, H. & DATTA, R. 2000. Modeling of Conductive Transport in Proton-Exchange Membranes for Fuel Cells. *Journal of The Electrochemical Society,* 147**,** 3242-3250.

TOMITA, A., KAJIYAMA, N., KAMIYA, T., NAGAO, M. & HIBINO, T. 2007. Intermediate-temperature proton conduction in Al3+-doped SnP2O7. *Journal of The Electrochemical Society,* 154**,** B1265-B1269.

TUNG, S. P. & HWANG, B. J. 2005. Synthesis and characterization of hydrated phosphor-silicate glass membrane prepared by an accelerated sol-gel process with water/vapor management. *Journal of Materials Chemistry,* 15**,** 3532-3538.

UKSHE, E. A., LEONOVA, L. S. & KOROSTELEVA, A. I. 1989. Protonic conduction in heteropoly compounds. *Solid State Ionics,* 36**,** 219-223.

UMA, T. & NOGAMI, M. 2007a. Characterization and performance improvement of H-2/O-2 fuel cells based on glass membranes. *Journal of The Electrochemical Society,* 154**,** B845-B851.

UMA, T. & NOGAMI, M. 2007b. A novel glass membrane for low temperature H_2/O_2 fuel cell electrolytes. *Fuel Cells,* 7**,** 279-284.

UMA, T. & NOGAMI, M. 2007c. Structural and transport properties of mixed phosphotungstic acid/phosphomolybdic acid/SiO_2 glass membranes for H_2/O_2 fuel cells. *Chemistry of Materials,* 19**,** 3604-3610.

UMA, T. & NOGAMI, M. 2007d. Structural and transport properties of mixed phosphotungstic acid/phosphomolybdic acid/SiO2 glass membranes for H-2/O-2 fuel cells. *Chemistry of Materials,* 19**,** 3604-3610.

UMA, T. & NOGAMI, M. 2008a. Properties of PWA/ZrO2-doped phosphosilicate glass composite membranes for low-temperature H-2/O-2 fuel cell applications. *Journal of Membrane Science,* 323**,** 11-16.

UMA, T. & NOGAMI, M. 2008b. Proton-Conducting Glass Electrolyte. *Anal. Chem.,* 80**,** 506-508.

UMA, T. & NOGAMI, M. 2008c. Proton-conducting glass electrolyte. *Analytical Chemistry,* 80**,** 506-508.

UMA, T. & NOGAMI, M. 2009. PMA/ZrO2-P2O5-SiO2 glass composite membranes: H_2/O_2 fuel cells. *Journal of Membrane Science,* 334**,** 123-128.

VICHI, F. M., TEJEDOR-TEJEDOR, M. I. & ANDERSON, M. A. 2000. Effect of pore-wall chemistry on proton conductivity in mesoporous titanium dioxide. *Chemistry of Materials,* 12**,** 1762-1770.

WAN, Y. & ZHAO, D. Y. 2007. On the controllable soft-templating approach to mesoporous silicates. *Chemical Reviews,* 107**,** 2821-2860.

WANG, D. L., LU, S. F. & JIANG, S. P. 2010. Pd/HPW-PDDA-MWCNTs as effective non-Pt electrocatalysts for oxygen reduction reaction of fuel cells. *Chemical Communications,* 46**,** 2058-2060.

WANG, H. & CAPUANO, G. A. 1998. Behavior of Raipore Radiation-Grafted Polymer Membranes in H_2O Fuel Cells. *Journal of The Electrochemical*

Society, 145**,** 780-784.

WEBER, J., KREUER, K.-D., MAIER, J. & THOMAS, A. 2008. Proton Conductivity Enhancement by Nanostructural Control of Poly(benzimidazole)-Phosphoric Acid Adducts. *Advanced Materials,* 20**,** 2595-2598.

WEE, L. H., BAJPE, S. R., JANSSENS, N., HERMANS, I., HOUTHOOFD, K., KIRSCHHOCK, C. E. A. & MARTENS, J. A. 2010. Convenient synthesis of Cu-3(BTC)(2) encapsulated Keggin heteropolyacid nanomaterial for application in catalysis. *Chemical Communications,* 46**,** 8186-8188.

WIECZOREK, W. & STEVENS, J. R. 1997. Proton transport in polyacrylamide based hydrogels doped with H_3PO_4 or H_2SO_4. *Polymer,* 38**,** 2057-2065.

WLODARCZYK, R., CHOJAK, M., MIECNIKOWSKI, K., KOLARY, A., KULESZA, P. J. & MARASSI, R. 2006. Electroreduction of oxygen at polyoxometallate-modified glassy carbon-supported Pt nanoparticles. *Journal of Power Sources,* 159**,** 802-809.

WLODARCZYK, R., KOLARY-ZUROWSKA, A., MARASSI, R., CHOJAK, M. & KULESZA, P. J. 2007. Enhancement of oxygen reduction by incorporation of heteropolytungstate into the electrocatalytic ink of carbon supported platinum nanoparticles. *Electrochimica Acta,* 52**,** 3958-3964.

WU, J. F., YUAN, X. Z., MARTIN, J. J., WANG, H. J., YANG, D. J., QIAO, J. L. & MA, J. X. 2010. Proton exchange membrane fuel cell degradation under close to open-circuit conditions Part I: In situ diagnosis. *Journal of Power Sources,* 195**,** 1171-1176.

XIAO, L. X., ZHANG, H. F., SCANLON, E., RAMANATHAN, L. S., CHOE, E. W., ROGERS, D., APPLE, T. & BENICEWICZ, B. C. 2005. High-temperature polybenzimidazole fuel cell membranes via a sol-gel process. *Chemistry of Materials,* 17**,** 5328-5333.

XIE, Z. & HOLDCROFT, S. 2004. Polarization-dependent mass transport parameters for orr in perfluorosulfonic acid ionomer membranes: an EIS study using microelectrodes. *Journal of Electroanalytical Chemistry,* 568**,** 247-260.

XIONG, L., YANG, Y., SHI, J. & NOGAMI, M. 2008. Synthesis and proton conductivity of large-sized crack-free mesostructured phosphorus-oxide-doped silica monoliths. *Microporous and Mesoporous Materials,* 111**,** 343-349.

XIONG, L. M. & NOGAMI, M. 2006. Proton-conducting ordered mesostructured silica monoliths. *Chemistry Letters,* 35**,** 972-973.

XU, C., FAGHRI, A., LI, X. L. & WARD, T. 2010. Methanol and water crossover in a passive liquid-feed direct methanol fuel cell. *International Journal of Hydrogen Energy,* 35**,** 1769-1777.

XU, Y. W., WU, Z. X., ZHANG, L. J., LU, H. J., YANG, P. Y., WEBLEY, P. A. & ZHAO, D. Y. 2009. Highly Specific Enrichment of Glycopeptides Using Boronic Acid-Functionalized Mesoporous Silica. *Analytical Chemistry,* 81**,** 503-508.

YAMADA, M. & HONMA, I. 2006. Heteropolyacid-encapsulated self-assembled materials for anhydrous proton-conducting electrolytes. *Journal of Physical Chemistry B,* 110**,** 20486-20490.

YAMADA, M., LI, D., HONMA, I. & ZHOU, H. 2005a. A Self-Ordered, Crystalline Glass, Mesoporous Nanocomposite with High Proton Conductivity of 2x10^{-2} S cm^{-1} at Intermediate Temperature. *Journal of the American Chemical Society,* 127**,** 13092-13093.

YAMADA, M., LI, D. L., HONMA, I. & ZHOU, H. S. 2005b. A self-ordered, crystalline glass, mesoporous nanocomposite with high proton conductivity of 2 x 10(-2) S cm(-1) at intermediate temperature. *Journal of the American Chemical Society,* 127**,** 13092-13093.

YAN, X. M., MEI, P., MI, Y. Z., GAO, L. & QIN, S. X. 2009. Proton exchange membrane with hydrophilic capillaries for elevated temperature PEM fuel cells. *Electrochemistry Communications,* 11**,** 71-74.

YANG, C., COSTAMAGNA, P., SRINIVASAN, S., BENZIGER, J. & BOCARSLY, A. B. 2001. Approaches and technical challenges to high temperature operation of proton exchange membrane fuel cells. *Journal of Power Sources,* 103**,** 1-9.

YANG, C., SRINIVASAN, S., BOCARSLY, A. B., TULYANI, S. & BENZIGER, J. B. 2004. A comparison of physical properties and fuel cell performance of Nafion and zirconium phosphate/Nafion composite membranes. *Journal of Membrane Science,* 237**,** 145-161.

YANG, C. M., SCHMIDT, W. & KLEITZ, F. 2005a. Pore topology control of three-dimensional large pore cubic silica mesophases. *Journal of Materials Chemistry,* 15**,** 5112-5114.

YANG, J., JANIK, M. J., MA, D., ZHENG, A. M., ZHANG, M. J., NEUROCK, M., DAVIS, R. J., YE, C. H. & DENG, F. 2005b. Location, acid strength, and mobility of the acidic protons in Keggin 12-H3PW12O40: A combined solid-state NMR spectroscopy and DFT quantum chemical calculation study. *Journal of the American Chemical Society,* 127**,** 18274-18280.

YANG, Y. X., BOURGEOIS, L., ZHAO, C. X., ZHAO, D. Y., CHAFFEE, A. & WEBLEY, P. A. 2009. Ordered micro-porous carbon molecular sieves containing well-dispersed platinum nanoparticles for hydrogen storage. *Microporous and Mesoporous Materials,* 119**,** 39-46.

YE, Y. S., CHEN, W. Y., HUANG, Y. J., CHENG, M. Y., YEN, Y. C., CHENG, C. C. & CHANG, F. C. 2010. Preparation and characterization of high-durability zwitterionic crosslinked proton exchange membranes. *Journal of Membrane Science,* 362**,** 29-37.

YU, J., YI, B., XING, D., LIU, F., SHAO, Z., FU, Y. & ZHANG, H. 2003. Degradation mechanism of polystyrene sulfonic acid membrane and application of its composite membranes in fuel cells. *Physical Chemistry Chemical Physics,* 5**,** 611-615.

YU, T., ZHANG, H., YAN, X., CHEN, Z., ZOU, X., OLEYNIKOV, P. & ZHAO, D. 2006. Pore Structures of Ordered Large Cage-Type Mesoporous Silica FDU-12s. *The Journal of Physical Chemistry B,* 110**,** 21467-21472.

ZAWODZINSKI JR, T. A., SPRINGER, T. E., URIBE, F. & GOTTESFELD, S. 1993. Characterization of polymer electrolytes for fuel cell applications. *Solid State Ionics,* 60**,** 199-211.

ZAWODZINSKI, T. A., SPRINGER, T. E., DAVEY, J., JESTEL, R., LOPEZ, C., VALERIO, J. & GOTTESFELD, S. 1993. A Comparative-Study of Water-Uptake by and Transport through Ionomeric Fuel-Cell Membranes. *Journal of the Electrochemical Society,* 140**,** 1981-1985.

ZENG, J., ZHOU, Y., LI, L. & JIANG, S. P. 2011a. Phosphotungstic acid functionalized silica nanocomposites with tunable bicontinuous mesoporous structure and superior proton conductivity and stability for fuel cells. *Physical Chemistry Chemical Physics,* 13**,** 10249-10257.

ZENG, J., ZHOU, Y. H., LI, L. & JIANG, S. P. 2011b. Phosphotungstic acid functionalized silica nanocomposites withn tunable bicontinuous mesoporous structure and superior proton conductivity and stability for fuel cells. *Phys Chem Chem Phys***,** DOI:10.1039/c1cp20076c.

ZHANG, J., TANG, Y., SONG, C., XIA, Z., LI, H., WANG, H. & ZHANG, J. 2008. PEM fuel cell relative humidity (RH) and its effect on performance at high temperatures. *Electrochimica Acta,* 53**,** 5315-5321.

ZHANG, J., XIE, Z., ZHANG, J., TANG, Y., SONG, C., NAVESSIN, T., SHI, Z., SONG, D., WANG, H., WILKINSON, D. P., LIU, Z.-S. & HOLDCROFT, S. 2006a. High temperature PEM fuel cells. *Journal of Power Sources,* 160**,** 872-891.

ZHANG, J. L., XIE, Z., ZHANG, J. J., TANGA, Y. H., SONG, C. J., NAVESSIN, T., SHI, Z. Q., SONG, D. T., WANG, H. J., WILKINSON, D. P., LIU, Z. S. & HOLDCROFT, S. 2006b. High temperature PEM fuel cells. *Journal of Power Sources,* 160**,** 872-891.

ZHAO, T. S., KREUER, K.-D. & NGUYEN, T. V. 2007. *Advances in Fuel Cell*, ELSEVIER.

ZHOU, J., ZHANG, Y., ZHAO, X. S. & RAY, A. K. 2006. Photodegradation of Benzoic Acid over Metal-Doped TiO2. *Industrial & Engineering Chemistry Research,* 45**,** 3503-3511.

ZHU, Z. R. & YANG, W. M. 2009. Preparation, Characterization and Shape-Selective Catalysis of Supported Heteropolyacid Salts K2.5H0.5PW12O40, (NH4)(2.5)H0.5PW12O40, and Ce0.83H0.5PW12O40 on MCM-41 Mesoporous Silica. *Journal of Physical Chemistry C,* 113**,** 17025-17031.

ZISEKAS, S., KARAGIANNAKIS, G. & STOUKIDES, M. 2005. Electrode polarization at the Pd/proton conductor interface. *Solid State Ionics,* 176**,** 2929-2934.